

OPTICAL NAVIGATION TECHNIQUES FOR MINIMALLY INVASIVE ROBOTIC SURGERIES

by

Hanh Nguyen Dung Le

A dissertation submitted to The Johns Hopkins University in conformity with
the requirements for the degree of Doctor of Philosophy.

Baltimore, Maryland

October, 2018

© Hanh Nguyen Dung Le 2018

All rights reserved

Abstract

Minimally invasive surgery (MIS) involves small incisions in a patient's body, leading to reduced medical risk and shorter hospital stays compared to open surgeries. For these reasons, MIS has experienced increased demand across different types of surgery. MIS sometimes utilizes robotic instruments to complement human surgical manipulation to achieve higher precision than can be obtained with traditional surgeries. Modern surgical robots perform within a master-slave paradigm, in which a robotic slave replicates the control gestures emanating from a master tool manipulated by a human surgeon. Presently, certain human errors due to hand tremors or unintended acts are moderately compensated at the tool manipulation console. However, errors due to robotic vision and display to the surgeon are not equivalently addressed. Current vision capabilities within the master-slave robotic paradigm are supported by perceptual vision through a limited binocular view, which considerably impacts the hand-eye coordination of the surgeon and provides no quantitative geometric localization for robot targeting. These limitations lead to unexpected surgi-

ABSTRACT

cal outcomes, and longer operating times compared to open surgery.

To improve vision capabilities within an endoscopic setting, we designed and built several image guided robotic systems, which obtained sub-millimeter accuracy. With this improved accuracy, we developed a corresponding surgical planning method for robotic automation. As a demonstration, we prototyped an autonomous electro-surgical robot that employed quantitative 3D structural reconstruction with near infrared registering and tissue classification methods to localize optimal targeting and suturing points for minimally invasive surgery. Results from validation of the cooperative control and registration between the vision system in a series of *in vivo* and *in vitro* experiments are presented and the potential enhancement to autonomous robotic minimally invasive surgery by utilizing our technique will be discussed.

Dissertation Readers:

Jin Ung Kang, PhD (Primary Advisor)

Jacob Suter Jammer Professor

Department of Electrical and Computer Engineering

Johns Hopkins Whiting School of Engineering

Axel Krieger, PhD

Assistant Professor

Department of Mechanical Engineering

University of Maryland A. James Clark School of Engineering

ABSTRACT

Simon Leonard, PhD

Assistant Research Professor

Department of Computer Science

Johns Hopkins Whiting School of Engineering

Mark Foster, PhD

Associate Professor

Department of Electrical and Computer Engineering

Johns Hopkins Whiting School of Engineering

Acknowledgments

Acknowledgment is the only section in the PhD dissertation fit for expressing gratitude for all the support I received during my PhD adventure. I am heartily thankful and owe my deepest gratitude to those who have helped me over the years. I wish all the best to you and hope our paths cross again.

First and foremost, I owe much to my advisor, Professor Jin Ung Kang, who has guided me through all my work with encouragement, insights and wisdom. Dr. Kang has helped me grow as a member of the photonics community and inspired me to expand my knowledge and ability in the field. Next I thank Professors Axel Krieger, Simon Leonard and Zhaoyang Wang for providing me the opportunity to work with them and for giving me chances to apply my skill set to robotic control and computer vision. I also appreciate your patience and inspiration across our collaborative projects. This work would also not have taken place without the support of the National Institute of Biomedical Imaging and Bioengineering (1R01EB020610) and the BRAIN Initiative (R24MH106083-03).

ACKNOWLEDGMENTS

Next I thank the Johns Hopkins community for its encouraging environment to push my intellectual curiosity, its commitment to drive innovation without barriers and the collaborative opportunities it enabled to work with cross-discipline communities both domestically and internationally. I thank the Global Engineering Innovations and the Optical Society of America for the outreach opportunities that let me serve and learn. I thank Cora Mayenschein, Debbie Race, Melissa Gibbins and Sathappan Ramesh from the ECE Department for your patience and resources to support my work and activities, and Justin Opfermann, Berk Gonenc and Jaepyong Cha for your career advice and objective scientific feedback.

I also wish to show my appreciation to the following collaborators, colleagues and friends for their support during my PhD work: Francis Peach; Professors Philippe Pouliquen, Trac Tran, Solange Brown, Dwight Bergles, Emad Bector, Amy Foster, Mark Foster, Peter Gehlbach, Jacob Khurgin and Xingde Li; and Dohyun Kim PhD, Peter Kim MD, Hieu Nguyen, Heather Valentine, Jeeun Kang PhD, Kai Zhang PhD, Kangmei Li PhD, Hongchen Sun PhD, Anji Gau, Juhyun Kim PhD, Soohyun Lee, Shuwen Wei, Shoujing Guo, Hamed Seidi PhD, Rebecca Pak, Michael Kam, Jiawei Ge, Gyeong Cheon PhD, Vy Bui and Nicole De Vera. Each of these individuals gave me their time, resources, and advice to strengthen my pursuits, enrich my knowledge and shape my thinking.

ACKNOWLEDGMENTS

My greatest gratitude goes to my parents Minh Le and Oanh Nguyen, my dear husband Daniel Stark, my brother Thao Le and my in-laws Susan and Joshua Stark, and Mary, Alan, Alexandra and Christopher Ford. Thank you for your constant love, support and wisdom.

Dedication

To my parents and my dear husband.

Contents

Abstract	ii
Acknowledgments	v
List of Tables	xix
List of Figures	xx
1 Introduction	1
1.1 An Overview of Robotic Assistance in Medicine	1
1.1.1 Surgical CAD/CAM Robot	2
1.1.2 Master-Slave Surgical Assistant System	3
1.1.3 Autonomous Surgical Robot	5
1.2 Development of Endoscopy in Medical Imaging	7
1.2.1 The Evolution of Endoscopy	8
1.2.2 Endoscopic Design for Minimally Invasive Surgery	10
1.2.2.1 Flexible Endoscope	12

CONTENTS

1.2.2.2	Rigid Endoscope	13
2	Imaging in Minimally Invasive Robotic Surgery	16
2.1	Assisted Functional Medical Imaging Modalities	16
2.1.1	Direct Functional Imaging using EEG, ERP, MEG	17
2.1.2	Indirect Functional Imaging	18
2.1.2.1	Positron Emission Tomography	18
2.1.2.2	Functional Magnetic Resonance Imaging	19
2.1.2.3	Ultrasound Imaging	20
2.1.2.4	Diffuse Optical Imaging	20
2.1.3	Multi-Functional Image-Guided Surgery	21
2.2	Visualizations in Minimally Invasive Surgery	23
2.2.1	Stereoscopy	24
2.2.2	Time-of-Flight	26
2.2.3	Plenoptic Imaging	27
2.2.4	Structured Illumination	28
3	Endoscopic Imaging System for Autonomous Robotic MIS	32
3.1	Motivation	32
3.2	Endoscopic Imaging System for 3D Reconstruction using Plenop- tic Technique	33
3.2.1	System Contributions	33

CONTENTS

3.2.2	System Setup	34
3.2.3	3D Reconstruction Principle	36
3.2.4	Accuracy assessment	38
3.2.4.1	Planar Checkerboard Surface	39
3.2.4.2	Inhomogeneous Sample	43
3.2.5	Lessons Learned	43
3.3	Endoscopic Imaging System for 3D Reconstruction using Struc- tured Illumination Technique	46
3.3.1	System Contributions	46
3.3.2	System Setup	47
3.3.3	System Synchronization	49
3.3.4	System Speed	50
3.3.5	Camera-Projector Calibration	51
3.3.5.1	Triangulation	51
3.3.5.2	Camera Parameter Optimization	54
3.3.6	Geometric Reconstruction using Structured Illumination Technique	56
3.3.7	Optical Characteristics of the System	59
3.3.7.1	Depth of Field and Axial Resolution	59
3.3.7.2	Lateral resolution	61
3.3.8	System Sensitivity in 3D Tissue Reconstruction	62

CONTENTS

3.3.8.1	Experimental Procedure	62
3.3.8.2	Result	67
3.3.9	Lessons Learned	73
4	Tissue Property Extraction using Multispectral Reflectance Imaging Technique	77
4.1	Motivation	77
4.2	First Prototype: Open-space Multispectral Imaging System . . .	79
4.2.1	System Contributions	79
4.2.2	System Setup	79
4.2.3	Experimental Procedures and Result	81
4.2.3.1	Tissue Classification	81
4.2.3.2	Tissue Perfusion Measurement	85
4.2.3.2.1	Tissue Perfusion during Mesentery Occlusion	87
4.2.3.2.2	Tissue Perfusion with Different Suturing Spacing and Tension Setting	87
4.2.4	Lessons Learned	93
4.3	Second Prototype: Multispectral Imaging Endoscope for Minimally Invasive Surgery	94
4.3.1	System Contribution	94
4.3.2	System Setup	95

CONTENTS

4.3.3	PCB Design for 3D-Perfusion Mode Control	95
4.3.4	Optical Coupling Assembly from LED to Light Delivery Fiber Bundle	97
4.3.5	Experimental Procedures and Result	98
4.3.6	Lessons Learned	102
5	Endoscopic Guidance for Minimally Invasive Surgical Robot	103
5.1	Motivation	103
5.2	First Prototype: Surgical Robot with 3D Imaging under Visible Illumination	105
5.2.1	System Contributions	105
5.2.2	System Setup	106
5.2.2.1	3D Imaging Endoscope	106
5.2.2.2	Robotic System and Control Method	108
5.2.2.3	Multi Degree of Freedom Electro Surgical Tool . .	108
5.2.3	Imaging System and Robotic Control Registration	110
5.2.4	Experimental Procedures and Computational Strategies for Target Localization	110
5.2.4.1	Targeting Test	111
5.2.4.2	Cutting Test	112
5.2.4.2.1	Cutting Trajectory Path and Normal Vec- tor Calculations	112

CONTENTS

5.2.5	Results	115
5.2.5.1	Targeting Accuracy	115
5.2.5.2	Cutting Accuracy	115
5.2.6	Lessons Learned	117
5.3	Second Prototype: Surgical Robot with 3D Imaging under dual VIS-NIR Illumination	120
5.3.1	System Contributions	120
5.3.2	System Improvements	121
5.3.2.1	Dual VIS-NIR Mode	121
5.3.2.1.1	NIR Imaging Sensor	121
5.3.2.1.2	NIR-Enhanced Endoscope	122
5.3.2.1.2.1	Transmission of The Light Deliv- ery Fiber of A Rigid Endoscope . .	122
5.3.2.1.2.2	Transmission of The Optical As- sembly Within A Rigid Endoscope	124
5.3.2.1.3	Light Source	126
5.3.2.1.4	Light Delivery Cable	126
5.3.2.2	Surgical Tool Modification	126
5.3.2.3	Projection Fringe Reduction	128
5.3.3	Dual VIS-NIR imaging system setup	129
5.3.4	System Registration	131

CONTENTS

5.3.5	Accuracy Evaluation	134
5.3.5.1	System Targeting 3D-printed Phantom	134
5.3.5.2	System Targeting Accuracy on Tissue	134
5.3.5.3	System Cutting Accuracy on Tissue	136
5.3.6	Lessons Learned	138
5.4	Third Prototype: Surgical Planning Strategy	139
5.4.1	Autonomous Laparoscopic Robotic Suturing with a Novel Actuated Suturing Tool and 3D Endoscope	139
5.4.1.1	System Contributions	139
5.4.1.2	System Setup	141
5.4.1.2.1	3D Imaging Endoscopic System	141
5.4.1.2.2	Suturing Tool	143
5.4.1.3	Surgical Task and Evaluation Criteria	145
5.4.1.4	Control System	145
5.4.1.5	Planning Strategy for Suturing	147
5.4.1.6	High-Level Suturing Logic and Task Planner	148
5.4.1.7	Test Conditions	152
5.4.1.8	Results	153
5.4.1.8.1	Completion Time	153
5.4.1.8.2	Distance Between Stitches	154
5.4.1.8.3	Bite Size	155

CONTENTS

5.4.1.8.4	Number of Stitch Re-Positions	155
5.4.1.9	Lessons Learned	155
5.4.2	An Extension of Cutting Segmentation with Planned NIR	
	Markers for Autonomous Suturing Planning	156
5.4.2.1	System Contributions	156
5.4.2.2	System Setup	157
5.4.2.3	Suturing Mapping Strategy	157
5.4.2.4	Lessons Learned	160
6	Intra-operative Guiding of the Cavernous Nerve Network using	
	Near-infrared Cyanine Voltage-Sensitive Dye	162
6.1	Motivation	162
6.2	System Contribution	166
6.3	Method	166
6.3.1	Fluorescence Imaging Fiberscope	166
6.3.2	Animal preparation	169
6.3.3	Electrical CN Stimulation and Intracavernosal Pressure	
	Monitoring	170
6.3.4	Frozen-section Histopathological Analysis of ex-vivo Rat	
	Prostate Samples	171
6.4	Experimental Procedure	171
6.5	Results	174

CONTENTS

6.5.1	Imaging System Resolution Evaluation	174
6.5.2	System Performance for Intra-operative Nerve Localiza- tion within Prostatetomy Setting	175
6.6	Lessons Learned	180
7	Concluding Remarks and Future Work	186
A	Through-skull Vasculature Assessment Using Fluorescence Brain Imaging on Murine Models at Around 800 nm	188
A.1	Motivation and System Contributions	188
A.2	System Setup	190
A.3	Experimental Procedure	191
A.3.1	In-vitro Fluorescence Imaging of Indocyanine Green Agent through Human Cadaver Bone	191
A.3.2	In-vivo Through Skull Brain Fluorescence Imaging in Murine Model	192
A.4	Image Enhancement Methods	193
A.5	System Resolution Evaluation	193
A.5.1	USAS 1951 Resolution Target	193
A.5.2	Through-Skull Fluorescence Imaging	194
A.5.3	Monitoring of Nano Particle Diffusion within Brain	196
A.6	Lessons Learned	202

CONTENTS

B Real-time intra-operative Guidance using a Dual Photoacoustic and Pulsed Fluorescence Imaging for Robotic Assisted Surgery	203
B.1 Motivation and System Contributions	204
B.2 System Setup	204
B.3 Imaging Sensitivity on an ICG Fluorescence Phantom	206
Bibliography	207
Vita	246

List of Tables

3.1	Reconstruction accuracy and precision at two planar angle deviations at 0 degree and 45 degrees. Unit is in millimeters.	41
3.2	Typical parameter settings for the camera.	50
3.3	Typical parameter settings for the projector.	51
4.1	Leak pressure test of the sutured intestinal tissue with multiple spacing and tension forces.	93
5.1	Results of the targeting accuracy test	115
5.2	Results of system accuracy on kidney phantom	135
5.3	Comparison of experiment results via completion time.	154
5.4	Comparison of experiment results via distance between stitches, bite size, and number of suture repositioning.	154

List of Figures

1.1	First designs of the endoscopic era. Adapted from [1].	9
1.2	Optical layout of a conventional endoscope with one-stage relay assembly	11
1.3	Optical layout of a flexible fiber endoscope	12
1.4	Optical layouts of relay systems for rigid endoscopes.	14
2.1	Triangulation is used in stereo imaging system for 3D reconstruction. Adapted from [2].	25
2.2	Geometrical reconstruction using structured illumination	31
3.1	Schematic of the endoscopic setup with the plenoptic camera and relay lens system.	36
3.2	Triangulation principle for virtual depth estimation. IP: Image plane, MLA: Micro lens array.	37
3.3	Resolution and contrast measurements.	39
3.4	(a) Micro lens image of the checker board at 0 degree with (b) its depth map and (c, d) point cloud data at different views.	40
3.5	(a) Micro lens image of the checker board at 45 degrees with (b) its depth map and (c, d) point cloud data at different views.	42
3.6	(a-c) Micro lens image of a plane and inhomogeneous objects and (d-f) its reconstructed depth maps.	44
3.7	(a) Micro lens image of a fowl ventricular specimen and (b-d) its 3D reconstructions at multiple angles.	44
3.8	3D SI imaging endoscopic system.	49
3.9	Workflow for 3D imaging system control and data collection. . . .	50
3.10	Triangulation in structure illumination using camera-projector setup. Adapted from [3]	52

LIST OF FIGURES

3.11	Bright-field image of the DOF target (Left) with relative intensity profile (Right) along the region within the red segment (from marker 15 mm to marker 45 mm on the target surface)	60
3.12	DOF height map. Camera exposure is set at 20 ms/fringed image. The colormap denotes height measurements from the reference zero plane—farthest from the distal end of the scope—to the closest plane from the distal end of the scope.	62
3.13	(a-c) 3D point cloud population of Left, Middle and Right regions (Marked as red ROIs in Figure 3.12(a). Colorbar displays height in millimeters. The plots are viewed along the 45° angle surface of the DOF target. The fit plane is calculated as the best fit of the collected point cloud population. (d-f) 3D precision of the Left, Middle and Right regions with blue middle lines referring to distal means between 3D point clouds to the fit plane, the blue shaded region indicating the standard deviation of distal error.	63
3.14	3D precision in 4 directions as described in the inset along the x -axis (X in red and XR in green) and along the y -axis (Y in blue and YR in magenta). The gray boundary box indicates a distal error constraint between -0.5 mm to 0.5 mm.	64
3.15	Lateral resolution of the system validated using a USAF 1951 target, indicating lateral resolution of 49.61 μm (Group 3, Element 3)	65
3.16	(a, b) Bright field reflectance images of a DOF target covered by intestine (Top) and skin flaps (Bottom). (c, d) The corresponding depth map with a depth color bar in millimeters. Camera exposure is set at 40 ms/fringed image. (e, f) 3D precision with mean and standard deviation of the distance from reconstructed point cloud to the fit plane. Blue middle line indicates mean distance between 3D point clouds to the fit plane, and the blue shaded region refers to the standard deviation of the distal error.	68
3.17	(a, b, c) Bright field reflectance images of a DOF target covered by intestine at different camera exposure of 20 ms (Top), 30 ms (Middle) and 40 ms (Bottom). (d, e, f) The corresponding depth map with depth color bar in millimeters. (g, h, i) 3D precision with mean and standard deviation of the distance from point cloud to the fit plane. Blue middle line shows mean distance, and the blue shaded region marks the standard deviation of the distal errors.	69
3.18	Height map translational scanning of an intestinal pile with different pigmentation. The depth color bar in Figure 3.18(b) is in millimeters. Video is at 5X speed and can be viewed online. . . .	70
3.19	3D reconstruction of human sample.	71

LIST OF FIGURES

3.20	Height map of anastomosis setup. Camera exposure is set at 33 ms/fringed image. Video is at 5x speed. Videos can be viewed online.	73
3.21	(a, b) Bright field reflectance images of intestinal anastomosis at a camera exposure time of 33 ms without (Top row) and with looping sutures (Bottom row). (c, d) The corresponding depth map with depth color bar in millimeters. (e, f) The corresponding 3D point cloud distribution with segmented tissue fold and suturing stitches marked in red points.	74
4.1	Open-space multispectral imaging setup.	80
4.2	Tissue type segmentation result using SAM method to classify mesentery, mesentery ridges and small intestine. (Top) Spectral images at each filtered illumination. (Middle) SAM endmember results. (Bottom) Endmember summation.	83
4.3	Tissue thickness segmentation result using SAM method on big and small intestine sample with corresponding microCT thickness comparisons. (Top) Combined spectral images from 441 nm, 508 nm and 670 nm spectral images. (Middle) SAM endmember results. Green indicating thinner layer and red indicates thicker layer. (Bottom) MicroCT image with representative thickness measurements.	84
4.4	Suture map and suture placement recommendations.	85
4.5	Perfusion monitoring of intestinal condition on an alive porcine model. Colorbar unit is in percentage.	88
4.6	Sample preparation with the designed looping stitches using the suturing frame.	90
4.7	Perfusion monitoring with multiple suturing and tension settings. Colorbar unit is in percentage.	91
4.8	Tissue segmentation into LEFT, CUT-LINE, and RIGHT regions for perfusion plots in Figure 4.9.	92
4.9	Perfusion monitoring within LEFT, CUT-LINE, and RIGHT regions in Figure 4.8 with multiple suturing and tension settings.	93
4.10	Multispectral imaging setup integrated with other multimodal imaging setup for MIS (used in Section 5.4).	96
4.11	Mode switching mechanism and PCB architecture design.	97
4.12	An example of system synchronization using Mode 3.	98
4.13	Simulated layout and the power view after the LED (D1) and at the fiber focusing plane (D2).	99
4.14	Oxygen saturation measurement of blood phantom. Colorbar unit is in percentage.	100

LIST OF FIGURES

4.15	Total hemoglobin and oxygen saturation measurement of blood phantom on intestinal tissue. Colorbar unit is in percentage. . . .	101
5.1	System layout of Prototype 1.	107
5.2	Controlling architecture of the STAR.	108
5.3	A multi degree of freedom electro surgical tool for semiautonomous electrosurgery. Adaptive from [4].	109
5.4	Computational procedure for targeting and cutting accuracy tests.	111
5.5	Surface reconstruction and path planning for cutting task: (a) Post-processing of point cloud. (b) Surface creation by Delaunay triangulation. (c) Cutting path calculation along the surface. (d) Normal vector generation along the cutting path.	114
5.6	Average normal vector along the trajectory	114
5.7	Pattern of target fiducials (white) and burned marks (black) on a cadaver porcine kidney sample for targeting accuracy assessment.	116
5.8	Procedures to evaluate cutting depth accuracy: a) Slicing the kidney along the cut, b) Segmenting of cut region, c) Calculating the depth via the distance between top and bottom edges.	117
5.9	(a) Transmission spectra of 4 different rigid endoscopic models with 4-mm and 10-mm diameter housing. (b) Light fiber arrangement at each endoscopic distal end. Image not to scale.	123
5.10	(Upper) Transmission of the combined light source. (Lower) Relative Transmission of optical assembly in each scope.	125
5.11	System layout of Prototype 2. IL: Imaging Lens, DM: Dichroic Mirror.	127
5.12	CAD layout of the electro-surgical tool with fixed needle electrode.	128
5.13	Spectral specification of (a) the dual VIS-NIR illuminations and (b) the dichroic mirror.	131
5.14	Coordination diagram of the system.	131
5.15	Registration error evaluation between the 3D CCD and the NIR CMOS camera. The point cloud distribution is de-sampled with 5 point step size for display purpose.	133
5.16	System Accuracy Validation Procedures on phantom.	134
5.17	Centroid locations of the NIR marker before and after the robot (yellow point). The two centroid populations are transformed to calculate RMSE	136
5.18	Cutting length (a) before and (b) after the robot. Unit is in millimeters.	137
5.19	Cutting accuracy determination using post image processing (a) Cross-section of the cut. (b) Thresholded cut segment. (c) Segmented cut boundary.	138
5.20	Laparoscopic robotic suturing system.	142

LIST OF FIGURES

5.21	3D imaging endoscope setup on an UR5 robot. IL: Imaging Lens.	143
5.22	Suturing tool with its components (a) Overall design of the suturing tool, (b) pitch actuation, c) roll actuation, (d) needle drive.	144
5.23	Suture task and metrics.	145
5.24	The autonomous control loop.	146
5.25	Suture planning strategy: (a) A white reflectance image of the cut sample. (b) Collected point cloud with ROI. (c) An example of calculated cut groove, left and right cut edges, and the suture point. (d) An overlay of the calculated coordinates with suture spacing of 4 mm.	149
5.26	Steps of executing a knot: (a) bite, (b) tensioning, (c) first loop, (d) tension of first loop, e) second loop, f) tension of second loop.	150
5.27	Manual suturing using a laparoscopic trainer.	152
5.28	Examples of suturing with (a) manual, (b) autonomous approach.	153
5.29	Multimodal imaging endoscopic setup for surgical planning in minimally invasive robotic surgery.	158
5.30	Suture planning procedure (a) Bright field reflectance image of a incised kidney tissue with planned NIR markers, (b) Collected 3D point cloud with slice sections normal to the cutting axis. (c) Cutting groove and edge detection. (d) Suture location (green dots) is an off-set distance away from the cutting edge (red dots).	160
6.1	Fluorescence fiberscope setup.	168
6.2	Optical design of the focusing assembly for the fiberscope.	169
6.3	In vivo experimental setup for a proof-of-concept of prostatic nerve imaging using near-infrared cyanine VSD: (a) in vivo protocol. (b) The validation of an erectile function using intracavernosal pressure (ICP) monitoring for the electrical stimulation on CN after the direct VSD administration. (c) Corresponding behavioral observation of erectile function at each experimental phase.	173
6.4	Spatial resolution with USAF 1951 Target.	174
6.5	In vivo intra-operative nerve localization: (a) white-light and fluorescence (FL) imaging, (b) time-averaged F/F ₀ trace during stimulation and pre-/post-stimulation phases. MPG, major pelvic ganglion; RCN, right cavernous nerve; Pr, prostate.	176
6.6	Fractional FL intensity change on localized nerve regions: (a) locations of regions-of-interest (ROIs). BG, background; ROICN, CN region; ROICNB, CNB region; (b) the plot of fractional change in FL intensity at each ROI. Note that the plots were corrected by the FL intensity trace quantified at the BG region.	177

LIST OF FIGURES

6.7	Evaluation on motion artifacts during in vivo experiment: (a) region-of-interest in white-light and fluorescence (FL) imaging, (b) normalized cross correlation coefficient and (c) fractional change in FL intensity over time at the entire region-of-interest.	178
6.8	Histopathological analysis on <i>ex vivo</i> rat prostate sample. Dotted line presents the levator fascia covering the prostatic fascia with CNB. White bar indicates 100 μm . PrG, prostatic gland; N, nerve.	180
A.1	(a) Near infrared fluorescence imaging setup and (b) its schematic.	191
A.2	(a) Reflectance image of a USAF resolution target, scale bar indicates 2 mm length (b) The intensity profiles along the lines indicated in red box in (a).	194
A.3	(a) Depth of field of the setup at two line set at frequency of 5 and 15 line pairs per millimeter.	195
A.4	Fluorescence imaging of ICG phantom using a CMOS camera and its post processing using Lucy Richardson deconvolution method.	196
A.5	Sensitivity comparison between a regular and a scientific CMOS cameras though human cadaver bone. Both cameras use the same capturing setting of 400 ms for exposure time, or relatively 2.5 frames per second.	197
A.6	Upper row: White reflectance images of (a) an exposed mice skull with indicated ROIs and (b, c) their corresponding zoom-in regions for ROI 1 and ROI 2. Lower row: Fluorescence images of mice vascular structures after ICG injection (d) corresponding to (a) and (e, f) corresponding to (b, c) for ROI 1 and ROI 2, respectively.	198
A.7	Preliminary test of Lexiscan effect in ICG dye diffusion.	199
A.8	System Setup and Sample Preparation.	199
A.9	Comparison of fluorescence strength under multiple excitation levels.	200
A.10	The nano particle diffusivity monitoring.	200
A.11	Horizontal and vertical intensity profiles for particle diffusivity comparison.	201
B.1	System diagram of a dual fluorescence-photoacoustic imaging. CL: Convex Lens, BS: Beam Splitter, NDF: Neutral Density Filter, OFB: Optical Fiber Bundle, DAQ: Data Acquisition Card, EF: Emission Filter.	205
B.2	System sensitivity comparison between PA and FL imaging of an ICG phantom.	206

Chapter 1

Introduction

1.1 An Overview of Robotic Assistance in Medicine

Computer integrated surgery (CIS) has been driven with the goals to enhance dexterity, visual feedback and information for surgeons, either for pre-operative planning or for indirect execution through robotic precision. The goal is to assist human surgeons with tool manipulation and medical assessments with minimal invasion and to complement and enhance the surgeons' skills. The CIS paradigm emerged in research laboratories in the mid-1980s and was introduced as a commercial medical product in the mid-1990s. Since then CIS systems have been rapidly developed and evaluated for use in neurology, or-

CHAPTER 1. INTRODUCTION

thopedics, radiation therapy, and cardiology, with or without laparoscopic aid. CIS benefits compared to traditional operations include surgical improvements in planning and execution precision, leading to reduction in surgical complications and shorter hospital stays. Modern CIS robots can be categorized into three mainstream technologies: The surgical CAD/CAM robot, the master-slave surgical assistant system [5–7], and the autonomous surgical robot [8,9].

1.1.1 Surgical CAD/CAM Robot

The surgical CAD/CAM paradigm incorporates preoperative and intra-operative modeling and planning for the operation, usually in three phases [10]:

- Pre-operative phase: 2D or 3D imaging of patient, targeting organ and related information about the patient anatomy are collected. If necessary, a biopsy examination for tissue study is executed or a patient-specific organ model is printed for interactive surgical planning.
- Intra-operative phase: A surgical plan and pre-operative imaging frameworks are registered to the patient with sensors and equipped surgical tools to execute the surgical plan. Updating and additional imaging and sensing may be pursued for necessary procedures to ensure surgical intervention is achieved. Data monitoring throughout this phase is often recorded for future reference.

CHAPTER 1. INTRODUCTION

- Post-operative phase: A summary and collection of information and results from the first two phases are archived to verify surgical diagnostics, technical issues, other long term assessment, and for surgical statistical studies.

These methods first started in the late 1980s with the ROBODOC system. The ROBODOC system (Integrated Surgical Systems) was developed to assist hip and knee replacement surgery [11, 12]. The goal was to help with improving implant fitting precision and repeatability, with pre-operative surgical planning supported by Computed Tomography (CT) images. Other registration method using the remote-center-of-motion device (RCM), have been shown feasible for percutaneous therapy to insert radiation therapy seeds into human organ with less cost and geometric error [13–15].

1.1.2 Master-Slave Surgical Assistant System

The current state-of-the-art surgical robot for clinical use during Robotic-Assisted Surgery (RAS) is based on the master-slave control principle, where a medical robot (slave) is directly controlled by a surgeon operating at the master console. Some representative robotic systems are the da Vinci robot (Intuitive Surgical Inc, Sunnyvale, CA) [16], the MiroSurge (Institute of Robotics and Mechatronics, German Aerospace Center) [17], and the Raven surgical robot (University of Washington) [18]. A typical master-slave robotic system includes multi-joint

CHAPTER 1. INTRODUCTION

robotic arms and binocular vision with endo-wrist instruments. At the master console, the surgeon views a perceptive 3D surgical scene through two binocular eyepieces (stereoscope) with the ability to manipulate the camera through foot pedals. Tool manipulation by the surgeon is accomplished by measuring hand movement and is transmitted to a controller for filtering, scaling, and relaying to the robotic arms and instruments. These functions allow for precise execution, mitigating tremors and sudden unwanted acts being sent to the robotic arms and tools. With the technical advantages in manipulating laparoscopic tools and operating on patients with minimal surgical invasion, master-slave surgical robots are used in a wide range of surgeries where open surgery is costly to the patient's health, and where the organ is hard to access. These systems are utilized in several types of cardiothoracic, gynecology, urology, abdominal, and general surgeries.

Due to the direct-control paradigm in master-slave robots, the functional outcomes of the surgery depend strongly on human factors, such as medical experience, experience with robotic tool manipulation, and hand-eye coordination. Moreover, repetitive task—especially on soft tissues—remains time consuming, with an average suturing and stapling time of 30 minutes to 90 minutes in intestinal [19] and 28 minutes for vascular anastomoses [20]. However, functional outcomes of the above-mentioned master-slave systems depend on the training, proficiency, and daily performance changes of the surgeons that

CHAPTER 1. INTRODUCTION

vary between the individuals and introduce human-related risk factors in the surgical system contributing to complication rates reaching up to 20% in general surgeries [21]. By automatizing RAS, with minimal human supervision, significant benefits to current RAS procedures can be obtained in improved safety, manipulating precision, and outcome consistency.

Other system designs for collaborative work such as joint holding of surgical tools by both the surgeon and the robot have been proposed to transfer human force exertion on the tool for robotic motion correspondence [22]. The design has been extended to microsurgery and with other visual processing and tissue interaction forces [23].

1.1.3 Autonomous Surgical Robot

Autonomy for robotic surgery refers to the ability of the robot to perform a specific task on its own, while supervised by human surgeons for necessary interventions. Moreover, the autonomy of the robot involves environmental adaptation and visualization of the surgical scene. Some robotic automation on surgical tasks such as knot-tying have been proposed, such as the EndoPAR robot using recurrent artificial neural networks [24,25]. Academic availability of RAS—such as with the Intuitive Surgical’s da Vinci Research Kit (dVRK), the da Vinci Robot, and the RAVEN II—have accelerated surgical automation development. In 2015, an autonomous surgical system incorporated the

CHAPTER 1. INTRODUCTION

da Vinci Surgical Robot with the dVRK to perform surgical debridement and multilateral cutting of 3D viscoelastic tissue phantoms through learning by observation [26]. The work was adapted and extended to performing tumor resection sub-tasks, such as palpation, incision, debridement, and injection [27]. These papers are limited to non-tissue phantom studies with marked full cutting loops.

The RAVEN II surgical system using 3D stereoscopic imaging with NIR tracking was developed to represent a proof of concept for detecting and surgical planning for neuroblastoma ablation [8]. However, the work did not consider system performance on tissues, tissue deformation, and motion in a clinical setting.

In 2016, the Smart Tissue Autonomous Robot (STAR) was introduced for automating soft tissue surgery and addressing robotic challenges in tissue motion and deformation on porcine intestinal tissue [9]. The robot included a seven degree-of-freedom (7-DOF) lightweight robot (KUKA LWR 4+) with a customized anastomosis tool set, motion planning and 3D visualization. STAR tracked tissue deformation and performed suturing tasks in the tracked markers, showing its feasibility in automating anastomosis surgery. Furthermore, it was comparable or more efficient with other contemporaneous RAS devices and human surgeon performance.

1.2 Development of Endoscopy in Medical

Imaging

Endoscopy, from ancient Greek *éndon* for “within, inside” and *skopéō* for “to see”, is an established technique using a tool that can be inserted into the body with minimal incision to support surgical procedures remotely to access inaccessible places in the human body. Another similar term for endoscopy is borescopy (occasionally called boroscopy), which describes an optical device consisting of an eyepiece on one end and an objective lens on the other end that are linked together by a set of relay optical lenses. Borescopes have a similar design to endoscopes in medicine but the term is usually applied to instrument inspection and visualization for non-medical purposes. The other term is laparoscope, from ancient Greek *lapára* for “flank, side” and *skopéō* for “to see”, to describe an endoscopic device used for abdominal or pelvis operations through a small incision. These surgical tools are inserted directly into the human body or an organ through a small hole (supported by a trocar device). Due to its endoscopic design for minimally invasive surgery, these tool can fundamentally reduces medical complications, such as the risk of infection, blood loss, postoperative pain and inflammatory response, commonly seen with open surgery [28, 29].

CHAPTER 1. INTRODUCTION

1.2.1 The Evolution of Endoscopy

The idea of applying endoscopic-like devices to medicine dates to 2640 BC. As documented in the Edwin Smith Papyrus, Egyptian physicians treated patients with great care through a discipline of minimal intervention and pain alleviation based on a philosophy that putting people in surgical trauma could aggravate their condition and endurance. Supporting the minimal intervention method were early gynecological procedures written in the Kahun Gynaecological Papyrus and several catheter devices described in ancient Asian history [30]. However, the most notable document of a endoscopic precursor application for practitioners on living patients is the work *The Art of Medicine*, written by Hippocrates around 400 BC, where he detailed several minimally invasive surgical procedures that reduced pain and mortality risk compared to the traditional open surgery at the time. His standards encouraged numerous technological developments for endoscopic precursors, catheters, and cannular instruments as well as later refinements of endoscopic techniques using reflected light and concave mirrors in the mid 17th century.

In the early 1800s, Philipp Bozzini documented and combined all the early technological elements to create the *Lichtleiter* (Light guiding instrument, Figure 1.1(a)), the first working portable scope for use for urinary tract, rectum and pharynx diagnostics on living patients. The device was unique with an

CHAPTER 1. INTRODUCTION

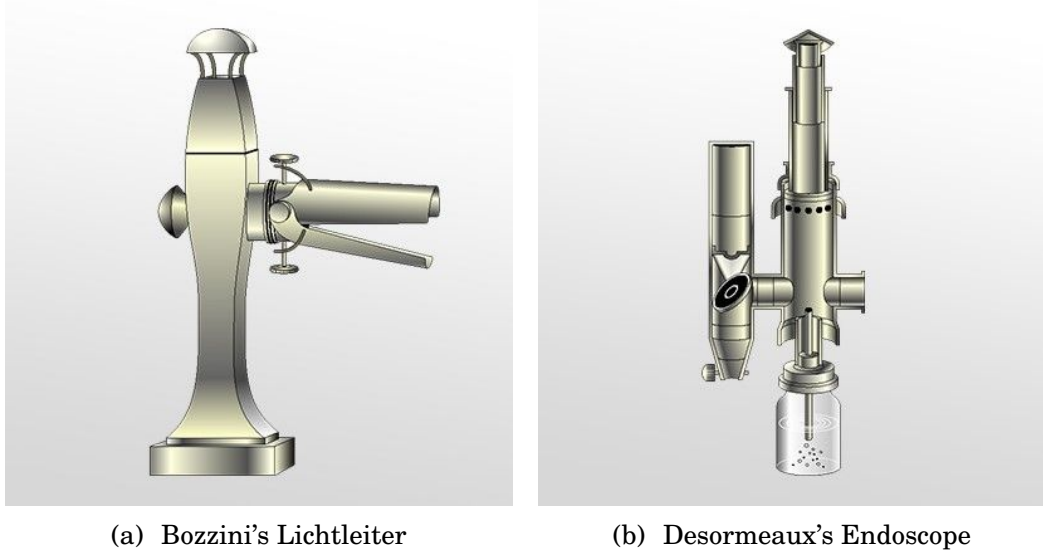


Figure 1.1: First designs of the endoscopic era. Adapted from [1].

45° angled mirror attachment, making the device the first visualization instrument with a 90° viewing angle [31]. By 1853, Antoine Jean Desormeaux had refined Bozzini's scope with burning alcohol for light illumination and a light focusing mechanism for urinary tract and bladder assessment. With this invention (Figure 1.1(b)), he also coined the term "endoscope" [32]. The endoscopic design evolved humbly until the mid-1900s, when the advancement in glass optics and camera technology started to blossom. In 1957, Raoul Palmer developed the smallest scope at the time with a 5-mm casing and the most powerful image magnification up to that date. In 1967, Harold Hopkins introduced quartz, rod-shape lenses that drastically improved endoscopic visualization [33]. Hopkins' rod lens advanced endoscopic design to smaller diameters and easier fabrication compared to previous endoscopic designs. In the 1970s,

CHAPTER 1. INTRODUCTION

quartz rod lens evolved to flexible fiber optics to create flexible endoscopes. Several other design foundations have advanced endoscopy to become more practical and widespread for commercialization. Completing the modern endoscopic design, a camera was first attached to a fiberscope for abdominal assessment in 1987, and high-fidelity display systems were introduced in the early 2000s.

1.2.2 Endoscopic Design for Minimally Invasive Surgery

There are many types of endoscope used in medical operations, with various sizes and structures depending on the type of surgery and the surgical site. Most endoscopes in medicine are used in places with limited access, such as the gastrointestinal tract, the respiratory tract, the ear, the urinary tract, the reproductive system, the orthopedic system and the spinal system.

A conventional endoscope consists of four main components (Figure 1.2), where the end which is closer to the examiner (the eyepiece side) is called the proximal end, and the end which is closer to the patient (the objective lens side) is called the distal end:

- An objective lens to form an image of the object (O) inside an embedded rod. The distal end of the objective assembly can have a set of prisms or mirror mechanisms for a specific or an adjustable viewing angle.
- A relay lens system to transfer an image collected from the object, through the objective lens along the length of the embedded rod to the eyepiece.

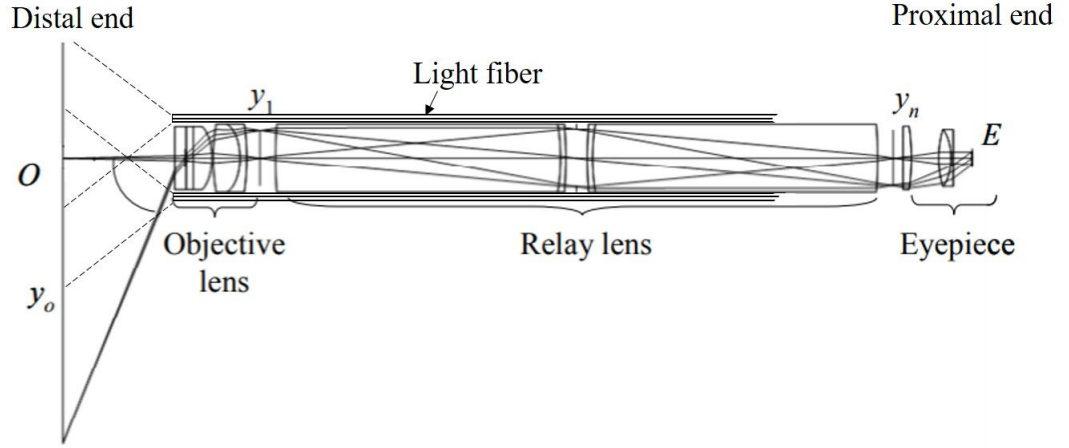


Figure 1.2: Optical layout of a conventional endoscope with one-stage relay assembly. Adapted from [34]

Depicted in Figure 1.2 is a one-stage relay lens endoscope. An object O with height y_0 forms an intermediate image with height y_1 through the objective lens, resulting in a final image with height y_n through the relay lens before exiting at the eyepiece E . In rigid endoscopes, this component is a collection of relay rod lenses, but for flexible endoscopes, fiber bundles are used.

- A light delivery system to illuminate the object for imaging. This component is usually made of optical fibers distributed around the relay lens system to illuminate the object with a desired uniform distribution. The light fibers are bundled from a separate light port near the proximal end.

CHAPTER 1. INTRODUCTION

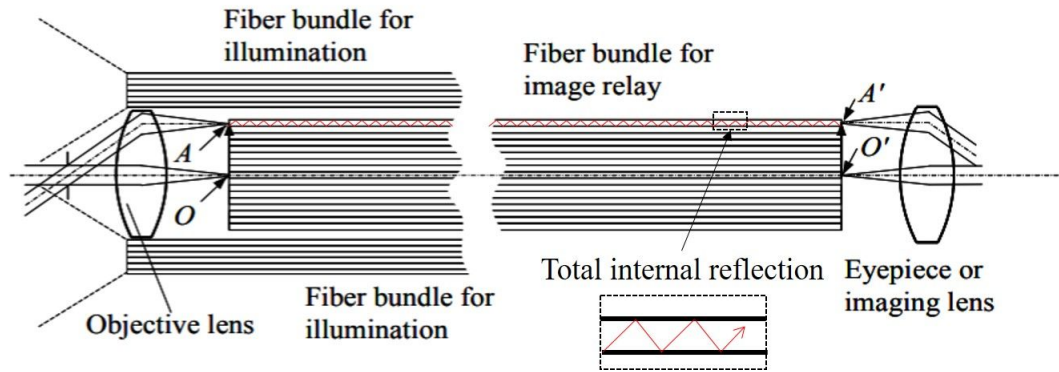


Figure 1.3: Optical layout of a flexible fiber endoscope. Adapted from [34]

- An eyepiece (E) that can be viewed directly to a surgeon's eye or connected to a imaging sensor.

1.2.2.1 Flexible Endoscope

A flexible endoscope is an imaging device with an objective assembly, a light delivery system and an eyepiece similar to the rigid endoscope. However, the optical relay system is replaced by a collection of flexible fibers in a bundle (Figure 1.3). The image formed by the objective lens is transferred along the endoscopic length to the eyepiece through multiple total internal reflections within the fiber bundle, and the image formed by the fiber bundle's distal end is the output of the fiber bundle at the proximal end (AO to $A'O'$).

Due to the small core size of the fibers in the fiber bundle for optical relaying, a flexible endoscope can be long and thin and is often housed with multiple channels for other purposes such as the suction valve, air/water valve and

CHAPTER 1. INTRODUCTION

biopsy tool. Flexible endoscopes have angulation control and a left/right control lock located near the eyepiece to manipulate the positional deflection of the endoscope body up- and downward and of the tip left- and rightward. Certain flexible endoscopes for colonoscopy have options for variable stiffnesses and shape-locking capabilities [34].

Due to the natural pixelated pattern of the fiber bundles, its resolution is limited to the core size of each fiber. A typical clinical multimode fiber bundle is often less than 2-mm to 3-mm in diameter and composed of 20,000 to 40,000 fiber cores, corresponding to an imaging resolution of each fiber core diameter of about $20\text{ }\mu\text{m}$ [34]. Moreover, compared to the refractive relay lens endoscope, flexible fiber scopes have smaller depths of field, and the resultant fiber images at the eyepiece cannot compensate for residual aberration due to the individual small core size of each fiber.

1.2.2.2 Rigid Endoscope

The fiber core size in a flexible endoscope limits the quality and resolution of the endoscopic image. Moreover, continued flexing of the fiber easily breaks the fiber. These limitations led to the invention of the rod-lens endoscope by Harold Hopkins in 1959. The design optimizes the lens quality and provides a more secure optical alignment of the first rigid endoscope design by fitting a collection of glass rod lenses between the traditional relay optics. The image quality

CHAPTER 1. INTRODUCTION

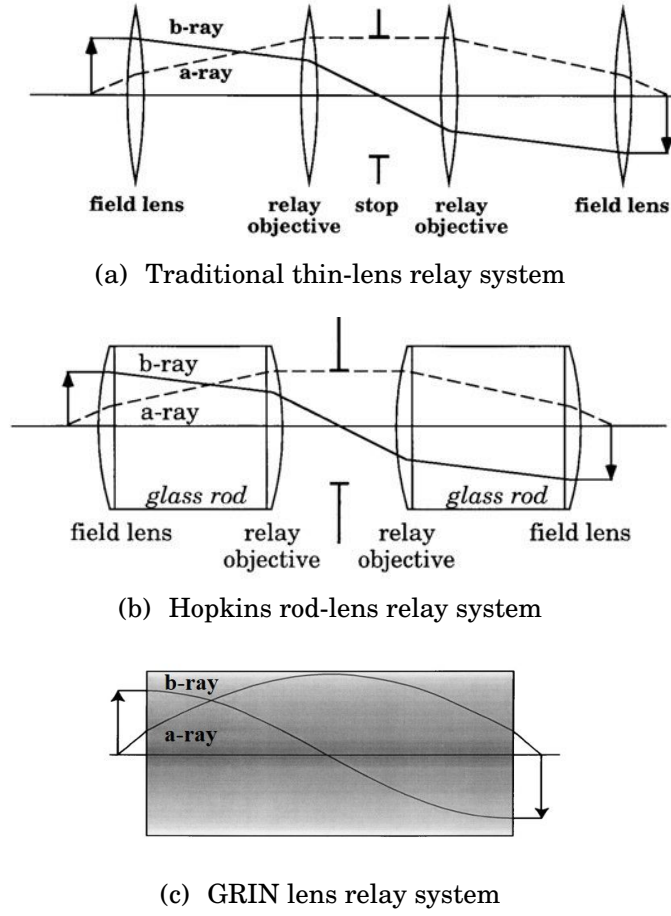


Figure 1.4: Optical layouts of relay systems for rigid endoscopes. Adapted from figures used in [35].

of a rigid endoscope is the result of the image transfer through the lenses in the relay system and the option for aberration correction by additional lenses in this stage. Moreover, as discussed in Section 1.2.2.1, the depth of field—the distance about the focal plane where objects appear acceptably sharp—of a rigid endoscope can be extended at the eyepiece to accommodate the observer.

The relay system of a rigid endoscope consists of multiple identical sections of image transfers with unity magnification (Figure 1.4). A traditional rigid

CHAPTER 1. INTRODUCTION

scope (Figure 1.4(a)) has at least four lenses: two identical sets of a field lens and a relay lens that are symmetric along two sides of a stop aperture. The system is telecentric; the marginal rays that enter and exit the relay stage are parallel.

In a Hopkins rod-lens relay system (Figure 1.4(b)), the air space between the relay lens and the field lens is replaced by a glass rod and was shown to have a higher light throughput (which is proportional to the square root of the refractive index of the relay rod, in comparison to 1 in air for a traditional scope) and a lower vignetting effect [29, 36].

Gradient Index (GRIN) (Figure 1.4(c)) rod-lens relays systems combine the separate lenses in the above two relay types into a single glass rod with a variable refractive index that follows a polynomial function. The rod lens and image quality, such as f-number ($f/\#$), are related to the designed refractive index profile of the rod [35].

Chapter 2

Imaging in Minimally Invasive Robotic Surgery

2.1 Assisted Functional Medical Imaging Modalities

Functional imaging refers to a medical imaging method of detecting or measuring variations in tissue chemical compositions, metabolism, blood flow, or tissue biological properties, such as absorption and scattering. Modern functional imaging includes direct and indirect methods. Some direct methods are electroencephalography (EEG), Event Related Potentials (ERP), magnetoencephalography

CHAPTER 2. VISUALIZATION IN MINIMALLY INVASIVE ROBOTIC SURGERY

(MEG). Some indirect methods include Positron Emission Tomography (PET), functional Magnetic Resonance Imaging (fMRI), and other optical imaging such as Ultrasonic Imaging and Diffuse Optical Imaging (DOI). Each method has its technical advantages and disadvantages related to penetration depth, systematic complexity, spatial resolution, and acquisition speed.

2.1.1 Direct Functional Imaging using EEG, ERP, MEG

These direct functional imaging modalities measure electric or magnetic signals generated by ionic currents flowing in neuron dendrites during synaptic transmission. The ultimate advantage is high temporal resolution (down to millisecond precision). However, the spatial resolution of these devices is a relatively high order of magnitude; thus, the recorded signals from these devices are often combined with other indirect functional imaging for better data visualization and analysis.

- Electroencephalography (EEG) records the spontaneous electrical activity of the brain using electrodes placed along the scalp (non-invasive) or between nerve ends (invasive) over a period of time for various medical diagnoses. An EEG system is mobile and offers temporal resolution down to the millisecond range.
- Event Related Potentials (ERP) measure averaged EEG responses from voltage potential variation to a stimulus.

CHAPTER 2. VISUALIZATION IN MINIMALLY INVASIVE ROBOTIC SURGERY

- Magnetoencephalography (MEG) measures the magnetic field produced by the inherent electrical currents in the brain or nerves, via a sensitive array of Superconducting QUantum Interference Devices (SQUIDs). Because the brain's magnetic field is smaller than the ambient magnetic field (10^3 fT versus 10^8 fT), shielding the magnetic field of the brain from external magnetic fields is necessary.

2.1.2 Indirect Functional Imaging

2.1.2.1 Positron Emission Tomography

Positron Emission Tomography (PET) is a nuclear functional imaging method to observe the metabolic condition of the body by collecting high energy gamma rays that are emitted from the subject by a tracer. Prior to imaging, a radioactive tracer is introduced in the body. The tracer is a mixture of natural biological molecules with an isotope label that can produce two gamma rays by emitting a positron from its nucleus. The PET tracer is designed to interact specifically with the organ of interest; for example, fluorodeoxyglucose (FDG) PET only highlights muscles due to their glucose uptake. To obtain more knowledge of the body, anatomical information is therefore often obtained from other imaging modalities. PET is often combined with X-ray Computed Tomography or MRI scanning to produce 3D scanned images.

When scanning the brain, clinical PET can reach a spatial resolution of (3-

CHAPTER 2. VISUALIZATION IN MINIMALLY INVASIVE ROBOTIC SURGERY

mm)³ in humans and of (1-mm)³ in small animals /citegambhir2002molecular.

The acquisition time depends on the exposure time of the sensor, ranging from a few seconds to several minutes [37,38].

2.1.2.2 Functional Magnetic Resonance Imaging

An functional Magnetic Resonance Imaging (fMRI) scanner has a powerful electromagnet coil of about 3 T to generate a strong magnetic field inside the scanner. The magnetic field is sufficiently strong to align the spin of the hydrogen nuclei (in H₂O) inside the body to the direction of the field. When the nuclear spin is aligned, their fields add up to a measurable signal that is collected from an array of SQUIDS.

In MRI, hydrogen nuclei signal strength varies on the regional components within the body, making the system capable of discriminating between each organ in the body. The patient can be asked to take contrast agents for clearer collected images (high imaging contrast). fMRI typically measures blood oxygenation level dependent (BOLD) values overlaid on a normal MRI image. The mechanism of functional imaging is from the magnetic property variations between oxygenated and de-oxygenated blood; oxygenated hemoglobin is diamagnetic and de-oxygenated hemoglobin is paramagnetic. A typical MRI or fMRI yields a spatial resolution of about 3 mm to 4 mm, with temporal resolution of about 60 ms [39].

CHAPTER 2. VISUALIZATION IN MINIMALLY INVASIVE ROBOTIC SURGERY

2.1.2.3 Ultrasound Imaging

Ultrasound utilizes high frequency sounds wave (higher than 20 kHz) to image internal body structures for medical diagnosis. An ultrasound image (sonogram) is reconstructed by collecting sound echos reflected off the tissue from emitted pulse ultrasound waves. Multiple scanning directions are collected by moving the ultrasound probe, which is a microphone or an array of microphones (transducer). The sonogram displays anatomic structure as well as blood flow, blood vessel localization, tissue motion and stiffness. The non-invasive instrument can be operated in real-time based on sound traveling time, echo signal strength and the transducer sensitivity without emitting any harmful ionizing radiation into the body. Ultrasound is used in a wide range of minimally invasive surgery (MIS), such as in cardiology, gynecology, otolaryngology, ophthalmology, pulmonology and urology.

The axial resolution of an ultrasound system is proportional to the pulse duration while the lateral resolution depends on the transducer aperture, frequency and focal properties. A conventional B-scan ultrasound has a typical axial resolution of 150 μm and lateral resolution of 450 μm [40].

2.1.2.4 Diffuse Optical Imaging

The principal of Diffuse Optical Imaging (DOI) is based on the photon propagation behavior of light within biological tissue. Incoming light penetrates

CHAPTER 2. VISUALIZATION IN MINIMALLY INVASIVE ROBOTIC SURGERY

to the tissue and once interacting with the biological tissue, can either absorb or scatter from the tissue molecules.¹ By analyzing the variations of the collected diffused reflectance from the sample, concentrations of oxygenated and de-oxygenated hemoglobin and melanin can be deduced from adaptation of Lambert-Beer's law. In DOI, near infrared (NIR) light is utilized as an illumination source due to its high penetration depth in biological tissue. The reflected photon is then collected by a photodetector, typically at about 3 cm away from the light source. Because of the hardware simplicity, the device can be setup to use a flexible fiber array, extending a 2D functional imaging method to detect 3D volumes, such as for breast cancer detection [41] or in neonatal imaging [42]. The most commonly used DOI systems utilize a continuous wave light source, either from a laser diode or a light-emitting diode (LED). A summary of different DOI systematic modifications along with each system sensitivity in tissue oxygenation saturation is reviewed in [43]. DOI spatial resolution in adult human brain imaging is about 1 cm [44].

2.1.3 Multi-Functional Image-Guided Surgery

Modern surgical navigation in current clinical minimally invasive surgeries incorporates a stereoscopic system with camera - NIR projector paradigm to spatially localize prominent positions of multiple NIR reflectance spheres. The

¹As the technique is *diffuse* optical imaging, transmitted light is not measured.

CHAPTER 2. VISUALIZATION IN MINIMALLY INVASIVE ROBOTIC SURGERY

spheres are calibrated with a reference calibration frame, allowing real-time tracking of surgical tools with a sphere attachment. In regular clinical practice, location of the tools are registered with *a priori* 3D scanned images from MRI [45] or CT scanners [46]. The registration between the tool coordinates and the 3D volume from the image library give the surgeon an overlay for targeting the tool and performing surgical tasks. The MRI and CT scanned images are done before the surgery for surgical strategic planning.

Further functionality is continuing to be added to multi-functional image-guided surgeries, including adding intra-operative ultrasound [47] and fluorescence imaging [48,49]. Focused ultrasound sonication is used along with many image-guided technologies in intracerebral hemorrhage treatment or tumor ablation [50,51]. Ultrasound imaging also finds extensive use in MIS to visualize the dynamic flow of fluids in 2D and to complement a full pathological mapping of the 3D volume generated from MRI, CT and PET by using a fused ultrasonogram. Another popular use of 3D ultrasound in MIS is for needle tracking and surgical planning [52–55].

For fluorescence imaging, IndoCyanine Green (ICG) dye has recently been used in MIS to identify vasculature anatomy and monitor blood perfusion of organs [49,56,57]. The binding of the dye molecule to the plasma protein within the vascular confinement is rather quick, within 3 minutes to 5 minutes of introduction, and is non-toxic with little allergic generation [58]. ICG

CHAPTER 2. VISUALIZATION IN MINIMALLY INVASIVE ROBOTIC SURGERY

fluorescence emits at about 830 nm under fluorescence excitation at around 785 nm, requiring an additional light illumination at this NIR wavelength and a bandpass filter to collect the fluorescence. The vasculature monitor has recently been introduced in clinical MIS such as the SKY and the PINPOINT Endoscopic Fluorescence Imaging System from Novadaq [59], the OPAL1 technology from Karl Storz [60], and the Firefly Fluorescence Imaging integrated with the da Vinci Robot from Intuitive Surgical [61].

2.2 Visualizations in Minimally Invasive

Surgery

Modern surgical procedures have been increasingly adopting MIS over traditional open surgery due to its main advantage in surgical trauma reduction, especially for ophthalmology, ear, nose, and throat (ENT) abdominal and cardiology surgeries [62, 63]. A typical MIS system supports visualization of the surgical anatomy and pathology of internal organs using a dedicated laparoscopic or endoscopic device. Conventional 2D and 3D vision in current clinical MIS technologies support surgical visualization; however, they are limited to either narrow fields of view (FOV) or scenic depth perceptions. These qualities serve the need of surgical depth estimation; however, visual perception contributes to low depth accuracy and impacts a surgeon's hand-eye coordina-

CHAPTER 2. VISUALIZATION IN MINIMALLY INVASIVE ROBOTIC SURGERY

tion, learning curve and clinical outcomes [64–66]. These human variations can critically affect functional outcomes in all acute surgeries, where precision and accuracy of dissection or suturing placements within 1 or 2 mm can make a significant difference [67]. In addition, with the recent advance in robotics, adapting autonomous robots for use in surgery requires a more precise depth quantification of the surgical site. Therefore, a quantitative 3D measurement during surgery would benefit both surgeons and surgical robots. Recent developments in MIS quantitative 3D visualization involve techniques such as stereoscopy, time of flight, plenoptic and structure illumination.

2.2.1 Stereoscopy

Stereoscopy is a well-developed technique for 3D reconstruction. For direct depth visualization in current medical devices using stereoscopy, such as the master-slave MIS console, the surgeon perceives depth information through viewing left and right binocular eyepieces and processes 3D perception from the two overlapped views of the scene. Currently, for robotic navigation using stereoscopy, depth information relies on the searching of stereo correspondence between two distinct images of the scene to produce an estimation of disparity between the both images. Considering a typical stereo imaging setup as in Figure 2.1, the disparity $u_L - u_R$ is the distance between two projected points of P in the left and right images. By using triangulation, 3D coordinate of a

CHAPTER 2. VISUALIZATION IN MINIMALLY INVASIVE ROBOTIC SURGERY

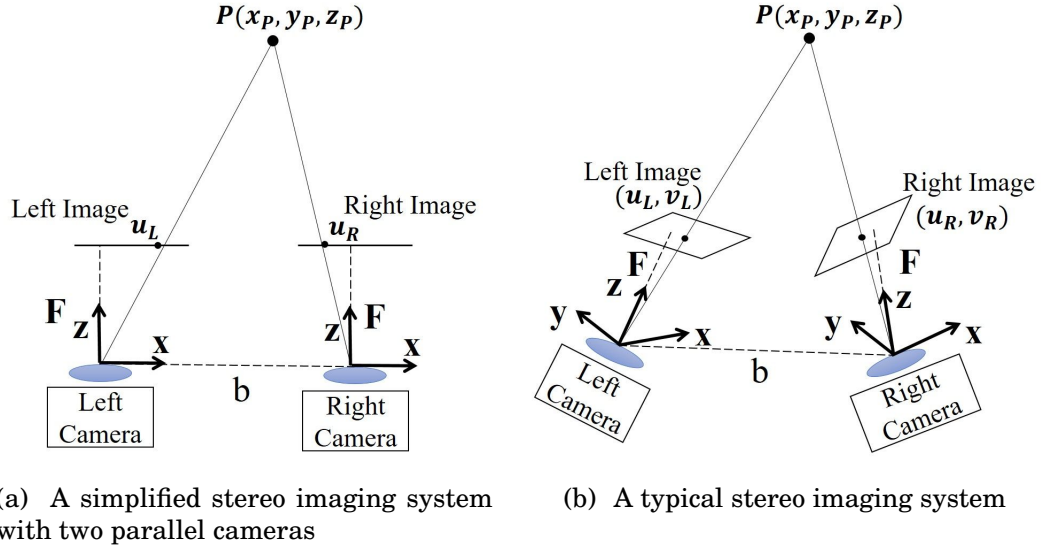


Figure 2.1: Triangulation is used in stereo imaging system for 3D reconstruction. Adapted from [2].

sample point P can be deduced. In a simplified stereo system such as in Figure 2.1(a), where the two cameras share the same focal length F , are parallel with each other and are b distance away from each other, coordinate $P(x_P, y_P, z_P)$ can be computed from similar triangle theory (Equation 2.1).

$$\begin{aligned}
 X_P &= \frac{u_L X_P}{F}, \\
 Y_P &= \frac{v_L X_P}{F}, \\
 Z_P &= \frac{F * b}{u_L - u_R}
 \end{aligned} \tag{2.1}$$

The disparity is calculated by determining camera intrinsic and extrinsic parameters and matching the correspondence between pixel (or pixel window) between the two cameras of the same object. Because of the need to match

CHAPTER 2. VISUALIZATION IN MINIMALLY INVASIVE ROBOTIC SURGERY

the correspondence from pixel to pixel (or pixel window to pixel window) between the two images, the computational time in dynamic conditions can be significant. Hence, many computational studies for stereo vision focus on improving the algorithmic speed to search for disparity, such as to use motion estimation between consecutive scenic frames for 3D flow recovering (stereoscopic scene flow prediction [68]), to use feature detection (the seed propagation method [69]), or to use an efficient convex optimization for disparity computing based on a 3D cost-volume configuration (the cost-volume method [70]). These methods have been used to obtain high 3D resolution up to 50 μm . However, the technique suffers when there are no features or textures on the sample, creating data "holes" in the 3D map, requiring a data interpolation method to be used.

2.2.2 Time-of-Flight

The Time-of-flight (ToF) imaging technique calculates depth information from the phase difference $\delta\phi$ between the emitted light pulse and the reflected pulse has been detected after reflecting off a sample (Equation 2.2). Therefore, this technique does not rely on a correspondence search or a baseline restriction, leading to a compact design for use in a surgical endoscopic system.

$$Depth = \frac{c}{2} \frac{\Delta\phi}{2\pi f} \quad (2.2)$$

CHAPTER 2. VISUALIZATION IN MINIMALLY INVASIVE ROBOTIC SURGERY

Depth resolution using 3D time-of-flight surgical endoscope ranges from 0.89 mm [71] to about 4 mm [72]. However, due to the low light environment in tissue imaging, a ToF camera often uses a high power laser source to illuminate internal targets. Some other limitations in depth evaluation using ToF come from specular reflectance, inhomogeneous illumination, and other systemic errors such as the sensor run-time, its temperature tolerance and imaging exposure time [73]. Other tissue-light interaction factors such as tissue biological properties in absorption and scattering also contribute in the ToF systematic error.

2.2.3 Plenoptic Imaging

Plenoptic imaging, or light field imaging, calculates depth from a single image collected by multiple reflected rays from the object through a microlens array located in front of a camera sensor. Each image from the sensor is comprised of multiple micro images from the microlens array, i.e. each pixel of a micro image is related to particular directions of different incoming light. The microlenses are aligned in a specific configuration and can come with different focusing lengths (multi-focus plenoptic camera) for an optimization of a maximal effective lateral resolution and the required depth of field [74]. The capability to capture light from multiple angles with multiple focal lengths supports not only depth mapping but also focal retrieval for post processing or provid-

CHAPTER 2. VISUALIZATION IN MINIMALLY INVASIVE ROBOTIC SURGERY

ing large depth of focus imaging. Depth reconstruction in plenoptic imaging is calculated similar as in stereoscopy, or using focus/defocus method [75].

The lateral resolution of a multi-focus plenoptic camera can achieve up to a quarter of the sensor pixel in lateral resolution [76] with an order of magnitude of 1 mm in axial resolution [77]. Although benefiting from high depth resolution, 3D reconstruction using plenoptic imaging often requires customized sensors and microlens arrays for a particular imaging field. Plenoptic imaging systems have also been commercially developed, primarily for consumer and non-medical applications [78]. Some early developments on using plenoptic imaging for surgical applications have recently been explored [79].

2.2.4 Structured Illumination

Structured illumination (SI) provides depth quantification similar to stereoscope techniques. However, SI relies on the parallax and triangulation of sample locations in relation to a camera (or more than one camera) and a projector. Instead of searching for disparities, SI detects depth from fringe patterns that are actively projected onto the tissue. The projected pattern can be grid pattern (dot or line) or sinusoidal modulated pattern. Grid pattern SI reconstructs 3D surface through disparity searching similar to stereoscopy. From the known grid geometry and active illumination on the tissue, reconstructed point cloud is calculated with higher accuracy and less prone to tissue homogeneous fea-

CHAPTER 2. VISUALIZATION IN MINIMALLY INVASIVE ROBOTIC SURGERY

ture, i.e. the technique is more robust with featureless object. These advantages in speed and less computational cost make grid SI a highly used method in computer vision to detect motion and track object in real time [80–82]. For tissue 3D imaging, some highlighted studies employ a unique projected light color spectrum [83,84] or a known pattern to triangulate the light-of-sight rays from the light source to the camera on tissue features with sub-millimeter accuracy [85,86]. However, the application of grid SI in endoscopy is still limited. Certain features of the grid such as the spacing between grid, grid projection collimation within certain depth range, grid distortion and the light spectrum of the grid should be considered when applying grid SI for tissue 3D reconstruction to achieve sub-millimeter accuracy.

The other SI method using sinusoidal modulated pattern (another name is the fringe projection profilometry) reconstructs 3D based on the relation between camera parameters with the phase distribution. The phase distribution is calculated from multiple modulated fringes at different shifted frequencies, thus, covers the object surface within the projected shifting range. This method can highlight features present in discontinuous surfaces or featureless regions, producing denser 3D point clouds than traditional stereoscopy. For in-vitro medical applications, sinusoidal pattern SI has been widely applied in dermatology for skin and wound inspection [87–89] and in health-care for idiopathic scoliosis diagnostics [90]. Despite its wide use in some fields, sinusoidal pattern

CHAPTER 2. VISUALIZATION IN MINIMALLY INVASIVE ROBOTIC SURGERY

SI endoscopic imaging for medical intra-operative inspection has been rather limited. Due to their limited working volume, many sinusoidal pattern SI endoscopic designs do not incorporate a baseline between the projector and the camera but use a common beam-splitter between them, resulting in non-uniform depth accuracy and a restricted range of 3D measurement [91] or providing only perceptual depth measurements [92, 93]. Many efforts have applied SI in confined spaces such as in fiber or endoscope systems [94–96]. They have primarily been reported with static and non-tissue objects [97].

Because of the advantages in hardware and the computational efficiency of sinusoidal pattern SI, the technique is adapted for 3D reconstruction in our setup (The sinusoidal pattern SI from here to later sections is referred as SI). We contribute a unique gradient gray coded pattern for 3D tissue reconstruction where the discontinuity of the object is solved using phase calculations from a sequence of low to high spatial frequency grid patterns to minimize the cost of color-coded illumination. The coded pattern features the shape of the tissue in vertical grids, deducing an object’s geometry across its entire surface, instead of just features as in stereoscopy. By deducing an object’s geometry across its entire surface, data “holes” can be reduced in the reconstructed point cloud of featureless to few-featured samples, such as the intestine or kidney. Moreover, the coded patterns are generated using low power light emitting diodes (LEDs), reducing the speckle pattern occurrence or specular reflectance

CHAPTER 2. VISUALIZATION IN MINIMALLY INVASIVE ROBOTIC SURGERY

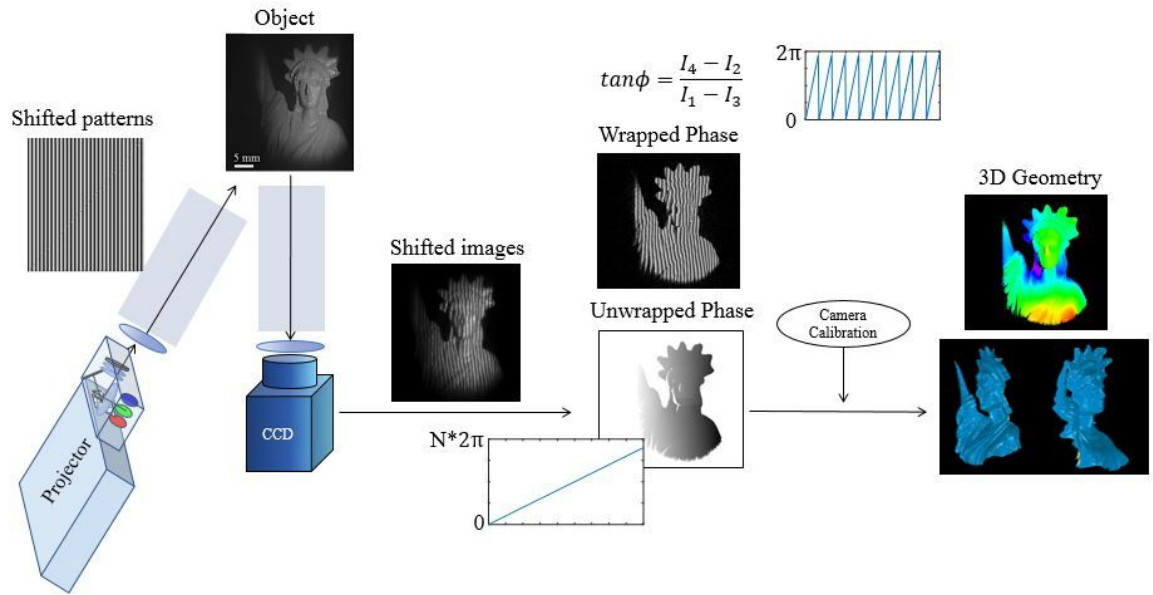


Figure 2.2: Geometrical reconstruction using structured illumination.

seen in high coherence light sources often used in SI endoscopic imaging using supercontinuum or laser sources. In addition, the baseline between the camera and the projector is utilized to provide high quantitative depth measurements.

Chapter 3

Endoscopic Imaging System for Autonomous Robotic MIS

3.1 Motivation

The current clinical 3D imaging standards used in minimally invasive surgery offer either non-quantitative 3D reconstruction for human surgeons or lossy 3D reconstructed point clouds that are inadequate for visualization by surgical robots. The most recent previous work in this field have advanced variations of 3D reconstruction techniques to provide quantitative imaging in endoscopy for MIS (Section 2.2); however, these prior attempts provide limited exposure to tissue imaging and quantification. In this section, to address these limitations,

CHAPTER 3. ENDOSCOPIC IMAGING SYSTEM FOR AUTONOMOUS ROBOTIC MIS

we introduce two compact prototypes for 3D endoscopic imaging using plenoptic and SI methods. We also evaluate the accuracy and precision of their point cloud reconstructions with different tissue types and discuss their applicability for robotic manipulation.

My contributions to the work present in this section include full development of the 3D imaging endoscopic system, including optical simulation, system setup, optical characterization, accuracy assessment and tissue validation. The work presented in this section resulted in publications in [79, 98–102] and a patent application [103].

3.2 Endoscopic Imaging System for 3D

Reconstruction using Plenoptic Technique

3.2.1 System Contributions

Plenoptic imaging is a fairly new 3D reconstruction technique in the biomedical field. The technique involves a micro lens array (MLA) integrated onto an imaging sensor, such that each point of the object can be viewed and imaged at different angles via adjacent micro lenses. The depth information can be deduced similarly to the stereoscopy approach. However, in stereoscopy, the two imagers should maintain a set angle of separation to obtain two distinct views

CHAPTER 3. ENDOSCOPIC IMAGING SYSTEM FOR AUTONOMOUS ROBOTIC MIS

of the object while ensuring the desired depth accuracy [104–106]. A stereoscope utilizes triangulation in which the two imagers maintain a set angle relative to the object for correspondence searching. As an extension of stereoscope, a plenoptic imager utilizes only one sensor with multiple micro lens to create a higher number of viewing positions, thus, improve the correspondence searching performance. Moreover, a plenoptic camera offers the reduction of systematic calibration due to the known separation between each micro lens (i.e. known distance between micro-sensors). In addition, plenoptic imaging also create the expansion of parallax computation in both horizontal and vertical directions compared to one dimension in a stereoscope. Currently, plenoptic imaging is widely accepted in industry for multi-focus imaging [74, 76]; however, plenoptic imaging in medicine is limited with current depth precision of 1 mm [77, 107] in wide-field imaging. To adapt this technique to an endoscopic setting for minimally invasive surgery, we propose a plenoptic endoscopy design that consists of a clinical surgical endoscope, a plenoptic camera and a relay optical system. The proposed setup compensates for the aperture mismatch between the endoscope and the MLA fabricated on the plenoptic camera.

3.2.2 System Setup

The endoscopic setup described in Figure 3.1 employs a 0-degree surgical borescope with scope housing diameter of 10 mm (Stryker, San Jose, California, USA) for

CHAPTER 3. ENDOSCOPIC IMAGING SYSTEM FOR AUTONOMOUS ROBOTIC MIS

both illumination and imaging. The light from a halogen bulb is coupled into the light pipe of the borescope to illuminate the surgical site and the image is coupled back to the plenoptic camera via the same borescope and a relay lens system. The plenoptic camera used is commercially available with a predefined MLA setting (Raytrix R5, Kiel, Germany). The relay lens system comprises four biconvex lenses with various focal lengths (Thorlabs, New Jersey, USA) to achieve the desired micro lens image on the plenoptic camera. In particular, a 20-mm-focal-length biconvex lens (LA1859, Thorlabs, New Jersey, USA) is used to form an image with output light rays from the borescope eyepiece. This image is then expanded via three biconvex lenses with focal lengths of 30 mm (LA1805, Thorlabs, New Jersey, USA), 400 mm (LA1172, Thorlabs, New Jersey, USA) and 35 mm (LA1027, Thorlabs, New Jersey, USA) to form the micro lens images with an aperture matching the aperture of the fabricated micro lens. Beam expansion could be achieved with fewer lenses; however the combination of F30 and F400 lenses are used to fine tune the image and to provide flexibility for beam delineation. A scale bar of 5cm length is added in the system schematic for optical alignment reference. The imaging system operated at 11 frames per second with CUDA GeForce GTX 690 on a Dell Precision T7600 workstation for image reconstruction.

CHAPTER 3. ENDOSCOPIC IMAGING SYSTEM FOR AUTONOMOUS ROBOTIC MIS

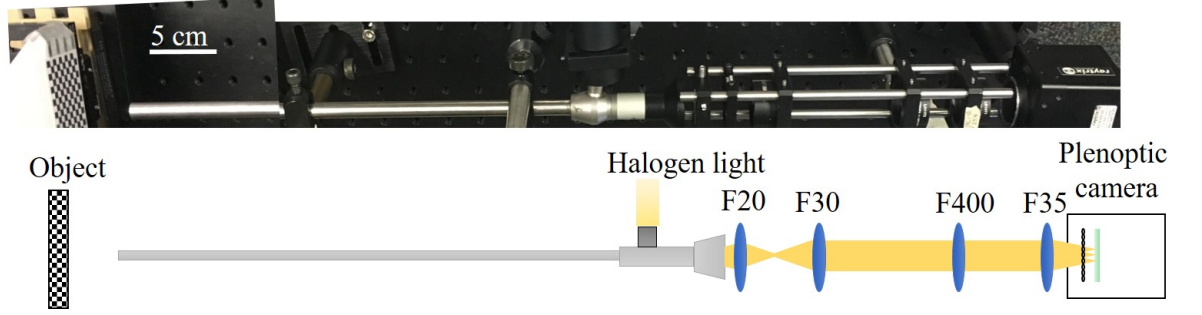


Figure 3.1: Schematic of the endoscopic setup with the plenoptic camera and relay lens system.

3.2.3 3D Reconstruction Principle

In the plenoptic imaging setting, a main lens produces an image from a real object, this image then acts as the object for the MLA. Through the MLA, the incident light cone is split into multiple sub-images collected by the sensor. Based on these collected micro lens images, depth calculation is defined by the relation between the calculated virtual depth and the metric transformation relation [108, 109]. Depth calculation of a plenoptic setup relates to stereoscopy technology, where the MLA performs as a micro camera array that generates multiple views of a small portion of the object, which is also the image generated by the main lens. First, a correspondence search is established with each pixel location from one micro sensor correlated with the other pixel location from the adjacent micro sensor using the sum of absolute difference method over a group of pixel points along the epipolar lines. The method searches for corresponding pixels between the two adjacent micro images by minimizing the

CHAPTER 3. ENDOSCOPIC IMAGING SYSTEM FOR AUTONOMOUS ROBOTIC MIS

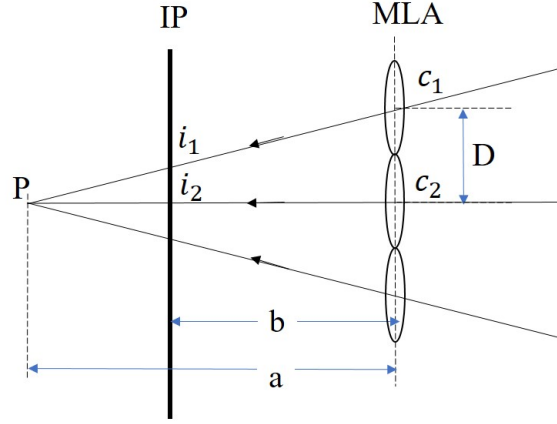


Figure 3.2: Triangulation principle for virtual depth estimation. IP: Image plane, MLA: Micro lens array.

absolute difference between the pixel values within a window size.

$$\sum_{i=1}^m \sum_{j=1}^n |I_1(i, j) - I_2(i + x, j + y)| \quad (3.1)$$

where (i, j) is the pixel index of adjacent micro images I_1 and I_2 , m and n are the pixel numbers along horizontal and vertical axes, and x and y represent the disparity along the two directions, respectively.

Once the correlated pixels of these micro images are determined, the intersection point of projected rays through these pixels into the virtual 3D space determines the virtual depth of the object. This virtual depth is related to the distance between the observed object and the camera. An example depicted in Figure 3.2 calculates virtual depth v_p to explain this calculation [109].

CHAPTER 3. ENDOSCOPIC IMAGING SYSTEM FOR AUTONOMOUS ROBOTIC MIS

$$v_P = \frac{a}{b} = \frac{D}{D - (i_1 - i_2)} \quad (3.2)$$

where a is the distance between MLA to the virtual parallax point, b is the distance between the sensor and the MLA. D is the baseline distance between two micro lenses with centers c_1 and c_2 ; i_1 and i_2 are the image pixels of the same object point projected by the two micro lenses.

From the information of the virtual depth, metric distance b_L of the virtual depth is computed as in Equation 3.3.

$$b_L = h + v_P b \quad (3.3)$$

where h is the distance between the main lens and the MLA.

As the optical property of the endoscope is proprietary, the overall system magnification is unknown theoretically; however, we determine the system magnification empirically using a known measurement height standard. Therefore, the scaled object height is determined using this magnification.

3.2.4 Accuracy assessment

To evaluate system performance, we calculate depth of field (DOF) via resolution and contrast measurement within a range of working distance. The

CHAPTER 3. ENDOSCOPIC IMAGING SYSTEM FOR AUTONOMOUS ROBOTIC MIS

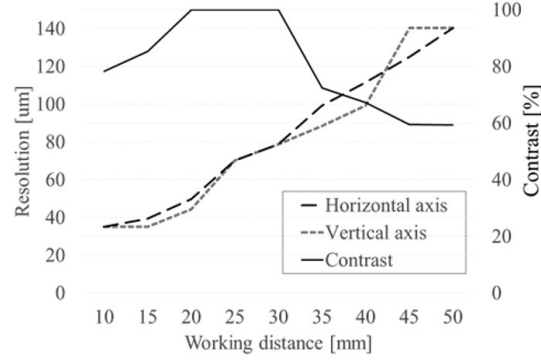


Figure 3.3: Resolution and contrast measurements

resolution is the smallest resolvable width of a horizontal or vertical line on a USAF test target 1951 (R3L3S1P, Thorlabs, New Jersey, USA). The standard target is moved away from the distal end of the borescope without refocusing with equal step size of 5 mm and increasing located distance from 10 mm to 50 mm. In addition, a contrast change with the set working distance was also recorded. The resolution and DOF plot in Figure 3.3 shows the best contrast occurs at 20 mm to 30 mm away from the borescope. At this distance, the resolution is recorded to be within 50 um to 80 um, which is sufficient for imaging biological samples such as intestinal organs in anastomosis surgery.

3.2.4.1 Planar Checkerboard Surface

To further validate the system's accuracy and precision, we used a checkerboard pattern with known square size of 3.5 mm on a depth-of-field target serving as the height standard (DOF 5-15, Edmund Optics, Barrington, New Jersey). The target is aligned at 0 degrees and 45 degrees and 20 mm away

CHAPTER 3. ENDOSCOPIC IMAGING SYSTEM FOR AUTONOMOUS ROBOTIC MIS

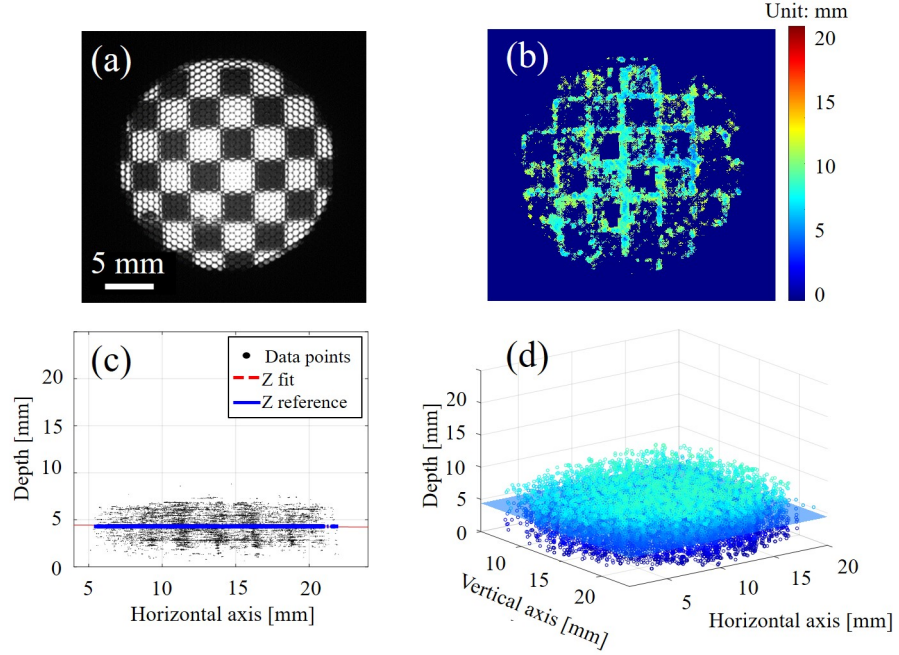


Figure 3.4: (a) Micro lens image of the checker board at 0 degree with (b) its depth map and (c, d) point cloud data at different views.

from the distal end plane of the borescope as indicated in Figure 3.4a and Fig. 5a. The accuracy error is characterized by mean distance and standard deviation between the fitted plane and the reference plane modeled at 0 degree and 45 degrees; while the precision error is defined by the variation (mean distance and standard deviation) of collected data points from the fitted planes (see Figure 3.4(c,d) and Figure 3.5(c, d)).

Due to the triangulation, the depth reconstruction is only possible when sufficient object features and local contrast are achieved, such as at edges and corners of the checkerboard as observed in Figure 3.4 and Figure 3.5. As the angle deviates from 0 degree to 45 degrees, the depth map and point cloud

CHAPTER 3. ENDOSCOPIC IMAGING SYSTEM FOR AUTONOMOUS ROBOTIC MIS

Table 3.1: Reconstruction accuracy and precision at two planar angle deviations at 0 degree and 45 degrees. Unit is in millimeters.

		0 degree	45 degree
Accuracy	Mean (Std)	0.085 (0.032)	0.818 (0.440)
	Maximum	0.103	1.439
Precision	Mean (Std)	1.141 (0.721)	2.367 (1.800)
	Maximum	3.863	11.658

accumulations illustrate the change presented in the corresponding colormap. The calculated accuracy and precision are displayed in Table 3.1 with an average maximum accuracy and precision error of about 1 - 2 mm with a field of view of $25 \times 25 \text{ mm}^2$. Depending on the object of interest, a required field of view (FOV), resolution, and depth precision is required accordingly. For a minimally-invasive surgical endoscope especially for anastomosis (a reconstructive surgery to connect two lumens together), a FOV of $25 \times 25 \times 25 \text{ mm}^3$ with spatial resolution of about 200 μm and depth precision of about 1 mm are sufficient for 3D image guided anastomosis [9].

A finer grid pattern for testing the system's accuracy and precision in Figure 3.4 and Figure 3.5 can improve the 3D reconstruction due to the increase in data points. However in medical applications imaging targets often lack dense features. We thus believe that a sparsely distributed checkerboard provides a more realistic test pattern. We also believe that a custom developed light field endoscopic camera with custom MLA will further improve the precision and accuracy in the future.

CHAPTER 3. ENDOSCOPIC IMAGING SYSTEM FOR AUTONOMOUS ROBOTIC MIS

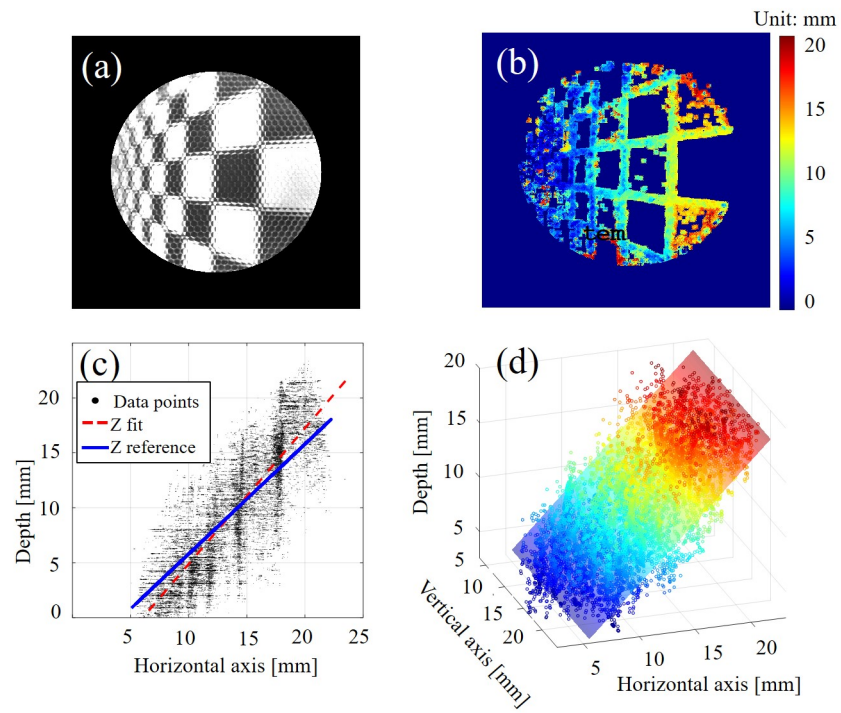


Figure 3.5: (a) Micro lens image of the checker board at 45 degrees with (b) its depth map and (c, d) point cloud data at different views.

CHAPTER 3. ENDOSCOPIC IMAGING SYSTEM FOR AUTONOMOUS ROBOTIC MIS

3.2.4.2 Inhomogeneous Sample

Other complicated 3D-printed objects of polydimethylsiloxane material with defined structures and known dimensions were further used to examine the system spatial reconstruction. The result indicates the distinct curvature and heights of the objects with the displayed depth color map (see Figure 3.6). In particular, an average reconstructed height from the L-shape base A to the lower base B of the second object (Figure 3.6b and Figure 3.6e) is 5.5 mm compared to the physical height of 6.64 mm, leading to an error of 1.14 mm. Another height error for the third 3D-printed object in Figure 3.6c and Figure 3.6f was also recorded to be 0.75 mm from the base A to the podium base B. A biological sample of a fowl ventricular specimen was harvested for 3D measurement (Figure 3.7). The specimen's structural features are contained, however, circular patterns between the micro lenses were also detected (Figure 3.7). This can be explained by the unresolved depth information between the micro lens' edges.

3.2.5 Lessons Learned

Due to the nature of the plenoptic technique for searching the disparity between adjacent micro lens images, the reconstruction algorithm depends strongly on the inherent features of the tested samples. In other words, featureless or

CHAPTER 3. ENDOSCOPIC IMAGING SYSTEM FOR AUTONOMOUS ROBOTIC MIS

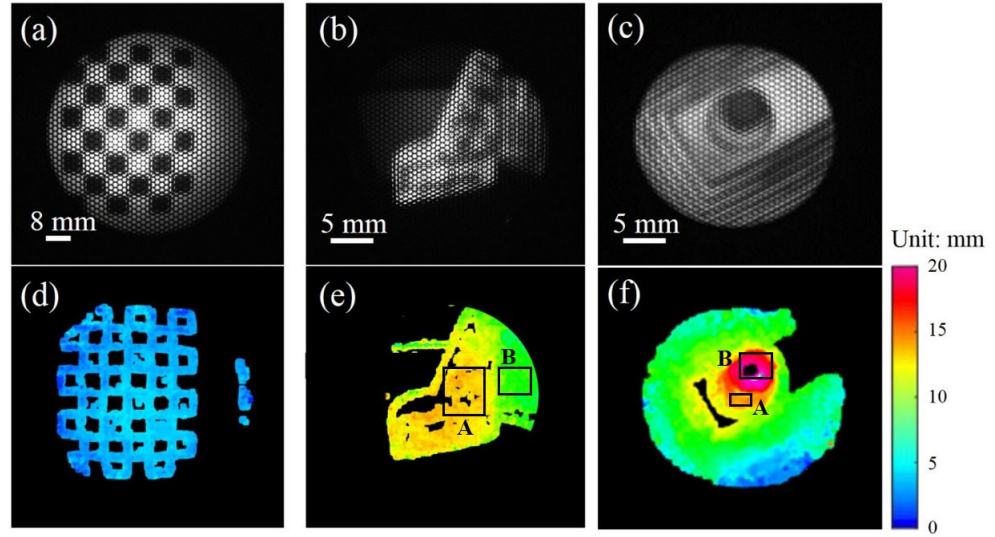


Figure 3.6: ((a-c) Micro lens image of a plane and inhomogeneous objects and (d-f) its reconstructed depth maps.

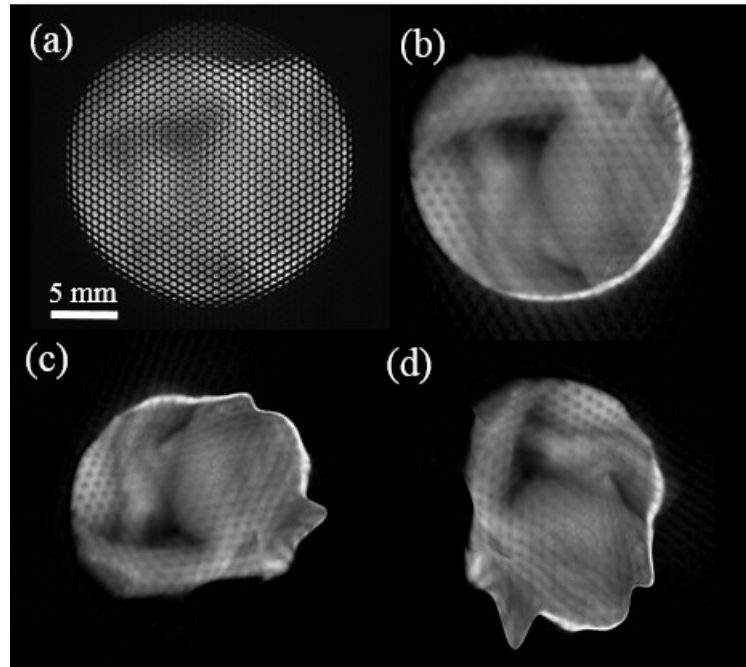


Figure 3.7: (a) Micro lens image of a fowl ventricular specimen and (b-d) its 3D reconstructions at multiple angles.

CHAPTER 3. ENDOSCOPIC IMAGING SYSTEM FOR AUTONOMOUS ROBOTIC MIS

homogeneous regions of the object create outliers or missing depth information, thus data interpolation is essential. To compensate for this limitation, a projector can be used to actively illuminate known features onto the object and an efficient illumination setting can be used to resolve the finer details of the object as well as to avoid reflection saturation. Non-existent data points have no effect on the accuracy and precision. The depth estimation depends on detectable features, which could be maximized by using active illumination. There are a few advantages of plenoptic endoscopy with active illumination over normal structured illumination. The first is that the plenoptic approach allows the user to observe the scene from a variety of angles in both horizontal and vertical directions due to the micro lens array arrangement. The second is that the entire scene can be brought into focus provided that it is within the FOV. Lastly, the structure of the illumination needs not be known beforehand, and is not a source of error. Typical structured light approaches rely on a precisely known projection pattern, whereas the plenoptic approach seeks only high contrast features, which can be provided in a myriad of ways. In conclusion, a three-dimensional endoscopic system using plenoptic imaging technique has been demonstrated with reconstructed dimensions of both planar and complex samples. We are currently working with the research and development team at the Raytrix Company to further improve the design of MLA that would benefit such endoscopic 3D vision for minimally invasive surgery. The

CHAPTER 3. ENDOSCOPIC IMAGING SYSTEM FOR AUTONOMOUS ROBOTIC MIS

improvement involves the f-matching performance of aperture size between the MLA and the optics of the commercial surgical borescope, while maintains an adequate frame rate for surgical guidance purpose (10 frames per second). Moreover, other optical analysis techniques such as multispectral imaging or laser speckle contrast can be registered onto the 3D rendering to provide the dynamic property of the studied tissue in minimally invasive surgery.

The system proposed in this section has been published in

3.3 Endoscopic Imaging System for 3D Reconstruction using Structured Illumination Technique

3.3.1 System Contributions

By using plenoptic imaging, the 3D surface geometry of tissue can be reconstructed within a compact endoscopic housing as discussed in Section 3.2. However, the system hardware requires modification of the micro lens configuration which matches numerical aperture of the relay scope, and the correspondence searching also suffers point cloud discontinuity for featureless or no feature object, similar to stereoscopic vision. These factors restrain surgical navigation and planning for autonomous robotic system. The system proposed in

CHAPTER 3. ENDOSCOPIC IMAGING SYSTEM FOR AUTONOMOUS ROBOTIC MIS

this section explores the adaptation of 3D structure illumination in MIS with hardware simplicity and flexible system calibration for further systematic registration with surgical robot. The system demonstrates quantitative, dense point cloud construction ability in video streaming mode. Tissue sensitivity evaluation of the system is performed within clinical anastomosis scenario on multiple porcine cadaveric samples.

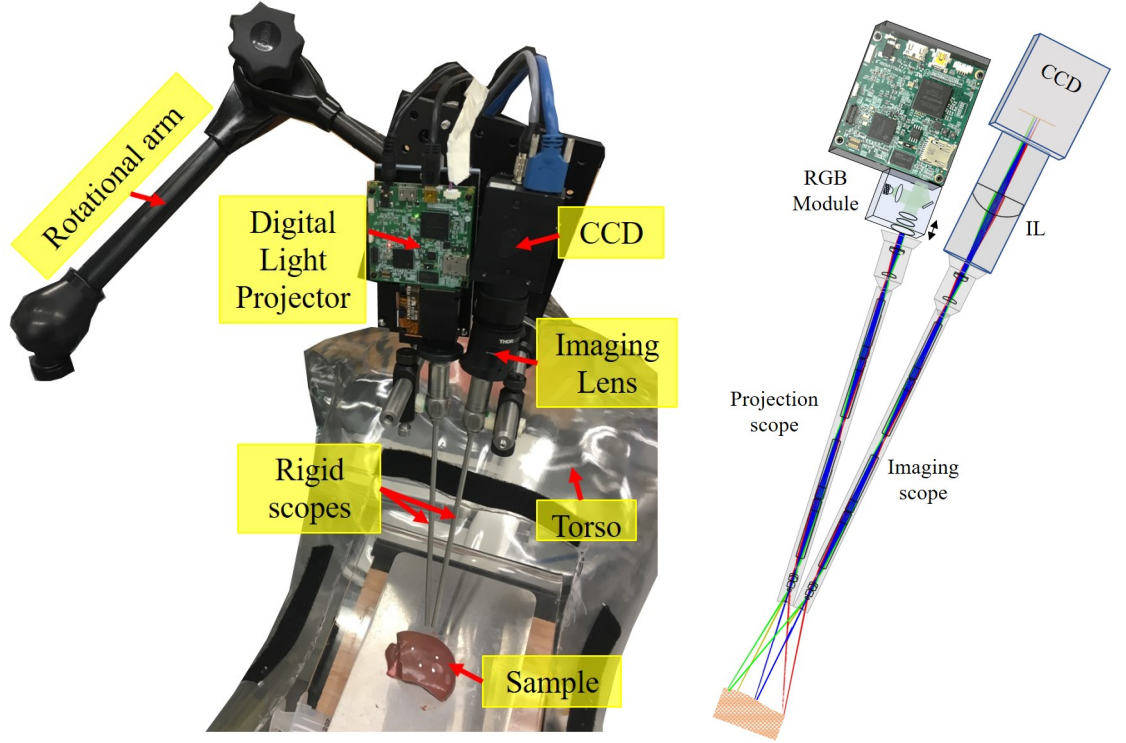
3.3.2 System Setup

To optically monitor how the tissue is deformed, we developed a 3D endoscope based on a structured illumination technique (Figure 3.8). The system consists of two identical rigid surgical endoscopes (HOPKINS 7230AA, 0°, 4-mm-diameter endoscope, Karl Storz GmbH & Co. KG, Tuttlingen, Germany) for illumination and imaging. The illumination endoscope (Illum. scope) guides the modulated patterns projected by a digital micromirror device (DMD) (TI-DLP EVM3000, Texas Instrument, Dallas, Texas, USA). These patterns shine on the objects and their reflection off the sample is captured via the imaging endoscope (Imag. scope), an achromatic doublet lens served as an imaging lens (IL, AC254-060-A, Thorlabs, Newton, New Jersey, USA) and a CCD camera (GS3-U3-15S5M-C, Point Grey Research Inc, Richmond, Canada). The projector is equipped with an optical chamber comprised of red, green and blue LEDs. To make the current system adequate for imaging pigmented samples such as

CHAPTER 3. ENDOSCOPIC IMAGING SYSTEM FOR AUTONOMOUS ROBOTIC MIS

intestines, we use green LED for illumination as the camera responsivity is highest compared to the other regions. The gray code modulated fringe follows a sinusoidal form (Equation 3.1). The two endoscopes are both designed with telescopic objective lens, the FOV for the projection and imaging varies depending on the distance between the endoscope's distal end to the object, the overlapped regions from the illumination and the imaging endoscopes with 70° acceptance angle, and the depth of field of the imaging optics. In our setup, all the projected fringes are aligned within the imaging FOV, and the distal ends of the two scopes are angled at about 12° . For low-noise triangulation and to minimize the overall form-factor of the endoscope, a minimum angle of 12° between the illumination and the imaging scopes is chosen to maintain the desired field of view and height accuracy. More quantification of the 3D accuracy in relations with the endoscopic separation angle can be obtained and referred to open SI setup [106]. To demonstrate ray-tracing through the optical assembly and to find the location for the focusing imaging lens to the sensor, we adapted a standard endoscope model with the relay lens system based on a combination of rod lenses and simulate the system using Optics Studio 15 SP1 (Zemax, Kirkland, Washington, USA). The control interface is written in C# using multi-thread computation on a Dell Precision T7600 workstation to control the synchronization of the camera frame grabber within the projector exposure time for each fringe and to export each fringed image and 3D point

CHAPTER 3. ENDOSCOPIC IMAGING SYSTEM FOR AUTONOMOUS ROBOTIC MIS



(a) 3D imaging endoscopic system on a mounting arm with the surgical tool on a robotic arm (not shown) targeting the sample inside a torso phantom.

(b) Imaging system with the optical layout inside the rigid scope

Figure 3.8: 3D SI imaging endoscopic system.

cloud visualization.

3.3.3 System Synchronization

Prior to each data collection, two defined system settings for the camera and the projector are loaded into each hardware platform. Typical parameter configurations of the camera and the projector are listed in Tables 3.2 and 3.3 for the 3D reconstruction method using SI. The varied parameters shown in the tables mostly depend on the camera sensitivity of capturing pigmented tissue.

CHAPTER 3. ENDOSCOPIC IMAGING SYSTEM FOR AUTONOMOUS ROBOTIC MIS

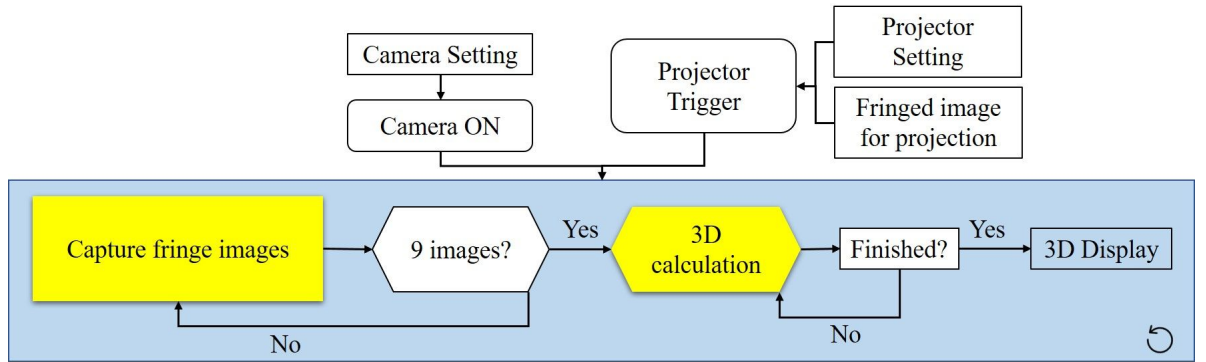


Figure 3.9: Workflow for 3D imaging system control and data collection.

The camera is set to integrate incoming light to output images within each projector trigger duration. The work flow of the system synchronization including the triggering, data collection to 3D computation, and display is described in Figure 3.9. The program is synchronized using computing threads and is written in C++. The computed point cloud is imported to RVIZ for visualization in the Robotic Operating System (ROS) framework.

Brightness [%]	633
Exposure [EV]	-2.727
Sharpness	525
Gamma	1.25 (varied)
Gain [dB]	17
Image Format	Mode 1
Shutter Trigger	Mode 1

Table 3.2: Typical parameter settings for the camera.

3.3.4 System Speed

For all intestinal 3D video streaming, the camera exposure is set to be around 30 ms/fringed image (camera received frame rate of 32 fps) with each image

CHAPTER 3. ENDOSCOPIC IMAGING SYSTEM FOR AUTONOMOUS ROBOTIC MIS

LED Current [mA]	633
Output Trigger Pulse Width [μ s]	20000
Delay [μ s]	0
Pattern Sequence Bit Depth	6
Pattern Count	9 or 16
LED Select	Green
Exposure [μ s]	25000 (varied)
Trigger Period [μ s]	25000 (varied)

Table 3.3: Typical parameter settings for the projector.

size is 516x692 pixels. For one 3D map reconstructed from 16 fringed images, 3D depth map and pointclouds are collected at 1.57 fps. The system speed is later enhanced by reducing the number of projected fringes during sample 3D reconstruction. Technical details of the speed improvement is provided in Section 5.3.2.3.

3.3.5 Camera-Projector Calibration

The camera-projector calibration is adapted from the work in [3], in which the geometric dimension is related to fringe phase and camera parameters as subsequently derived from triangulation (Section 3.3.5.1).

3.3.5.1 Triangulation

A typical setup using camera-projector configuration is similar to stereo vision schematic, with the second camera replaced by a projector. Considering a 3D setup described in Figure 3.10, where P is a point that could be presented in the reference plane $Oxyz$, B is the imaging points of P on the camera coordi-

CHAPTER 3. ENDOSCOPIC IMAGING SYSTEM FOR AUTONOMOUS ROBOTIC MIS

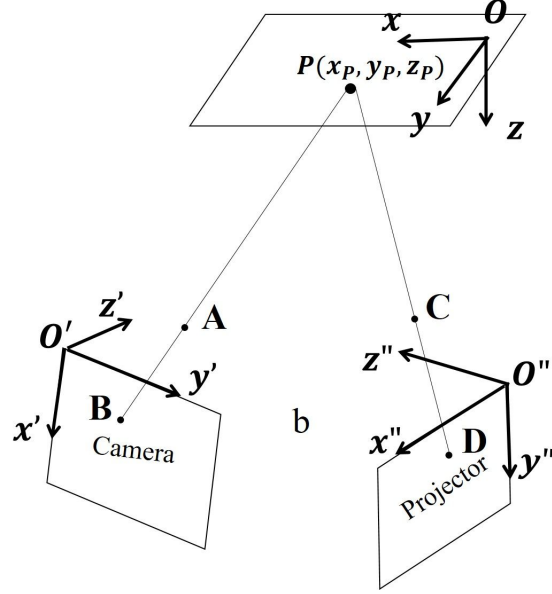


Figure 3.10: Triangulation in structure illumination using camera-projector setup. Adapted from [3].

nates $O'_{x'y'z'}$, D is projected point on the projector coordinates $O''_{x''y''z''}$ to point P , A and C are the centers of the camera and the projector, respectively. From triangulation of the coordinate points P , A , B in the reference coordinate system O_{xyz} , we get Equation 3.4.

$$\begin{bmatrix} x_P & y_P \end{bmatrix} = \begin{bmatrix} z_P - z_A & z_B - z_P \end{bmatrix} \begin{bmatrix} x_B & y_B \\ x_A & y_A \end{bmatrix} / (z_B - z_A) \quad (3.4)$$

From triangulation of the coordinate points P , C , D in the reference coordi-

CHAPTER 3. ENDOSCOPIC IMAGING SYSTEM FOR AUTONOMOUS ROBOTIC MIS

nate system O_{xyz} , we also get Equation 3.5

$$\begin{bmatrix} x_D & y_D \end{bmatrix} = \begin{bmatrix} z_D - z_C & z_P - z_D \end{bmatrix} \begin{bmatrix} x_P & y_P \\ x_C & y_C \end{bmatrix} / (z_P - z_C) \quad (3.5)$$

Applying transformation matrix R with rotational angles α , β and γ about the x' , y' and z' axes, we can transform point B from the camera coordinate system $O'_{x'y'z'}$ to the reference coordinate system O_{xyz} using Equation 3.6

$$\begin{bmatrix} x_B & y_B & z_B \end{bmatrix} = \begin{bmatrix} x_{O'} & y_{O'} & z_{O'} \end{bmatrix} + \begin{bmatrix} x'_B & y'_B & z'_B \end{bmatrix} R_{\alpha,\beta,\gamma}^T \quad (3.6)$$

In a similar way, point D is transformed from O_{xyz} to $O''_{x''y''z''}$ with the rotational matrix R around rotational angles θ , ϕ and ψ about the x'' , y'' and z'' axes as in Equation 3.7

$$\begin{bmatrix} x''_D & y''_D & z''_D \end{bmatrix} = - \begin{bmatrix} x_{O''} & y_{O''} & z_{O''} \end{bmatrix} + \begin{bmatrix} x_D & y_D & z_D \end{bmatrix} R_{\theta,\phi,\psi}^T \quad (3.7)$$

The fringe phase Φ_B at point B must be identical to Φ_D at point D and P, we have:

$$\Phi = \Phi_B(x'_B, y'_B) = \Phi_D(x''_D, y''_D) = \Phi_{O''} + \frac{2\pi}{p} x''_D, \quad (3.8)$$

where p is the pitch of the original projected fringe.

CHAPTER 3. ENDOSCOPIC IMAGING SYSTEM FOR AUTONOMOUS ROBOTIC MIS

The right-most side of Equation 3.8 indicates the continuous phase distribution during the unwrapping along the image width with an off-set phase distribution at the projector frame Φ''_O . Finally, depth of point P is summarized in Equation 3.9 by substituting Equations 3.4, 3.5, 3.6, 3.7 into Equation 3.8.

$$\begin{aligned}
 z = & \left[1 + c_1\Phi + (c_2 + c_3\Phi)x'_B + (c_4 + c_5\Phi)y'_B + (c_6 + c_7\Phi)(x'_B)^2 + (c_8 + c_9\Phi)(y'_B)^2 \right. \\
 & + (c_{10} + c_{11}\Phi)x'_B y'_B \left. \right] \cdot \left[d_o + d_1\Phi + (d_2 + d_3\Phi)x'_B + (d_4 + d_5\Phi)y'_B + (d_6 + d_7\Phi)(x'_B)^2 \right. \\
 & + (d_8 + d_9\Phi)(y'_B)^2 + (d_{10} + d_{11}\Phi)x'_B y'_B \left. \right]^{-1}
 \end{aligned} \tag{3.9}$$

Since (x'_B, y'_B) is directly related to the pixel intensity collected by the camera, z_P can be rewritten as in Equation 3.16. The coefficients $c_{(1-11)}$ and $d_{(0-11)}$ include parameters such as $x_A, y_A, z_A, x_C, y_C, z_C, x_{O'}, y_{O'}, z_{O'}, x_{O''}, y_{O''}, z_{O''}, \alpha, \beta, \gamma, \theta, \phi, \psi, p$, and $\Phi_{O''}$.

3.3.5.2 Camera Parameter Optimization

The calibration to determine $c_{(1-11)}$ and $d_{(0-11)}$ is performed using a similar procedure as in [110] with a flat checkerboard or circular pattern calibration board. The calibration board is translated and rotated to a number of positions and tilting angles to cover the imaging volume of interest. The purpose is to minimize the difference of z in Equation 3.9 and the transformed height

CHAPTER 3. ENDOSCOPIC IMAGING SYSTEM FOR AUTONOMOUS ROBOTIC MIS

z_{mn} at each control point on the calibration board at multiple positions and angles (Equation 3.11). The first board position is defined as the reference plane where the height is zero. From the calibrated extrinsic parameters, each control point n at each position m in physical world frame is transformed to corresponding point $(X_{c,mn}, Y_{c,mn}, Z_{c,mn})$ in camera frame. Since the physical world coordinate of each control point on the checkerboard is known, and the control points on the camera coordinate can be computed from feature detection (edge detection, ellipse fitting method), the initial camera parameters are computed, the virtual reference plane (zero plane) is determined by fitting a planar equation (with parameter (A, B, C) in Equation 3.10) to all the points $(X_{c,1n}, Y_{c,1n}, Z_{c,1n})$ for the first checkerboard position. The height of other point at other position $(X_{c,mn}, Y_{c,mn}, Z_{c,mn})$ with respect to the virtual reference plane is calculated using Equation 3.10.

$$z_{mn} = \frac{AX_{c,mn} + BY_{c,mn} + CZ_{c,mn} + 1}{\sqrt{A^2 + B^2 + C^2}} \quad (3.10)$$

where A , B , and C are the planar coefficients of the reference plane.

$$\operatorname{argmin}_c \sum_{m=1}^k \sum_{n=1}^l (z - z_{mn})^2, \quad (3.11)$$

CHAPTER 3. ENDOSCOPIC IMAGING SYSTEM FOR AUTONOMOUS ROBOTIC MIS

where m is each calibration position, k is the number of board positions used for the calibration, n is each calibration control point, and l is the number of control points on the calibration board.

3.3.6 Geometric Reconstruction using Structured Illumination Technique

As demonstrated from governing equation 3.9, 3D reconstruction using SI method utilizes the relation between camera parameters and phase (unwrapped) information, 3D reconstruction using a structured illumination method is based on relations between a wrapped phase from the captured fringes on the sample. The projected fringe set is composed of multiple vertical, phase-shifted sinusoidal fringe wave I_i generated by the Equation 3.12:

$$I_i(u, v) = I_o \left[1 + \cos\left(\frac{2\pi f u}{w} + \delta_i\right) \right], \quad (3.12)$$

where I_o is the intensity modulation amplitude, (u, v) is the spatial pixel indices, δ is the shifted phase, f is the fringe number, and w is the pattern width. In this prototype setup, $f = \{1, 4, 12, 36\}$ and $\delta_i = \{0, \pm\pi/2, 3\pi/4\}$. A defined fringe number is set uniquely for 3D imaging of tissue samples for a smooth reconstruction, for a lower accuracy with sample of relatively flat with little to no tissue gap, a lower number for the last value of f such as $f = \{1, 3, 12\}$ with

CHAPTER 3. ENDOSCOPIC IMAGING SYSTEM FOR AUTONOMOUS ROBOTIC MIS

shifted phase of $\delta_i = \{0, \pm/2\pi/3\}$ can be used, reducing the number of projected fringe from 16 to 9, hence, increasing the system speed.

The fringed patterns are sequentially projected onto the sample surface, resulting in a collection of fringed images. A wrapped phase of each fringe number is calculated using the conventional four-step phase shift method [111] as given by Equation 3.13.

$$\tan [\Phi^w(u, v)] = \frac{I_4(u, v) - I_2(u, v)}{I_1(u, v) - I_3(u, v)}, \quad (3.13)$$

where w indicates wrapped phase, and $I_{(1-4)}$ represents the intensity of four shifted image of each f number.

Because of the periodic structured patterns of the fringes, the phase map at each pixel point is restrained to a principal range, creating phase discontinuity for high frequency fringes. Hence, phase-unwrapping is necessary to compute the absolute phase values. The phase unwrapping is formulated in Equation 3.15 from the relation of the current and the previous unwrapped phase information from the previous frequency. The lowest frequency patterns has a single fringe in it, which makes its unwrapped phase identical to the wrapped phase (Equation 3.14). Other higher frequency patterns have the unwrapped phase distribution defined from the unwrapped phase distribution of the pre-

CHAPTER 3. ENDOSCOPIC IMAGING SYSTEM FOR AUTONOMOUS ROBOTIC MIS

vious frequency as in Equation 3.15.

$$\Phi_1^{uw}(u, v) = \Phi_1^w(u, v), \quad (3.14)$$

$$\Phi_n^{uw}(u, v) = \Phi_n^w(u, v) + 2\pi \left\langle \frac{\Phi_{n-1}^{uw} \frac{f_n}{f_{n-1}} - \Phi_n^w}{2\pi} \right\rangle, \quad (3.15)$$

where the operator $\langle \bullet \rangle$ denotes the argument rounding to the closest integer, the superscript uw means "unwrapped", f represents fringe frequency as explained in Equation 3.12, and $n = \{2, 3, 4\}$ is the n th frequency of the fringes.

The out-of-plane depth z at each pixel index (u, v) is a function of the unwrapped phase, and it is written as:

$$z = \frac{1 + c_1\Phi + (c_2 + c_3\Phi)u + (c_4 + c_5\Phi)v + (c_6 + c_7\Phi)u^2 + (c_8 + c_9\Phi)v^2 + (c_{10} + c_{11}\Phi)uv}{d_o + d_1\Phi + (d_2 + d_3\Phi)u + (d_4 + d_5\Phi)v + (d_6 + d_7\Phi)u^2 + (d_8 + d_9\Phi)v^2 + (d_{10} + d_{11}\Phi)uv}, \quad (3.16)$$

where $c_{(1-11)}, d_{(0-11)}$ are constants determined by geometrical and other relevant parameters (as discussed in Section 3.3.5), Φ is the unwrapped phase distribution. The second-order terms of u and v are adopted for the purpose of accuracy enhancement in practice.

3.3.7 Optical Characteristics of the System

The optical performance of the system is evaluated based on its depth of field (DOF), field of view (FOV), along with the axial and lateral resolutions within the DOF area.

3.3.7.1 Depth of Field and Axial Resolution

To determine the DOF, the FOV and the axial resolution of the imaging system, we use a DOF Target (DOF 5-15, Edmund Optics, York, UK) with a 45° inclination surface and on-surface line pair ruler for height variation indication. To mitigate the specular reflection from the projector light on the target surface, the target base is moved 10 mm away from the distal end of the two endoscopes. The system's DOF is measured by the region with high intensity contrast within the red segment (Figure 3.11). The intensity of the ruler marker between mark 15 mm and mark 45 mm shown in Figure 3.11 indicates the highest contrast occurs between 15 mm to 35 mm. Hence, reconstructed sample within 20 mm in height gives the best height accuracy.

To evaluate the system accuracy across the FOV, the distal error between the 3D reconstructed DOF target and a synthesized fit plane is calculated in 4 rotational directions (Figures 3.12, 3.13, 3.14). The distal error is the mean μ (Equation 3.17) and standard deviation σ (Equation 3.18) of all binned xyz distances d between the reconstructed 3D point clouds $f_{pc}(x, y, z)$ to the fit plane

CHAPTER 3. ENDOSCOPIC IMAGING SYSTEM FOR AUTONOMOUS ROBOTIC MIS

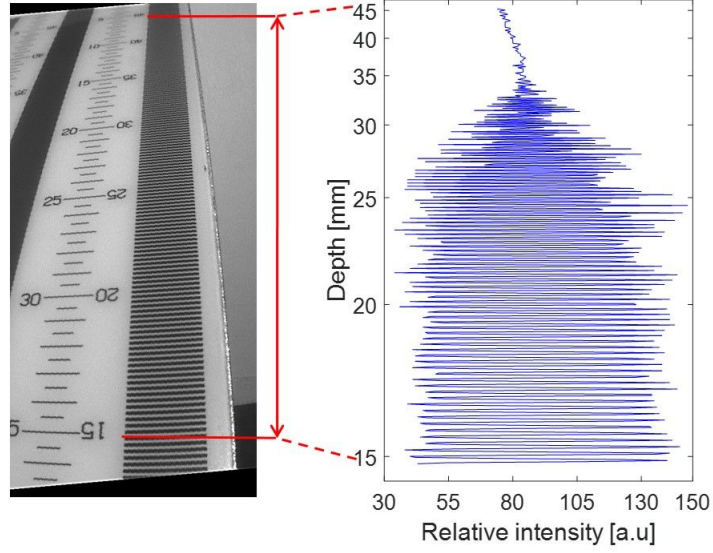


Figure 3.11: Bright-field image of the DOF target (Left) with relative intensity profile (Right) along the region within the red segment (from marker 15 mm to marker 45 mm on the target surface).

$f_{fit}(x, y, z)$ (Equation 3.19). Binning distance, selected with a binning width, is the ratio of the total data range along the inclination direction (along the y -axis in Figures 3.13, 3.16, 3.17, for example) over the square root of the total number of data points. The synthesized fit plane is calculated using the maximum likelihood estimation method in MATLAB R2017b, Computer Vision System ToolboxTM with a maximum allowed distance from the data inlier points to the fit plane of $5 \mu\text{m}$ and a maximum allowed absolute angular distance between the normal vector of the fit plane and the reference orientation of 3° . Because the planar geometry of the DOF target is known and is 45° inclination, the reference orientation is the principal direction (principal component) in which

CHAPTER 3. ENDOSCOPIC IMAGING SYSTEM FOR AUTONOMOUS ROBOTIC MIS

the majority of data points vary. To attain the system performance in tissue reconstruction, the distal error is also calculated with biological samples draped over the DOF target surface.

$$\mu = \frac{1}{N} \sum_{i=1}^N d_i \quad (3.17)$$

where N is the total number of point cloud.

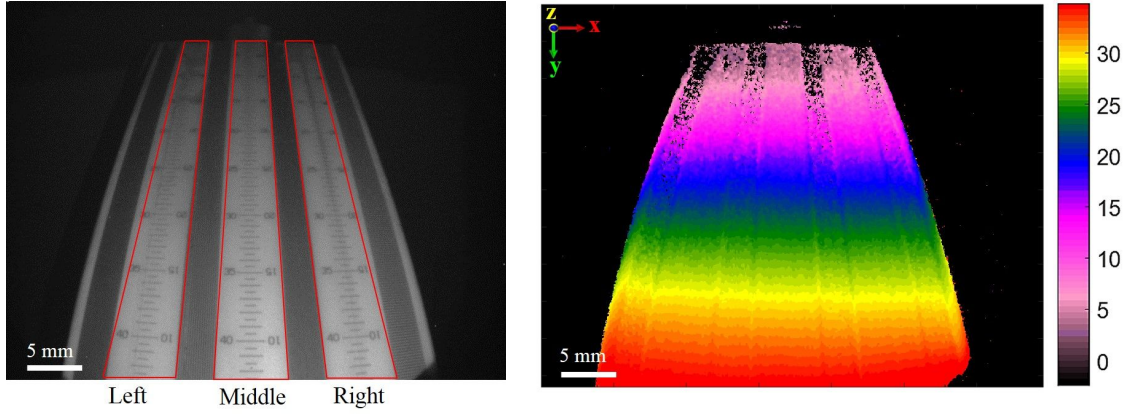
$$\sigma = \sqrt{\frac{1}{N-1} \sum_{i=1}^N |d_i - \mu|^2} \quad (3.18)$$

$$d = |f_{pc}(x, y, z) - f_{fit}(x, y, z)|, \quad (3.19)$$

3.3.7.2 Lateral resolution

To assess the lateral resolution of the system, we image a 1951 USAF glass slide resolution target under a broad band xenon light source as shown in Figure 3.15. The bright circle appeared in Figure 3.15(a) is the reflection of the ring light from the endoscopic distal end on the target glass surface. The target is located within the DOF of the system and is about 3 cm away from the distal end of the endoscope. From the reflection image in Figure 3.15(a) and the contrast profile in Figure 3.15(b), the best resolution of the system is located

CHAPTER 3. ENDOSCOPIC IMAGING SYSTEM FOR AUTONOMOUS ROBOTIC MIS



(a) DOF target with chosen Left, Middle and Right regions of interest for 3D error assessment in Figure 3.13. (b) The corresponding depth map of the DOF surface with depth color bar in millimeters.

Figure 3.12: DOF height map. Camera exposure is set at 20 ms/fringed image. The color map denotes height measurements from the reference zero plane—farthest from the distal end of the scope—to the closest plane from the distal end of the scope.

in Group 3, Element 2 or Element 3 in horizontal axis (X2, X3 regions) and in Group 3, Element 3 in vertical axis (Y region), therefore, the lateral resolution of the system is $49.61 \mu\text{m}$.

3.3.8 System Sensitivity in 3D Tissue Reconstruction

3.3.8.1 Experimental Procedure

The 3D tissue reconstruction is conducted using biological samples such as porcine skin and intestinal tissue. Porcine skin samples (purchased from local shop) with removed excess fat layers was preserved in salt cure (Hormel Foods, Austin, Minnesota). Porcine intestine samples (Animal Technologies,

CHAPTER 3. ENDOSCOPIC IMAGING SYSTEM FOR AUTONOMOUS ROBOTIC MIS

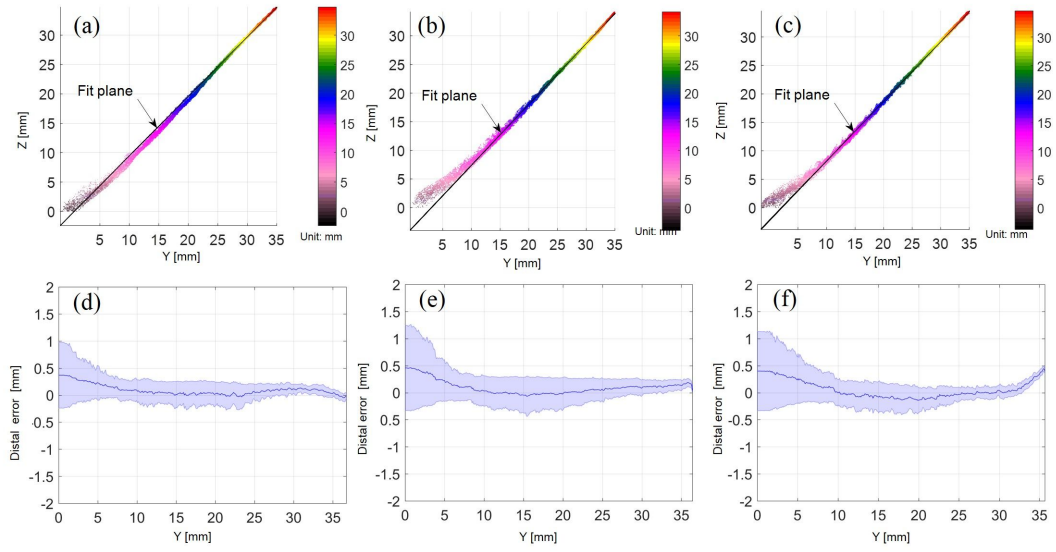


Figure 3.13: (a-c) 3D point cloud population of Left, Middle and Right regions (Marked as red ROIs in Figure 3.12(a)). Color bar displays height in millimeters. The plots are viewed along the 45° angle surface of the DOF target. The fit plane is calculated as the best fit of the collected point cloud population. (d-f) 3D precision of the Left, Middle and Right regions with blue middle lines referring to distal means between 3D point clouds to the fit plane, the blue shaded region indicating the standard deviation of distal error.

CHAPTER 3. ENDOSCOPIC IMAGING SYSTEM FOR AUTONOMOUS ROBOTIC MIS

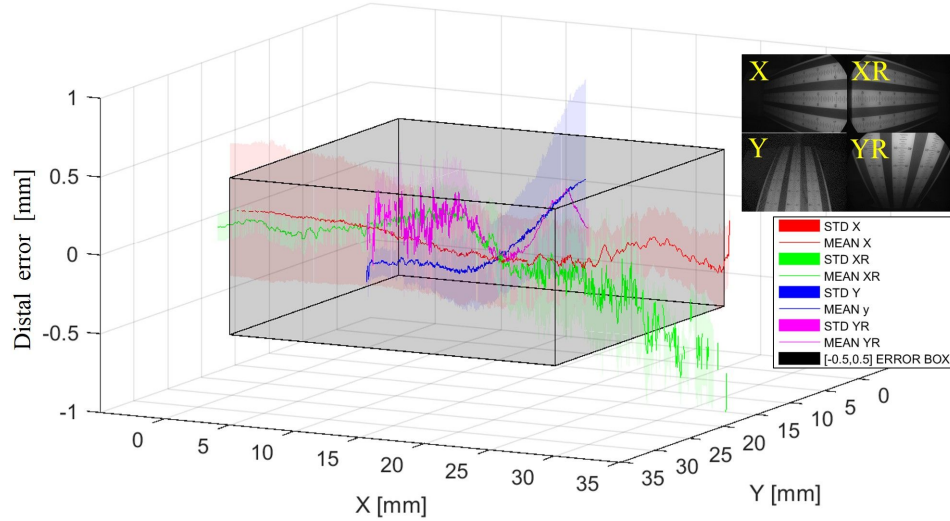
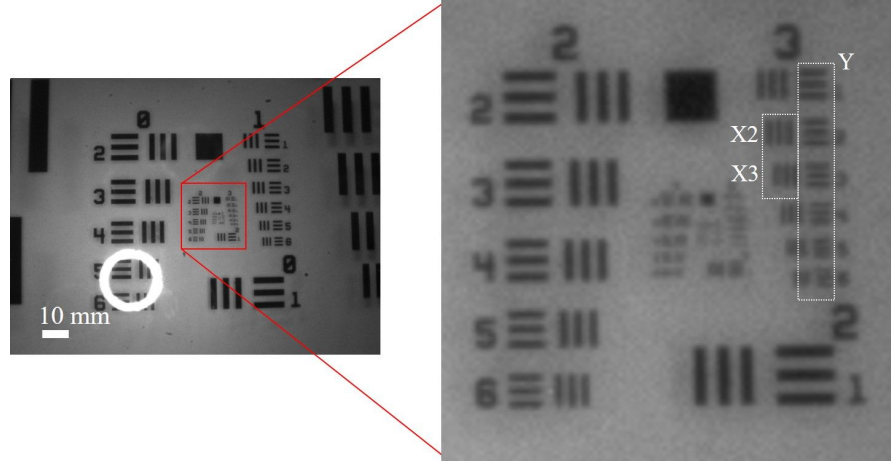


Figure 3.14: 3D precision in 4 directions as described in the inset along the x -axis (X in red and XR in green) and along the y -axis (Y in blue and YR in magenta). The gray boundary box indicates a distal error constraint between -0.5 mm to 0.5 mm.

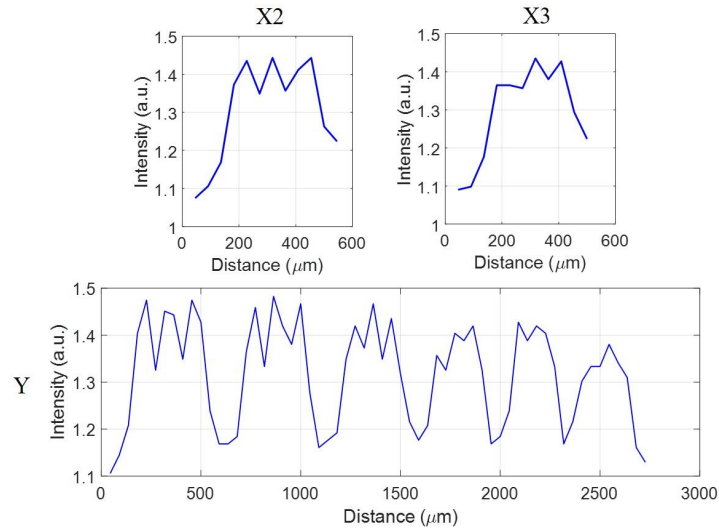
Tyler, Texas) were prepared by washing out all the biological waste from inside of the tissue, and cut into 6-inch-long segments. Prepared samples of skin and intestine were then rinsed using a pressure washer and preserved in vacuum sealing safe bags at -20°C (Sheikh Zayed Institute for Pediatric Surgical Innovation, Children's National Health System, Washington, D.C.). Prior to the imaging process, the tissues were thawed to room temperature and used for the following imaging tests:

1. 3D reconstruction of sample with different thickness levels: Small intestine and skin samples were cut into $5 \times 10 \text{ cm}^2$ flaps and draped onto the DOF target surface. 3D images are collected to compute the depth er-

CHAPTER 3. ENDOSCOPIC IMAGING SYSTEM FOR AUTONOMOUS ROBOTIC MIS



(a) Bright-field raw image of the USAF 1951 target captured by the system described in 3.8 (Left) and a zoom-out image of the region focused on Group 3.



(b) Intensity profile along X2, X3 and Y regions indicated in 3.15(a).

Figure 3.15: Lateral resolution of the system validated using a USAF 1951 target, indicating lateral resolution of about $49.61 \mu\text{m}$ (Group 3, Element 3).

CHAPTER 3. ENDOSCOPIC IMAGING SYSTEM FOR AUTONOMOUS ROBOTIC MIS

ror with similar analysis method as described in Section 3.3.7.1 (Figure 3.16). The test is extended to imaging tissue with the same thickness under different sensor exposure (Figure 3.17).

2. 3D reconstruction of sample with different pigmentation levels: A mixture of small and big intestines with natural pigmentation was fixed on a Styrofoam platform inside a petri dish. A video stream of the 3D intestinal map was recorded as the disc was translated (Figure 3.18). Other dynamic and static human mouth cavity and bone cadaver are also imaged for 3D surface reconstruction (Figure 3.19).
3. 3D reconstruction of sample in clinical intestinal anastomosis setting: A porcine small intestine was transversally cut and four stay sutures were placed to expose the two intestinal lumens in a diamond shape as in Figures 3.20 and 3.21, with two placement sutures close to the mesenteric and anti-mesenteric corners of the lumen, and two additional sutures are in the middle, similar to a standard clinical staging technique for an end-to-end bowel anastomosis scenario [112]. All stay sutures were suspended and multiple running stitches were performed. 3D measurements was recorded as video stream when surgical tools and suture lines were introduced.

CHAPTER 3. ENDOSCOPIC IMAGING SYSTEM FOR AUTONOMOUS ROBOTIC MIS

3.3.8.2 Result

In Test 1, two tissue samples of small intestine with mean thickness of 0.497 mm and skin tissue with mean thickness of 3.490 mm. The thickness measurements were done using a caliper ruler. Both samples were imaged for 3D collection with the same camera exposure of 40 ms/fringed image. The depth maps shown in Figure 3.16 indicate the inclination of the DOF target's surface, in addition to the homogeneous texture on the skin compared to inhomogeneous texture in intestine. The thinner intestine tissue yields a distal error of 0.5 mm standard deviation, which is lower than in thicker skin tissue depth, with standard deviation of about 1 mm in distal error. The distal error magnitude jumps in the intestine sample between 10 mm and 15 mm in Figure 3.16(e) is due to the excess tissue protrusion at the right edge of the target. When the thickness is small (tissue is almost transparent), the average distal error is less than in the thicker tissue. An explanation is due to the higher contrast of the projected fringe onto the sample surface. The higher contrast of the vertical fringes creates a smooth phase distribution, therefore, increases depth reconstruction performance.

To improve tissue imaging sensitivity, either LED illumination power or camera exposure is increased. In this circumstance, camera exposure is increased due to hardware limitation of the LED power and the endoscopic op-

CHAPTER 3. ENDOSCOPIC IMAGING SYSTEM FOR AUTONOMOUS ROBOTIC MIS

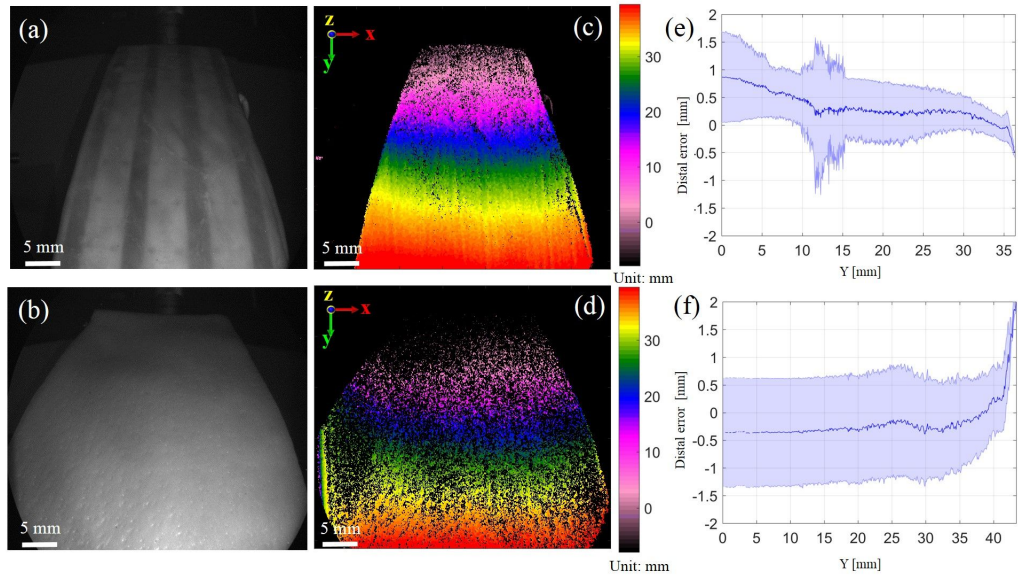


Figure 3.16: (a, b) Bright field reflection images of a DOF target covered by intestine (Top) and skin flaps (Bottom). (c, d) The corresponding depth map with a depth color bar in millimeters. Camera exposure is set at 40 ms/fringed image. (e, f) 3D precision with mean and standard deviation of the distance from reconstructed point cloud to the fit plane. Blue middle line indicates mean distance between 3D point clouds to the fit plane, and the blue shaded region refers to the standard deviation of the distal error.

CHAPTER 3. ENDOSCOPIC IMAGING SYSTEM FOR AUTONOMOUS ROBOTIC MIS

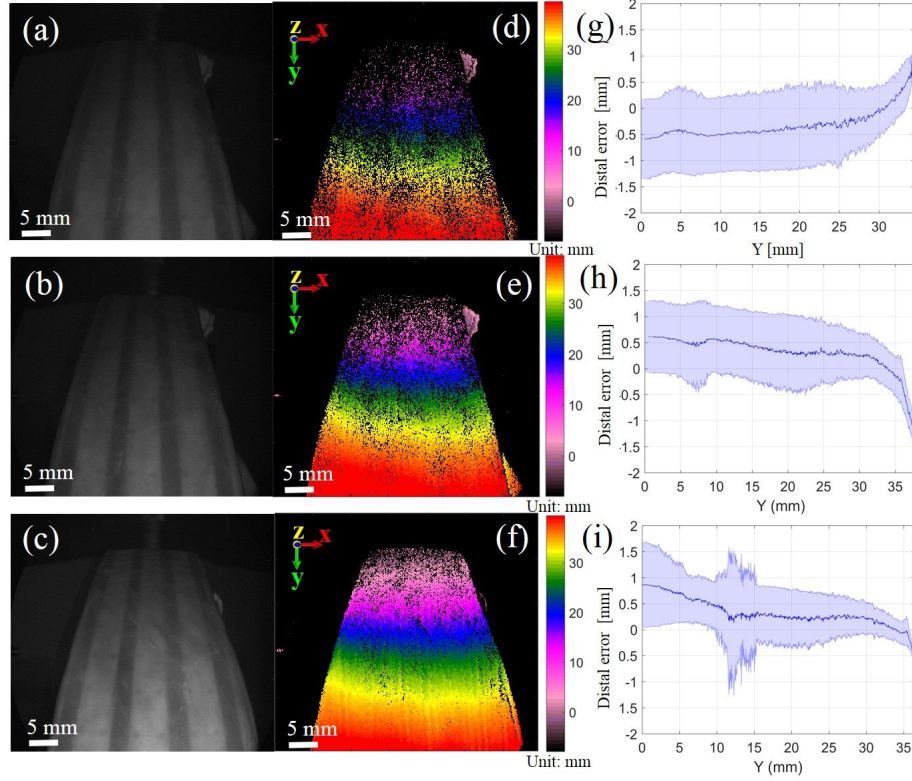
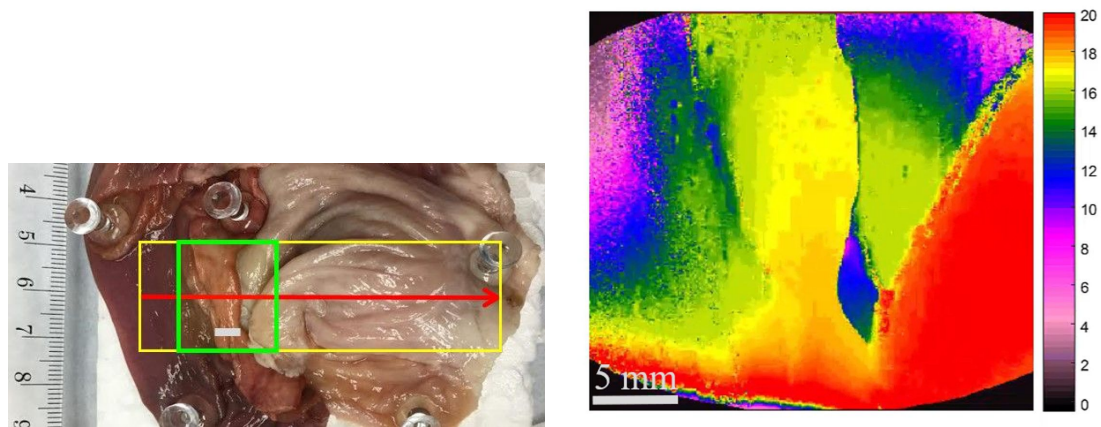


Figure 3.17: (a, b, c) Bright field reflection images of a DOF target covered by intestine at different camera exposure of 20 ms (Top), 30 ms (Middle) and 40 ms (Bottom). (d, e, f) The corresponding depth map with depth color bar in millimeters. (g, h, i) 3D precision with mean and standard deviation of the distance from point cloud to the fit plane. Blue middle line shows mean distance, and the blue shaded region marks the standard deviation of the distal errors.

tical transmittance property. In Figure 3.17, distal error is evaluated using collected images of the small intestinal segment with different camera exposures of 20 ms, 30 ms and 40 ms. The higher sensor exposure, the more photon counts is gathered, thus, more 3D data points are collected, therefore the error variation in the case of intestinal 3D is reduced from around 0.8 mm to 0.5 mm with imaging exposure time is increased from 20 ms to 40 ms.

CHAPTER 3. ENDOSCOPIC IMAGING SYSTEM FOR AUTONOMOUS ROBOTIC MIS



(a) Digital color image of the intestinal sample for 3D scanning in Figure 3.18(b). The sample consists of smaller to larger intestines with different tissue pigmentation and thickness. The scanning area is within the yellow boundary, with the scanning direction from left to right along the red arrow. The green region shows a demonstrated frame for the 3D depth still image excerpts extracted from Figure 3.18(b). Ruler unit is in millimeters.

(b) Still image excerpts from video recordings of the depth map scanning (Green ROI in Figure 3.18(a)) along the yellow region in Figure 3.18(a). Camera exposure is set at 33 ms/fringed image.

Figure 3.18: Height map translational scanning of an intestinal pile with different pigmentation. The depth color bar in Figure 3.18(b) is in millimeters. Video is at 5X speed and can be viewed online ¹

In Test 2 (Figure 3.18), 3D reconstruction performance on biological tissue is evaluated in video mode. A mixture of porcine intestines on a translated platform was set to mimic a realistic anastomosis scenario. The green region of interest (ROI) in Figure 3.18(a) (Green ROI) is scanned along the red arrow, and within the yellow boundary. The depth map of the scanned ROI indicates thickness variations of the intestinal mixture.

In Test 3, an ex-vivo experiment with the end-to-end anastomosis in porcine

¹<https://doi.org/10.1117/1.JBO.23.5.056009.1>

CHAPTER 3. ENDOSCOPIC IMAGING SYSTEM FOR AUTONOMOUS ROBOTIC MIS

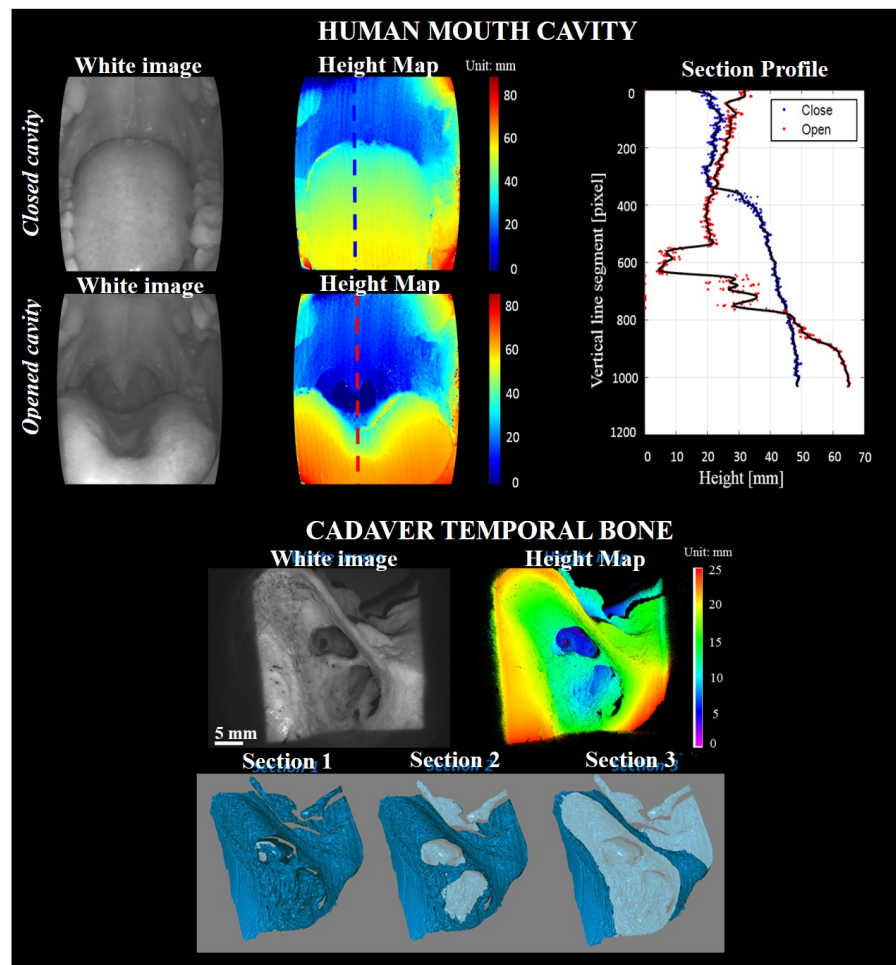


Figure 3.19: 3D reconstruction of human sample.

CHAPTER 3. ENDOSCOPIC IMAGING SYSTEM FOR AUTONOMOUS ROBOTIC MIS

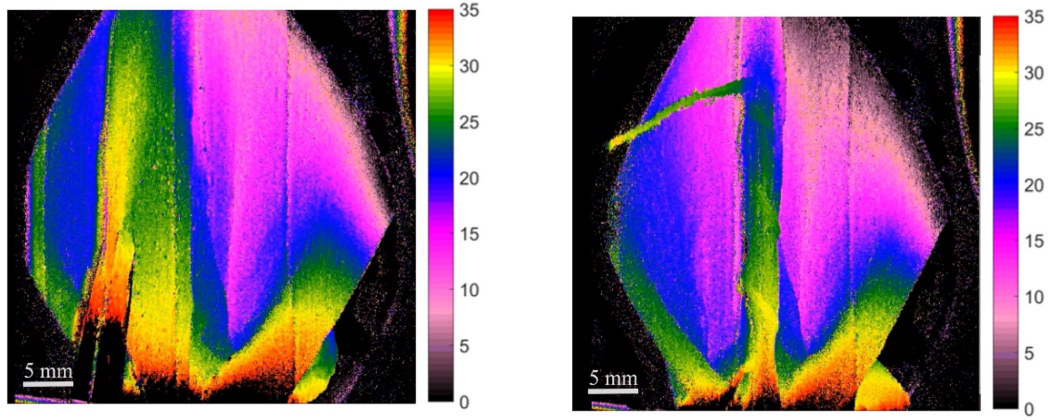
bowel tissue is conducted in video mode (Figures 3.20 and 3.21). The detection of small feature such as suture line, and tissue deformity and the metallic surgical tweezers at a reasonable speed in a clinically relevant setting shows the feasibility of the system in clinical application. Similar to previous depth images, a depth ruler within 0 mm to 35 mm is used to display depth profile from the zero-reference plane to the interested sample depth. Therefore, when the surgical tool is presented (Figure 3.20(a)), part of the tool closer to the distal end of the scope is out of the interested depth range and therefore that depth was not displayed. The depth reconstruction records a dense point cloud distribution across the tissue surface without data "holes", which are often collected with little to no texture surface (3D stereoscopic reconstruction).

Figure 3.21 details more features of the end-to-end intestinal sample. For example, the middle tissue section detects flap features marked in red point clouds in Figure 3.21 (Top row). In Figure 3.21 (Bottom row), the three suture lines are segmented based on intensity thresholding and marked in red. An average height of 0.726 ± 0.0075 mm above the baseline is recorded, comparing to a real height of suture line of 0.723 ± 0.022 mm measured by a caliper.

²Link to Video 3.20(a): <https://doi.org/10.1117/1.JBO.23.5.056009.2>.

³Link to Video 3.20(b): <https://doi.org/10.1117/1.JBO.23.5.056009.3>.

CHAPTER 3. ENDOSCOPIC IMAGING SYSTEM FOR AUTONOMOUS ROBOTIC MIS



(a) Still image excerpts from video recordings of the depth map of the anastomosis setup without looping sutures. Forceps are used to show a simple typical tool manipulation during the 3D recording.

(b) Still image excerpts from video recordings of the depth map of the anastomosis setup with looping suture lines.

Figure 3.20: Height map of anastomosis setup. Camera exposure is set at 33 ms/fringed image. Video is at 5x speed. Videos can be viewed online ^{2,3}.

3.3.9 Lessons Learned

By using structured illumination technique, the system is able to reconstruct a dense 3D point cloud distribution for tissue samples. In contrast to techniques such as ToF and plenoptics imaging, the SI 3D system yields higher quantified depth sensitivity in pigmented sample. Moreover, the system offers hardware flexibility into endoscopic setting with different magnification and DOF with other focusing lens and fringe design parameters, without a dedicated micro-lens array fabrication as in plenoptic, or low 3D accuracy as in ToF. Furthermore, the SI 3D system maintains dense point cloud distribution for robotic navigation and surgical planning, with no or little data “holes” compared to

CHAPTER 3. ENDOSCOPIC IMAGING SYSTEM FOR AUTONOMOUS ROBOTIC MIS

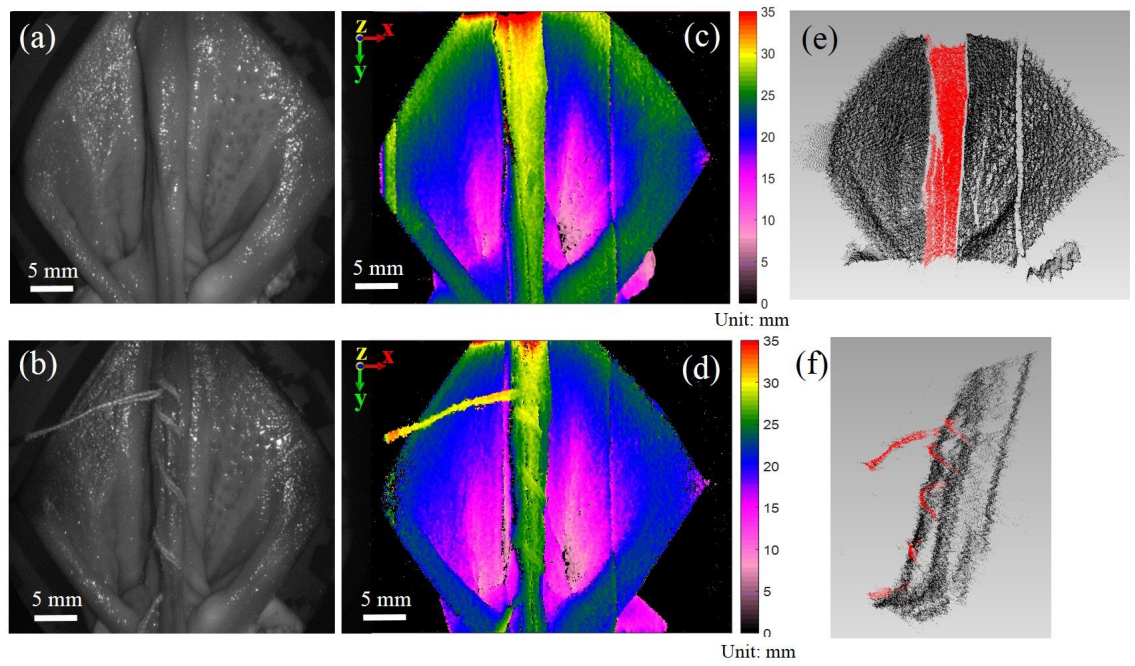


Figure 3.21: (a, b) Bright field reflection images of intestinal anastomosis at a camera exposure time of 33 ms without (Top row) and with looping sutures (Bottom row). (c, d) The corresponding depth map with depth color bar in millimeters. (e, f) The corresponding 3D point cloud distribution with segmented tissue fold and suturing stitches marked in red points.

CHAPTER 3. ENDOSCOPIC IMAGING SYSTEM FOR AUTONOMOUS ROBOTIC MIS

stereoscopy or other hybrid laser dot-like structure illumination. Finally, the compact design of the demonstrated system utilizes a low power LED illumination, and can be mounted on another surgical robotic arm.

The residue fringes and motion artifacts observed in video streaming mode is directly related to the speed of the imaging system. Fortunately, the dominant tissue motion that we encounter for abdominal operation is a slow and periodic motion resulted from patient breathing. Therefore, the current acquisition speed does not pose a significant issue. However, it does introduce relative position error for faster motion and can only be corrected if the speed is improved.

The system speed of 1.57 fps is mainly due to high number of projected fringes when performing 3D reconstruction and the camera sensitivity for tissue imaging. Moreover, the scopic transmission is measured to be around 40% using a collimated laser diode at 532 nm. For LEDs installed in the projector optical chamber, this transmission drops to around 7% due to the high angle dispersion (0.8 mW at the distal end, compared to 12 mW at the proximal end). Faster acquisition time can be achieved by 1) increasing light delivery throughput in both illumination and imaging scopes by installing higher LED power, or increasing the scope diameter. Replacing the current scopes with two identical 10-mm scopes can increase the 3D reconstruction to about 6.25 fps, with 10 ms for each fringed image under the same system hardware and image resolu-

CHAPTER 3. ENDOSCOPIC IMAGING SYSTEM FOR AUTONOMOUS ROBOTIC MIS

tion. 2) Reducing the projection fringe number to a desirable number without scarifying the accuracy.

The demonstrated 3D imaging system provides enough structural information to reconstruct homogeneous surfaces of the intestines without the use of additional markers. The separation between the imaging and illumination scopes is within 12° , therefore, a dual access port or a single access port of about 12 mm diameter for the two 4-mm scopes is required for a 40-mm insertion depth. Several designs of a compact endoscopic system with dual endoscope assembly aim to reduce the insert port housing by using smaller endoscope, flexible fiberscope, or with angle prisms and angle fixation mechanism has been proposed [103].

Chapter 4

Tissue Property Extraction using Multispectral Reflectance Imaging Technique

4.1 Motivation

While propagating through tissue, photons of different spectral illumination interact randomly with chemical chromophores through absorption and scattering effects. In addition, reflected photons carry distinguishing spectral signatures of different chromophore rotations and translation movements. Analyzing these signatures reveal the distribution of each chromophore compo-

CHAPTER 4. TISSUE PROPERTY EXTRACTION USING MULTISPECTRAL REFLECTANCE IMAGING TECHNIQUE

nent; therefore, highlighting features that a broadband bright light can not distinguish. Multi-spectral imaging in the medical field has been widely applied to highlight chemical concentrations within chromophore mixtures, such as for tissue classification for burn evaluation [113], for contamination quantification [114], or to monitor hemoglobin chemical temporal distribution for ischemia monitoring and other blood flowmetry calculation [115–117]. The motivation is to explore multiple tissue-related parameter extraction through spectral imaging modalities in free space and in endoscopic housing, for a safe surgical strategic planning and diagnostic.

My contributions entail designing and building a multi-spectral imaging system integrated in free space with an endoscopic housing to conduct specific spectral analysis to extract tissue-related parameters for perfusion monitoring, such as the tissue thickness, tissue types, blood vessels and oxygen saturation. The work proposed in this section results in publications in [118,119]

4.2 First Prototype: Open-space Multispectral Imaging System

4.2.1 System Contributions

The goal of this system is used to evaluate the ischemic condition of an *in-vivo* porcine model during an open-field surgery. The system utilizes spectral component analysis between signature spectral peaks of different chromophores inside the tissue to deduce tissue information such as the percentage of oxygenate saturation, tissue types and thickness variations.

4.2.2 System Setup

The imaging system as depicted in Figure 4.1 consists of a broad-band halogen light source that is coupled through a rotational filter wheel, which sequentially switches between three bandpass filters with central wavelengths at 540 nm, 560 nm and 580 nm and a bandwidth of 10 nm (FB540-10, FB560-10, FB580-10, Thorlabs, New Jersey). The rotation is controlled by applying an electric current to the filter wheel and rotating unit stopping at each filter location for image capturing within its desired exposure time. The filtered light is then coupled into a light-guided fiber and a slit-ring to illuminate the object. The spectral light reflects from the tissue surface and is focused on a CMOS de-

CHAPTER 4. TISSUE PROPERTY EXTRACTION USING MULTISPECTRAL REFLECTANCE IMAGING TECHNIQUE

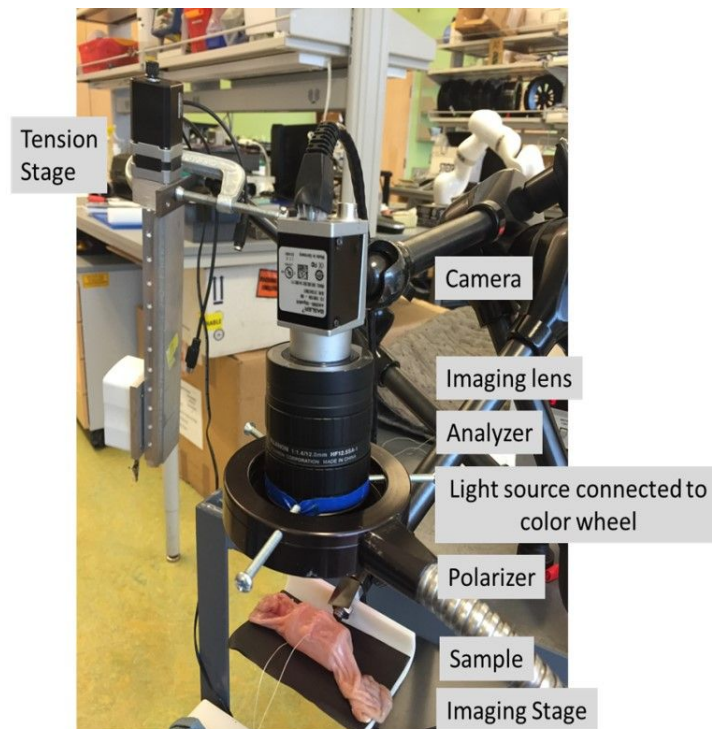


Figure 4.1: Open-space multispectral imaging setup.

vice (acA2000-50gmNIR, Basler, Pennsylvania, USA) through an imaging lens (Fujinon HF 12.5 SA-1, Phoenix Imaging Ltd., Michigan, USA). A set of cross polarizers and an analyzer are installed in front of the slit-ring light and the imaging lens, respectively, to reduce the effect of Fresnel specular reflection from the tissue surface.

The system is installed on a rotational NOGA arm fixed on a side table next to a clinical bench bed. To minimize motion artifacts, the sample is laid on a 3D printed tray located within the depth of field of the imaging lens (about 6 cm away from the slit-ring light surface)

CHAPTER 4. TISSUE PROPERTY EXTRACTION USING MULTISPECTRAL REFLECTANCE IMAGING TECHNIQUE

4.2.3 Experimental Procedures and Result

The system is evaluated using two *in-vivo* porcine perfusion monitoring experiments performed in a clinical room.

4.2.3.1 Tissue Classification

Different tissue types such as blood vessel, messentery and intestinal thickness variation are critical factors to locate a safe anastomosis suture for an autonomous surgical robot, or simply to suggest a suturing map of the surgical site for human surgeon. Thickness variation requires photon optical penetration from a wide wavelength range, and blood vessel with strong hemoglobin absorption shows up within 540-600 nm. Therefore, additional bandpass filters with central wavelengths at 470 nm, 600 nm and 760 nm (FB470-10, FB600-40, FB760-10, Thorlabs, New Jersey, USA) are added to the filter wheel from the system described in Sec 4.2.2.

A spectral analysis method such as the spectral angle mapper (SAM) [114] is used to extract thickness variation based on the reflected photon accumulation on the sensor. Knowledge of the tissue optical properties such as absorption, scattering and anisotropy factor can numerically simulate the amount of photons reflected from a ballistic beam geometry [120]. SAM is a supervised spectral analysis technique that specifies spectral similarity of each pixel to a known reference spectra by calculating the angle between two spectra accord-

CHAPTER 4. TISSUE PROPERTY EXTRACTION USING MULTISPECTRAL REFLECTANCE IMAGING TECHNIQUE

ing to Equation 4.1, treating the spectra as vectors in an n dimensional space defined by n reference spectral bands [121, 122]. The smaller the angle, the closer the pixel spectrum \vec{pxl}_i matches the reference spectra \vec{ref}_i .

$$\alpha = \cos^{-1} \frac{\sum_{i=1}^n \vec{pxl}_i \cdot \vec{ref}_i}{\sqrt{\sum_{i=1}^n \vec{pxl}_i^2} \sqrt{\sum_{i=1}^n \vec{ref}_i^2}} \quad (4.1)$$

The threshold used to determine a pixel endmember depends on the definition of maximum angle, which is the maximum acceptable angle that a pixel is verified as an endmember. The parameters for SAM are chosen to yield up to 2 or 3 endmembers for number of thickness variations to be extracted, and the default maximum angle is kept at 0.1 radian (5.7°) for full classification.

Global threshold is used in this study to maintain the consistency of the SAM results on the same materials within the imaging view, the effect of local threshold for each material in a complex structure will be studied in the future. The reference endmember collection used for angle computation was imported from the predefined ROI as user inputs for an estimated thickness on the sample. The outcome of SAM is an image with color-coded pixels where the number of colors represents the number of endmembers.

Several porcine small and big intestinal samples with mesentary folds (Figure 4.2) and with thickness variations (Figure 4.3) are used to validate our system and method. The results in Figure 4.2 shows different tissue types

CHAPTER 4. TISSUE PROPERTY EXTRACTION USING MULTISPECTRAL REFLECTANCE IMAGING TECHNIQUE

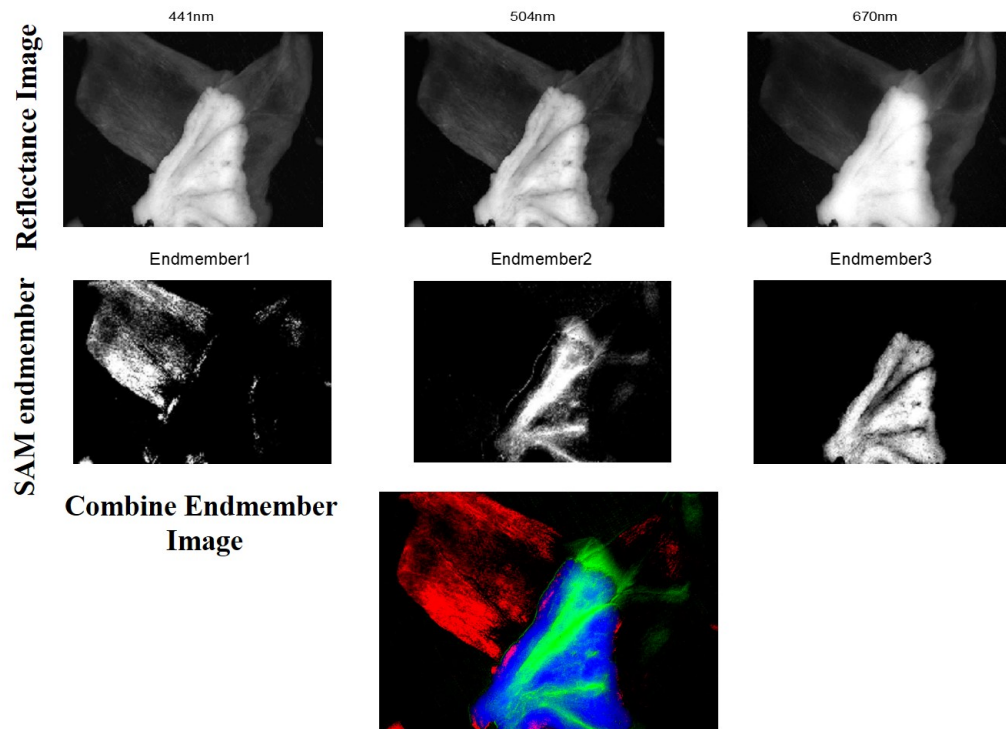


Figure 4.2: Tissue type segmentation result using SAM method to classify mesentery, messentery ridges and small intestine. (Top) Spectral images at each filtered illumination. (Middle) SAM endmember results. (Bottom) End-member summation.

such as the small intestine layer and the mesentary features are classified in separate endmembers and can be overlaid for visualization in red, green and blue, respectively. Similarly, the spectral difference between thin and thick tissue in big intestinal sample (Figure 4.3) can be deduced and contribute to tissue thickness classification. The thickness variation is consistent with the MicroCT slice scanning measurements.

Moreover, spectral analysis allows other tissue parameters such as tissue boundary (or bite size which is the area near tissue edge suitable for suturing),

CHAPTER 4. TISSUE PROPERTY EXTRACTION USING MULTISPECTRAL REFLECTANCE IMAGING TECHNIQUE

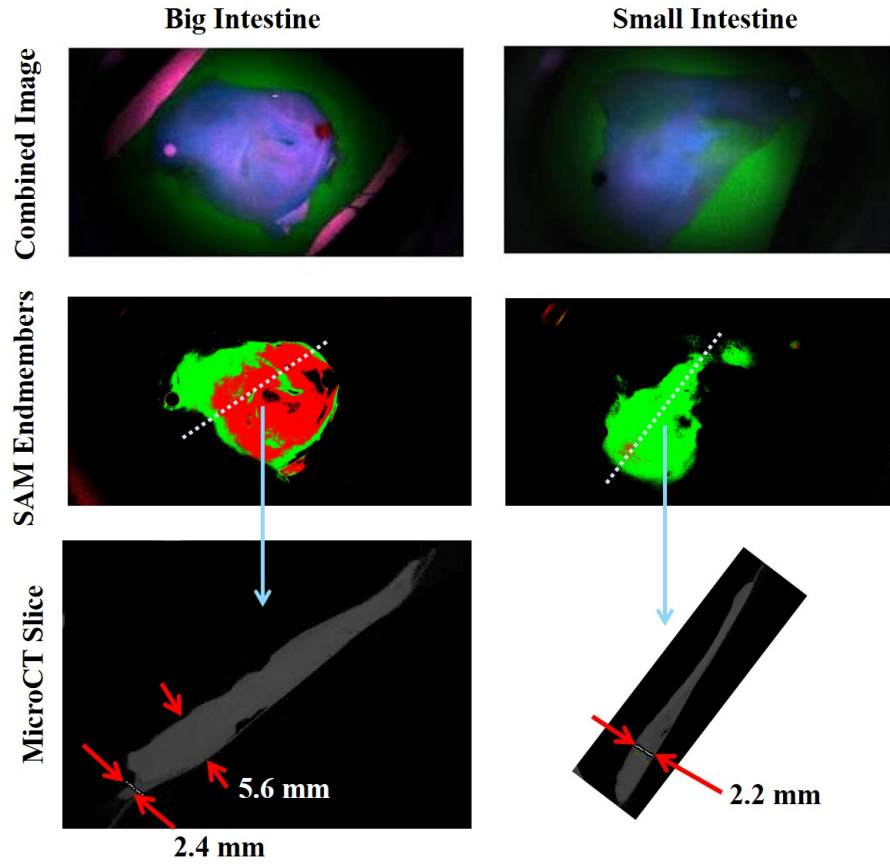


Figure 4.3: Tissue thickness segmentation result using SAM method on big and small intestine sample with corresponding microCT thickness comparisons. (Top) Combined spectral images from 441 nm, 508 nm and 670 nm spectral images. (Middle) SAM endmember results. Green indicating thinner layer and red indicates thicker layer. (Bottom) MicroCT image with representative thickness measurements.

CHAPTER 4. TISSUE PROPERTY EXTRACTION USING MULTISPECTRAL REFLECTANCE IMAGING TECHNIQUE

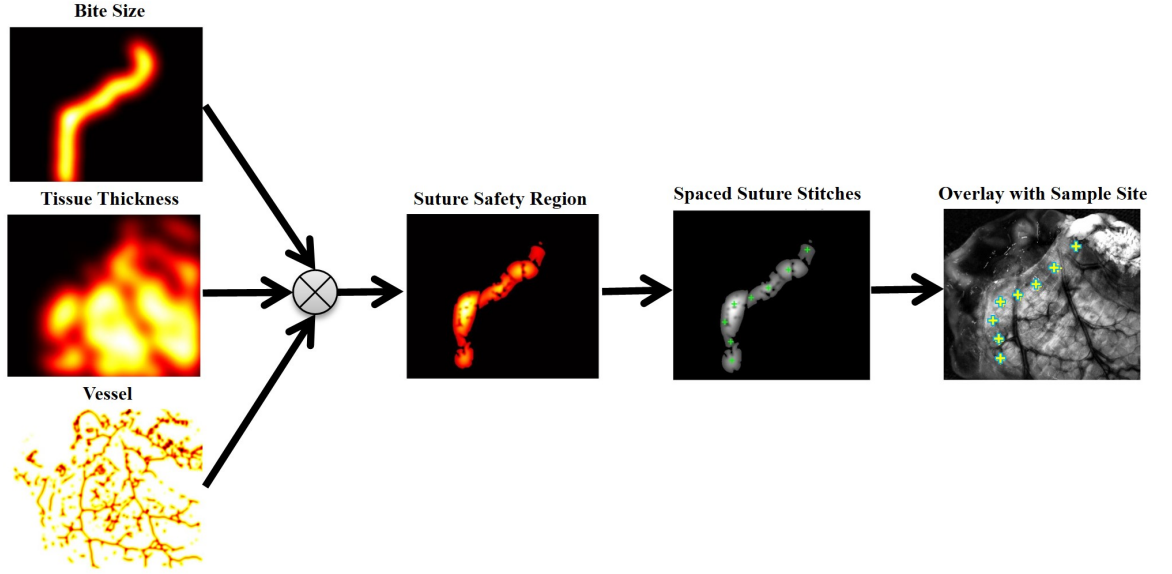


Figure 4.4: Suture map and suture placement recommendations.

blood vessels and thickness variation can be combined and covoluted to create a suture suggestion map (Figure 4.4) for safe and autonomous suture guidance [119].

4.2.3.2 Tissue Perfusion Measurement

Tissue perfusion through oxygen saturation is a common measurement for early detection of blood supply restriction causing oxygen shortage in tissue, i.e. ischemia. The oxygen saturation SO_2 (Equation 4.3) is calculated based on the absorption ratio collected at hemoglobin spectral distinguished peaks at 540 nm, 560 nm and 580 nm. The absorption calculation is based on the modified Beer-Lambert Law (Equation 4.2) with assumptions that the exposed intestinal sample is with no scattering variations across the three wavelength,

CHAPTER 4. TISSUE PROPERTY EXTRACTION USING MULTISPECTRAL REFLECTANCE IMAGING TECHNIQUE

and the absorption depends only on the oxygenated hemoglobin HbO and de-oxygenated hemoglobin HbR.

$$A(\lambda) = \log\left(\frac{I_o(\lambda) - I_d(\lambda)}{I(\lambda) - I_d(\lambda)}\right) = \varepsilon_{HbO}(\lambda)[HbO] + \varepsilon_{HbR}(\lambda)[HbR] \quad (4.2)$$

where $I_o(\lambda)$ is the reflected intensity of a white standard at each wavelength (>98% reflectivity), $I(\lambda)$ is the reflected intensity of the sample at each wavelength, $I_d(\lambda)$ is the reflected intensity of dark ambient light, ε is the known molar extinction coefficient [123] and $[.]$ is the concentration of each hemoglobin chemicals. The oxygen saturation measurement is computed by the ratio of the oxygenated hemoglobin [HbO] and total hemoglobin [HbT] as in Equation 4.3.

$$[HbT] = [HbO] + [HbR]; SO_2 = \frac{[HbO]}{[HbT]} \quad (4.3)$$

Two preliminary experiments for perfusion monitoring such as through blood occlusion via mesentary clamping and through different suturing spacing and tension are discussed in Sections 4.2.3.2.1 and 4.2.3.2.2.

CHAPTER 4. TISSUE PROPERTY EXTRACTION USING MULTISPECTRAL REFLECTANCE IMAGING TECHNIQUE

4.2.3.2.1 Tissue Perfusion during Mesentery Occlusion

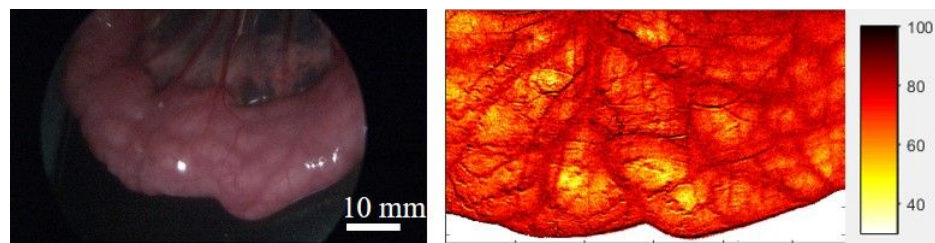
The purpose of this experiment was to verify the sensitivity of the system to capture oxygenation differentiation before, during, and after the blood supply was occluded. A segment of small intestine was selected randomly and positioned on the designated platform as indicated in Figure 4.5 while it is still connected with the pig's bowel. The tissue segment is imaged at 3 states: its original state, after the mesentery is clamped for 5 minutes, and after the clamp is released (twelve minutes after the initial state).

The result of perfusion, indicated in Figure 4.5, shows that there is about 30% oxygenation reduction from the initial state to the occlusion state. At the re-perfusion state, the oxygenation increases about 15%. This observation is consistent with the measurements from [124].

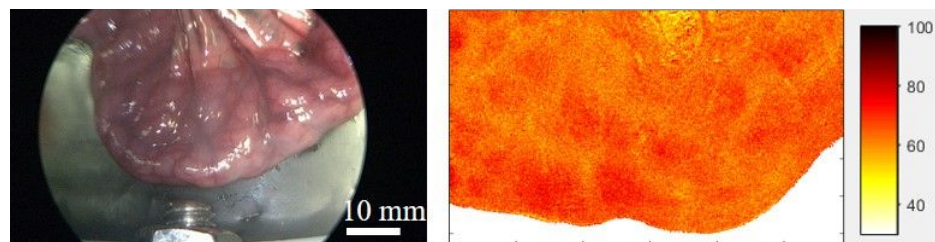
4.2.3.2.2 Tissue Perfusion with Different Suturing Spacing and Tension Setting

Influence of distance between interrupted sutures and suture tension was studied on murine through histology [125] and porcine models through flowmetry imaging [126] before and after suture healing. The goal of this experiment is to study the affect of suturing spacing and tension on perfusion across the suture line within 20 minute after the suturing. Two sets of suture spacings (2 mm and 4 mm) and tension (0.5 N and 1.5 N) are used to perform looping

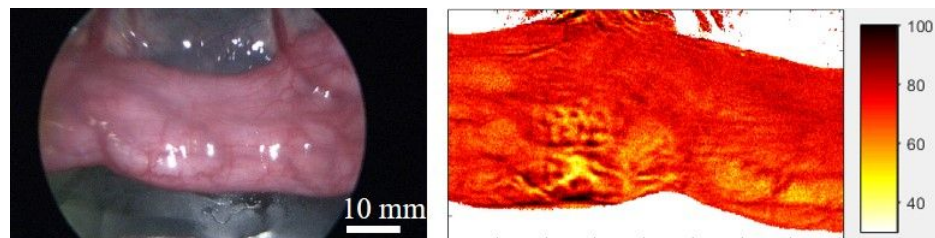
CHAPTER 4. TISSUE PROPERTY EXTRACTION USING MULTISPECTRAL REFLECTANCE IMAGING TECHNIQUE



(a) Initial state. Saturated oxygenation of the intestine.



(b) Masentary occlusion. Saturated oxygenation after clamping the masentary vessels for 5 minutes.



(c) Re-perfusion. Saturated oxygenation after un-clamping.

Figure 4.5: Perfusion monitoring of intestinal condition on an alive porcine model. Colorbar unit is in percentage.

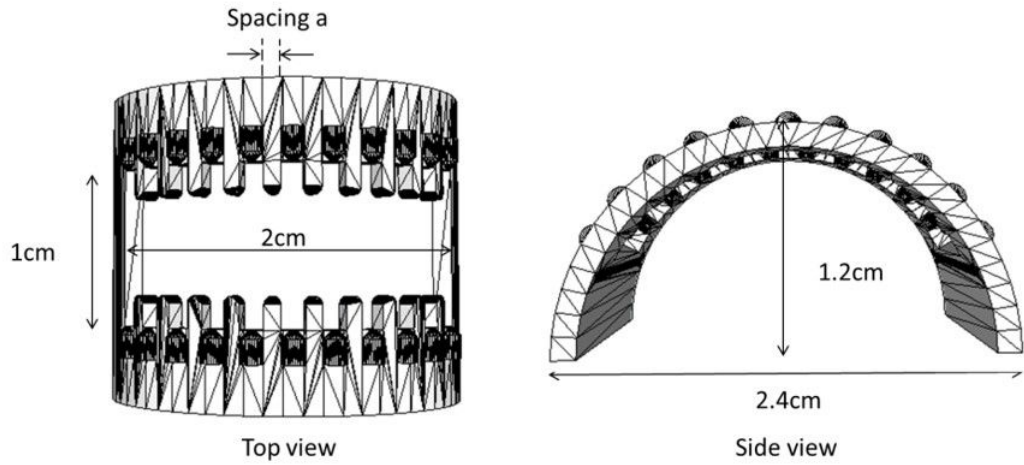
CHAPTER 4. TISSUE PROPERTY EXTRACTION USING MULTISPECTRAL REFLECTANCE IMAGING TECHNIQUE

suture on a cut perpendicular to the intestine length (Figure 4.7). The in-vivo experiments were performed on an alive pig and the sample was imaged right after the suturing and 20 min after suturing using the imaging setup indicated in Figure 4.1.

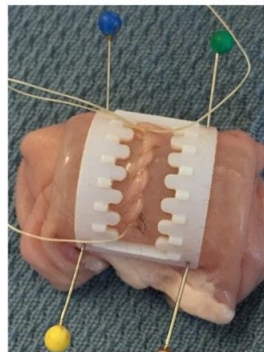
To quantify the oxygen saturation in part, three tissue segments on the left, right and cut-line (with sutures) (Figure 4.8) are segmented based on convolution between the intensity thresholding of total hemoglobin concentration HbT and the total hemoglobin HbT measurement.

The SO_2 measurements of the three segments are summarized in Figure 4.9. From 0 to 20 min after suturing, perfusion reduction happens more apparent and consistent across the three segments with higher suture spacing (4 mm) in both tension strengths. With lower suture spacing (2 mm), blood leakage through suture holes create noise in blood perfusion in the cut-line region. This high leakage is confirmed with leak pressure test shown in Table 4.1, where the intestine is submerged inside a water tank, with air pumped into the lumen body. The leakage pressure in psi is the maximum pressure when air bubbles are observed inside the water tank. Small change in SO_2 of 2-3% was recorded in the middle cut-line in cases of higher tension (1.5 N), and less than 2% reduction of SO_2 in lower tension (0.5 N), indicating flow across the cut-line is not apparent within 20 min monitoring. The SO_2 levels are higher in the cut-line segment compared to the left and right segments, and the increase

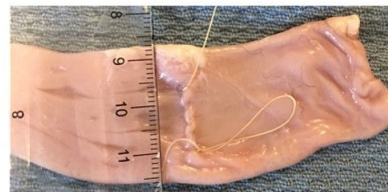
CHAPTER 4. TISSUE PROPERTY EXTRACTION USING MULTISPECTRAL REFLECTANCE IMAGING TECHNIQUE



(a) Suturing frame (Spacing a is set to 2 mm or to 4 mm).



(b)



(c)

(b) Running suturing stitches on intestinal tissue using the designed frame, (c) The sutured tissue is flattened for imaging.

Figure 4.6: Sample preparation with the designed looping stitches using the suturing frame.

CHAPTER 4. TISSUE PROPERTY EXTRACTION USING MULTISPECTRAL REFLECTANCE IMAGING TECHNIQUE

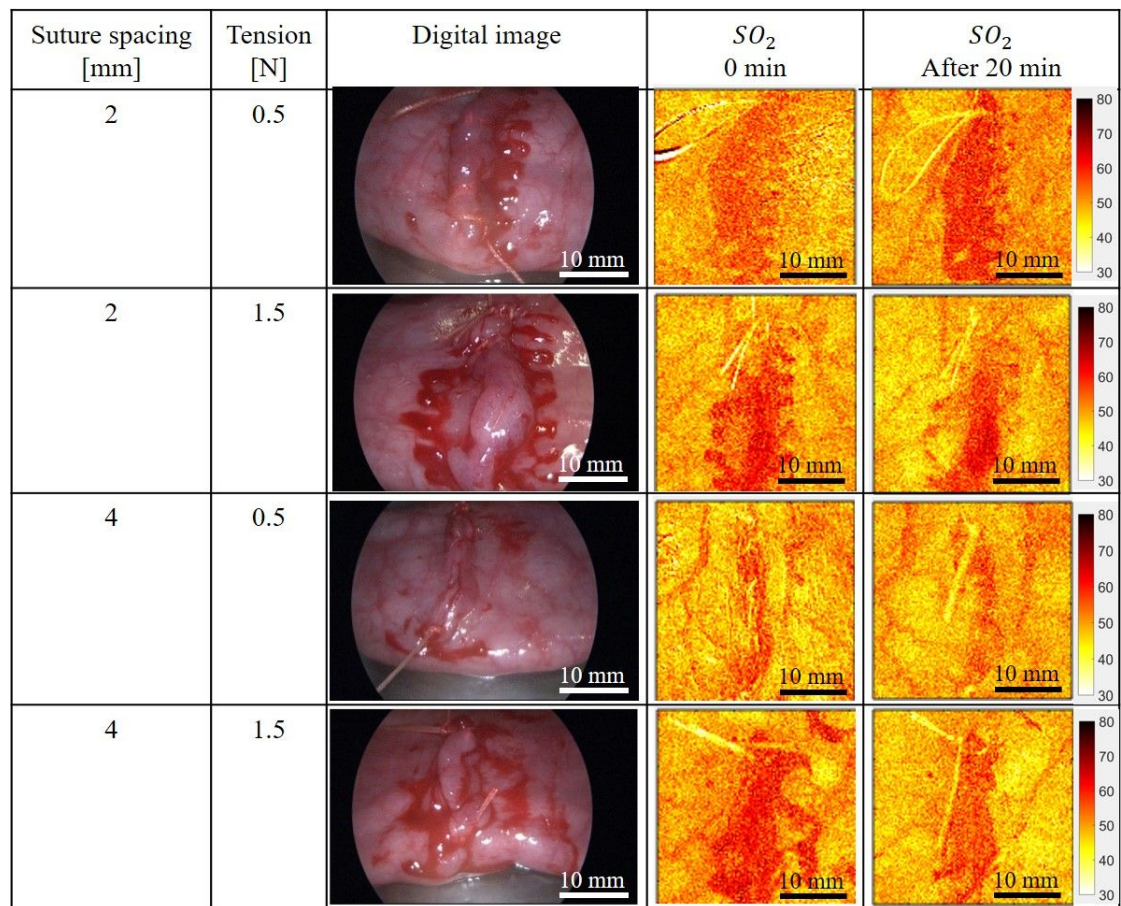


Figure 4.7: Perfusion monitoring with multiple suturing and tension settings. Colorbar unit is in percentage.

CHAPTER 4. TISSUE PROPERTY EXTRACTION USING MULTISPECTRAL REFLECTANCE IMAGING TECHNIQUE

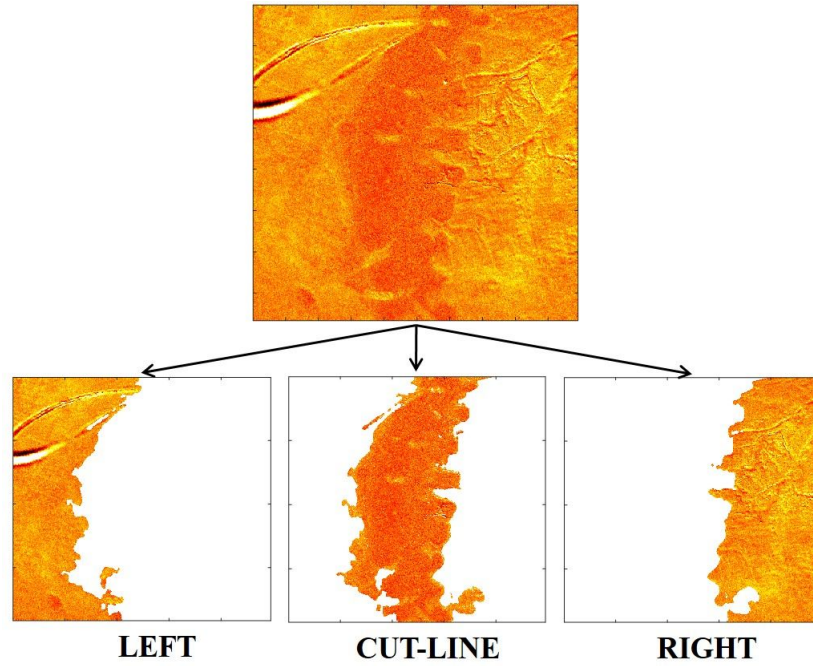


Figure 4.8: Tissue segmentation into LEFT, CUT-LINE, and RIGHT regions for perfusion plots in Figure 4.9.

of SO_2 at the cut-line segment in case of 2-mm spacing, 0.5-N tension indicates measurement error from the HbO coverage when blood leakage through the suture holes and combined with oxygen when exposing to air. The higher leakage in smaller spacing than in larger spacing can be counter-intuitive in the case of suturing of live tissue where the tissue flexibility is still withstand. In this cadaver tissue, we notice higher leak in smaller spacing may due to two reason:

- 1) The cadaver tissue does not maintain its stretch and is torn with the suture needle when a tension is applied;
- 2) Smaller spacing creates higher number of suture holes.

CHAPTER 4. TISSUE PROPERTY EXTRACTION USING MULTISPECTRAL REFLECTANCE IMAGING TECHNIQUE

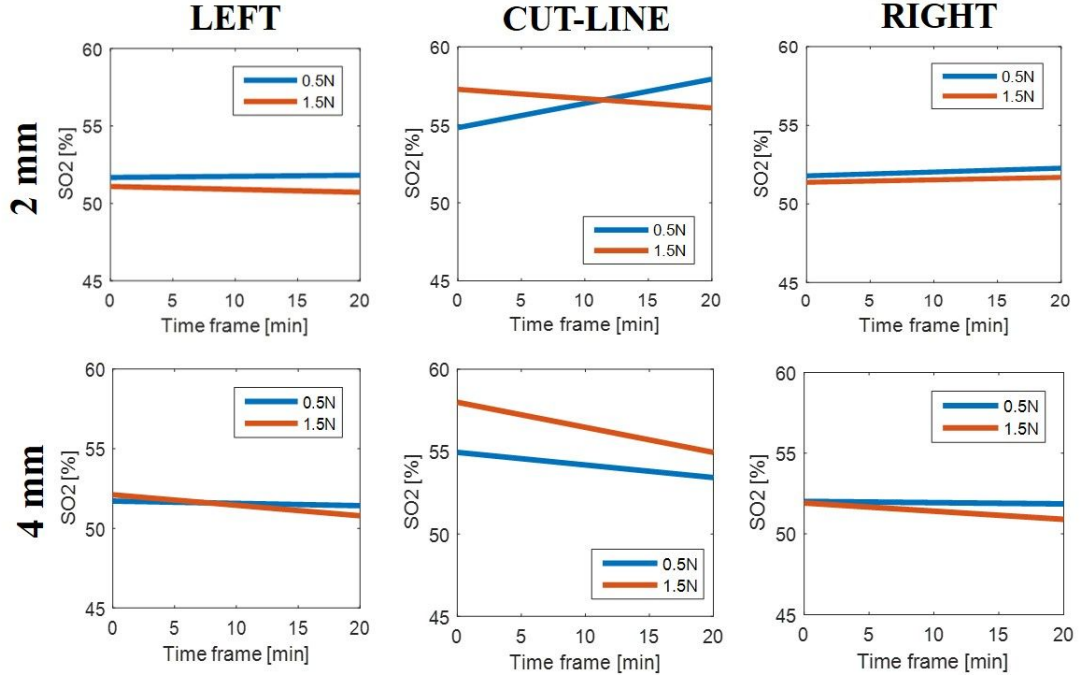


Figure 4.9: Perfusion monitoring within LEFT, CUT-LINE, and RIGHT regions with multiple suturing and tension settings.

4.2.4 Lessons Learned

The open space multispectral imaging setup provides a non-invasive imaging method for determination of multiple tissue-related information such as tissue types with different pigmentations and density, thickness variations and ischemia condition. For higher order of chemical composition of the tissue, the

Spacing [mm]	Tension [N]	Leakage Pressure [PSI]
2	0.5	0.41
2	1.5	0.86
4	0.5	0.76
4	1.5	0.99

Table 4.1: Leak pressure test of the sutured intestinal tissue with multiple spacing and tension forces.

CHAPTER 4. TISSUE PROPERTY EXTRACTION USING MULTISPECTRAL REFLECTANCE IMAGING TECHNIQUE

spectral illumination should match the spectral signature peaks of the interested chemicals. Either the use of sequential filtering like in this system or with a variable wavelength filter module such as a spectrograph in front of the collecting sensor can be used [114]. The system hardware should accommodate the tissue pigmentation for an adequate reflected photon counts for a low noise reading of the segmentation result.

4.3 Second Prototype: Multispectral Imaging Endoscope for Minimally Invasive Surgery

4.3.1 System Contribution

The multispectral hardware and analysis setting is adapted into endoscopy to assist tissue extract for minimally invasive robotic surgery. This involves light delivery coupled into an endoscopic light port. In addition, smaller optics requires higher restriction in numerical aperture (NA) and light throughput. Therefore, in this system, we improve the speed by replacing mechanical switching between filtered lights to electronic switching from three LEDs. The system is integrated with the 3D VIS-NIR endoscope setup detailed in Section 5.4 for surgical planning surgeries.

CHAPTER 4. TISSUE PROPERTY EXTRACTION USING MULTISPECTRAL REFLECTANCE IMAGING TECHNIQUE

4.3.2 System Setup

The imaging system for calculating SO_2 levels consists of three identical LED chips (Lime LED, SP-01-L1, Luxeon Star LEDs, Alberta, Canada) with mounted focusing lens to confine the high order beams (Carclo 8°, Luxeon Star LEDs, Alberta, Canada). An optical coupling system described in Section 4.3.4 to couple LED light to a trifurcated light fiber (77536, Newport Corporation, MA, USA). Three bandpass filter with central wavelengths at 540 nm, 560 nm and 580 nm similar to the system in Section 4.2.2 is used to narrow the illuminated spectra and avoid the overlapped between the adjacent filter bandwidths. Light after the trifurcated probe is index matching to the light port of the surgical rod-lens through an refractive index matching fluid (F-IMF-105, Newport Corporation, MA, USA). The system is integrated with other multimodal imaging system for automating surgical planning in minimally invasive robotic surgeies (Figure 4.10).

4.3.3 PCB Design for 3D-Perfusion Mode Control

The synchronization circuit is designed with four operating modes for the purpose of collecting images from the camera is synchronized with the projector triggering for only 3D reconstruction and display (Mode 1), for only SO_2 calculation and display (Mode 2), or for a sequential collection and calculation

CHAPTER 4. TISSUE PROPERTY EXTRACTION USING MULTISPECTRAL REFLECTANCE IMAGING TECHNIQUE

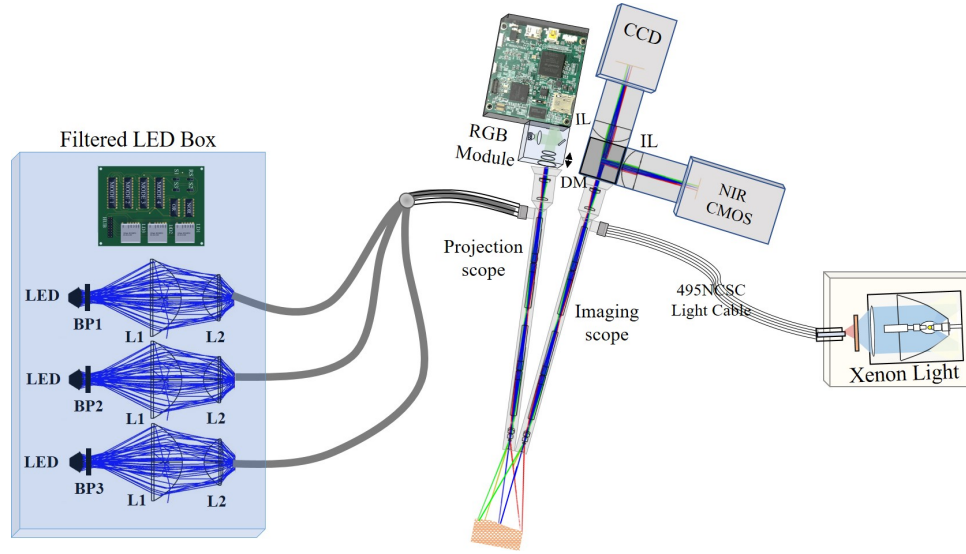


Figure 4.10: Multispectral imaging setup integrated with other multimodal imaging setup for MIS (used in Section 5.4).

for 3D and SO_2 (Mode 3 and Mode 4). The camera is triggered with the projector to collect images within the triggering period, except in Mode 4 when the camera exposure is extended into 2 projector trigger (for a higher reflected photon count with darker sample). The PCB design is displayed in Figure 4.11 with high-performance electrically erasable programmable logic device (Atmel ATF22LV10CQZ) to control the trigger count and duration with 4 main output signals (one to the camera and three to the LED control). The inputs of the PCB are to deliver suitable power and grounds to the LEDs (24 V), the microchip and other logical gates (5 V). An OSC output of the PCB is for the oscilloscope reference and checking purpose. RS is the trigger reset, which is switch every time restart a mode. An example of combined 3D- SO_2 measurements such as Mode 3 is display in Figure 4.12. Three other switches S1, S2

CHAPTER 4. TISSUE PROPERTY EXTRACTION USING MULTISPECTRAL REFLECTANCE IMAGING TECHNIQUE

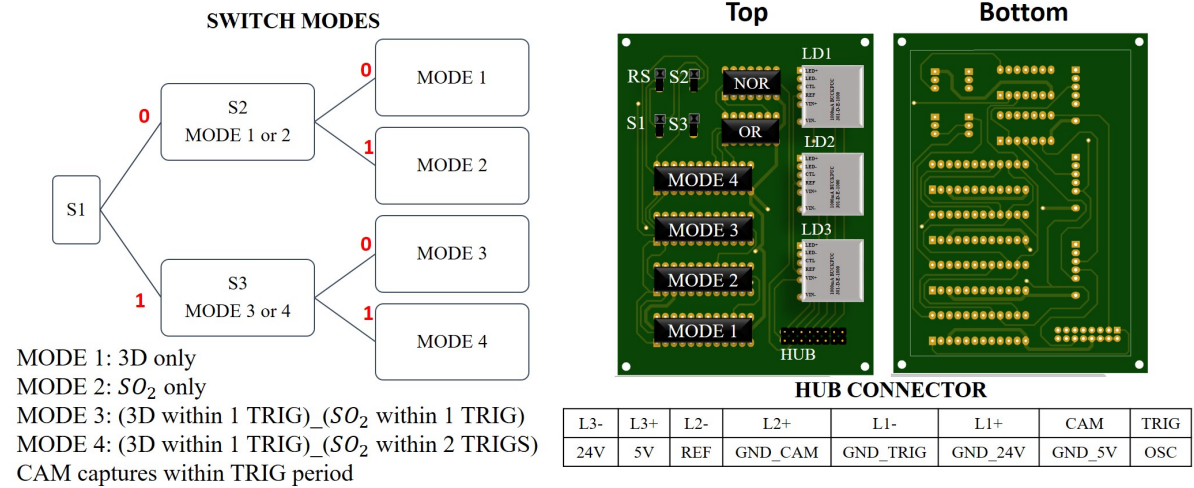


Figure 4.11: Mode switching mechanism and PCB architecture design.

and S3 are to switch between the Mode. For example, to go to Mode 3, $S1 = 1$, $S3 = 0$.

4.3.4 Optical Coupling Assembly from LED to Light

Delivery Fiber Bundle

The optical assembly to couple the LED chip to the trifurcated light fiber is done using two aspheric condenser lenses (L1: ACL7560U-A and L2: ACL4532U-A, Thorlabs, New Jersey, USA). The geometric of the optical component is simulated and optimized using Zemax to match the NA of the light fiber (Figure 4.13). The optical sketch shows ray tracing from the LED source through the optical assembly with two detector views, one after the LED focusing optics (D1) and another at the fiber detector location (D2). The total power focusing circle

CHAPTER 4. TISSUE PROPERTY EXTRACTION USING MULTISPECTRAL REFLECTANCE IMAGING TECHNIQUE

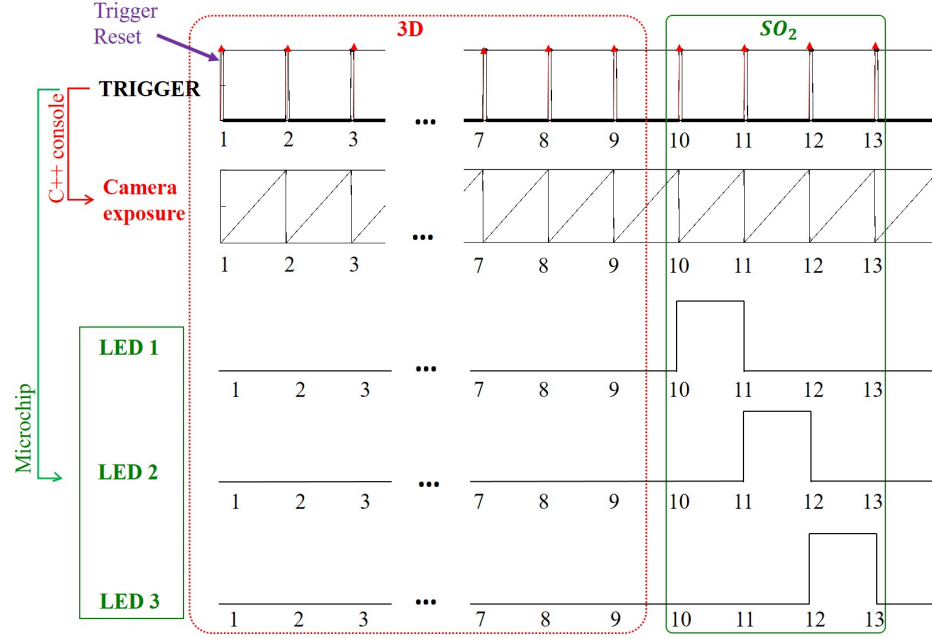


Figure 4.12: An example of system synchronization using Mode 3.

to the fiber contains 40% concentration to the total energy at D2 plane, and contains 80% total power in the detector plane D2

4.3.5 Experimental Procedures and Result

The system is validated using bovine blood phantom (Lampire Biological Laboratories, Piperville, PA) with sodium dithionite powder (157953, Sigma-Aldrich, St. Louis, MO) for two degrees of deoxygenations. The blood phantom is dropped on a flat white paper and the topical surface of a small intestine sample. Prior to the sample imaging, the same imaging setting was used to image a white reflectance standard. The result in Figures 4.14 and 4.15 shows the distinguish SO_2 levels between two states. In the blood phantom on white

CHAPTER 4. TISSUE PROPERTY EXTRACTION USING MULTISPECTRAL REFLECTANCE IMAGING TECHNIQUE

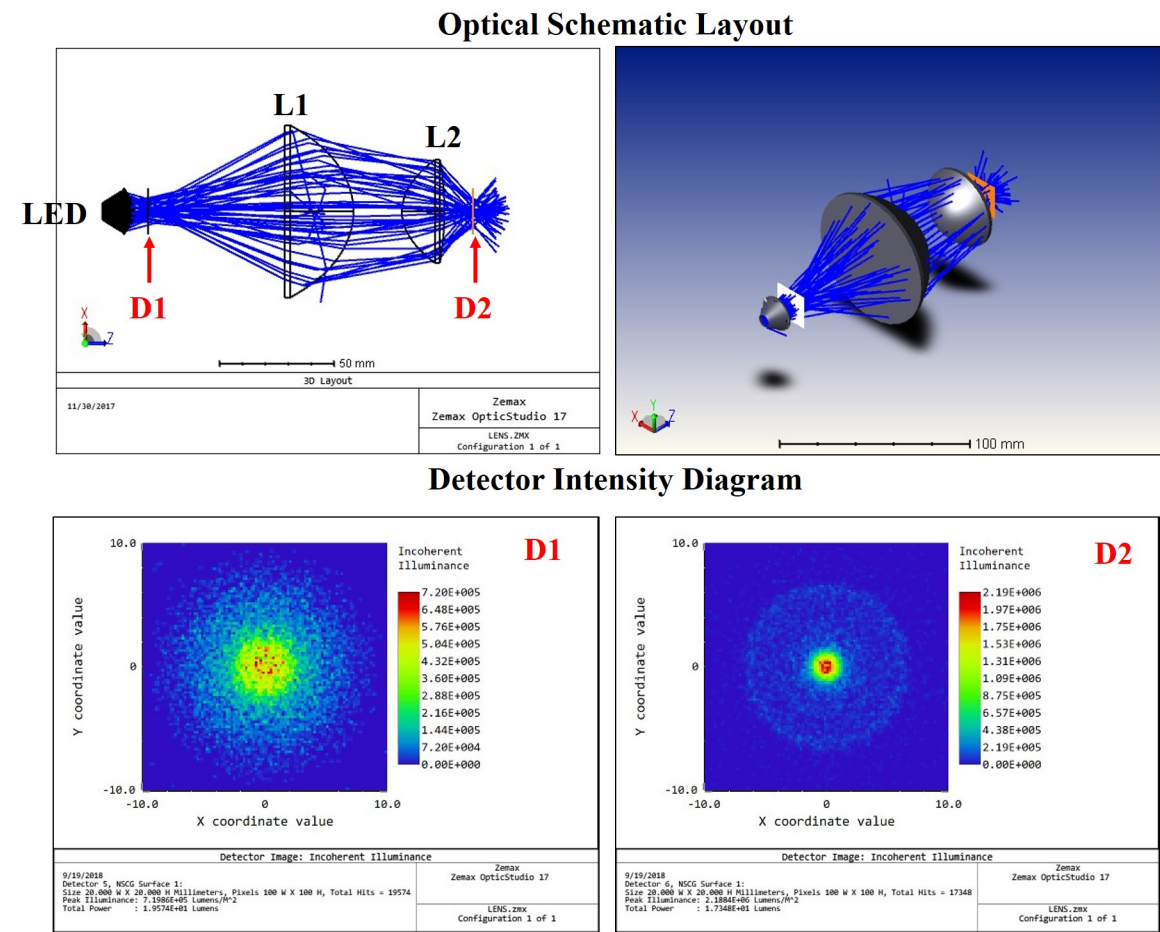


Figure 4.13: Simulated layout and the power view after the LED (D1) and at the fiber focusing plane (D2).

CHAPTER 4. TISSUE PROPERTY EXTRACTION USING MULTISPECTRAL REFLECTANCE IMAGING TECHNIQUE

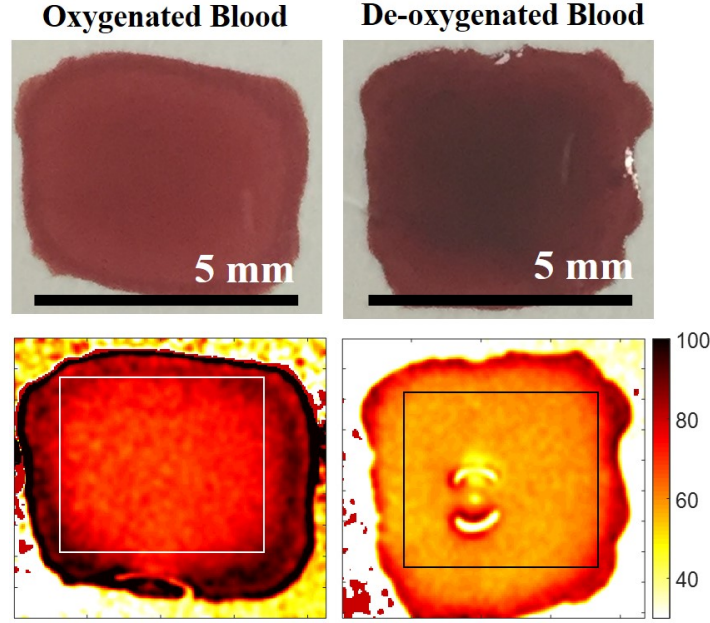


Figure 4.14: Oxygen saturation measurement of blood phantom. Colorbar unit is in percentage.

surface (Figure 4.14), SO_2 is 73.671 ± 5.684 % for the oxygenated blood and SO_2 is 58.26 ± 5.165 % for the de-oxygenated blood within the selected ROI coverage. The SO_2 change on the tissue is within 83.286 ± 5.748 % within the oxygenated blood (O ROI) indicating higher oxygen concentration than in the de-oxygenated blood (D ROI) with SO_2 of 61.11 ± 7.192 %, when the total hemoglobin coverage can be seen in HbT image. This preliminary data shows the relative reduction of SO_2 with an amount of sodium dithionite powder addition to the oxygenated blood phantom. More experiments to calibrate and compare this relative measurements to a calibrated oxygen saturation reading from arterial and venous blood can be done using blood gas analyzer [127,128].

CHAPTER 4. TISSUE PROPERTY EXTRACTION USING MULTISPECTRAL REFLECTANCE IMAGING TECHNIQUE

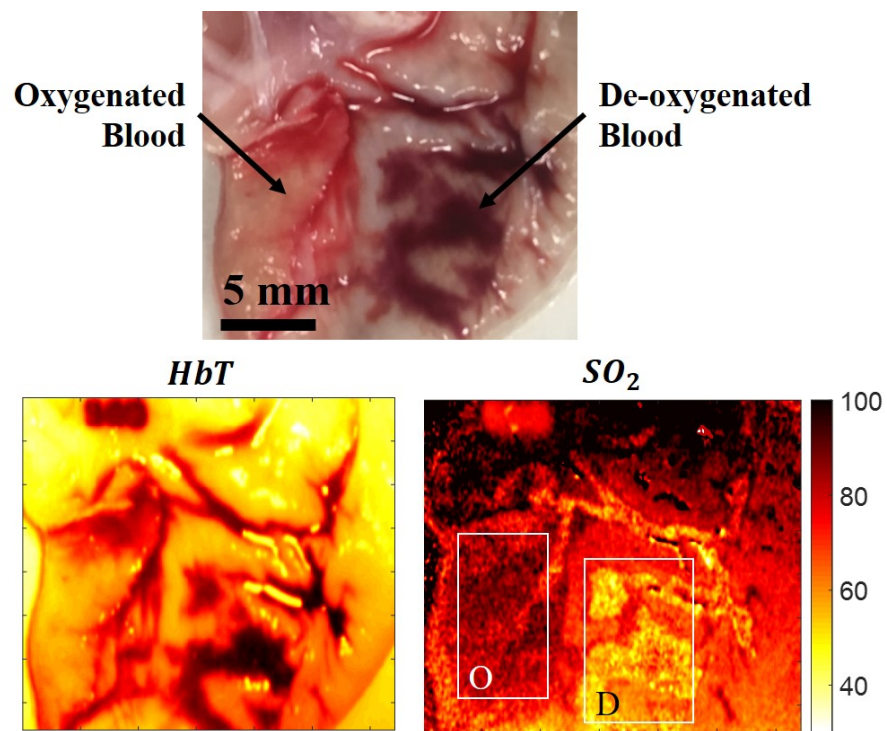


Figure 4.15: Total hemoglobin and oxygen saturation measurement of blood phantom on intestinal tissue. Colorbar unit is in percentage.

4.3.6 Lessons Learned

An endoscopic imaging system using multispectral technique is demonstrated on *in vitro* experiments with blood samples on tissue. The system facilitates filtered illumination from LED and electronic synchronization using a designed PCB control. An optical coupling assembly is determined to deliver the filtered light from the LEDs through a 3-to-1 trifurcated probe to the light port of the rod lens system. The dispersion of the LED in this system is high, with the measured power after the band pass filter is 100 mW, the coupling efficiency after the optical coupler is 50 mW, which then reduced to 5 mW after the trifurcated probe. The measured power at the distal end of the rigid scope is within 2 mW. To improve the system speed, as well as the illumination power, a coherence beam such as from a laser diode can be used in this system.

Chapter 5

Endoscopic Guidance for Minimally Invasive Surgical Robot

5.1 Motivation

Reducing collateral tissue damage, along with other previously mentioned benefits of minimally invasive surgery with robots, has motivated the transition to laparoscopic surgeries [129, 130]. Laparoscopic surgical methods entail their own challenges, however, such as limitation in the motion of surgical tools and few visual cues of the surgical scene. Such limitations can turn simple

CHAPTER 5. ENDOSCOPIC GUIDANCE FOR MINIMALLY INVASIVE SURGICAL ROBOT

tasks in open surgery to inconsistent and time-consuming tasks in laparoscopic surgery [131]. Such simple tasks can be crucial and commonly done. Tasks for anatomic reconstruction, such as targeting, cutting and suturing suffer from such limitations. Current robotic systems in laparoscopic surgery use a tele-operated control paradigm, which relies on human-related risk factors in the surgical system. This paradigm contributes to complication rates reaching up to 20% for general surgeries [21]. These rates could be reduced by removing the human-related risk factors. In particular, kidney-sparing partial nephrectomy (PN) and anastomosis are two examples in which the high precision and the high repetition rate of a robot can improve surgical outcomes. Further, due to the higher precision and reduced learning curve for surgeons, surgery with a MIS robot with proper quantification and display of the surgical area can reduce excisional volume loss (EVL) of healthy tissues compared to open and conventional laparoscopic approaches. In this section, we introduce two surgical robotic prototypes that use quantified 3D point cloud inputs in the visible and NIR to guide a surgical strategic plan for navigation while cutting and suturing.

My contributions for the work presented in this section include the hardware development of the 3D imaging endoscope from design optimization to systemic modification for visible and NIR imaging and the imaging system-robotic accuracy assessment during the targeting and cutting trial. My con-

CHAPTER 5. ENDOSCOPIC GUIDANCE FOR MINIMALLY INVASIVE SURGICAL ROBOT

tributions also involved software development covering new algorithms to segment point clouds for fiduciary determinations and to plan a surgical strategy on targeting phantom, kidney and suture pad samples. The work proposed in this section resulted in publications in [132–134]

5.2 First Prototype: Surgical Robot with 3D

Imaging under Visible Illumination

5.2.1 System Contributions

In this prototype, STAR with the quantitative 3D endoscopic imaging system discussed in Chapter 3, Section 3.3 are integrated to explore semi-autonomous targeting and cutting tasks on porcine cadaver kidney tissue. The evaluation demonstrates the system performance for autonomous visualization in constructing dense point cloud in highly pigmented tissue. Axial and lateral positional accuracy of the overall 3D imaging and robotic mechanical performance are assessed via tissue targeting and cutting tasks on cadaverous kidney samples based on a programmed robotic planning. The evaluation process is set within electro-surgery using a customized electro cautery tool.

CHAPTER 5. ENDOSCOPIC GUIDANCE FOR MINIMALLY INVASIVE SURGICAL ROBOT

5.2.2 System Setup

The purpose of this prototype is to evaluate the system performance with the integration of the mechanical and hardware control with the SMART robot and the surgical tool. Therefore, the system setup incorporates three main components: the SMART robot, the 3D imaging endoscope, and the multi-degree of freedom electro-surgical tool.

5.2.2.1 3D Imaging Endoscope

Details of the imaging endoscopic setup and methodology are laid out and discussed in Section 3.3. The imaging system is mounted on an aluminum optical plate (MB6, Thorlabs, New Jersey) and is attached to a NOGA rotational arm with 7 degrees of freedom adjustments. The location and angle of the imaging system in relation to the robotic arm is adjusted using a trial and error approach, for the imaging field of view covers the motion range for the robotic manipulation.

For each tissue imaging, the camera exposure is kept to within 30 ms to 40 ms per fringed image, leading to 1.57 fps (3D frame (or 3D set) per second). This speed is mostly due to the high number of fringed images for precised and continuous phase distribution. A smaller fringe number will be discussed in the second prototype.

CHAPTER 5. ENDOSCOPIC GUIDANCE FOR MINIMALLY INVASIVE SURGICAL ROBOT

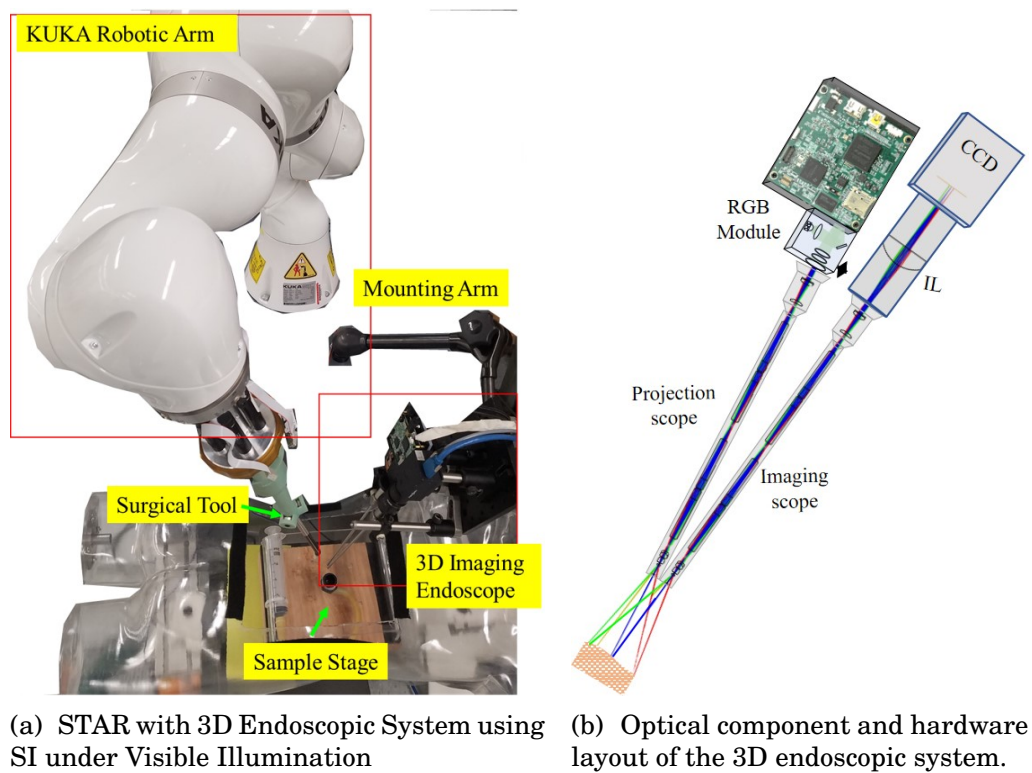


Figure 5.1: System layout of Prototype 1.

CHAPTER 5. ENDOSCOPIC GUIDANCE FOR MINIMALLY INVASIVE SURGICAL ROBOT

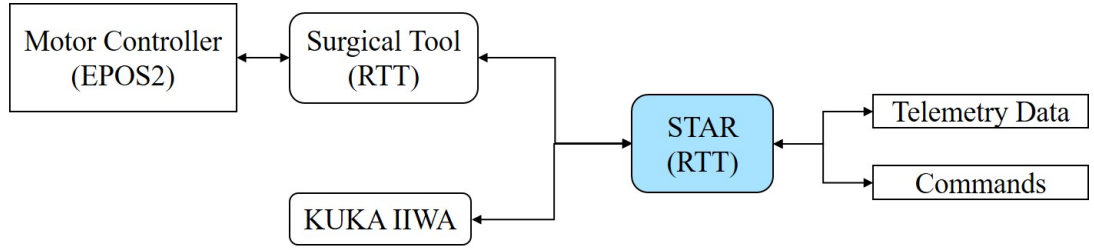


Figure 5.2: Controlling architecture of the STAR.

5.2.2.2 Robotic System and Control Method

The STAR includes 8 joint robotic arms with 7 KUKA IIWA control joints and one degree of freedom from the surgical tool. STAR is controlled in software architecture layouted in Figure 5.2 with two controller inputs from the KUKA IIWA and the surgical tool. KUKA IIWA is controlled via a ROS framework [135] and the surgical tool is controlled by an Orocos Real-Time Toolkit (RTT) framework [136] with motor controller EPOS2. Both devices (KUKA IIWA and surgical tool) are controlled from another Orocos RTT that agglomerates the telemetry data, computes inverse kinematics and dispatches joint commands to the devices. The Reflexxes motion library [137] is used to compute the Cartesian trajectory coordinates.

5.2.2.3 Multi Degree of Freedom Electro Surgical Tool

The surgical tool is an adaptation of a custom two degree of freedom electro-surgical tool [4] with the tip pressure-pushed with an insulated needle electrode. The needle electrode is coupled with an electro-surgical unit (DRE Med-

CHAPTER 5. ENDOSCOPIC GUIDANCE FOR MINIMALLY INVASIVE SURGICAL ROBOT

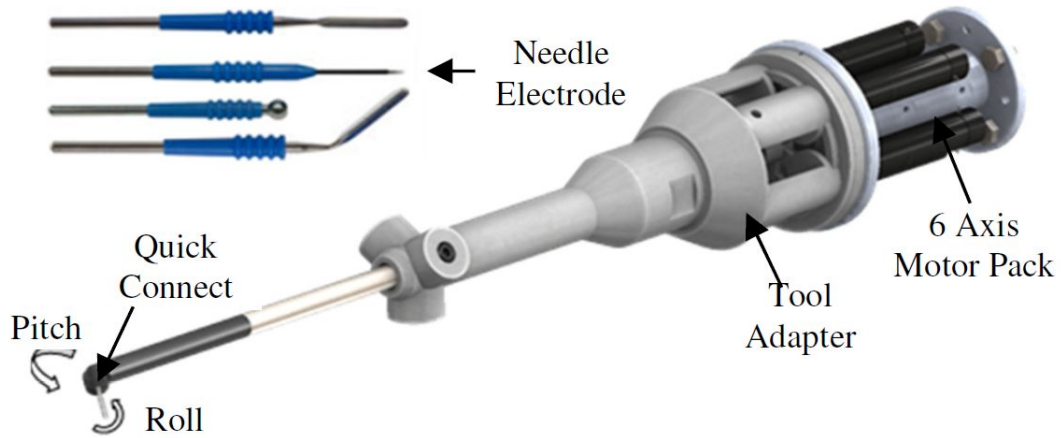


Figure 5.3: A multi degree of freedom electro surgical tool for semiautonomous electrosurgery. Adaptive from [4].

ical, Louisville, KY) and programmed with a 60-W cutting waveform for cauterization on the kidney sample and maintained within 5 s to mark each position when cauterizing the kidney sample. Figure 5.3, illustrates the CAD design of the electro-surgical tool used for cauterization. The tool incorporates 6-axis motor packs (DC brush motors, Maxon Motors, Sachseln, Switzerland), a universal tool adapter, and quick release electrode holder. Two motors control the pitch and roll of the cutting electrode. Each motor includes an encoder for precise positioning using EPOS2 controllers. Communication between the robot and tool is through a Controller Area Network (CAN). The tool is homed by energizing the pitch motor with current control until it reaches a hard stop.

5.2.3 Imaging System and Robotic Control Registration

The hand-eye calibration between the imaging endoscope and the robot is achieved by mounting a customized pointing rigid rod on the KUKA IIWA and the robot is commanded to touch a series of fiducials (>3 points) on a defined checkerboard. These point locations being in the robot coordination (world coordinates) are then registered to the 3D point cloud and the eye-to-hand transformation to the camera coordination is computed by using a least squares solution [138]. In these experiments, the calibration process using 4 co-planar fiducials on the checkerboard is performed and the hand-eye calibration takes approximately 10 minutes.

5.2.4 Experimental Procedures and Computational Strategies for Target Localization

The accuracy tests of surgical robot under the 3D imaging visualization is summarized in Figure 5.4. The 3D point cloud provided by the SI endoscopic system are collected and analyzed by segmenting the fiduciary centroids (fiduciary centroids are the center of mass of ink marker created for robotic targeting or centroids of burn marker created by the robot), or extended to calculate a trajectory line for robotic line cutting.

CHAPTER 5. ENDOSCOPIC GUIDANCE FOR MINIMALLY INVASIVE SURGICAL ROBOT

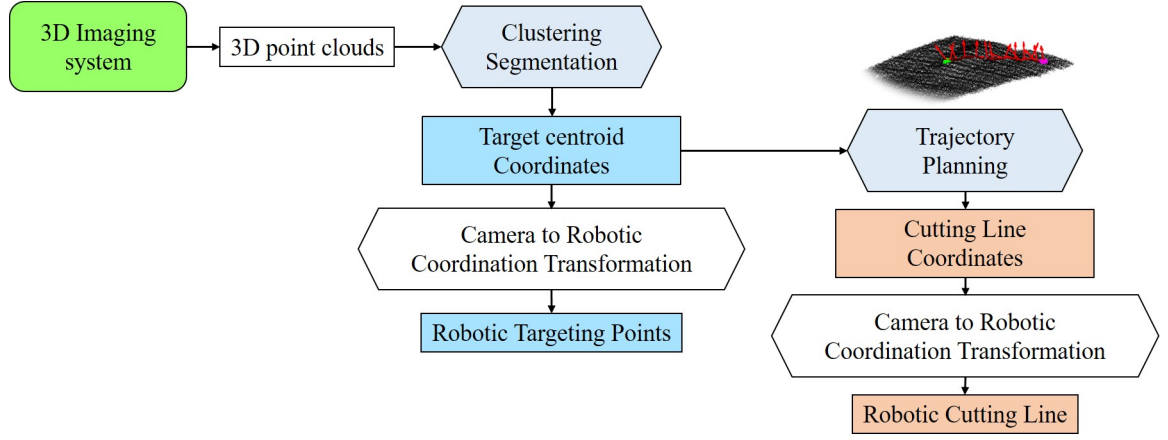


Figure 5.4: Computational procedure for targeting and cutting accuracy tests.

5.2.4.1 Targeting Test

The targeting test is to evaluate the system positional accuracy in aiming at planned points. The target is a kidney sample with 6 white-painted dots in a 3x2 matrix, with 5 mm and 10 mm separations between rows and columns, respectively (Figure 5.7). 3D point clouds of the sample are collected by the SI endoscopic setup. Due to the high contrast difference between the fiducial points and the kidney background, the points are easily clustered by intensity thresholding and k-means clustering. The centroid of each 3D fiducials are transformed to KUKA LWR coordinates and passed to the IIWA controller. The surgical tool is operated under cutting waveform mode with 60 W for 5 s for each fiducial point when the robot approaches the tissue.

The accuracy is calculated by average x-y norm distance between each physical fictional centroid to the corresponding burned mark performed by the robot.

CHAPTER 5. ENDOSCOPIC GUIDANCE FOR MINIMALLY INVASIVE SURGICAL ROBOT

5.2.4.2 Cutting Test

After performing targeting task, the system is evaluated on the cutting accuracy on another cadaver kidney tissue. The kidney was marked at two locations 2 cm apart from each other with similar marker as in Section 5.2.4.1. After the kidney surface point cloud is collected by the 3D SI imaging system, a trajectory line using Dijkstras algorithm generates a linear surgical cutting plan for STAR to follow. STAR then cuts along the trajectory line with a predetermined depth of 3 mm. The depth accuracy is evaluated by measuring the average cutting discolored mark made from electro-surgical tool in the kidney sample to the kidney surface. The electro-cutting tool was maintained at 60-W cutting waveform mode during the cutting length.

5.2.4.2.1 Cutting Trajectory Path and Normal Vector Calculations

The cutting trajectory and the normal vector for tool direction when moving along the tissue surface are calculated in 5 steps:

1. Determining of fiduciary centroids. This process is similar to the fiduciary centroids extraction discussed in Section 5.2.4.1 using intensity thresholding and k-means clustering for the applied markers.
2. Post-processing of the collected point cloud for a smooth and low noise distribution. Outlier removal was done by the statistical outlier removal

CHAPTER 5. ENDOSCOPIC GUIDANCE FOR MINIMALLY INVASIVE SURGICAL ROBOT

module in Point Cloud Library and a moving least square method was used to create a smooth point cloud distribution [139, 140]. Fiduciary centroid locations are added in this distribution (Figure 5.5a).

3. Surface meshing reconstruction using 2D Delaunay triangulation [141] (Figure 5.5b).
4. Calculating of cutting trajectory coordinates. Shortest distance along the constructed data mesh between the two fiducial centroids is computed using Dijkstras algorithm [142] (Figure 5.5c).
5. Calculating of tool orientation via normal vector determination. To ensure the cutting tool (end-effector) is directed normally to the surface of the tissue, a normal vector along the cutting trajectory line is computed using Equation 5.1 (Figure 5.5d).

$$\vec{n}_{path} = \frac{\vec{P}_{nk} \times \vec{P}_{nn+1} + \vec{P}_{nn+1} \times \vec{P}_{nm}}{|\vec{P}_{nk} \times \vec{P}_{nn+1} + \vec{P}_{nn+1} \times \vec{P}_{nm}|} \quad (5.1)$$

where \vec{n}_{path} is the unit normal vector along the cutting path \vec{P}_{nn+1} . The average between the cross products of vectors \vec{P}_{nk} with \vec{P}_{nn+1} and \vec{P}_{nm} with \vec{P}_{nn+1} forms the normal vectors along the trajectory as shown in Figure 5.6.

CHAPTER 5. ENDOSCOPIC GUIDANCE FOR MINIMALLY INVASIVE SURGICAL ROBOT

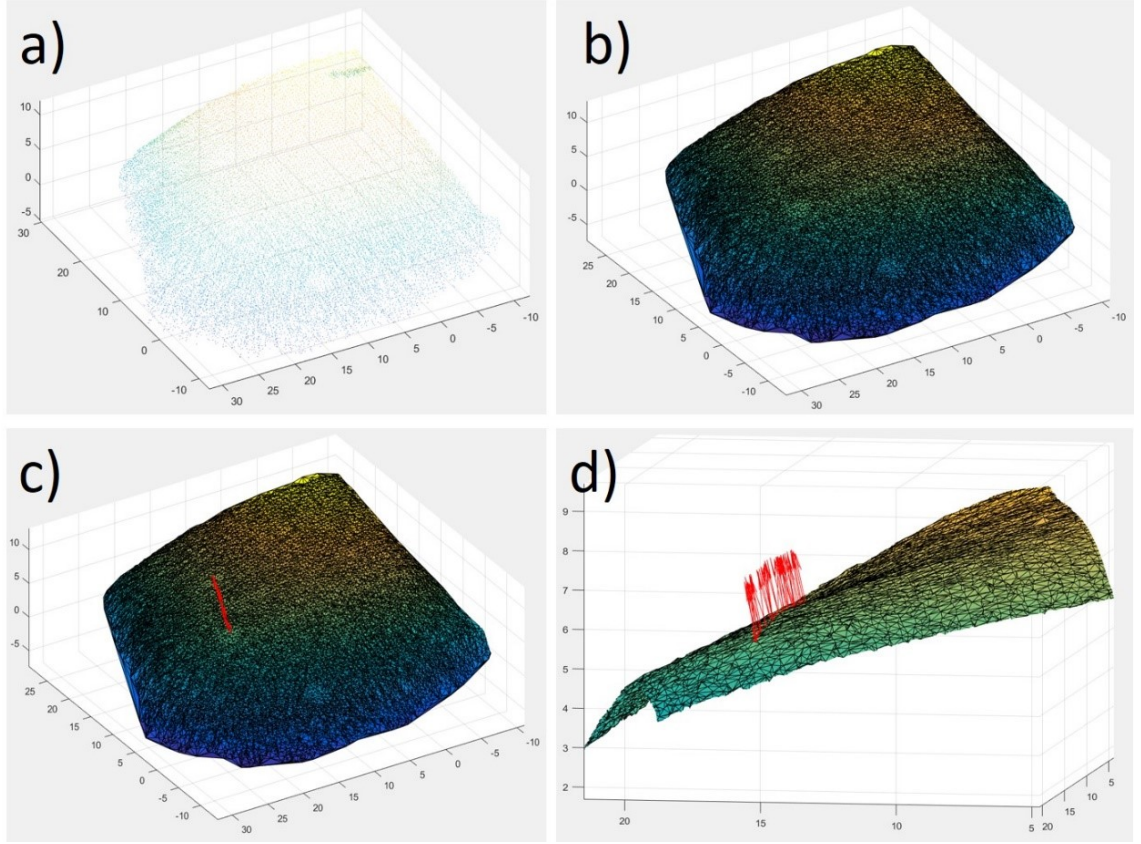


Figure 5.5: Surface reconstruction and path planning for cutting task: (a) Post-processing of point cloud. (b) Surface creation by Delaunay triangulation. (c) Cutting path calculation along the surface. (d) Normal vector generation along the cutting path.

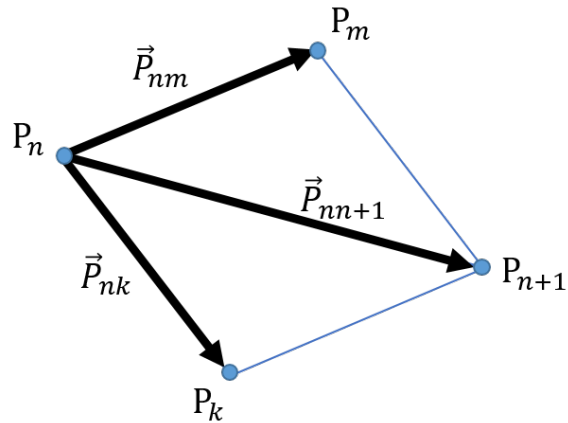


Figure 5.6: Average normal vector along the trajectory

CHAPTER 5. ENDOSCOPIC GUIDANCE FOR MINIMALLY INVASIVE SURGICAL ROBOT

Table 5.1: Results of the targeting accuracy test

#	Fiducial		Burned Mark		Error [mm]
	X [mm]	Y [mm]	X [mm]	Y [mm]	
1	8.94	26.43	10.38	27.45	1.76
2	20.02	27.41	22.68	30.73	4.25
3	10.13	20.65	11.86	20.21	1.78
4	21.88	20.73	24.6	22.79	3.40
5	11.42	14.83	13.18	13.43	2.25
6	23.17	13.94	26.18	13.78	3.01

5.2.5 Results

5.2.5.1 Targeting Accuracy

A digital image of the targeting result is collected for calculating the positional error. The planned fiduciary targets denoted as T1-T6 and the burned marked by the robot denoted as B1-B6 (Figure 5.7) and the corresponding coordinates listed in Table 5.1. The targeting accuracy of the system is determined as the norm distance between each T and B. Centroid location is determined by center of mass weighted by pixel intensity of the segmented region of each mark (intensity thresholding). The average targeting accuracy of the system was 2.74 ± 0.99 mm.

5.2.5.2 Cutting Accuracy

The cauterization discolors kidney tissue, leaving a means to measure thickness difference between the planned cutting depth (3 mm) and the actual cut-

CHAPTER 5. ENDOSCOPIC GUIDANCE FOR MINIMALLY INVASIVE SURGICAL ROBOT

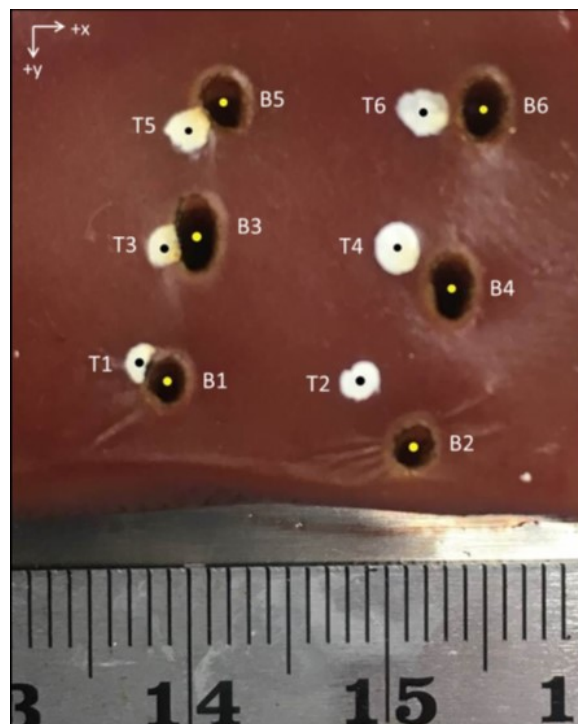


Figure 5.7: Pattern of target fiducials (white) and burned marks (black) on a cadaver porcine kidney sample for targeting accuracy assessment.

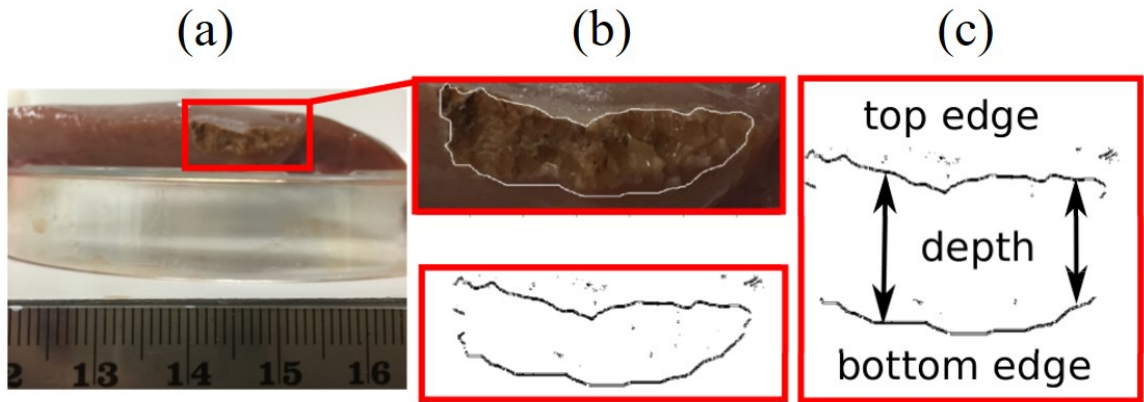


Figure 5.8: Procedures to evaluate cutting depth accuracy: a) Slicing the kidney along the cut, b) Segmenting of cut region, c) Calculating the depth via the distance between top and bottom edges.

ting line made by the robot. Procedures to analyze the cutting depth accuracy is described in Figure 5.8: 1) A section of the cut kidney region is dissected using a scalpel. 2) The intensity variation of the cut section is segmented to highlight the cut region. 3) Mean depth error is the average difference from the segmented cut and 3 mm planned cut. The depth accuracy of the system was found to be an average of 2.44 ± 0.34 mm.

5.2.6 Lessons Learned

STAR is the first robot capable of semi-autonomous surgical tasks in soft tissue. By incorporating a novel laparoscopic imaging system capable of three dimensional reconstruction, STAR can perform clinical tasks in a simulated surgical environment. Although initial targeting accuracy was not sub-millimeter, the system successfully performed a cutting task in porcine cadaver tissue within

CHAPTER 5. ENDOSCOPIC GUIDANCE FOR MINIMALLY INVASIVE SURGICAL ROBOT

a simulated surgical phantom.

One limitation of the work is positional accuracy of the system. For these tasks, STAR is operated in an open loop control scheme where target locations and cutting trajectories are calculated from the imaging system and streamed to the LWR. The open loop system is more prone to positioning error, due to the propagation of errors in camera registration and calibration. Despite best efforts to minimize this error, the average positional accuracy of the STAR system is 0.50 ± 0.20 mm [143]. The additional error observed in this experiment is most likely attribute to backlash within the gearing of the distal tip of the tool, which is magnified by the length of the needle electrode. To minimize this error, a closed loop control scheme will be implemented as detailed in previous work using STAR to autonomously reset pseudo-tumors for porcine tissue.

Secondly, the system did not consider the effects of tissue motion or soft deformations. This limitation is the result of the integration between camera, surgical planner, and LWR. While the laparoscopic imaging system can reconstruct the surgical scene in real-time, the work flow to calculate surface normals for a cutting trajectory has not been optimized for time yet. In previous work, a plenoptic imaging system was used to generate surgical plans that were streamed directly to the LWR [9]. In future iterations, a similar strategy will be implemented with the laparoscopic imaging system, so STAR can detect and react to deformations in real time.

CHAPTER 5. ENDOSCOPIC GUIDANCE FOR MINIMALLY INVASIVE SURGICAL ROBOT

Thirdly, the 3D depth quality depends strongly on the initial camera-projector calibration for the 3D imaging endoscope. The calibration is done by varying multiple positions of a printed chessboard within the endoscopic view, where the first position is regarded as the zero-reference plane and is positioned normal to the longitudinal axis of the endoscope. In that, the first position should be carefully adjusted and a high number of calibration position (>10) is desired to cover the field of view and correct for the radial distortion of the surgical scope. Moreover, the current 3D imaging system utilizes two separate rigid scopes, which limits its use in applications with restrained access. Therefore, a more compact design, which combines the two scopes into one when maintaining the triangulation quality is important and can be achieved by using flexible imaging fiber as the relay optics.

Finally, the excessive length of the distal joint of the cutting tool limits autonomous cutting routines to superficial tissue and organs. When a commercial needle electrode is used with the cutting tool, the length of the distal joint is 9.42 cm. When used with a remote center of motion, the excessive length limits its access to deep regions such as the pelvis. To expand the use of the STAR to other minimally invasive procedures, the quick connect interface and electrode length should be shortened as far as possible. The resulting geometry would substantially improve the kinematics of the system, and allow for additional cutting motion within deep structures.

CHAPTER 5. ENDOSCOPIC GUIDANCE FOR MINIMALLY INVASIVE SURGICAL ROBOT

Despite study limitations, this work has the potential to transform clinical care for patients in need of partial nephrectomy. The integration of a laparoscopic structured light camera, multidegree of freedom electro-surgical tool, and open loop control scheme demonstrate the first successful cutting task on soft tissue within a simulated minimally invasive procedure. Additionally, impact to the clinical work flow is minimal as the setup and location of the kidney phantom is physiologically correct, and all interventions were performed with laparoscopic access. The current cutting strategy relies on an open loop control strategy to follow cutting trajectories. Prior to clinical implementation, a closed loop cutting strategy should be implemented to minimize targeting and cutting error.

5.3 Second Prototype: Surgical Robot with 3D Imaging under dual VIS-NIR Illumination

5.3.1 System Contributions

The first prototype provides an interface of manipulating robotic electro-surgical task using 3D visualization under visible illumination. During the experiments, mechanical motion of the needle tip when approaching and leaving tissue medium is observed. This error hypothetically causes the accuracy differ-

CHAPTER 5. ENDOSCOPIC GUIDANCE FOR MINIMALLY INVASIVE SURGICAL ROBOT

ence between the targeting (x-y) and depth (z) accuracy of the first prototype. Hence, we optimize the first prototype with a rigid cautery tool design that prevents this motion error. In addition, we expand the vision capacity of the system to NIR vision for marker tracking and future flow dynamic visualization. In addition, system speed is enhanced based on certain hardware and software modifications.

5.3.2 System Improvements

5.3.2.1 Dual VIS-NIR Mode

In addition to the 3D reconstruction using a CCD, this prototype is equipped with another camera sensor for NIR fluorescence imaging for surgical planning and navigation purpose. To ensure the light throughput within near infrared is adequate, several NIR-compatible hardwares are considered.

5.3.2.1.1 NIR Imaging Sensor

A CMOS is considered for the purpose of NIR target tracking with adequate frame collection speed and image resolution. In this prototype, we choose the GS3-U3-41C6NIR-C CMOS model (FLIR Integrated Imaging Solutions, British Columbia, Canada) with 1024x1024 pixel image and the frame speed is maintained within 45 fps.

CHAPTER 5. ENDOSCOPIC GUIDANCE FOR MINIMALLY INVASIVE SURGICAL ROBOT

5.3.2.1.2 NIR-Enhanced Endoscope

To study the optical transmission of several endoscopes and to confirm the optimal available scope for our NIR configuration, we measured relative transmission of the light fiber delivery system (wrapping around the scope body), and the optical assembly within the scope body (including objective lens, relay lens and eyepiece) of 4 different available rigid scopes with 2 common endoscope housing diameter for MIS (4-mm diameter scopes: 7230 AA, ICG 26046 ACA and 10-mm diameter scopes: 260030 AA and ICG 260030 ACA). All scopes are from Karl Storz Endoscopy, Tuttlingen, Germany). A bigger diameter endoscope housing of 10 mm is evaluated to increase more light throughput (thus increases system speed), while still within clinical MIS constraints (less than 12 mm endoscopic housing).

5.3.2.1.2.1 Transmission of The Light Delivery Fiber of A Rigid Endoscope

As mentioned in Section 1.2.2.2, a bundle of light fibers is arranged around the body of a rigid scope from the light port near the eyepiece to the distal end of the scope to deliver light. The fiber arrangement of each scope is configured differently depending on each model (Figure 5.9b) and the optical properties of the fiber types are proprietary, therefore, to understand the transmission behavior of each scope within NIR region, a broadband light source within 630

CHAPTER 5. ENDOSCOPIC GUIDANCE FOR MINIMALLY INVASIVE SURGICAL ROBOT

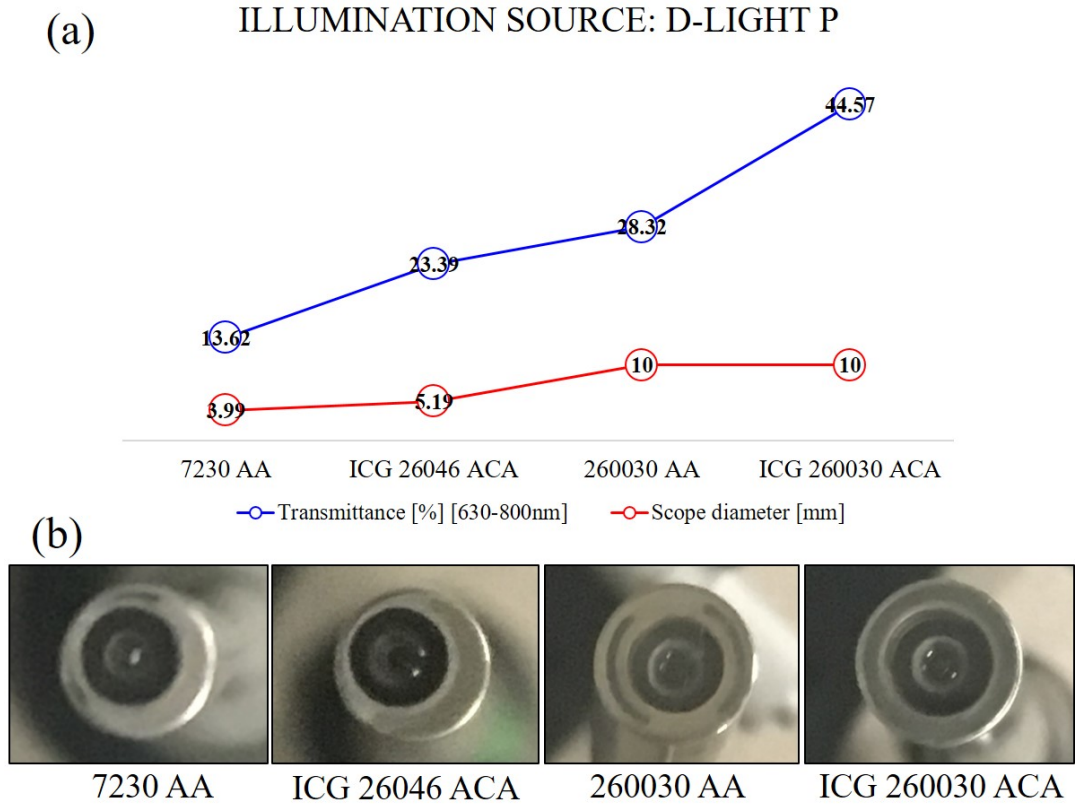


Figure 5.9: (a) Transmission spectra of 4 different rigid endoscopic models with 4-mm and 10-mm diameter housing. (b) Light fiber arrangement at each endoscopic distal end. Image not to scale.

nm to 800 nm (D Light P Light source, Karl Storz Endoscopy, Tuttlingen, Germany) is used. From Figure 5.9a, it is obvious that the bigger the scope diameter is, the higher the transmission. However, within the same endoscopic housing, the ICG endoscopic models show more than 1.5 times higher transmission throughput than the conventional endoscope. Hence, we decide to use ICG 260030 ACA with 10 mm for light delivery.

CHAPTER 5. ENDOSCOPIC GUIDANCE FOR MINIMALLY INVASIVE SURGICAL ROBOT

5.3.2.1.2.2 Transmission of The Optical Assembly Within A Rigid

Endoscope

A combination of multiple broad band light sources such as a halogen light, a broad band within 680 nm to 800 nm (D Light P Light source, Karl Storz Endoscopy, Tuttlingen, Germany) and a high power LED with central wavelength around 850 nm (M850LP1, Thorlabs, New Jersey, USA) is used as the input power to measure the relative transmittance through optical assembly within the scope body. These light sources are used to cover mostly the wavelength range for the 3D imaging (500-560nm), hemoglobin oxygenation spectral window (530-590nm), ICG absorption (750-790nm) and ICG emission window (>800nm). Relative intensity spectra of the combined light source is illustrated in Figure 5.10. In general, ICG enhanced scope and bigger diameter scopes have higher transmittance. However, the ICG enhanced scope give higher throughput within NIR (>800 nm) and have cut-off from 660 nm to 824 nm, i.e. ICG enhanced scope is good for NIR imaging, however, is not adequate for those functions within that cut-off range. Therefore, in this prototype, we use ICG 260030 ACA with 10 mm housing with NIR enhanced transmission for NIR imaging.

CHAPTER 5. ENDOSCOPIC GUIDANCE FOR MINIMALLY INVASIVE SURGICAL ROBOT

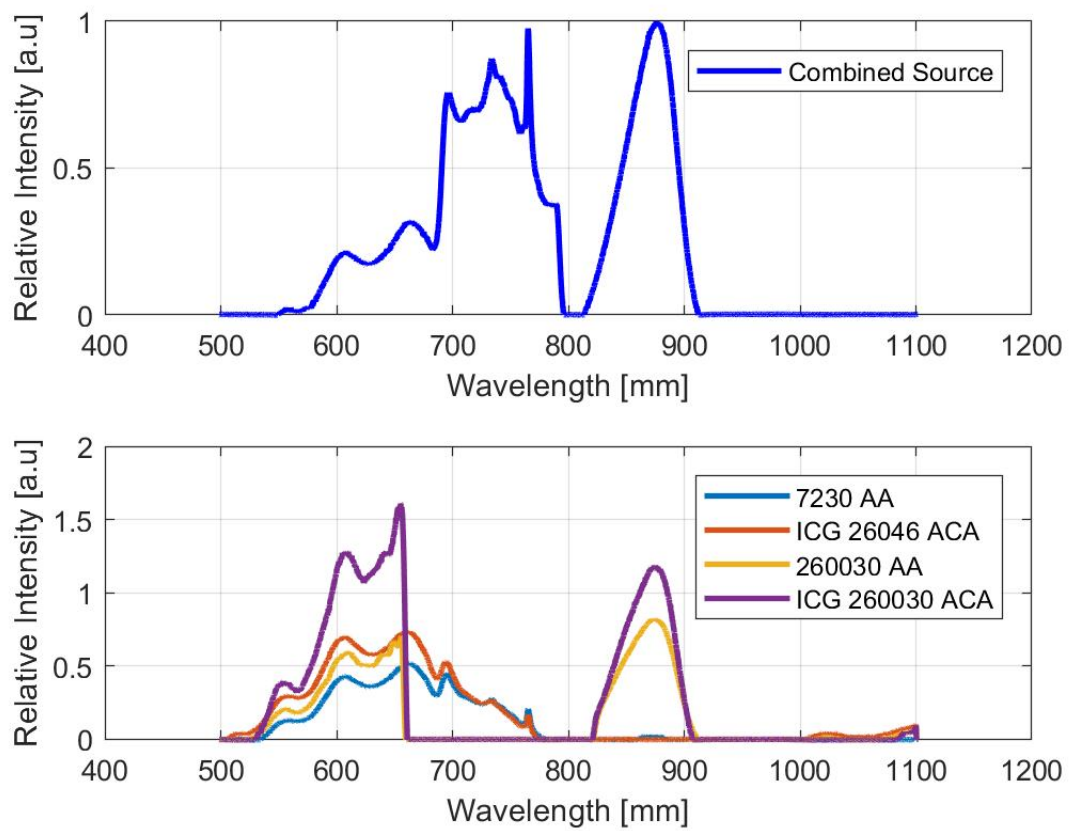


Figure 5.10: (Upper) Transmission of the combined light source. (Lower) Relative Transmission of optical assembly in each scope.

CHAPTER 5. ENDOSCOPIC GUIDANCE FOR MINIMALLY INVASIVE SURGICAL ROBOT

5.3.2.1.3 Light Source

A Xenon fiber optic light source (Intuitive Surgical Corporation, CA) is modified to become NIR light source to excite NIR fluorescence dye agent by replacing the equipped band pass filter with a NIR band pass filter with central wavelength at 750 ± 8 nm, FWHM = 40 ± 8 nm (FB750-40, Thorlabs, New Jersey, USA). The chosen illumination wavelength is used for the common fluorescence indocyanine green (ICG) dye to absorb and emit at longer wavelengths around 830 nm.

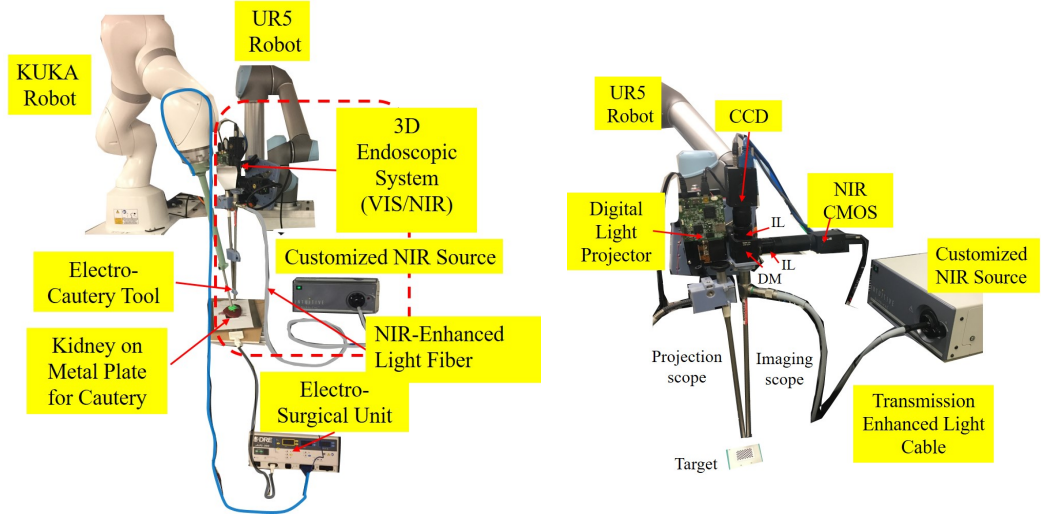
5.3.2.1.4 Light Delivery Cable

The fiber optic light cable with enhanced light transmission (495 NCSC, Karl Storz Endoscopy, Tuttlingen, Germany) is used to deliver filtered NIR light to the light port of the imaging endoscope. A CW 488-nm diode laser is used to measure a relative transmittance of the 495 NSCS light cable to be 72.7% in comparison to 21.8% in a conventional light cable. The light cable is fitted to the foci position of the customized filtered NIR light source with a 3D-printed ring coupler.

5.3.2.2 Surgical Tool Modification

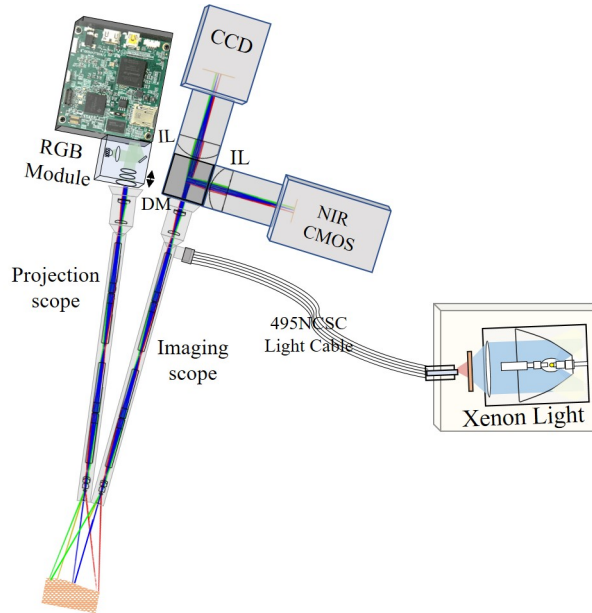
To address the positional error from the needle tip movement when contacting with tissue, we develop a new design for the cauterization with fixed needle

CHAPTER 5. ENDOSCOPIC GUIDANCE FOR MINIMALLY INVASIVE SURGICAL ROBOT



(a) Collaborative setup with KUKA robot for electro-surgery with the 3D Endoscopic imaging in VIS-NIR mode.

(b) Imaging Endoscope with 3D Reconstruction with NIR tracking mounted on a UR5 Robot.



(c) Imaging Endoscope for 3D Reconstruction with NIR tracking with optical ray tracing simulation. IL: Imaging Lens, DM: Dichroic Mirror.

Figure 5.11: System layout of Prototype 2. IL: Imaging Lens, DM: Dichroic Mirror.

CHAPTER 5. ENDOSCOPIC GUIDANCE FOR MINIMALLY INVASIVE SURGICAL ROBOT

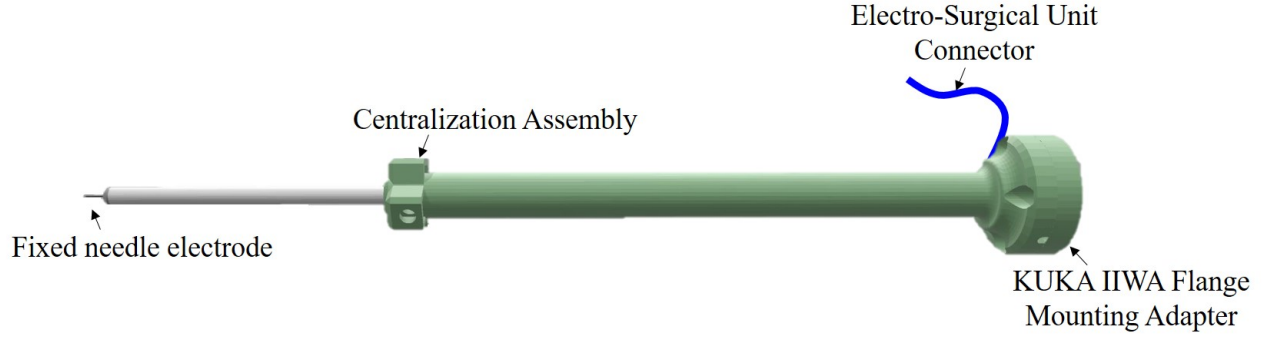


Figure 5.12: CAD layout of the electro-surgical tool with fixed needle electrode.

electrode (Figure 5.12) housed inside an aluminum rod. The aluminum rod is centralized to the tool adapter to KUKA IIWA flange with 4 fixation screws. The needle electrode is coupled with a wire connector to the electro-surgical unit for cauterization. The tool's total length is 50.35 cm.

5.3.2.3 Projection Fringe Reduction

A solution for reducing number of projected fringes is to lower phase shift value ($2\pi/4$ to $2\pi/3$) and lower the last frequency fringes. In the first prototype, we use 4 frequencies with 4 shifts to compute phase distribution, the purpose is to provide a smooth and precised phase from knowledge of previous phase from lower frequency images (Equation 3.15). In this prototype, we maintain the 4×4 modulated frequencies for calibration (1, 3, 12, 36) to obtain the camera extrinsic and intrinsic parameters. However, for 3D imaging calculation and for data streaming speed, we shorten the system speed by using 3×3 modulated frequencies (1, 3, 12), with the last frequency sequence be the 3^{th} frequency of

CHAPTER 5. ENDOSCOPIC GUIDANCE FOR MINIMALLY INVASIVE SURGICAL ROBOT

the calibration fringe for a phase constant conversion. The 3-shifted method hence decreases the image projection and collection from 16 to 9 images. The wrapped phase of each fringe number is calculated using three-step phase shift method (a replacement of Equation 3.13) as given in Equation 5.2. The rest of the point cloud calculations remains the same as in Section 3.3.6.

$$\phi = \tan^{-1} \frac{\sqrt{3}(I_2 - I_1)}{2I_0 - I_2 - I_1} \quad (5.2)$$

where w indicates wrapped phase, and $I_{(1-3)}$ represents the intensity of three shifted image of each fringe number f .

The system speed for 3D imaging is improved from 1.57 fps to 4.4 fps with 9 fringe projections and the camera exposure is within 25 ms/fringed image.

5.3.3 Dual VIS-NIR imaging system setup

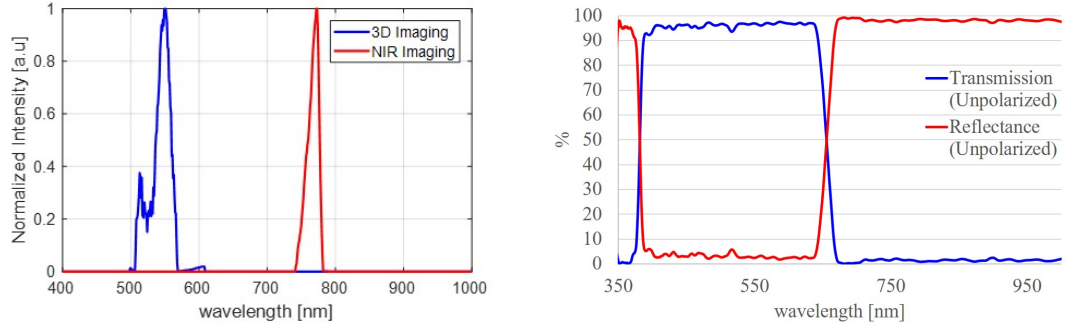
The system setup illustrated in Figures 5.11 incorporates the STAR with the electro-surgical tool (Section 5.3.2.2). The cautery operating setting from the electro-surgical unit is the same as the experimental setup in Prototype 1 (60-W cutting waveform). Another robotic arm (Universal Robot UR5, Odense, Denmark) carries the dual 3D imaging and NIR tracking (dual VIS-NIR) system. The imaging system consists of two 10-mm 0-degree rigid endoscopes for projection (260030 AA, Karl Storz Endoscopy, Tuttlingen, Germany) and imag-

CHAPTER 5. ENDOSCOPIC GUIDANCE FOR MINIMALLY INVASIVE SURGICAL ROBOT

ing (ICG 260030 ACA, Karl Storz Endoscopy, Tuttlingen, Germany). From the transmission measurements between multiple scopes in Section 5.3.2.1.2, the imaging scope with enhanced transmission across VIS-NIR is used as imaging scope. The light port of this scope is connected to a customized NIR light source (Section 5.3.2.1.3) through a light delivery cable with optimized transmittance (Section 5.3.2.1.4) . The dual modality is possible due to the simultaneous imaging of two spectral windows (Figure 5.13(a)), through spectral splitting using a short-pass dichroic mirror (DMSP650R, Thorlabs, New Jersey, USA) with central wavelength at 650 nm between the collimated paths through the CCD and NIR CMOS cameras, allowing photon with wavelengths below 650 nm to pass to the CCD for 3D imaging, and longer than 650 nm to NIR CMOS for fluorescence imaging (Figure 5.13(b)). The imaging lens for focusing to the two cameras are identical with different anti-reflection coatings within visible (300-700 nm) and NIR range (650-1050 nm) (LB1596-A and LB1596-B, Thorlabs, New Jersey, USA).

The imaging system for Prototype 2 is classified into two modes: 1) VIS Mode using only visible illumination from the projector to provide 3D imaging point cloud of the surgical scene, 2) VIS-NIR mode using dual visible and NIR illuminations to provide the robot with 3D coordinates of the surgical scene along with 3D centroids of the planned fluorescence markers.

CHAPTER 5. ENDOSCOPIC GUIDANCE FOR MINIMALLY INVASIVE SURGICAL ROBOT



(a) Normalized spectra of LED illumination used for 3D imaging (blue) and for fluorescence absorption (red). (b) Transmittance of the dichroic mirror for spectral filtering in Prototype 2.

Figure 5.13: Spectral specification of (a) the dual VIS-NIR illuminations and (b) the dichroic mirror.

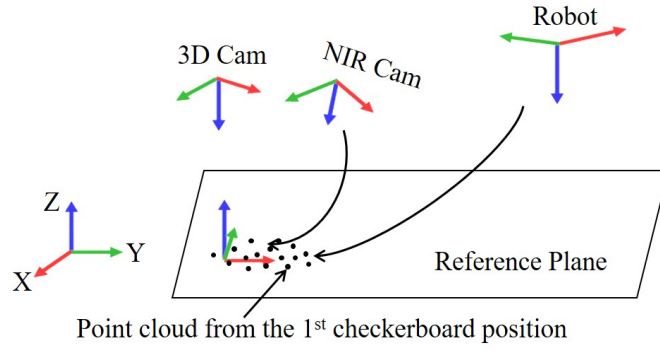


Figure 5.14: Coordination diagram of the system.

5.3.4 System Registration

The system registration includes the registration between the two cameras (i.e. the imaging system), and the registration between the robot and the imaging system. The common reference is the 3D point cloud of the reference zero plane created by the 3D imaging system, this plane is also defined as the first position of the checkerboard during the 3D camera calibration process (Figure 5.14).

CHAPTER 5. ENDOSCOPIC GUIDANCE FOR MINIMALLY INVASIVE SURGICAL ROBOT

The registration between the robot and the imaging incorporates is the hand-eye calibration process discussed in Section 5.2.3 by using a pointing rod to register four 3D points on the checkerboard surface to the robotic coordinates. The RMSE for the hand-eye calibration is within 0.30 mm with a checkerboard calibration surface.

The registration between the two cameras is obtained as follows: 1) Camera intrinsic and extrinsic parameters for 3D imaging are obtained through MOIRE Analysis calibration software version 0.956b [144] using multiple position images of the checkerboard. 2) The first position of the checkerboard at zero plane is fixed. 3) Camera intrinsic and extrinsic parameters for NIR imaging are obtained using a monocalibration package [145]. 4) A 2D image of the reference checkerboard position is captured with the NIR camera. 5) The 3D point cloud of the reference plane is projected to the NIR camera frame after the camera is moved to the correct position/orientation using the calibrated extrinsic parameters. The registration error between the two cameras (Figure 5.15) is the error between the detected corners of the 2D image and the projected corner of the 3D point cloud of the checkerboard. The position of the checkerboard is the same for both camera imaging. The corner of the 2D checkerboard image is detected using the *detectCheckerboardPoints* command (Computer Vision System Toolbox, MATLAB R2018b) and the projected point cloud corners are selected based on the noise level contrast between the black

CHAPTER 5. ENDOSCOPIC GUIDANCE FOR MINIMALLY INVASIVE SURGICAL ROBOT

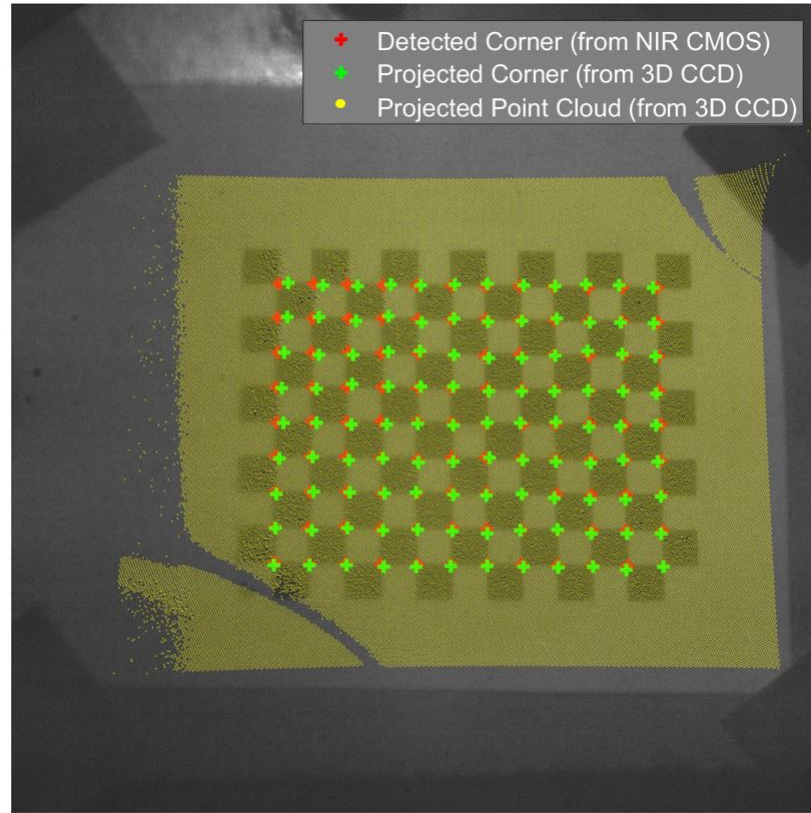


Figure 5.15: Registration error evaluation between the 3D CCD and the NIR CMOS camera. The point cloud distribution is de-sampled with 5 point step size for display purpose.

and white edge at each corner. The error between the two corner population is 4.5913 ± 2.6956 pixels in a 1024x1024-pixel image or 0.2848 ± 0.167 mm with each checker size length of 2.73 mm.

CHAPTER 5. ENDOSCOPIC GUIDANCE FOR MINIMALLY INVASIVE SURGICAL ROBOT

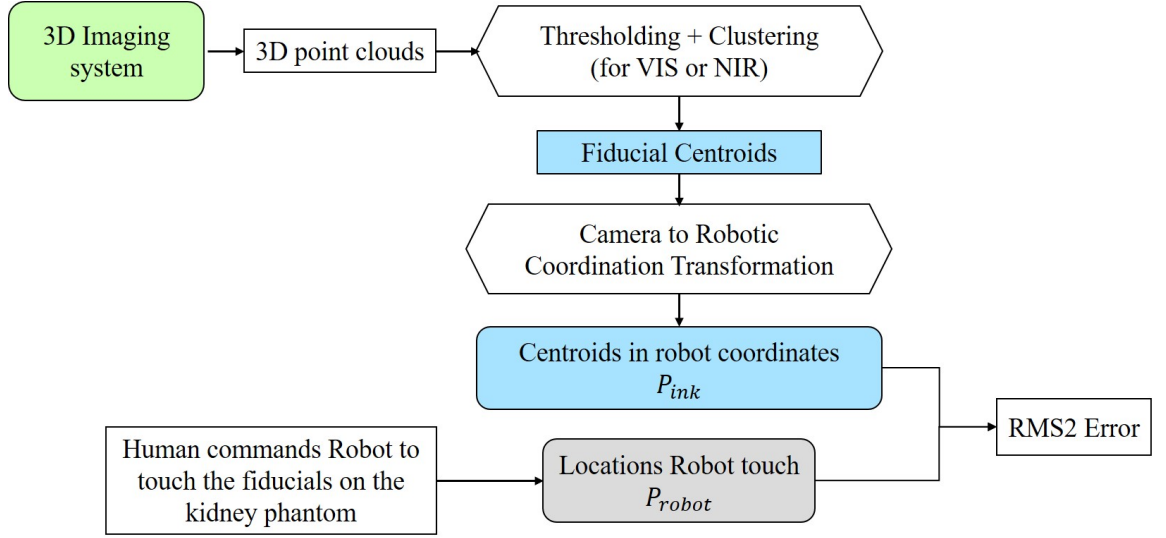


Figure 5.16: System Accuracy Validation Procedures on phantom.

5.3.5 Accuracy Evaluation

5.3.5.1 System Targeting 3D-printed Phantom

To determine the system accuracy in VIS mode and VIS-NIR mode, a defined phantom mimicking a kidney shape is 3D printed containing wells of 1 mm^3 on the surface to hold either white ink or ICG fluorescence mixture. System accuracy is validated in multiple ways for possible imaging, mechanical and human error. A summary of these accuracy errors is listed in Table 5.2. Procedure for calculating this accuracy is outlined in Figure 5.16.

5.3.5.2 System Targeting Accuracy on Tissue

Porcine kidney sample with 6 embedded NIR markers was used as accuracy targeting in this experiment. NIR markers were prepared with a mixture of

CHAPTER 5. ENDOSCOPIC GUIDANCE FOR MINIMALLY INVASIVE SURGICAL ROBOT

Table 5.2: Results of system accuracy on kidney phantom

Accuracy Error of	Description	RMSE [mm]	
		VIS Mode	VIS-NIR Mode
Calibration with checkerboard	How accurate the robot registered with the 3D imaging system	0.3038	0.0839
Robot vs. Kidney CAD model	How accurate the robot targets the phantom	0.250	0.575
3D point cloud vs. Kidney CAD model	How accurate the 3D imaging system reconstructs the phantom	0.284	0.280
Kidney phantom (Robot+Imaging Endoscope)	How accurate the robot performs using imaging setup on the phantom	0.863	0.861

ICG powder, Permabond glue, and Ethanol. The procedure for this accuracy validation is outlined in Figure 5.17, where the marker centroid location is sent to the robot to target.

Inasmuch as the cauterization process creates a different cauterized coverage than than the original NIR markers, and the two marker populations before and after the robot are captured at different times, a transformation matrix (R , T) between the two centroid populations (before and after robot) is calculated to measure the root-mean-squared error (RMSE) of these markers before and after robot. Two images of the markers with ruler (in millimeters) before and after the robot were captured (Figure 5.17). These RGB images were converted to 8-bit gray scale images. A combination of contrast enhancement and Renyi Entropy thresholding was performed to segment these marker regions. The center of mass based on the weighted intensity of these marker re-

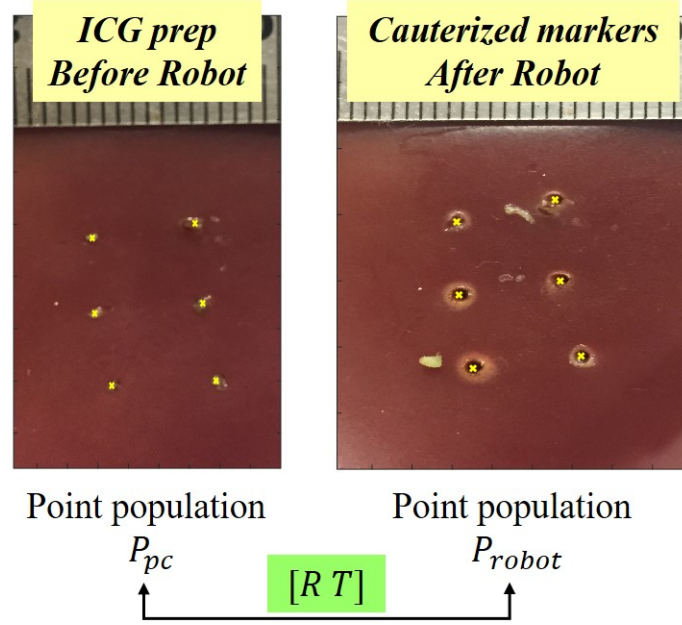


Figure 5.17: Centroid locations of the NIR marker before and after the robot (yellow point). The two centroid populations are transformed to calculate RMSE

gions were performed to calculate the marker x-y location, relative to a defined original coordination. Because the cauterization discolors the kidney tissue, the centroids of markers after the robot is done on an inverted thresholding result, compared to those markers before the robot. The result of the system targeting accuracy on kidney tissue sample is 0.288 mm.

5.3.5.3 System Cutting Accuracy on Tissue

The goal of this study is to compute the accuracy of the robot in cutting of tissue using electro-cautery tool explained in Section 5.3.2.2. The cutting trajectory giving to the robot is calculated similar as the trajectory planning in Section 5.2.4.2.1 between two ends of planned marker centroids. The cutting

CHAPTER 5. ENDOSCOPIC GUIDANCE FOR MINIMALLY INVASIVE SURGICAL ROBOT

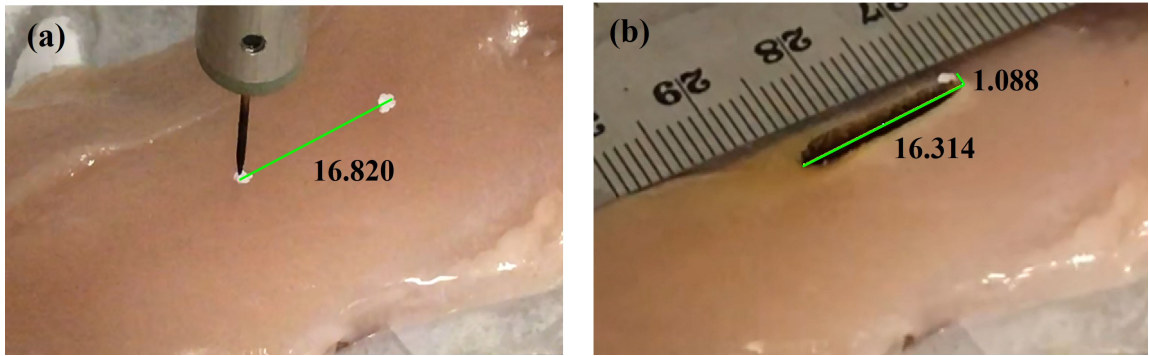


Figure 5.18: Cutting length (a) before and (b) after the robot. Unit is in millimeters.

validation of the system is done on a fowl tissue (chicken breast tissue) by the average error between the total length between the two markers and the cut length done by the robot (Figure 5.18). The error between the cut length before and after the robot is 16.820 mm compared to 16.314 mm, respectively, with 1.088 mm offset error at one cut end point. In addition, the average depth error of the cauterized segment is compared with the planned 3-mm planned depth on the robot control (Figure 5.19). The depth error is calculated on the edge detection from thresholded cut segment. The thresholding is done through multiple image post processing in orders as follows: RGB to gray scale conversion, Gaussian median filter for low noise removal, color balance and brightness/contrast enhancement, binary thresholding, binary hole filling and dilation. The average error along the depth is computed to be 0.087 ± 0.168 mm.

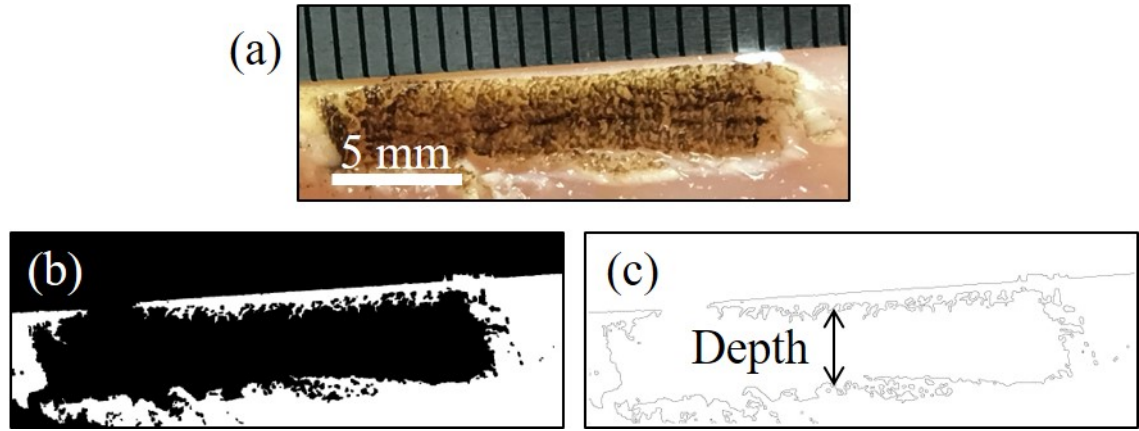


Figure 5.19: Cutting accuracy determination using post image processing (a) Cross-section of the cut. (b) Thresholded cut segment. (c) Segmented cut boundary.

5.3.6 Lessons Learned

The Prototype 2 is enhanced with dual VIS-NIR modality to collect 3D point cloud of the scene with NIR tracking capability at the same time through spectral splitting between visible and near infrared bandwidth. This dual modality also allows further observations of flow dynamic using injected NIR agent. Moreover, the system speed is improved by back-calculation of phase distribution from higher modulated fringe projection to lower fringe projection, making speed improvements from 1.57 fps in Prototype 1 to 4.4 fps in Prototype 2. In addition, with the improved surgical tools, Prototype 2 accomplishes sub-millimeter accuracy on tissue sample within 0.288 mm for targeting and 0.087 ± 0.168 mm for cutting task on tissue sample.

The current calibration between the two cameras (CCD for 3D imaging and

CHAPTER 5. ENDOSCOPIC GUIDANCE FOR MINIMALLY INVASIVE SURGICAL ROBOT

CMOS for NIR tracking) is based on the 3D point cloud of the reference zero plane. This procedure requires the reference plane to be fixed for NIR camera calibration. This calibration process can be modified so that the reference frame is at the camera frame, therefore, requires no fixation of the first calibration board position. Moreover, once the reference frame is in the camera frame, the correspondence between the two cameras can be the relations between the two 2D frames (instead of the projection between the 3D point cloud to the 2D image of the NIR camera). This modification potentially makes the calibration process between the two cameras programmable and more flexible with less calibration steps.

5.4 Third Prototype: Surgical Planning

Strategy

5.4.1 Autonomous Laparoscopic Robotic Suturing with a Novel Actuated Suturing Tool and 3D Endoscope

5.4.1.1 System Contributions

This prototype further extends our smart tissue autonomous robot (STAR) [9, 146, 147] and enables autonomous laparoscopic suturing. The STAR aims to provide consistent and effective laparoscopic suturing via a specifically-designed

CHAPTER 5. ENDOSCOPIC GUIDANCE FOR MINIMALLY INVASIVE SURGICAL ROBOT

robotic system and ultimately substitute human skills. This can be achieved by reducing the total time of suturing task compared to the state-of-the-art tele-operated RAS [148], and standardizing and uniforming the quality of suturing outcome [149]. The STAR system consists of 1) a robotic arm equipped with, 2) an actuated suturing tool, and 3) a camera system to support vision-guidance and control system. Our contributions in this paper are threefold and expand on the components 2 and 3 of STAR. As the first contribution, we develop and test a novel laparoscopic 3D camera system suitable for surgical robotic applications. The 3D imaging endoscope provides a quantified peripheral construction of the surgical scene with an expansion to point cloud segmentation for autonomous planning of suturing.

As the second contribution, we develop a new robotic laparoscopic suturing tool via modifying the commercially available Proxisure suturing tool (Ethicon Inc. Somerville, NJ, United States). Proxisure is the only commercial suturing tool designed to compensate for laparoscopic constraints by adding 2 additional degrees of freedom (DOF) at the distal tip. By motorizing and mounting the Proxisure tool on a 7 DOF medical light weight robot (LWR) from KUKA (KUKA AG, Augsburg Germany), we enable STAR to place sutures in any orientation in the surgical field. We design and implement specialized hardware and software based on the developed camera and tool to execute autonomous suturing steps under supervision of human.

CHAPTER 5. ENDOSCOPIC GUIDANCE FOR MINIMALLY INVASIVE SURGICAL ROBOT

Finally, as the third contribution of this study, we propose a segmented suturing planning method based on point clouds obtained from the 3D endoscope. The proposed method calculates the suture point locations based on the coordinates of the incision groove and cut. We experimentally demonstrate the accuracy and consistency of our new laparoscopic robotic suturing system and compare the results against manual laparoscopic suturing performed by experienced surgeons.

5.4.1.2 System Setup

The experimental testbed developed in this paper is shown in Figure 5.20. This testbed includes our novel robotic laparoscopic tool which is mounted on a 7-DOF KUKA Med lightweight arm (KUKA LWR Med) as the surgical robot, and our novel 3D imaging endoscope. The 3D endoscope and robotic suturing tools are detailed in the following.

5.4.1.2.1 3D Imaging Endoscopic System

The vision system supporting robotic manipulation in this section incorporates a quantified 3D reconstruction with surgical planning method for autonomous suturing path. The main components of the imaging system (Figure 5.21) are similar to the setup described in Section 3.3.2. However, the two endoscopes are replaced by a rigid endoscope with bigger housing diam-

CHAPTER 5. ENDOSCOPIC GUIDANCE FOR MINIMALLY INVASIVE SURGICAL ROBOT

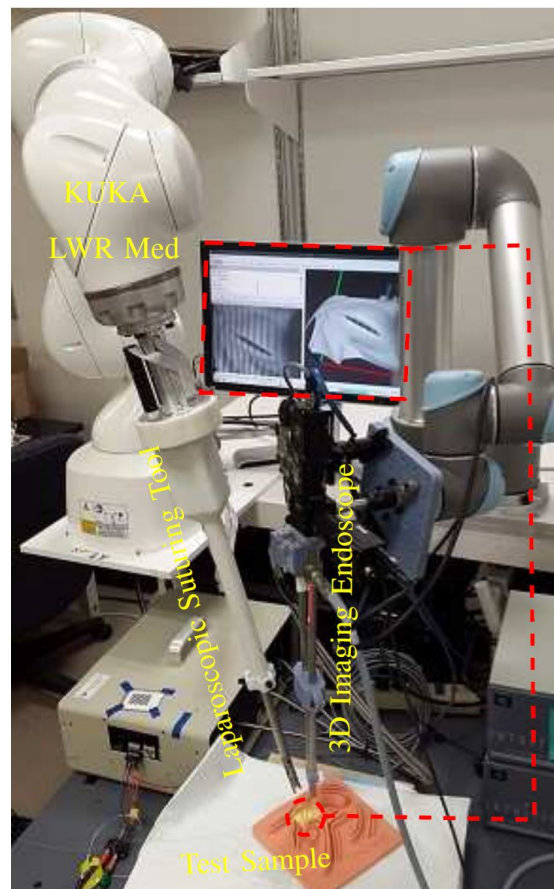


Figure 5.20: Laparoscopic robotic suturing system.

CHAPTER 5. ENDOSCOPIC GUIDANCE FOR MINIMALLY INVASIVE SURGICAL ROBOT

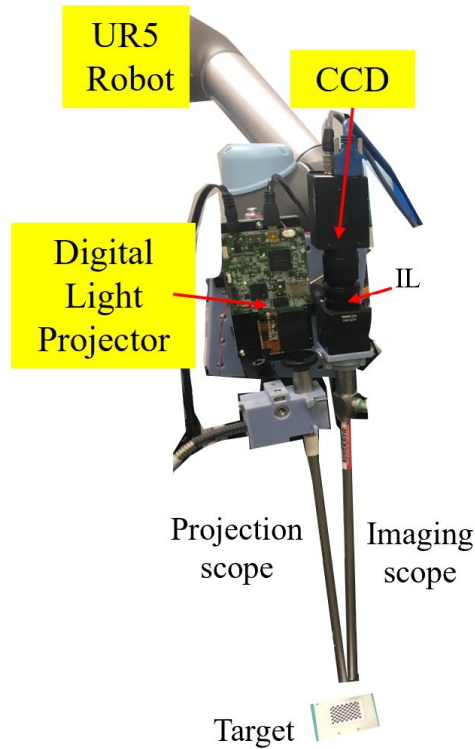


Figure 5.21: 3D imaging endoscope setup on an UR5 robot. IL: Imaging Lens.

eter (260030 AA, Karl Storz Endoscopy, Tuttlingen, Germany) for fringe projections, and a second rigid scope with enhanced transmittance (ICG 260030 ACA, Karl Storz Endoscopy, Tuttlingen, Germany) for imaging.

5.4.1.2.2 Suturing Tool

A novel multi-axis suturing tool (Figure 5.22) was designed and prototyped to perform the autonomous suturing tasks in this study. The suturing tool was assembled by deconstructing the handle of a commercially available Proxisure suturing device and individually coupling each joint to a three axis motor pack using a customized tool adapter (Figure 5.22a). Each of the motors are ener-

CHAPTER 5. ENDOSCOPIC GUIDANCE FOR MINIMALLY INVASIVE SURGICAL ROBOT

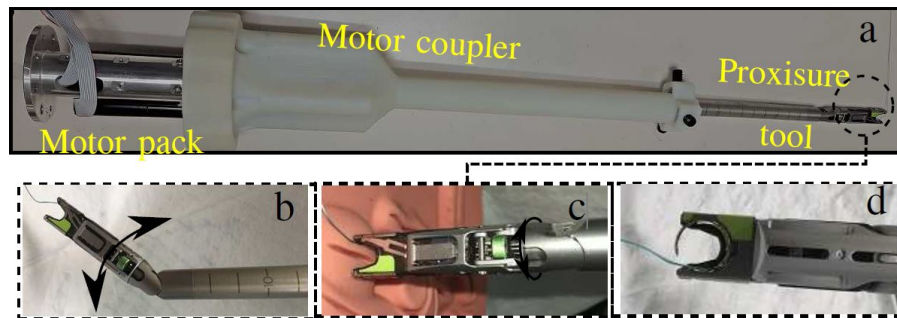


Figure 5.22: Suturing tool with its components (a) Overall design of the suturing tool, (b) pitch actuation, (c) roll actuation, (d) needle drive.

gized independently to actuate one of three actions: pitch (Figure 5.22b), roll (Figure 5.22c), and needle drive (Figure 5.22d). The pitch and roll motions of the tool can be combined to provide an extra two degrees of freedom within the surgical space. When the tool is used under laparoscopic constraints, these two degrees of freedom restore full 6 degree of freedom positioning of the tool tip, enabling the robotic system to suture in any orientation. Each motor includes an encoder for precise positioning using EPOS2 controllers (Maxon Motors, Sachseln, Switzerland). Communication between the robot and tool is through a controller area network (CAN). The pitch and needle drive motors are homed by energizing each motor with current control until they reach a hard stop. The multi-axis tool is compatible with Ethicon brand suture of various size and materials. In the following studies, 2-0 polyester Ethibond suture is used for testing.

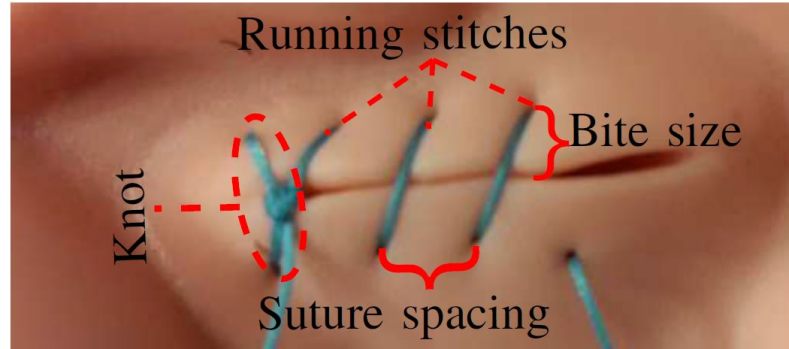


Figure 5.23: Suture task and metrics.

5.4.1.3 Surgical Task and Evaluation Criteria

The surgical task considered in this paper includes performing a laparoscopic suturing on a straight incision. For the experiments, surgeons and STAR were instructed to complete a knot and 3 running stitches to close a 21-mm incision (Figure 5.23) on a 3-Dmed (Ohio, United States) training suture pad. The metrics for measuring the efficiency of STAR consist of i) task completion time, ii) the distance between consecutive stitches, iii) bite size (i.e. distance between stitch and the incision edge), and iv) repositioning mistakes during suturing. The latter three measures are known to influence the complications of healing process such as breaking and infections [150, 151].

5.4.1.4 Control System

Figure 5.24 shows the block diagram of the autonomous controller. In this control loop, 3D surface of tissue is constructed via the point cloud obtained by the camera shown in Figure 5.21 described earlier in this section. A suture

CHAPTER 5. ENDOSCOPIC GUIDANCE FOR MINIMALLY INVASIVE SURGICAL ROBOT

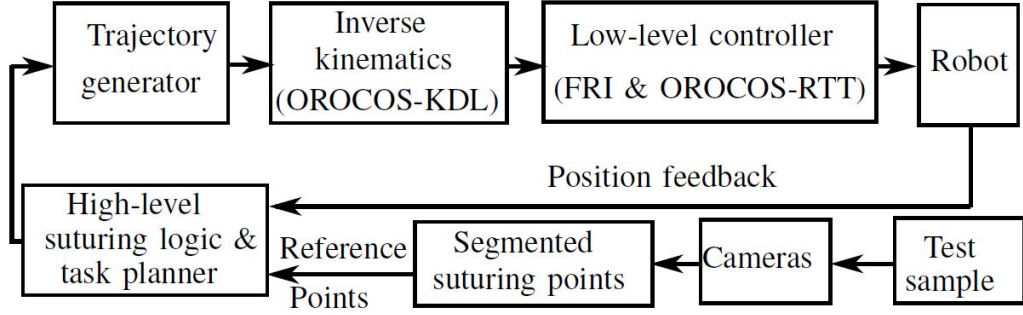


Figure 5.24: The autonomous control loop.

point planning strategy uses the 3D surface information to determine the desired location of each knot and running stitch (later detailed in Section 5.4.1.5). The resulting 3D coordinates of the reference suture points in the robot frame along with the current robot positions are passed to a high-level suturing logic and task planner (later detailed in Section 5.4.1.6) which plans the sequence of robot motions to complete the knot and running stitches on the desired and equally spaced positions. The corresponding smooth time-based trajectories of the robot motion are calculated in real-time using Reflexxes Motion Libraries [152]. These trajectories are converted from task space to joint space of the robot via Kinematics and Dynamics Library (KDL) in Open Robot Control Systems (OROCOS) [153]. Finally, communication with the robot and tool are implemented via Fast Research Interface (FRI) [154] and real-time toolkit (RTT) [155] in OROCOS issued to guarantee that the robot and tool follow the desired joint-space trajectories. Next, we explain the suture planning method.

5.4.1.5 Planning Strategy for Suturing

The suture pad is placed approximately 5 cm from the distal end of the endoscope for a desired field of view and to mitigate specular reflection from the projected light. The cut line on a suture pad is located within the imaging field of view. A 3D point cloud distribution of the cut is analyzed to calculate the suture points for the robot based on the coordinates of the segmented cut groove and edge. The algorithm is executed in these 5 steps:

1. Region of interest (ROI) localization: An interactive polygon is drawn manually with boundary coordinates defining the point cloud boundary to focusing subsequent point cloud segmentation analysis within a smaller ROI (black polygon in Figure 5.25b). The purpose of this sampling method is to speed up the subsequent cut analysis by restraining only the cut feature ROI.
2. Point cloud sectioning: The overall point cloud with the cut feature inside the cropped ROI is sub-sampled along one direction that most reveals the cut groove (black dots in Figure 5.25c and Figure 5.25d). The spacing between each section is the planned suture spacing. In this study, we chose a 4-mm spacing to provide adequate and equal spacing on the desired 21 mm suture path.
3. Cut groove determination: The cut groove is identified by finding a promi-

CHAPTER 5. ENDOSCOPIC GUIDANCE FOR MINIMALLY INVASIVE SURGICAL ROBOT

nent minimal peak along the point cloud section based on height differentiation from the neighboring depth values (red circles in Figure 5.25c and Figure 5.25d).

4. Cut edge calculation: Once the cut groove is defined, two regions on the left and right side of the cut groove are selected to find the cut edge. The index of the cut edge is deduced based on a point, which is farthest from the line connecting the cut groove point and the boundary point (blue and magenta cross markers in Figure 5.25c and Figure 5.25d).
5. Suture point detection: The suture point is determined with x-y coordinates from the cut groove and z-coordinates as the average depth of the left and right cut edge (red triangles in Figure 5.25c and Figure 5.25d). The 3D coordinates of the calculated suture points are transformed to world coordinates for robotic manipulation.

With the total size of the targeted cut line of 21 mm, 4 target points representing the location of knot and three running sutures are computed for a 4-mm suture spacing. The computational time for all 5 steps is within 30 seconds on an Intel Core i7-6500 CPU, 16 GB RAM laptop.

5.4.1.6 High-Level Suturing Logic and Task Planner

As mentioned earlier in Section 5.4.1.3, the suturing task includes a first knot followed by 3 running stitches. The location of the knot and each stitch is

CHAPTER 5. ENDOSCOPIC GUIDANCE FOR MINIMALLY INVASIVE SURGICAL ROBOT

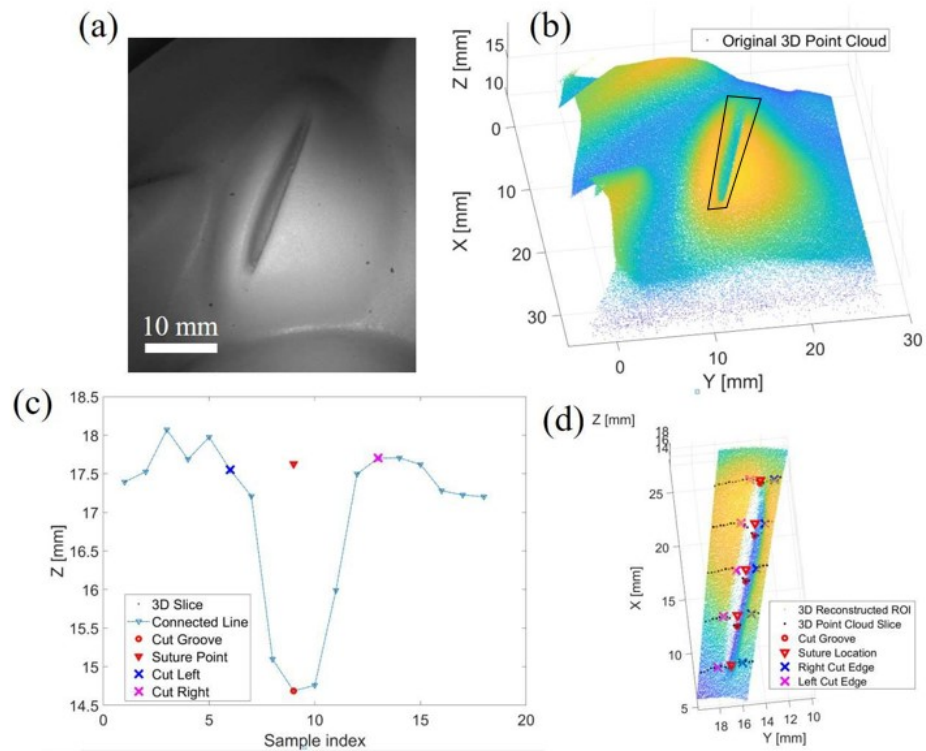


Figure 5.25: Suture planning strategy: (a) A white reflection image of the cut sample. (b) Collected point cloud with ROI. (c) An example of calculated cut groove, left and right cut edges, and the suture point. (d) An overlay of the calculated coordinates with suture spacing of 4 mm.

CHAPTER 5. ENDOSCOPIC GUIDANCE FOR MINIMALLY INVASIVE SURGICAL ROBOT

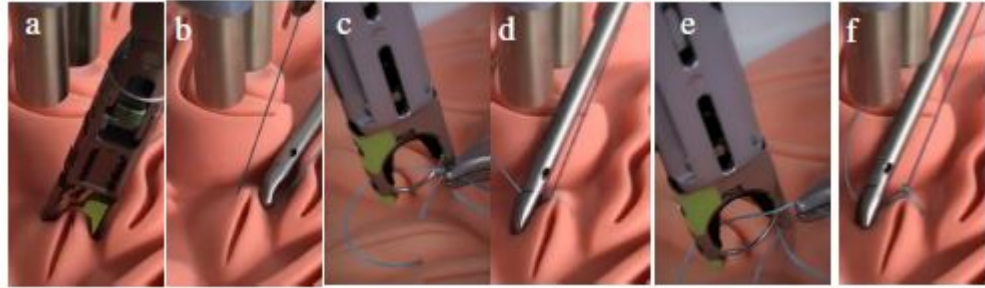


Figure 5.26: Steps of executing a knot: (a) bite, (b) tensioning, (c) first loop, (d) tension of first loop, e) second loop, f) tension of second loop.

determined on the suture line (incision) via the algorithm explained in Section 5.4.1.5. These points will be the references for the tool control point (TCP) of the robot. The reference/desired orientation of TCP is determined in a way that the jaw of the suturing tool is perpendicular to the suturing path.

The first subtask is to complete a knot at the first reference position and orientation. Completing a knot requires biting the tissue, tensioning the thread, and making two loops of suture to lock the knot into place. As shown in Figure 5.26, the TCP of robot is commanded to the first position of the knot on the incision. The needle drive is then actuated so that the suture completes a bite of the suture pad (i.e. insert the needle through the tissue) (Figure 5.26a). Next, the initial bite of suture is tensioned to a height of 9cm (Figure 5.26b) and the tool is rotated to an orientation parallel to the suture line. To perform the first loop of the knot, a surgical assistant places the tail of the suture within the jaw of the suturing tool using a laparoscopic needle driver, and STAR actuates the needle drive (Figure 5.26c). The first loop of the knot is then tensioned

CHAPTER 5. ENDOSCOPIC GUIDANCE FOR MINIMALLY INVASIVE SURGICAL ROBOT

by raising the suture tool above the suture plane (Figure 5.26d). After STAR tensions the first loop, the process is repeated to throw and tension a second loop of the knot, locking it into place on the suture pad (i.e. Figure 5.26e and Figure 5.26f).

The second subtask is to complete three running stitches along the length of the incision. To complete the running stitches, STAR executes the first two steps of the knot tying sequence for each suture location that was found in Section 5.4.1.5 (i.e. Figure 5.26a and Figure 5.26b). The position and orientation of the suture tool is autonomously adjusted for each stitch, such that the jaws of the tool remain perpendicular to the cut line. The amount of thread needed for completing the running sutures can be estimated according to the following equation [146]:

$$L > 2TN + (N - 1)\sqrt{2T^2 + d^2} \quad (5.3)$$

where L is the total length of thread needed to complete N stitches of width T with the distance between stitches of d . In our experiments, $N = 4$, $T = 8$ mm, and $d = 4$ mm and hence an estimation of required length is $L = 100$ mm. The tensioning distance at each stitch can be easily calculated by reducing the amount of thread used before the current stitch from the total required length of thread at the start of the suturing. Here on average 18 mm is subtracted

CHAPTER 5. ENDOSCOPIC GUIDANCE FOR MINIMALLY INVASIVE SURGICAL ROBOT

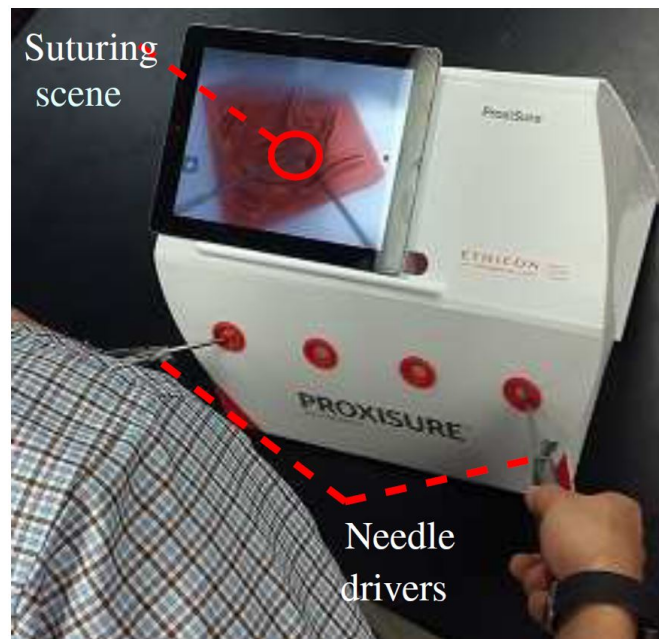


Figure 5.27: Manual suturing using a laparoscopic trainer.

from the tensioning distance after each completed stitch.

5.4.1.7 Test Conditions

For each of the manual and autonomous suturing tasks, 5 experiments were conducted and the aforementioned criteria were recorded and analyzed. The manual suturing experiments were completed by two surgeons using a laparoscopic trainer shown in Figure 5.27. During the suturing, the surgeon views the suturing scene via a tablet screen and operates two needle drivers through the ports available on the laparoscopic trainer box.

For the autonomous suturing, first the tissue surface is detected by the 3D endoscope described earlier in Section 5.4.1.2.1. The suturing way-points are

CHAPTER 5. ENDOSCOPIC GUIDANCE FOR MINIMALLY INVASIVE SURGICAL ROBOT

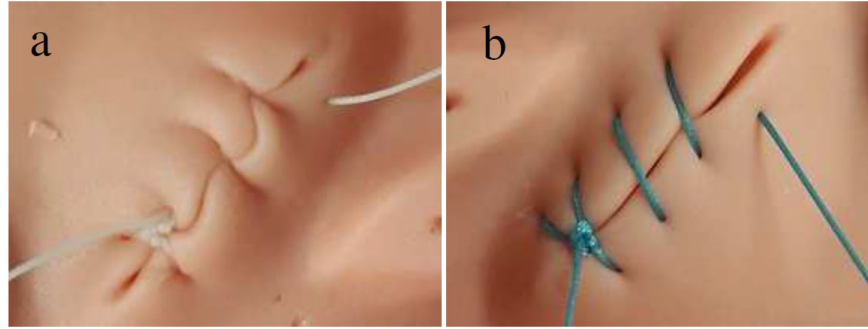


Figure 5.28: Examples of suturing with (a) manual, (b) autonomous approach.

determined via the method detailed in Section 5.4.1.5. Finally, we complete the knot and running stitches with an autonomous control loop detailed earlier in Section 5.4.1.4 (Figure 5.24). Since the robotic suturing is performed by one robotic arm, a surgical assistant uses a laparoscopic needle driver to manage the excess length of the suture thread.

5.4.1.8 Results

The results of the experiments are summarized in Tables 5.3 and 5.4. Representative examples of manual suturing and autonomous suturing results via STAR are shown in Figure 5.28.

5.4.1.8.1 Completion Time

As presented in Table 5.3, the average total task completion time for the autonomous method is 106.4 seconds longer than manual method. Completing the knot contributes to the majority of this difference (i.e. 83.2 seconds longer in the autonomous mode with $p < 0.001$), while the remaining difference is re-

CHAPTER 5. ENDOSCOPIC GUIDANCE FOR MINIMALLY INVASIVE SURGICAL ROBOT

Table 5.3: Comparison of experiment results via completion time.

	Total (sec)		Knot (sec)		Stitches (sec)	
Test	Avg.	Std.	Avg.	Std.	Avg.	Std.
Manual	180.20	13.53	92.2	17.28	88.00	9.59
STAR	286.60	6.68	175.4	6.34	111.2	5.56

Table 5.4: Comparison of experiment results via distance between stitches, bite size, and number of suture repositioning.

	Dist between stitches (mm)		Bite size (mm)		Number of repositioning	
Test	Avg.	Std.	Avg.	Std.	Avg.	Std.
Manual	3.68	1.19	2.53	0.86	1.60	0.80
STAR	4.70	0.41	3.41	0.83	0.00	0.00

lated to the speed of the stitching steps (i.e. 23.2 seconds longer in autonomous mode, $p < 0.01$, for 3 stitches).

5.4.1.8.2 Distance Between Stitches

The average suturing distance obtained by STAR is statistically 1.02 mm larger than the manual, $p < 0.001$. The desired value of spacing between the stitches for STAR is 4 mm and the experimental results show an average spacing of 4.7 mm. However, variance of suture spacing is significantly less for STAR than human $p < 0.001$ which indicates that STAR placed the running stitches more uniformly (2.9 times better) compared to the human surgeons.

CHAPTER 5. ENDOSCOPIC GUIDANCE FOR MINIMALLY INVASIVE SURGICAL ROBOT

5.4.1.8.3 Bite Size

Although the average bite size of STAR is statistically larger than manual $p < 0.001$ the variance of the bite size is non significant for STAR and human ($p = 0.837$). This indicates that STAR is just as consistent as human surgeons when suturing a specified depth.

5.4.1.8.4 Number of Stitch Re-Positions

In the experiments, the human surgeons made an average of 1.6 suture corrections per test (i.e. 1.6 corrections for 1 knot and 3 stitches). In contrast, because of the positioning accuracy and repeatability of the robotic system, STAR required zero corrections per test.

5.4.1.9 Lessons Learned

From the total of four criteria used in this study, the consistency of STAR outperforms manual suturing in two metrics. High consistency and accuracy in suture spacing provides a reliable method for placing sutures at the desired planned locations. Also, compared to manual method, STAR prevents additional throws for placing the sutures as the number of suture corrections are zero, minimizing unnecessary damage to the tissues. Furthermore, in our experiments the consistency of bite size is equal to human.

Despite high consistency and accuracy of STAR in performing the suturing

CHAPTER 5. ENDOSCOPIC GUIDANCE FOR MINIMALLY INVASIVE SURGICAL ROBOT

task, the overall process is slower than the manual method. One of the main reasons behind the slower pace of suturing in autonomous mode is due to the limited maximum speed of the motors used in the suturing tool. Given the current motors and internal mechanism of the tool, when the needle drive motor is actuated at full speed, completing each knot loop or bite with the tool takes 18 seconds (i.e. the time for the needle to complete a full circular drive). With faster motors this can be reduced to 2 seconds. Moreover, the maximum values of robot speed were intentionally chosen low (1 cm/s) to ensure safety during tests (e.g. preventing sudden suture tensions or fast contacts with the suture pad). These values, can be optimized in future to make a balance between safety and speed.

5.4.2 An Extension of Cutting Segmentation with Planned NIR Markers for Autonomous Suturing Planning

5.4.2.1 System Contributions

Suturing segmentation proposed in Section 5.4.1.5 requires no additional tissue marker to identify cutting direction. In situation where multiple cuts are applied on one surface, it is sometimes necessary to keep track of cutting directions for even suture spacing and a precised suture locations. In such

CHAPTER 5. ENDOSCOPIC GUIDANCE FOR MINIMALLY INVASIVE SURGICAL ROBOT

cases, either correlations between point cloud sampling in both x-y directions is required for cutting analysis, or cutting direction is identified, through NIR markers at the cut ends. In this section, a suture planning strategy based on analysis on the 3D reconstructed point clouds with cutting direction determination using NIR marker is proposed. The method detects cutting landmarks such as the cutting depth and cutting edge as inputs to create safe suture point mapping for automating robotic anastomosis.

5.4.2.2 System Setup

The system illustrated in Figure 5.29 is an extension of Prototype 2 in Section 5.3 with NIR sensing capability. The role of NIR sensor is to detect centroid coordinates mapped on the 3D point cloud provided by the 3D endoscope.

5.4.2.3 Suturing Mapping Strategy

The suturing mapping strategy is calculated based on natural groove shape of the cutting line across the tissue surface. This cut-line is detected through point cloud groove detection along the perpendicular direction to the cutting axis (Figure 5.30b), making the groove shape more apparent for the detection. Cutting direction is computed by the two point cloud locations of the NIR end markers of each cut line. The number of the cross sections and the spacing between them are defined as the desired number of suturing points and the

CHAPTER 5. ENDOSCOPIC GUIDANCE FOR MINIMALLY INVASIVE SURGICAL ROBOT

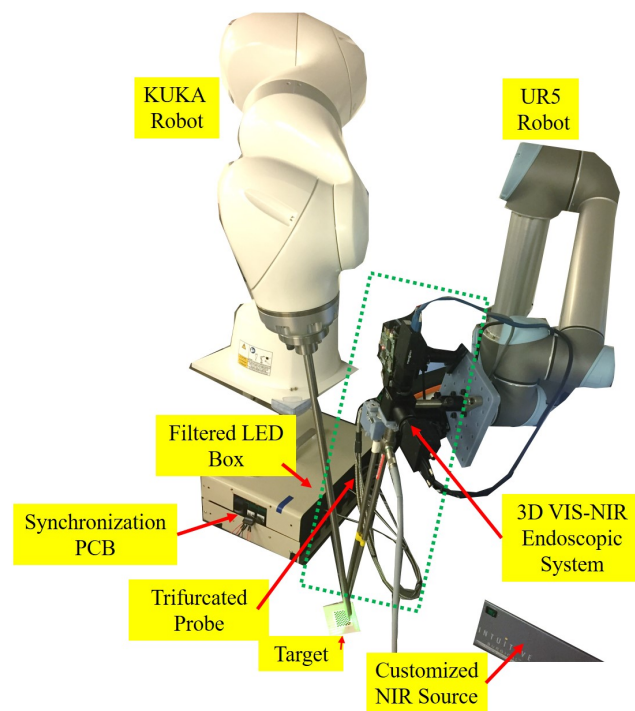


Figure 5.29: Multimodal imaging endoscopic setup for surgical planning in minimally invasive robotic surgery.

CHAPTER 5. ENDOSCOPIC GUIDANCE FOR MINIMALLY INVASIVE SURGICAL ROBOT

suture spacing on each side of the cut. The cutting direction is calculated from the two NIR marker coordinates applied at the two ends of the desired cutting line (Figure 5.30a). In the case when NIR marker is not applicable, a correlation between x and y section slices of the point cloud can be used to calculate the correct cutting groove and edge.

For each cross section, we detect the groove of the cutting segment (magenta crosses in Figure 5.30c) by calculating the index position n at which occurs the maximum of the convolution between the cutting segment g_n and the modeled groove shape f_n from Equations 5.4 and 5.5.

$$f_n = \begin{cases} |n| - \frac{1}{2b+1} \cdot \sum_{n=-b}^b |n| & ; -b \leq n \leq b \\ 0 & ; otherwise \end{cases} \quad (5.4)$$

$$n = \operatorname{argmax}_n (g_n * f_n) \quad (5.5)$$

where b indicates half of the designated groove width.

After the groove detection, we apply a poly fit line (4^{th} order) along the left and right sides of the groove points where the fitted line from the groove has a low slope threshold value, i.e. the cutting edge (red circles in Figure 5.30c). The final step is to map the cutting edge points along with suggested suturing

CHAPTER 5. ENDOSCOPIC GUIDANCE FOR MINIMALLY INVASIVE SURGICAL ROBOT

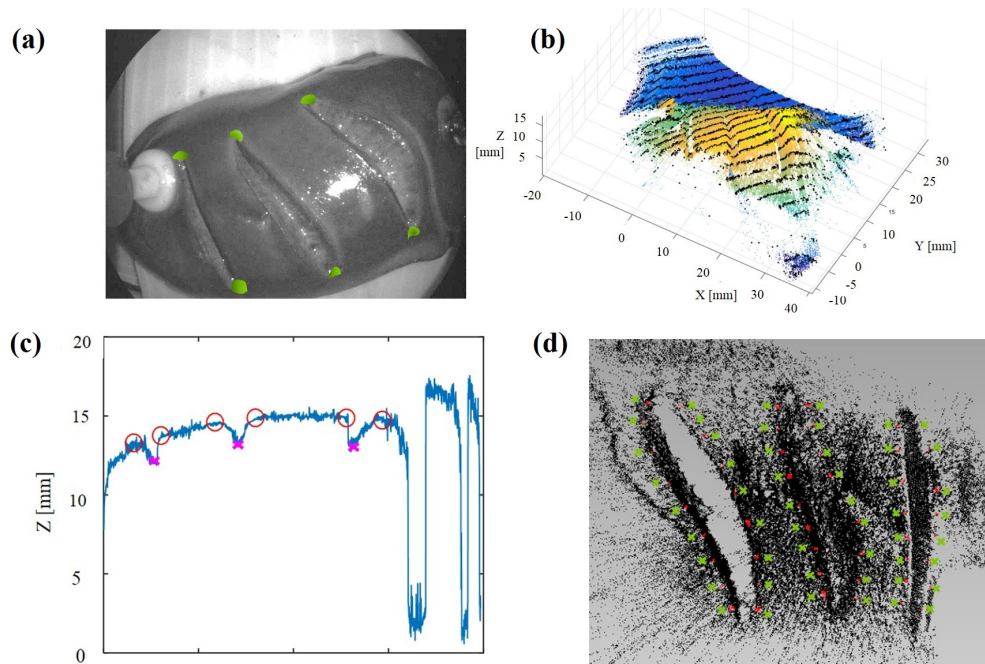


Figure 5.30: Suture planning procedure (a) Bright field reflection image of a incised kidney tissue with planned NIR markers, (b) Collected 3D point cloud with slice sections normal to the cutting axis. (c) Cutting groove and edge detection. (d) Suture location (green dots) is an off-set distance away from the cutting edge (red dots).

points to the 3D point clouds. The suggested suture points are defined at a fixed distance away from the cutting edge with consistent pre-programmed spacing. The plan is applied to a cut kidney using an electro-cautery tool, the indicated results in Figure 5.30) show that the natural shape of the kidney as well as the cuts are well-indicated in the 3D maps.

5.4.2.4 Lessons Learned

The results demonstrate the feasibility to detect cutting edge and suggest a suture map for robotic surgery with additional NIR tracking of cutting direction.

CHAPTER 5. ENDOSCOPIC GUIDANCE FOR MINIMALLY INVASIVE SURGICAL ROBOT

Moreover, the method explains the cut groove with a running groove shape detection, which provides robust groove shape detection of multiple cuts within a tissue region. Future work aims at expanding the method to more variety of the cutting shapes and directions.

Chapter 6

Intra-operative Guiding of the Cavernous Nerve Network using Near-infrared Cyanine Voltage-Sensitive Dye

6.1 Motivation

Since the first report of radical perineal prostatectomy by Young to the nerve-sparing Radical Retropubic Prostatectomy (RRP) by Walsh [156–158], several risks for post-operative complications remain, such as erectile dysfunction due

CHAPTER 6. INTRA-OPERATIVE GUIDING OF THE CAVERNOUS NERVE NETWORK USING NEAR-INFRARED CYANINE VOLTAGE-SENSITIVE DYE

to nerve damage during prostate cancer treatment. Due to the small average distance between the cavernous nerves (CN) and the prostate gland (2.8 mm), these nerves are at a high risk of injury during removal of a cancerous prostate gland. Also, it is still unknown how many CN branches (CNB) surrounding a prostate [159] contribute to erectile function. Each individual CN are a few hundred micrometers in diameter and vary between patients, making it difficult to predict the exact location and path of these nerves [160]. With laparoscopic RRP [161], potency at 12 months post-operation is only restored in 70% of surgeries [162]. Robot-assisted RRP is projected to provide better preservation of erectile nerves due to its closer endoscopic vision [163]. However, current RRP is limited in providing real-time nerve dynamics, leading to low post-operative complication rates for surgeries addressing both incontinence (4.7% versus 2.1%, respectively) and erectile dysfunction (26.8 versus 19.2 per 100 person-years, respectively) [8]. Therefore, a nerve-sparing RRP with exploration in the prostatic nerve network is critical.

Fluorescence (FL) imaging has been recently introduced in commercial endoscopic products such as the FireFlyTM (Intuitive Surgical Inc., United States) and the FLARETM systems (Curadel ResVet Imaging, LLC., United States) [164, 165] with several exogenous fluorophores targeting specific tissue types also being proposed [166–168]. The enthusiasms in academy and industry for this technique originates from its wide field-of-view (FOV) that is directly su-

CHAPTER 6. INTRA-OPERATIVE GUIDING OF THE CAVERNOUS NERVE NETWORK USING NEAR-INFRARED CYANINE VOLTAGE-SENSITIVE DYE

perimposable on that of the surgeon, which makes it amenable to several current surgical methods including RRP. However, most current nerve-specific fluorophores present high affinity to nerve networks, only yielding the stationary locations of the nerves, rather than the functional contrast of their electrophysiological activity representing erectile functionality [167, 169]. Also, most of these nerve-specific fluorophores only provide superficial imaging depth as they have peak absorption and emission wavelengths at the visible wavelength range (400-650 nm). Recent scholarly work has yielded near-infrared dyes applicable to intra-operative nerve localization, but they are still based on the nerve-specific affinity mechanism and do not provide functional resolution of a patient's erectile function. [170, 171]. Furthermore, nerve labeling with this affinity-based mechanism takes from few a hours to days. The direct administration of these near-infrared dyes has recently proposed to address this problem, but it is still based on the affinity-based mechanism [169].

Recently we proposed using cyanine voltage-sensitive dye (VSD). VSD redistributes according to cell membrane potential, leading to a FL quenching yield change—a functional contrast—related to the electrophysiological events in biological tissue [172, 173]. In detail, the cyanine dye, with positively-charged chemical structure (e.g., IR780 perchlorate), would be attracted into a cell membrane when the neuronal cells are in polarized resting state (i.e., -90 mV [174]). The VSD aggregates as its concentration increases inside the cell

CHAPTER 6. INTRA-OPERATIVE GUIDING OF THE CAVERNOUS NERVE NETWORK USING NEAR-INFRARED CYANINE VOLTAGE-SENSITIVE DYE

membrane, leading to FL quenching, i.e., the dissipation of absorbed light energy in the form of thermal energy. Conversely, when the neuronal cells are depolarized, VSD will disaggregate and exit the membrane. This redistribution restores FL emission. This functional contrast change will be activated in sequences of the neuronal depolarization and can be quantified by FL imaging at absorption and emission wavelengths (790 nm and 820 nm) beneficial for deep tissue FL imaging. Using the commercially-available VSD compound (IR780 perchlorate), we have shown 69.69% of fractional contrast in FL emission can be obtained using a 6- μ M VSD concentration when the membrane potential was depolarized to -120mV [173]. Our team also presented the feasibility of transcranial FL VSD neuroimaging using the VSD compound [175].

To explore the prostatic nerve network contribution from cavernous nerves and their branches for nerve-sparing radical retropubic prostatectomy, we have facilitated utilizing the VSD quenching mechanism to monitor nerve activity through FL imaging within minimally invasive standards.

My contributions were the fluorescence imaging fiberscope development, including the optical design and the optical assessment of the fabricated imaging fiberscope in *in vivo* experiments. This work is in preparation to submit for publication.

6.2 System Contribution

We present functional intra-operative guidance of the cavernous nerve (CN) network for nerve-sparing radical prostatectomy using near-infrared cyanine voltage-sensitive dye (VSD) imaging, which visualizes membrane potential variations in the CN and its branches (CNB) in real-time. As a proof-of-concept experiment, we demonstrated a functioning complex nerve network in response to electrical stimulation of the CN, which was clearly differentiated from surrounding tissues in an *in vivo* rat prostate model. Stimulation of erection was confirmed by correlative intracavernosal pressure (ICP) monitoring. Within ten minutes we performed trans-fascial staining of the CN by direct VSD administration. Our findings suggest the applicability of VSD imaging for nerve-sparing radical prostatectomy.

6.3 Method

6.3.1 Fluorescence Imaging Fiberscope

The FL imaging fiberscope was designed to provide similar endoscopic view as in a clinical flexible fiberscope discussed in Section 1.2.2.1. At the distal end of the fiberscope is a customized optical assembly to focus high angle beams (70° field of view) from the object into the fiber core body. The focused im-

CHAPTER 6. INTRA-OPERATIVE GUIDING OF THE CAVERNOUS NERVE NETWORK USING NEAR-INFRARED CYANINE VOLTAGE-SENSITIVE DYE

age at the distal fiber end is then relayed multiple times to the proximal fiber end through total internal reflectance. The customized optical assembly with 1.5-mm lens diameter was optimized using Optics Studio 15 SP1 (Zemax, Kirkland, Washington, USA), fabricated, and housed in front of the fiber relay body. The simulation layout, spot diagram, and modulated transfer function (MTF) of the optical assembly is shown in Figure 6.2. The resultant numerical aperture (NA) of the fiberscope was approximately 0.398. The fiber relay body (not shown in Figure 6.2) is a fiber bundle with 50000 cores in 1100- μm diameter at 4.5- μm pixel center-to-center spacing (FIGH-50-1100N, Fujikura Image Fiber Bundles, Myriad Fiber Imaging, MA). The relayed image near the proximal fiber end is focused to a scientific CMOS sensor (Hamamatsu ORCA-Flash4.0) using a 10X microscope objective lens (Bausch & Lomb Objective, Microscope Central, PA). The FL signal from the collected relayed image is filtered to the sensor with a long pass hard-coated dielectric coating filter at cut-on wavelength at 800 nm (FELH0800, Thorlabs, New Jersey, USA).

For the laser illumination, a 100-mW diode laser with central wavelength at 785 nm (FWHM 3 nm) equipped with a variable beam expansion lens is mounted on a separated arm to illuminate the sample. The position of laser illumination was aimed to cover a rat prostate region with illumination circle of 1 cm. The overall system configuration with the imaging fiber, the laser source, the nerve excitation and ICP monitoring is shown in Figure 6.1.

CHAPTER 6. INTRA-OPERATIVE GUIDING OF THE CAVERNOUS NERVE NETWORK USING NEAR-INFRARED CYANINE VOLTAGE-SENSITIVE DYE

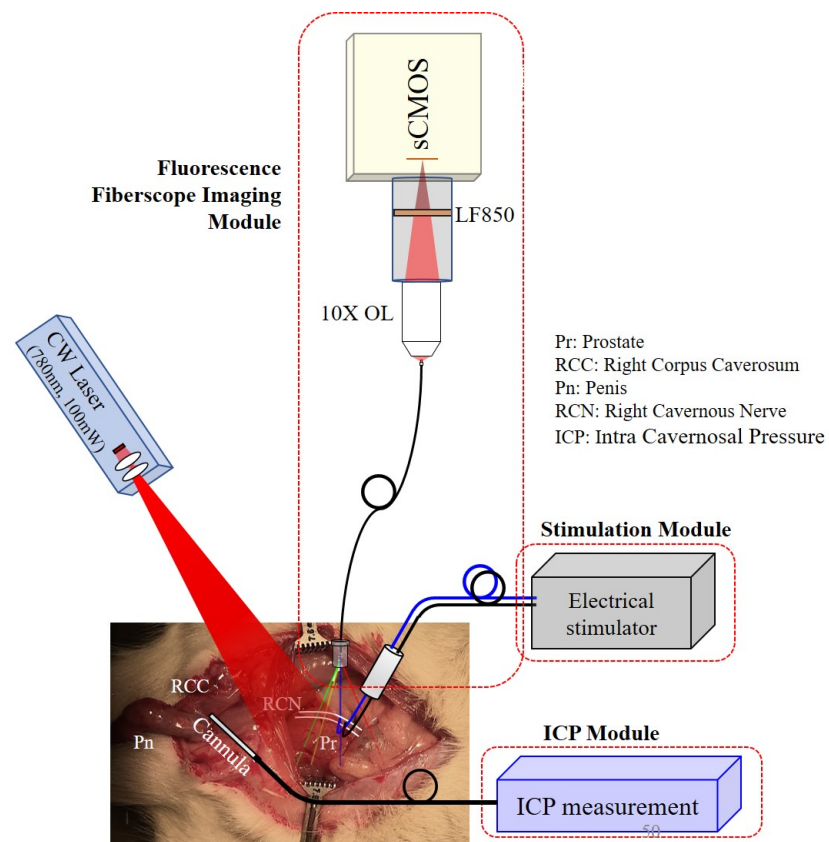


Figure 6.1: Fluorescence fiberscope setup.

CHAPTER 6. INTRA-OPERATIVE GUIDING OF THE CAVERNOUS NERVE NETWORK USING NEAR-INFRARED CYANINE VOLTAGE-SENSITIVE DYE

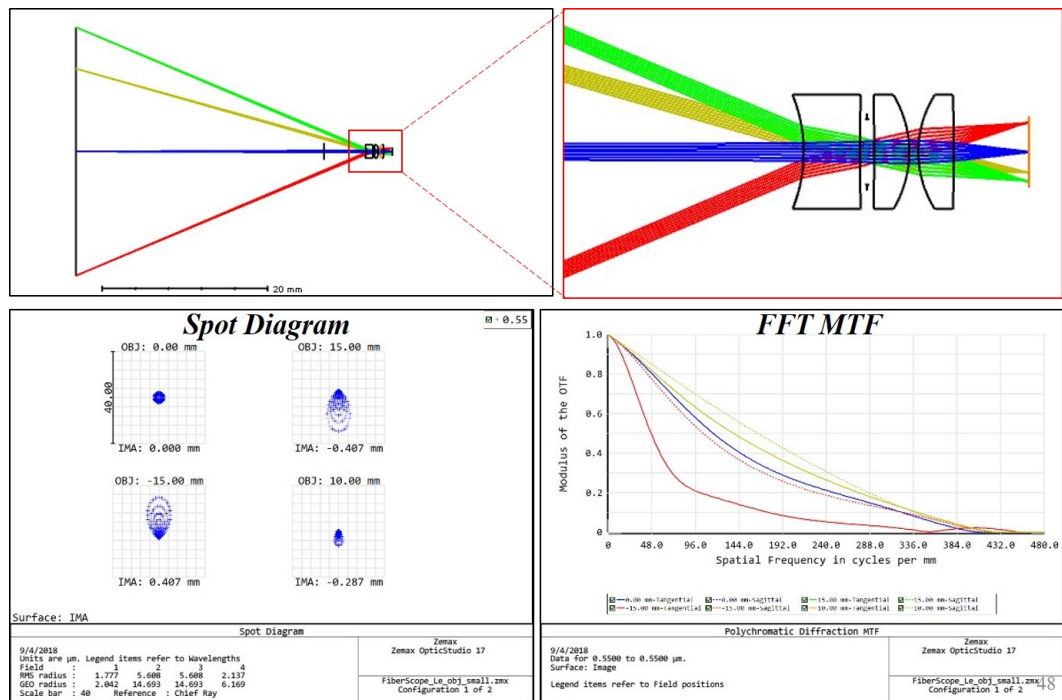


Figure 6.2: Optical design of the focusing assembly for the fiberscope.

The FL frames recorded during the first half minute (0 min – 0.5 min) without any electrical stimulation were averaged to form a reference image. Afterwards, the fractional change of FL emission (F/F_0) was calculated at each pixel and at each time point at each time point to derive the VSD response evoked by electrical stimulation.

6.3.2 Animal preparation

Adult male Sprague-Dawley rats (325-350 g; Charles River Breeding Laboratories, Wilmington, MA, USA) were used. All experiments were approved by the Johns Hopkins University School of Medicine Institutional Animal Care and

CHAPTER 6. INTRA-OPERATIVE GUIDING OF THE CAVERNOUS NERVE NETWORK USING NEAR-INFRARED CYANINE VOLTAGE-SENSITIVE DYE

Use Committee in accordance with the National Institutes of Health Guide for the Care and Use of Laboratory Animals. The rats were anesthetized with intraperitoneal injection of a ketamine (100 mg/kg) and xylazine (5 mg/kg) mixture. The prostate was exposed via a midline abdominal incision, and CNs and MPGs were located bilaterally posterolateral to the prostate.

6.3.3 Electrical CN Stimulation and Intracavernosal

Pressure Monitoring

The ICP measurement validates the erectile function induced by the CN electrical stimulation [176]. Experiments were conducted on rats with and without VSD staining procedures. To monitor ICP, the shaft of the penis was denuded of skin and fascia, and the right crus was punctured with a 23-gauge needle connected via polyethylene-50 tubing to a pressure transducer. For electrically stimulated penile erections, a bipolar electrode attached to a Grass Instruments S48 stimulator (Quincy, MA, USA) was placed on CNs. Stimulation parameters were 4 V, 16 Hz, with square-wave duration of 5 msec for 1 min. ICP was recorded (DI-190, Dataq Instruments, Akron, OH, USA) for 5 min; pre-stimulation (1min), stimulation (1 min), and post-stimulation (3 min). Results were analyzed using the MATLAB program (Mathworks, Natick, MA, USA). At the conclusion of experiments, animals were sacrificed by a lethal intracardiac injection of saturated potassium chloride and prostate, both MPGs, and CNs

CHAPTER 6. INTRA-OPERATIVE GUIDING OF THE CAVERNOUS NERVE NETWORK USING NEAR-INFRARED CYANINE VOLTAGE-SENSITIVE DYE

were collected.

6.3.4 Frozen-section Histopathological Analysis of ex-vivo Rat Prostate Samples

After getting the FL recording, a whole rat prostate was immediately harvested. It was placed in fresh 10 % formalin for more than 48 hours with gentle agitation using a conical rotator. Cryoprotection processing was done via a series of sucrose gradients (15 %, 20 %, 30 % for 12-24 hours each). Prostates was frozen-sectioned at 300 μm thickness. Slides with tissue sections in ProLong Diamond Anti-face mountant were imaged using the LI-COR Odyssey for FL visualization of VSD perfusion.

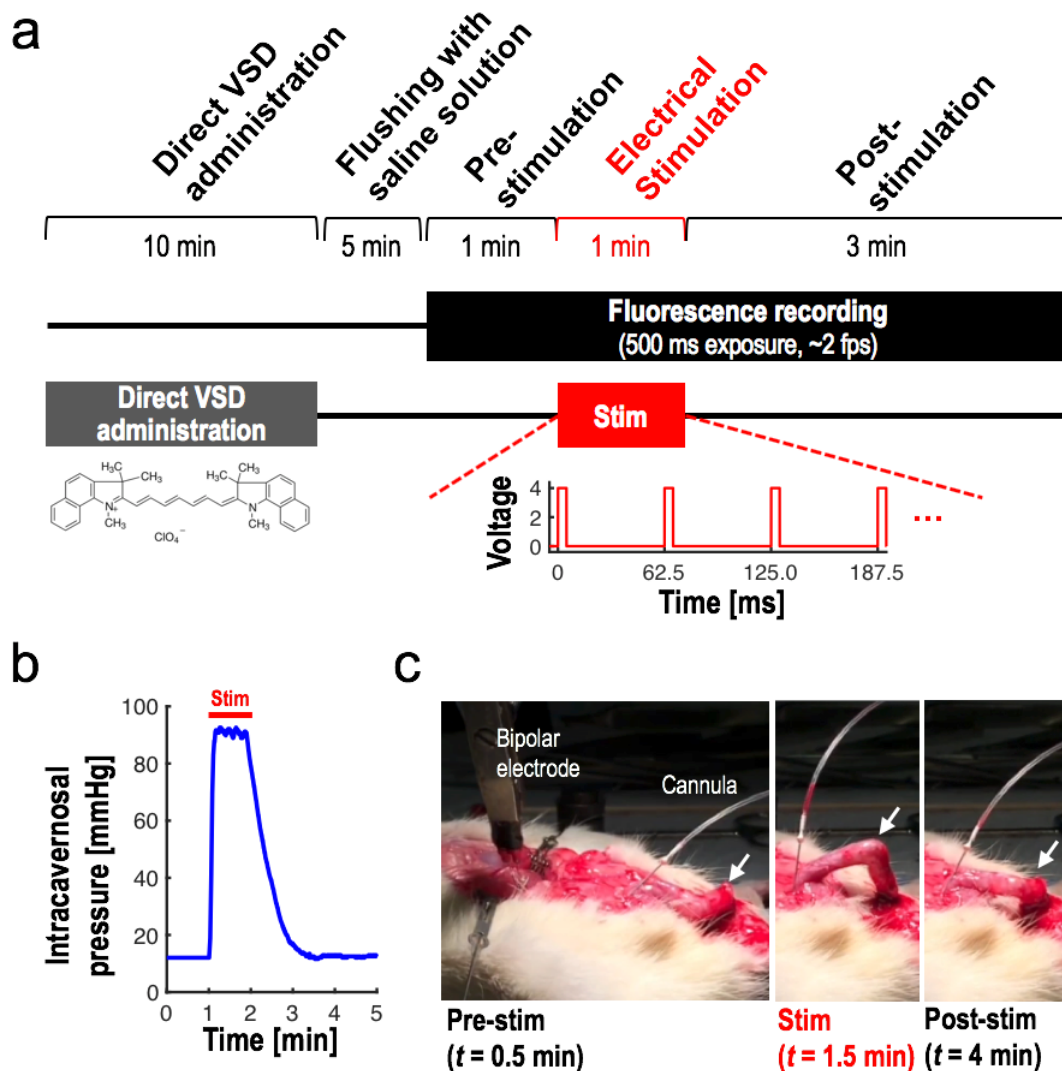
6.4 Experimental Procedure

The subject control and data monitoring is summarized in Figure 6.3 which incorporates the VSD application, administration and flushing with saline, as well as electrical stimulation and ICP monitoring. The 200 μl of 1 mM VSD in DMSO + Cremophore EL solvent was directly administrated to the rat prostate surface for 10 min before starting FL recording. The VSD not bound to the prostate nerve membrane was flushed out for 5 min with 2-ml phosphate buffered saline (PBS) solution. The bipolar electrical stimulation module was

CHAPTER 6. INTRA-OPERATIVE GUIDING OF THE CAVERNOUS NERVE NETWORK USING NEAR-INFRARED CYANINE VOLTAGE-SENSITIVE DYE

connected to the right CN to induce the controlled erectile stimulation upon the electrical pulse excitation: 4-V square-wave pulse for 5 ms at 16 Hz [176]. At the same time, an intracavernosal pressure (ICP) was measured to quantify the blood flow into penis evoked by neurovascular coupling from the stimulation. The FL imaging was conducted for 5 min after the VSD staining procedures onto the rat prostate surface, and stimulation was performed for 1 min (1 min – 2 min) during the image recording 6.3a.

CHAPTER 6. INTRA-OPERATIVE GUIDING OF THE CAVERNOUS NERVE NETWORK USING NEAR-INFRARED CYANINE VOLTAGE-SENSITIVE DYE



CHAPTER 6. INTRA-OPERATIVE GUIDING OF THE CAVERNOUS NERVE NETWORK USING NEAR-INFRARED CYANINE VOLTAGE-SENSITIVE DYE

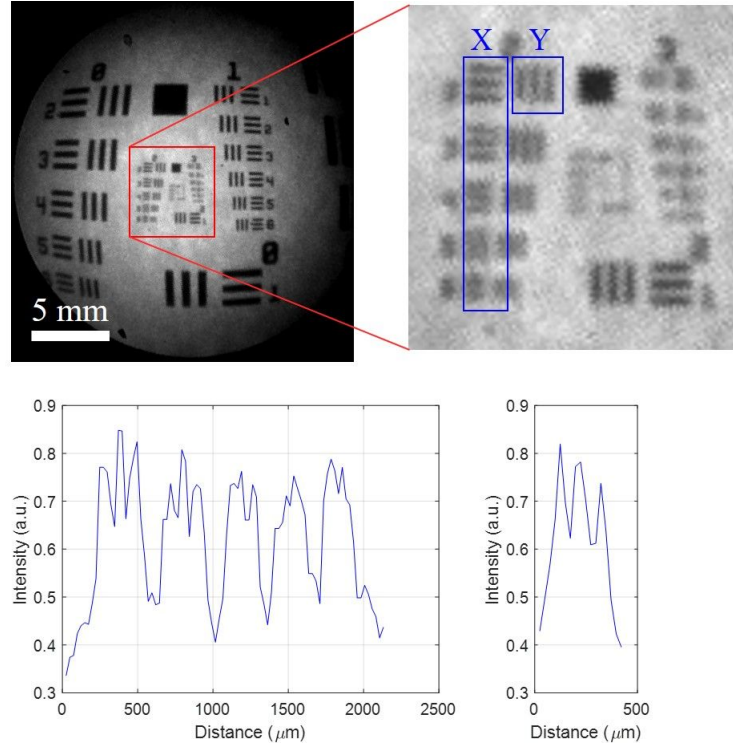


Figure 6.4: Spatial resolution with USAF 1951 Target.

6.5 Results

6.5.1 Imaging System Resolution Evaluation

The spatial resolution of the imaging fiberscope is evaluated using a USAF 1951 Resolution Target (R3L3S1P, Thorlabs, New Jersey, USA) with line pair designed in multiple contrast Group and Element. From Figure B.2, the best resolution of the system along horizontal line (Y ROI) and vertical line (X ROI) is within Group 2, Element 1 and 2, indicating the system spatial resolution is within $111.36 \mu\text{m}$ to $125 \mu\text{m}$.

6.5.2 System Performance for Intra-operative Nerve

Localization within Prostatotomy Setting

Figure 6.5a presents the white-light and FL images obtained from the given FOV on the rat prostate. The right CN (RCN) branched from major pelvic ganglion (MPG) was differentiable in bare eye during the surgery in white-light image, and clear FL emission was detected from the entire prostate surface after performing the direct VSD administration and flushing out procedures. This confirms the successful bounding of VSD at the prostate tissue. Figure 6.5b shows the time-averaged progress of fractional FL intensity change (F/F_0) at each image pixel in pre-stimulation, stimulation, and post-stimulation phases from the reference frame averaged for 0 – 0.5 min duration (across 60 frames). The stimulation phase revealed respectively up to $10.56 \pm 4.14\%$ and $7.04 \pm 4.77\%$ of F/F_0 at the CN and CNB structures with photo-bleaching correction (Figure 6.6).

These results hypothetically represent the chained reaction of nerve network from CN to CNB with different nerve area under stimulation. The slight motion in the ROI was generated potentially by the instantaneous blood volume change as a product of the electrical stimulation, but it was not significant in our validation study (Figure 6.7). The normalized cross-correlation coefficient was calculated from the $4 \times 4 \text{ mm}^2$ ROI indicated by the dotted square in

CHAPTER 6. INTRA-OPERATIVE GUIDING OF THE CAVERNOUS NERVE NETWORK USING NEAR-INFRARED CYANINE VOLTAGE-SENSITIVE DYE

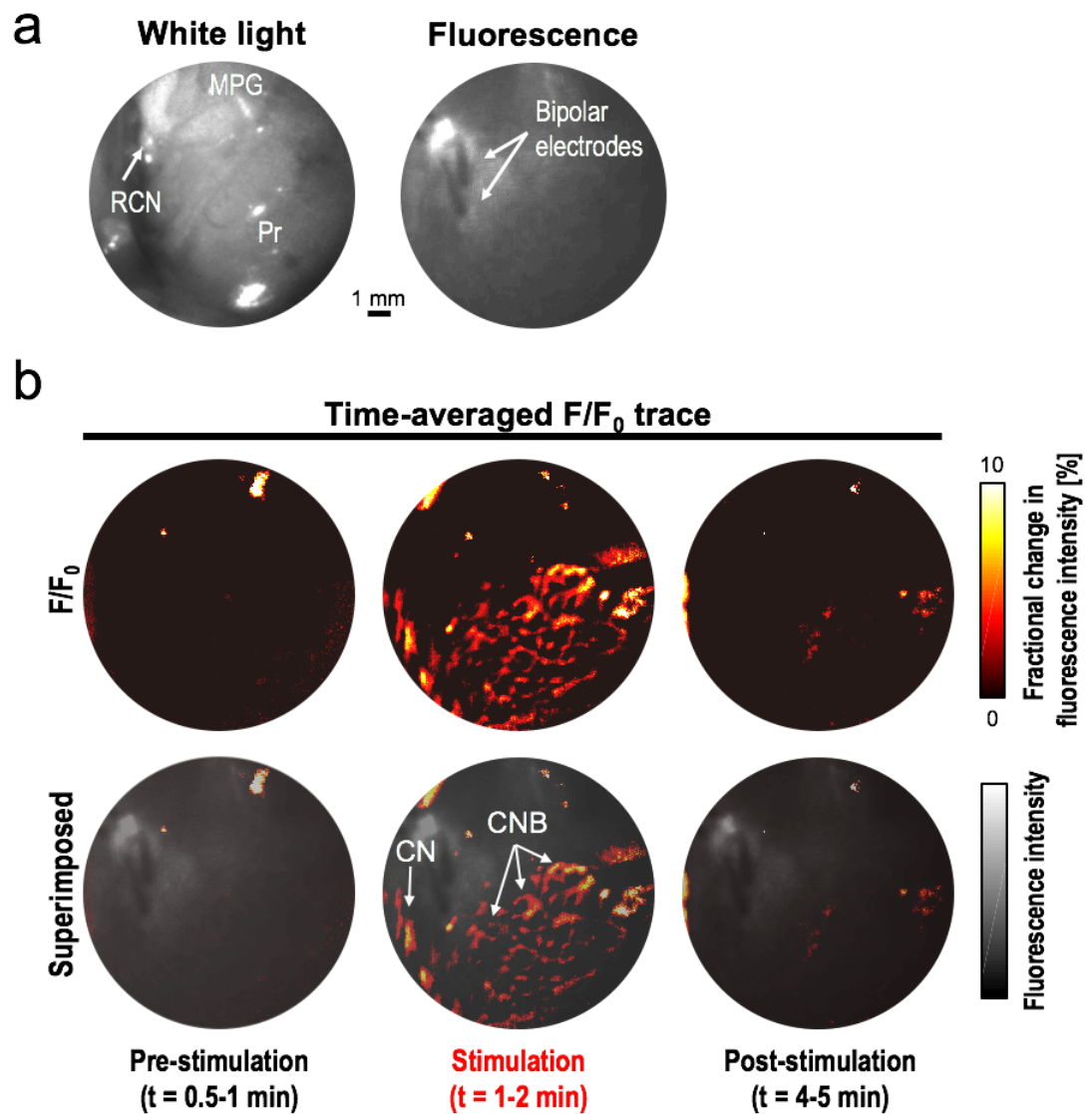


Figure 6.5: In vivo intra-operative nerve localization: (a) white-light and fluorescence (FL) imaging, (b) time-averaged F/F_0 trace during stimulation and pre-/post-stimulation phases. MPG, major pelvic ganglion; RCN, right cavernous nerve; Pr, prostate.

CHAPTER 6. INTRA-OPERATIVE GUIDING OF THE CAVERNOUS NERVE NETWORK USING NEAR-INFRARED CYANINE VOLTAGE-SENSITIVE DYE

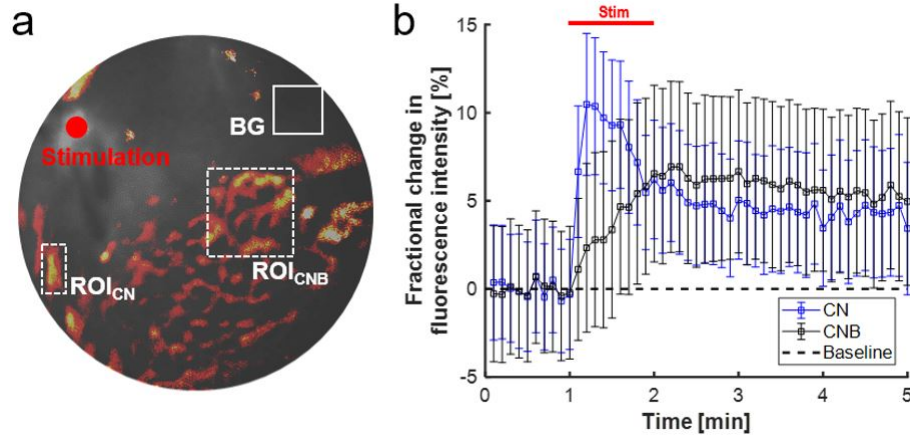


Figure 6.6: Fractional FL intensity change on localized nerve regions: (a) locations of regions-of-interest (ROIs). BG, background; ROICN, CN region; ROICNB, CNB region; (b) the plot of fractional change in FL intensity at each ROI. Note that the plots were corrected by the FL intensity trace quantified at the BG region.

Figure 6.5b. Note that this ROI was selected as it yielded the highest F/F_0 from the prostate surface. From this, the worst correlation coefficient was at 0.979 during the stimulation and post-stimulation phase. This confirms the fractional FL contrast in the ROI was not generated by any structural change over time. In addition, we made a counter-hypothesis that the mean FL intensity in the ROI should be constant regardless of stimulation if the contrast was solely caused by the motion artifacts. However, the global FL intensity in the ROI was increased in the stimulation phase, and restored back to basal level in the post-stimulation phase. This also confirms the fractional contrast was contributed by the VSD redistribution mechanism.

Figure 6.3b shows the trace of ICP value change over time during *in vivo*

CHAPTER 6. INTRA-OPERATIVE GUIDING OF THE CAVERNOUS NERVE NETWORK USING NEAR-INFRARED CYANINE VOLTAGE-SENSITIVE DYE

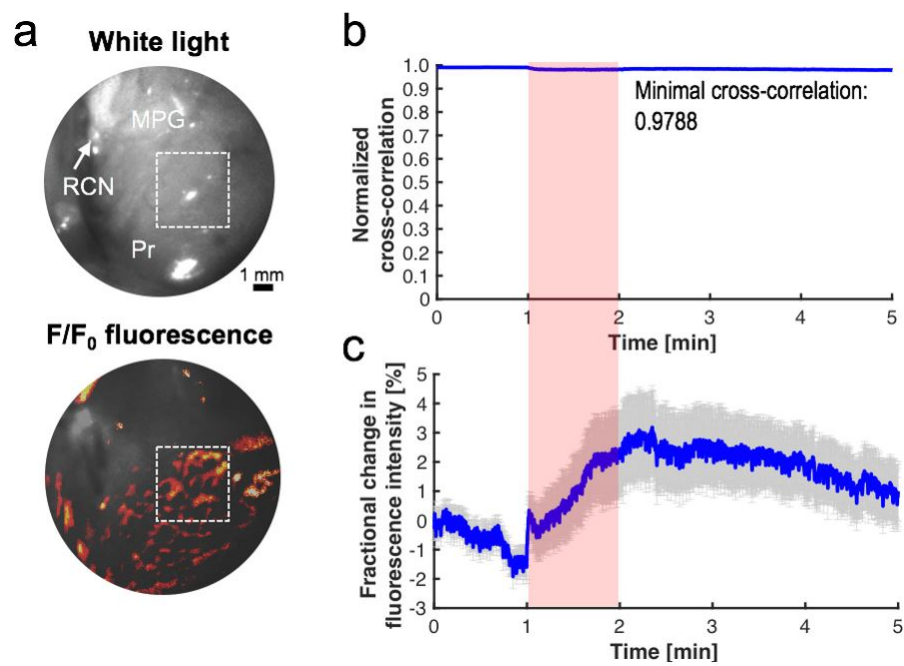


Figure 6.7: Evaluation on motion artifacts during *in vivo* experiment: (a) region-of-interest in white-light and fluorescence (FL) imaging, (b) normalized cross correlation coefficient and (c) fractional change in FL intensity over time at the entire region-of-interest.

CHAPTER 6. INTRA-OPERATIVE GUIDING OF THE CAVERNOUS NERVE NETWORK USING NEAR-INFRARED CYANINE VOLTAGE-SENSITIVE DYE

experiment. The significant ICP increase was detected from the rat with VSD staining when electrical stimulation is induced. Maximal and basal ICP values were 92.60 mmHg and 12.04 mmHg, respectively. On the other hand, the control rat group ($n = 3$) presented comparable level of ICP trace with maximal and basal ICP values at 79.01 ± 8.42 mmHg and 16.37 ± 0.96 mmHg, respectively. This indicates the preserved erectile function despite of the surgical procedures and direct VSD administration with given concentration, staining duration, and flushing procedures, etc. In the post-stimulation phase, the ICP gradually went down to basal level after about 1 min: 12.46 ± 0.32 mmHg. The stimulated erectile function was also validated with the behavioral observation as shown in Figure 6.3c.

The direct VSD staining procedures was validated on rat nerve layer in periprostatic fascia covered by levator fascia from the surface. Frozen-sectioning histopathological analysis was performed to validate the penetration of VSD into the prostate nerve systems with the direct administration protocol proposed. Figure 6.8 presents the white-light and FL microscopic images obtained from prostate slices, and it confirms sufficient VSD staining depth through nerve layer pose between prostate gland and levator fascia whose thickness is few hundreds of μm . The clear round cross-sections of nerve branches were successfully differentiated.

CHAPTER 6. INTRA-OPERATIVE GUIDING OF THE CAVERNOUS NERVE NETWORK USING NEAR-INFRARED CYANINE VOLTAGE-SENSITIVE DYE

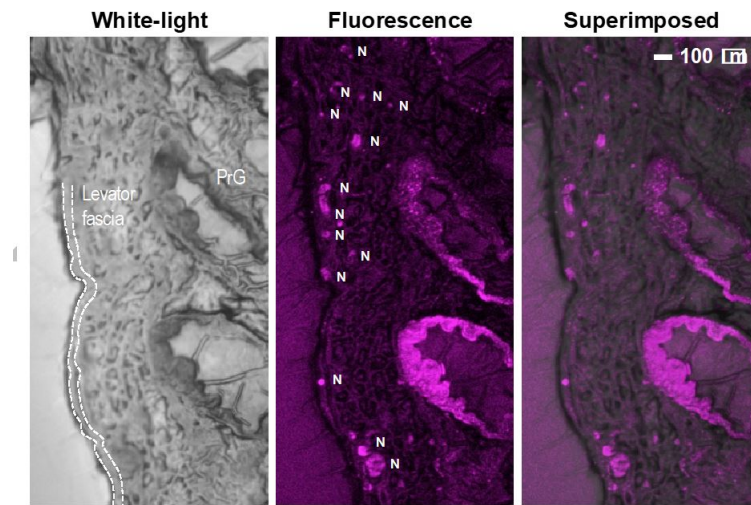


Figure 6.8: Histopathological analysis on *ex vivo* rat prostate sample. Dotted line presents the levator fascia covering the prostatic fascia with CNB. White bar indicates 100 μm . PrG, prostatic gland; N, nerve.

6.6 Lessons Learned

A novel functional nerve-guidance imaging method is proposed to improve current nerve sparing RRP protocol with fluorescence nerve monitoring of nerve network (CN + CNB). The results facilitates FL quenching yield changing VSD mechanism reflecting how much depolarization events happened in the nerve network in response to the stimulation applied on CN. The successful direct VSD administration to nerve layer for 10 min was confirmed by histopathological analysis (Figure 6.8). In a conventional open RRP, prostate is accessed through seminal vesicles, anterior abdominal wall, endopelvic fascia, and periprostatic fat, following by suturing the dorsal venous complex for about 10 min before starting nerve-sparing procedures such as peeling out the prostatic fas-

CHAPTER 6. INTRA-OPERATIVE GUIDING OF THE CAVERNOUS NERVE NETWORK USING NEAR-INFRARED CYANINE VOLTAGE-SENSITIVE DYE

cia with CNB and sided incision detouring CN. Therefore, a 10-min duration for dorsal venous complex suturing should be the time window for VSD staining not to hamper the surgical procedures. This method will be useful for both open and laparoscopic RRP.

Future study should focusing on improving fractional contrast of the VSD in FL emission between polarized and depolarized states, while providing higher absorption coefficient at near-infrared range for better imaging sensitivity. In addition, having more positively-charged electrochemical property with VSD to enhance the staining efficiency as the dye molecules are then more responsive to the membrane potential variation in nerve network. Furthermore, the temporal features of VSD redistribution may be important parameter to understand. The results shown in Figure S2 suggests the different temporal features of VSD redistribution in membrane depolarization and repolarization events during transitions in stimulation and post-stimulation phases, respectively. Therefore, further analysis in VSD characteristics will provide perspectives how it could be optimized to quantify real-time nerve functionality in real time.

The detailed methodology of the direct VSD staining protocol should be further improved to represent more quantitative measure of membrane potential variations. In *in vivo* study shown in this paper, the majority of VSD solution was ran down based on the angle along with the prostate surface, so that only

CHAPTER 6. INTRA-OPERATIVE GUIDING OF THE CAVERNOUS NERVE NETWORK USING NEAR-INFRARED CYANINE VOLTAGE-SENSITIVE DYE

the top part of prostate could have large amount of VSD solution. This might lead to the results in Figure reffig:prostateFL presenting the highest F/F_0 at the center of prostatic region. Therefore, high uniformity in the direct trans-fascia VSD delivery should be obtained in our future study. A patch-based delivery method can be investigated to achieve both fast, uniform VSD delivery and easier translation at the same time.

Photo-acoustic imaging is an emerging hybrid imaging modality providing both optical absorptive contrast and acoustic imaging depth, and also supports versatile imaging scales by microscopic ($5\text{ }\mu\text{m}$ of spatial resolution for up to 2 mm-depth) and tomographic imaging configurations (approximately $800\text{ }\mu\text{m}$ of spatial resolution for up to 7-cm depth) [177–179]. Recently, several PA neuroimaging researches were proposed to quantify membrane potential variations using genetically-encoded calcium indicator or non-radiative voltage sensor [176]. Our previous work have also shown the novel functional PA imaging of membrane potential variation *in vivo* using same cyanine VSD used in this study (i.e., IR780 perchlorate) [180,181]. The study is based on the complementary PA and FL contrast according to the given VSD redistribution mechanism. When in polarized state, the absorbed light energy on VSD aggregates will be more dissipated in form of thermal energy, which will trigger a thermal expansion of the surrounding thermoelastic medium, e.g., water contents or soft tissue. The acoustic energy can be detected by clinical ultrasound transducer

CHAPTER 6. INTRA-OPERATIVE GUIDING OF THE CAVERNOUS NERVE NETWORK USING NEAR-INFRARED CYANINE VOLTAGE-SENSITIVE DYE

posed at transrectal configuration or outside of body. This PA-FL approach can provide complement information for nerve-sparing guidance.

Further translational study may advance the concept of CN stimulation. In the clinical management field of erectile dysfunction, electrical nerve stimulation has been used in general due to its simple and intuitive configuration. However, there is the possibility to cause nerve damage from direct physical contact of electrodes on nerve structures, and the erectile function response is inconsistent, indicating low specificity of this proposed method. Moreover, there have been several studies citing the frequent degradation of parallel recording accuracy with electrical activity [182]. Several promising and safer stimulation methods can be used. A continuous-wave infrared sub-surface optical stimulation method using infrared wavelengths (i.e., 1,490nm and 1,870nm) was successfully used to induce erection in a rat model comparable to that obtained from electrical stimulation. The non-contact configuration on the CN is advantageous in terms of prevention of any physical damage [182–184]. Also, the impact of non-invasive ultrasound stimulation has recently been highlighted with safe acoustic intensity at a localized region with high spatial selectivity [185, 186]. The realization of remote control of erectile function using its deep focusing capability would be enormous to improve the safety for the controlled activation of erection during RRP.

In our future translation, a greater number of rodent animals will be in-

CHAPTER 6. INTRA-OPERATIVE GUIDING OF THE CAVERNOUS NERVE NETWORK USING NEAR-INFRARED CYANINE VOLTAGE-SENSITIVE DYE

cluded based on an improved experimental setup, and the practical CNB contribution to erectile function will be further studied. The extent of the localized nerve damage induced to CNB with various distances from the primary CN will be assessed, and the area of the damage will be controlled based on various techniques [187]. CN stimulation and ICP measurement protocols will be also applied for quantitative evaluation. This investigation will show the extent to which CNB actually contribute to the erectile function in addition to the primary CN.

A translatable model may be considered for our future validation. Even though the current experimental results are encouraging with the rodent animal model, the guidance specification may not be optimal for other larger animal models or humans – In the rat prostate, the fascia layers surrounding the prostate are very thin at around 100 μm of thickness, whereas the human prostatic fascia is much thicker. In practice, variability in fascia thickness should be further evaluated because this factor may substantially affect the trans-fascial FL imaging and effectiveness of the VSD staining procedure. For this investigation, an *ex vivo* human prostate sample with intact levator and periprostatic fascia layers would be used. VSD droplets with various concentrations would be administered on the sample for various durations, and depths of penetration would be recorded with measurements of local sample thickness. FL imaging would be performed to validate the imaging depth, and the

CHAPTER 6. INTRA-OPERATIVE GUIDING OF THE CAVERNOUS NERVE NETWORK USING NEAR-INFRARED CYANINE VOLTAGE-SENSITIVE DYE

VSD-stained depth could be quantified by subsequent histopathological analysis. This study design would serve to optimize the VSD administration scheme as a function of fascia thickness for further translational *in vivo* study using large animal models (e.g., canine, porcine, etc.) and/or a human trial. In the *in vivo* evaluations, the instant calibration of the direct VSD administration setup may be allowed by a local fascia thickness given by pre-operative tomographic imaging with narrow axial resolution (e.g., US, OCT) or by pre-operative imaging (e.g., CT, MRI).

Chapter 7

Concluding Remarks and Future Work

This dissertation details multiple imaging systems and planning strategies for robotic automation in minimally invasive surgeries. Visual localization was improved on current clinical MIS imaging techniques by providing increased 3D accuracy to within 500 μm 3D with dense quantitative point cloud distributions to assess a tissue surface for a 70° field of telescopic view. The overall system accuracy, including taking into account robotic manipulation, is sub-millimeter (300–860 μm) in electro-targeting and cutting kidney tissue. A surgical planning strategy using a multispectral imaging technique spanning from visible to near-infrared (500 nm to 850 nm) illumination is also elaborated to quantify

CHAPTER 7. CONCLUDING REMARKS AND FUTURE WORK

tissue conditions for intraoperative monitoring. A series of *in vivo* and *in vitro* experiments using porcine tissue validated the system for automated robotic surgical manipulation for proper cutting and suturing.

Future work includes rigorous accuracy testing of the surgical robot and of the VIS-NIR surgical planning with dynamic tissue deformations and perfusion conditions in a live animal. Other future work includes registration optimization and increase in the system speed. System registration procedures between the robotic coordinate and the two cameras (or 3D reconstruction and NIR tracking) employs a reference coordination based on the checkerboard position. Although the calibration accuracy between the system is high (80 to 300 μm with a calibration board), this step can be optimized so the calibration of the overall system depends only on the coordinates of one camera. Moreover, current system speed is within 4 fps (four 3D point clouds collected within 1 second). For a significantly increased system speed, fringe extraction from an RGB fringe pattern can be implemented. Future work should explore the relation between the extracted RGB fringe and the 3D accuracy due to endoscopic optical distortions such as chromatic and spherical aberrations.

The triangulation mechanism within the current 3D endoscope creates an angle separation between the two scopes. In operations with limited entrance access, smaller endoscopic housings with rigid scopes or flexible fiber can reduce the number of ports needed for access into the body to one.

Appendix A

Through-skull Vasculature

Assessment Using Fluorescence

Brain Imaging on Murine Models

at Around 800 nm

A.1 Motivation and System Contributions

Understanding the vasculature dynamics within the brain can help facilitate the validation of many areas of pharmaceutical research [188, 189] and of neuroscience applications [190–192]. The phenomenon of photoluminescence is

APPENDIX A. THROUGH-SKULL VASCULATURE ASSESSMENT USING FLUORESCENCE BRAIN IMAGING ON MURINE MODELS AT AROUND 800 NM

widely used to illuminate the brain's vasculature for subsequent imaging a sample of interest [193–195]. In brain imaging, certain sample preparations such as craniotomy, cranial windows or skull-thinning procedures are used to minimize the effect of absorption and scattering from the scalp, cranium, dura matter and fluids. Moreover, to enhance the emission strength from the tagged fluoresce agent, several efforts used carbon-nanotube and quantum dot fluorescent agents, which have longer near-infrared emission capturing windows, during through-skull imaging of murine models. These studies demonstrated the capability of reaching deeper penetration depths [196–199]. Here we contribute a near-infrared fluorescence-based scanning imager design for non-invasive brain imaging of live murine models. The design reduces toxicity of the illuminated light power via a scanning illumination schematic. The vasculature features in the brain are monitored via the inherent photoluminescence of the injected non-toxic indocyanine green fluorescence dye. The system performance was validated and image quality was ascertained using a scientific CMOS (sCMOS) camera operating around 800 nm.

My contributions involved the development of the fluorescence imaging setup, including optical performance evaluation using an accuracy standard and tissue samples for *in vitro* and *in vivo* imaging, the development and execution of the imaging strategy and the collection and analysis of data. The work was published in [172, 200–204].

APPENDIX A. THROUGH-SKULL VASCULATURE ASSESSMENT USING FLUORESCENCE BRAIN IMAGING ON MURINE MODELS AT AROUND 800 NM

A.2 System Setup

As indicated in Figure A.1, the laser-scanning fluorescence imaging system consists of a 780-nm diode laser (70 mW) as the excitation source for the near infrared fluorescence dye. The laser is scanned in horizontal and vertical directions using a 2D galvo system with two Galvo mirror GM1 and GM2 (GVSM002, Thorlabs, New Jersey, USA) and the scanned light is directed through a dichroic mirror (DM) with a cut-off wavelength at 806 nm (DMSP805R, Thorlabs, New Jersey, USA). The excited light absorbed by the target indocyanine green dye (ICG, Sigma Aldrich, Missouri, USA) creates the emittance of fluorescence signal at longer wavelength. This fluorescence at deeper layer in the sample is collected through an emission filter (EM, 850-nm long pass filter (FEL0850, Thorlabs, New Jersey, USA)) and the collected fluorescence is imaged onto a sCMOS sensor (Hamamatsu ORCA-Flash4.0 sCMOS camera) or a CMOS sensor (BasleracA2000-50gmNIR) through an imaging lens (IL). This long pass filter can be alternated with other long-pass filter or band pass filter with cut-on wavelength above 805 nm and covers the emission range of the prepared ICG solution for a desired target of interest. Study with different near-infrared windows for emission capturing at specific layer of interest through scattering media such as mouse brain have been proposed in [199].

APPENDIX A. THROUGH-SKULL VASCULATURE ASSESSMENT USING FLUORESCENCE BRAIN IMAGING ON MURINE MODELS AT AROUND 800 NM

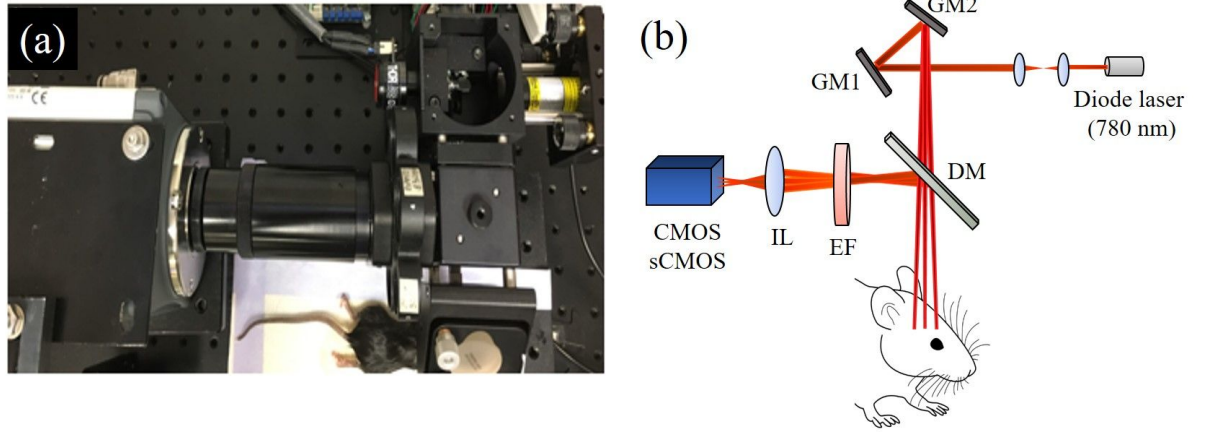


Figure A.1: (a) Near infrared fluorescence imaging setup and (b) its schematic.

A.3 Experimental Procedure

A.3.1 In-vitro Fluorescence Imaging of Indocyanine

Green Agent through Human Cadaver Bone

To validate our setup performance in capturing fluorescence through scattering medium, we designed several phantoms from mixtures of indocyanine green solution, ethanol and glue. The phantom is attached behind a human cadaver temporal bone with an average thickness of 1.75 mm as the fluorescence target for imaging.

APPENDIX A. THROUGH-SKULL VASCULATURE ASSESSMENT USING FLUORESCENCE BRAIN IMAGING ON MURINE MODELS AT AROUND 800 NM

A.3.2 In-vivo Through Skull Brain Fluorescence Imaging in Murine Model

Experiment was carried out in strict accordance with protocol MO14M390 approved by the Animal Care and Use Committee at Johns Hopkins University. A C57BL/6N mouse aged P84 (Charles River) was anaesthetized by i.p. injection of ketamine (100 mg/kg) and xylazine (10 mg/kg). The animal's head is shaved and then placed in a stereotaxic frame on a heating blanket. The respiratory rate and body temperature are monitored every 15 minutes throughout the procedure. Sterile ointment is placed on both eyes. The surgical area is disinfected with three alternating swabs of alcohol and betadine. An incision is made along the midline of the scalp, subcutaneous tissue and periosteum cleaned and removed and skull exposed for imaging. To identify blood vessel in mice brain, ICG powder is reconstituted in saline (10 mg/mL 0.9% NaCl). After the scalp incision, 50 μ L of the prepared ICG solution is injected into the lateral tail vein of the animal. For the vascular monitoring, top-view of the animal's head is imaged right after the injection using the proposed near-infrared imaging setup.

A.4 Image Enhancement Methods

Due to the nature of the scanning imagery and the emission signatures of the tested dye, fluorescence signal is collected and highlighted within the scanned regions under the light illuminated section. The scanning regions covers an area of 12 mm-by-12 mm with each scanning step of 0.63 mm. All scanning image frames are combined by summation to result in the full fluorescence frames as displayed in Figures A.2, A.5, A.6. The signal-to-noise ratio (SNR) in dB is computed as the ratio between the difference of average signal value and the average background value with the root-mean-square of the noise level.

A.5 System Resolution Evaluation

A.5.1 USAS 1951 Resolution Target

We first validate our optical imaging capability by testing the spatial and lateral resolution using a standard positive 1951 USAF test target (R3L3S1P, Thorlabs, New Jersey, USA) and a depth of field target (DOF 5-15, Edmund Optics Inc., New Jersey, USA), respectively. The horizontal and vertical line pattern from group 5, element 1 is recorded in Figure 2 indicating the resolved line width of $15.63\ \mu\text{m}$ and the DOF of the setup is indicated as within 5 mm to 6 mm range (Figure A.3).

APPENDIX A. THROUGH-SKULL VASCULATURE ASSESSMENT USING FLUORESCENCE BRAIN IMAGING ON MURINE MODELS AT AROUND 800 NM

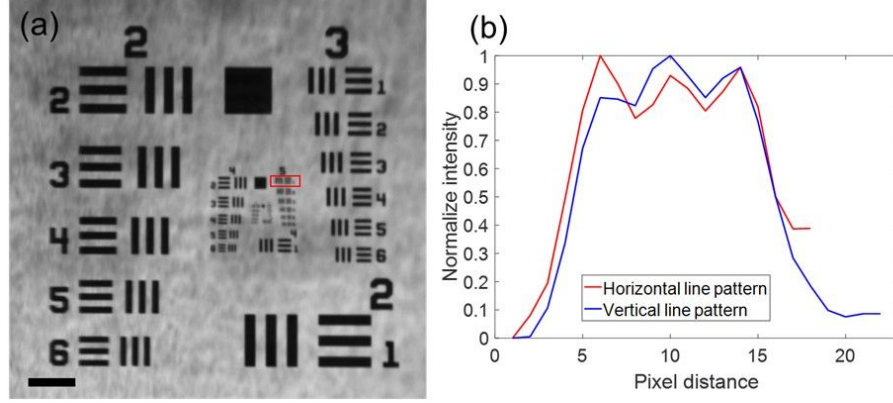


Figure A.2: (a) Reflectance image of a USAF resolution target, scale bar indicates 2 mm length (b) The intensity profiles along the lines indicated in red box in (a).

A.5.2 Through-Skull Fluorescence Imaging

Next, we experimented fluorescence imaging through a cadaver human temporal bone. Inasmuch as a high signal-to-noise ratio is essential in low light and strongly diffusive systems, such as through-bone imaging, we also conducted a comparison study between a standard and a highly sensitive CMOS sensor in detecting ICG signal through a human head bone (Figures A.5). The results indicate apparent features of the ICG phantoms behind the bone for both sensor types. When the phantoms are placed behind the skull, due to the highly scattering nature of the skull, the images became highly diffusive. This effect can be enhanced by using an iterative procedure such as the Richardson- Lucy deconvolution or a highly sensitive sCMOS sensor improve the SNR of the image. The SNR captured using a CMOS and enhanced by the deconvolution method in Figure A.4 was calculated as an increase from 18.55 dB to 28.48 dB;

APPENDIX A. THROUGH-SKULL VASCULATURE ASSESSMENT USING FLUORESCENCE BRAIN IMAGING ON MURINE MODELS AT AROUND 800 NM

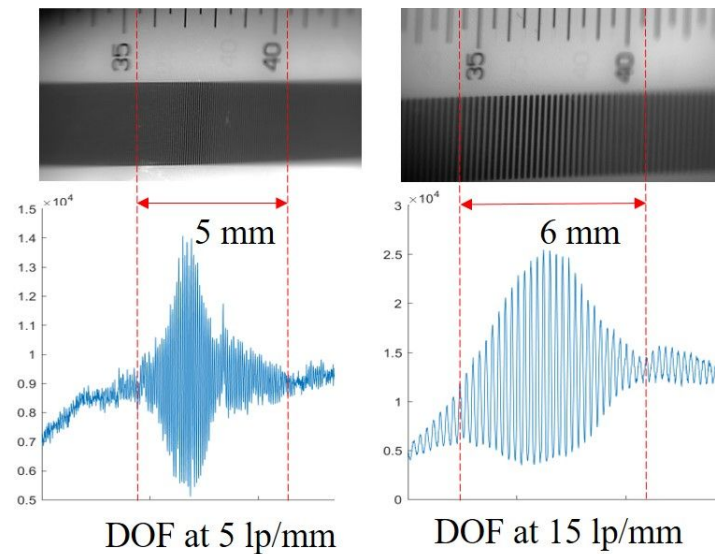


Figure A.3: Depth of field of the setup at two line set at frequency of 5 and 15 line pairs per millimeter.

and the SNR improvement using a sCMOS camera as indicated in Figure A.5 is increased from 22.45 dB to 37.37 dB.

The imaging system is next validated with alive murine head imaging without removing the skull bone. From Figure A.6, fluorescence from murine brain vessel is visible through skin and skull intact, with clear contrast of the vessel network. The imaging enables certain drug effect on the brain vessel such as the blood-brain-barrier opening effect cause by Lexiscan when injecting to the animal. From Figure A.7, the diffusion of the fluorescence agent is apparent compared to the dye concentration around the suture head lines without Lexiscan injection.

APPENDIX A. THROUGH-SKULL VASCULATURE ASSESSMENT USING FLUORESCENCE BRAIN IMAGING ON MURINE MODELS AT AROUND 800 NM

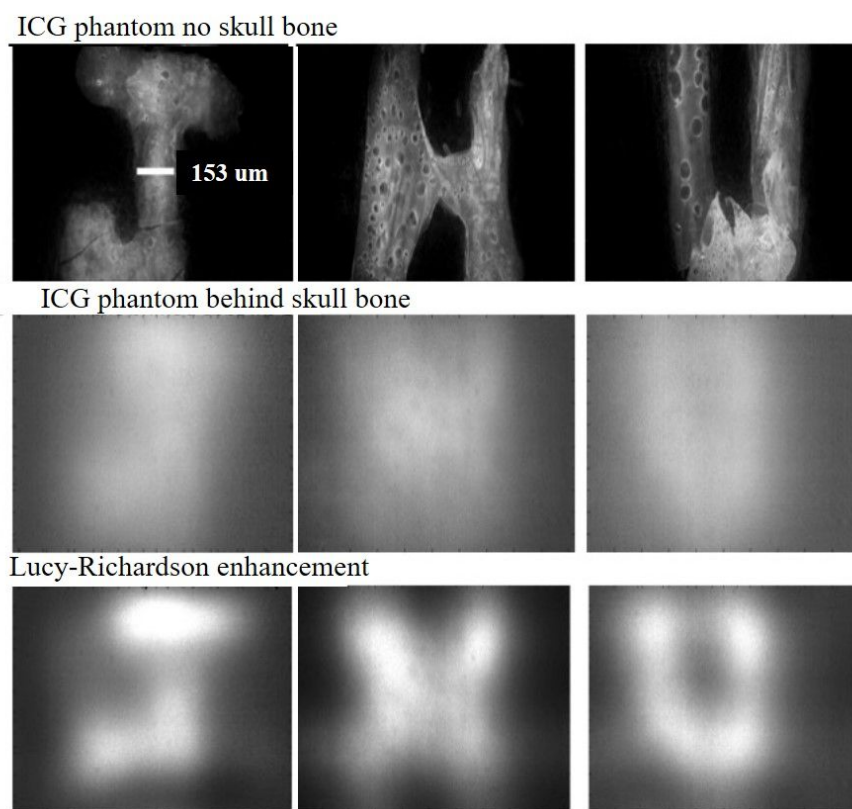
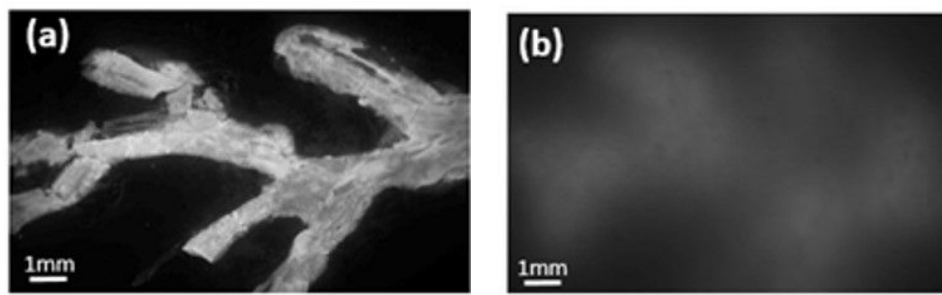


Figure A.4: Fluorescence imaging of ICG phantom using a CMOS camera and its post processing using Lucy Richardson deconvolution method.

A.5.3 Monitoring of Nano Particle Diffusion within Brain

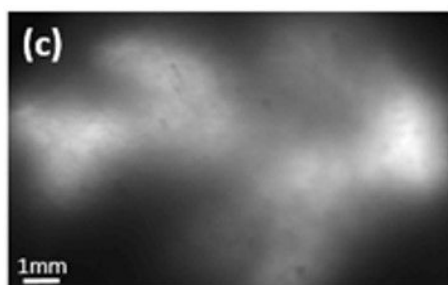
Other dye encapsulation method such as in polymer nano-particles enables drug delivery with desired localization and concentration. The fluorescence imaging system can be used to monitor the lifetime of the dye-encapsulated nano particle. The nanoparticle was prepared with the concentration of 0.8 mg of IR780 dye in 1 mL nanoparticle suspension. An amount of 20 μL of this mixture is injected in the right hemisphere section as indicated in Figure A.8. The drill depth is measured within 0.2 mm. This concentration (IR780-NP1

APPENDIX A. THROUGH-SKULL VASCULATURE ASSESSMENT USING FLUORESCENCE BRAIN IMAGING ON MURINE MODELS AT AROUND 800 NM



(a) ICG fluorescence image without human cadaver bone

(b) ICG fluorescence image behind the human cadaver bone using a regular CMOS sensor.



(c) ICG fluorescence image behind the human cadaver bone using a scientific CMOS sensor.

Figure A.5: Sensitivity comparison between a regular and a scientific CMOS cameras through human cadaver bone. Both cameras use the same capturing setting of 400 ms for exposure time, or relatively 2.5 frames per second.

0.8 mg/mL) is used due to its high relative fluorescence strength compared to other higher dye concentration (IR780-NP1 5.9 mg/mL) and the conventional ICG dye (0.5 mg/mL) (Figure A.9).

As indicated in Figure A.10, the dye-encapsulated nanoparticle distribution is expanded until 4 days after the initial injection. The increase in fluorescence intensity throughout the days shows the dye distribution is sparse, making the fluorescence quenching is easier compared to earlier day when dye particles

APPENDIX A. THROUGH-SKULL VASCULATURE ASSESSMENT USING FLUORESCENCE BRAIN IMAGING ON MURINE MODELS AT AROUND 800 NM

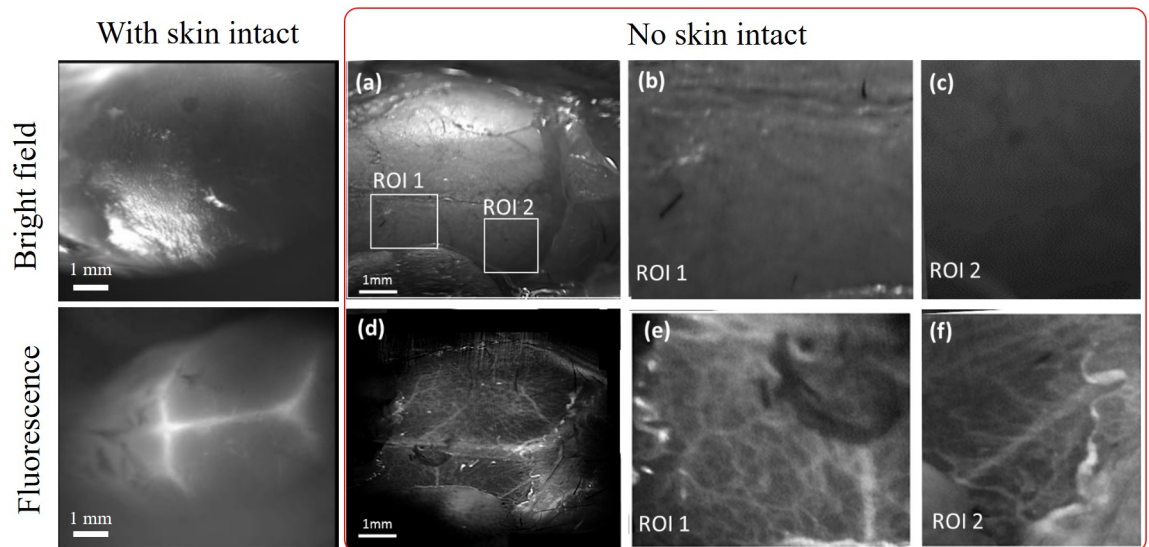


Figure A.6: Upper row: White reflectance images of (a) an exposed mice skull with indicated ROIs and (b, c) their corresponding zoom-in regions for ROI 1 and ROI 2. Lower row: Fluorescence images of mice vascular structures after ICG injection (d) corresponding to (a) and (e, f) corresponding to (b, c) for ROI 1 and ROI 2, respectively.

accumulated within a smaller volume. To quantify the increase of dye fluorescence, which related to the sparse distribution at the later day, relative intensity along the horizontal and vertical axes of the collected fluorescence image is displayed in Figure A.11.

APPENDIX A. THROUGH-SKULL VASCULATURE ASSESSMENT USING FLUORESCENCE BRAIN IMAGING ON MURINE MODELS AT AROUND 800 NM

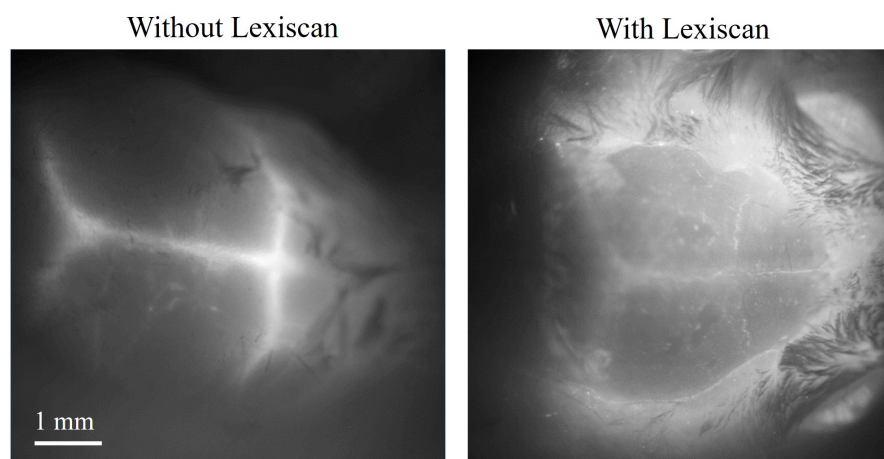


Figure A.7: Preliminary test of Lexiscan effect in ICG dye diffusion.

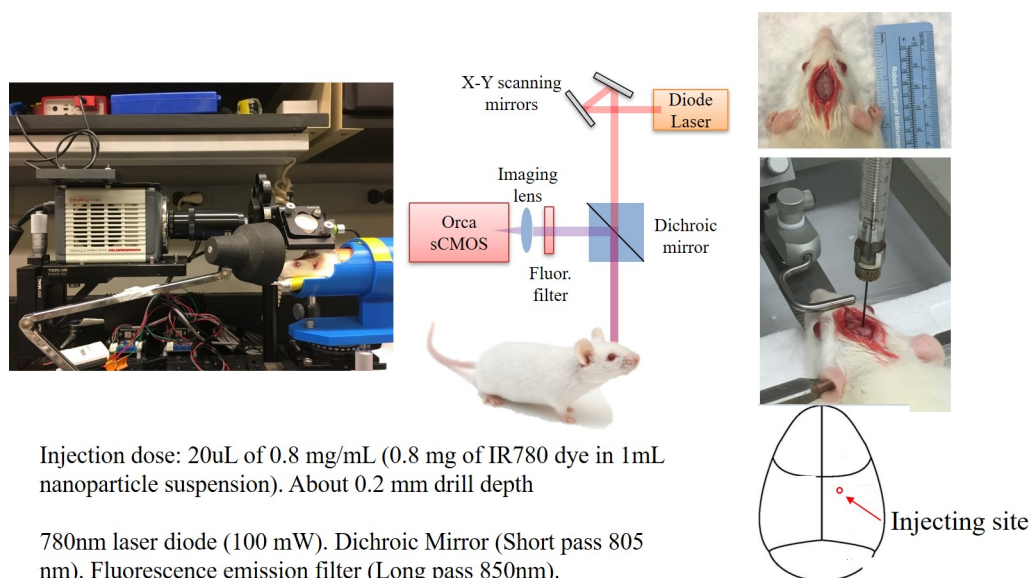


Figure A.8: System Setup and Sample Preparation.

APPENDIX A. THROUGH-SKULL VASCULATURE ASSESSMENT USING FLUORESCENCE BRAIN IMAGING ON MURINE MODELS AT AROUND 800 NM

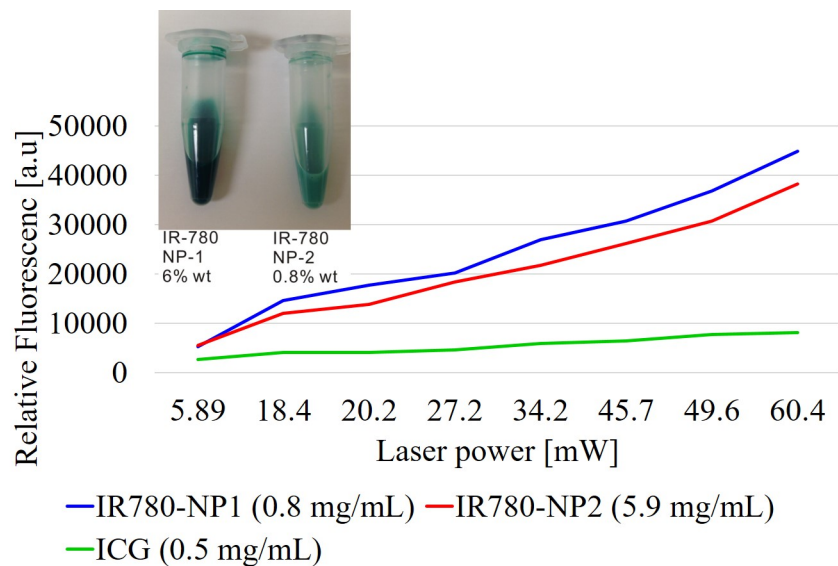


Figure A.9: Comparison of fluorescence strength under multiple excitation levels.

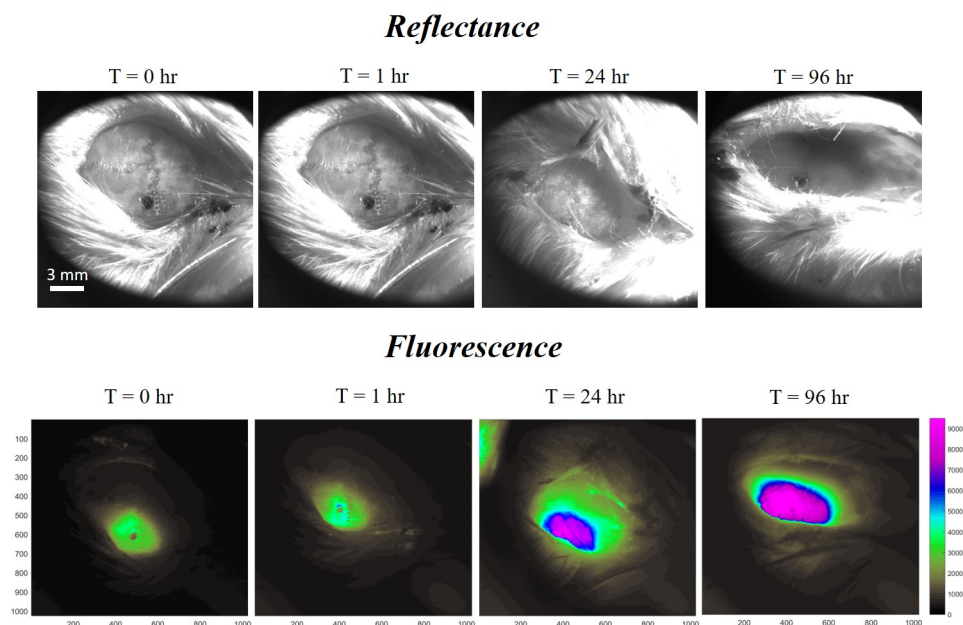


Figure A.10: The nano particle diffusivity monitoring.

APPENDIX A. THROUGH-SKULL VASCULATURE ASSESSMENT USING FLUORESCENCE BRAIN IMAGING ON MURINE MODELS AT AROUND 800 NM

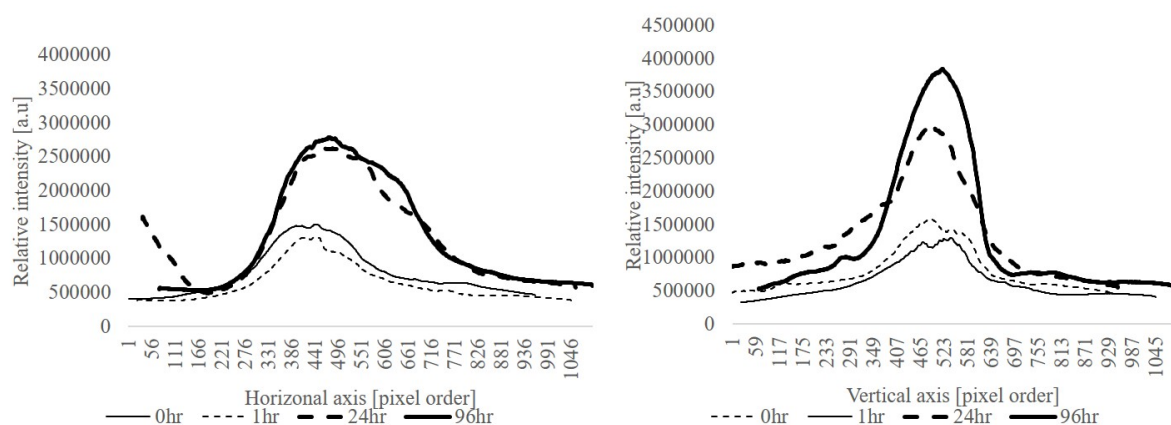


Figure A.11: Horizontal and vertical intensity profiles for particle diffusivity comparison.

A.6 Lessons Learned

Fluorescence imaging through scattering media such as skull bone successfully demonstrated using both in *in vitro* and *in vivo* experiments on murine model. This confirms the ability to minimize the invasive sample preparations such as craniotomy, cranial windows or skull-thinning procedures while maintaining an adequate brain imaging quality. The proposed setup utilizing the scanning scheme of a laser diode, which induces a highly concentrated power of laser circular beam with diameter of 2 mm, however, prolongs the imaging collection time. A high power light emitting diode for a single-shot capturing of the fluorescence event is possible to assist the real-time monitoring of vasculature dynamic and neural circuit functions in the brain. The imaging system enables multiple observations of the vasculature structures as well as the studies of drug effects or nano particle distribution within murine model through the collected fluorescence quantification without opening the skull.

Appendix B

Real-time intra-operative Guidance using a Dual Photoacoustic and Pulsed Fluorescence Imaging for Robotic Assisted Surgery

B.1 Motivation and System Contributions

Multimodal systems have offered medical advantages, such as complimentary information and higher layers of medical diagnostics. It is most beneficial to critical medical applications in which traditional imaging cannot distinguish tissue type well, such as in prostatectomy surgery, where the differentiation between cancerous tumor and the cavernous nerve is acute. This work reports a real-time multimodal imaging system for assisting prostatectomy using the combination of fluorescence imaging (FL) with photoacoustic imaging (PA). My contribution includes designing and building the fluorescence system setup and combining it with the PA imaging modality. I also collected and analyzed imaging data. The work proposed in this section resulted in publications in [180, 181].

B.2 System Setup

The system consists of a pulsed laser light generated from a second-harmonic Nd:YAG laser-pumped optical parametric oscillator system (Phocus Inline, Opotek Inc., USA). The laser pulse focused at 200 mm is delivered to a target through the dual-axis scanning galvo system (GVS 012, Thorlabs, Inc., USA). For each light delivery, the PA pixel data were collected by the transrectal ultrasound

APPENDIX B. REAL-TIME INTRA-OPERATIVE GUIDANCE USING A DUAL PHOTOACOUSTIC AND PULSED FLUORESCENCE IMAGING FOR ROBOTIC ASSISTED SURGERY

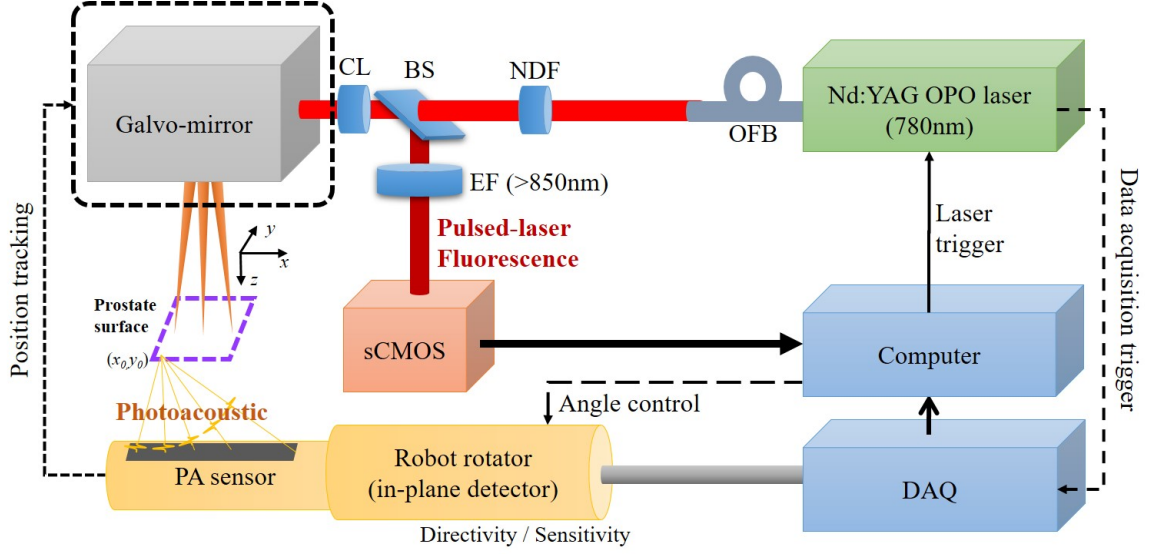


Figure B.1: System diagram of a dual fluorescence-photoacoustic imaging. CL: Convex Lens, BS: Beam Splitter, NDF: Neutral Density Filter, OFB: Optical Fiber Bundle, DAQ: Data Acquisition Card, EF: Emission Filter.

array transducer (BPL9-5/55, Ultrasonix Corp., Canada) connected to ultrasound research package (SonixDAQ), while the emitted fluorescence selectively captured by scientific CMOS camera (ORCA-Flash 4.0 V2, Hamamatsu K. K., Japan) through the dichroic mirror (805 nm) and emission filter (λ 830 nm). The system was validated using an acoustic tissue-mimicking phantoms mixed with indocyanine green for spectral absorption at 780 nm and emission at around 830 nm.

APPENDIX B. REAL-TIME INTRA-OPERATIVE GUIDANCE USING A DUAL PHOTOACOUSTIC AND PULSED FLUORESCENCE IMAGING FOR ROBOTIC ASSISTED SURGERY

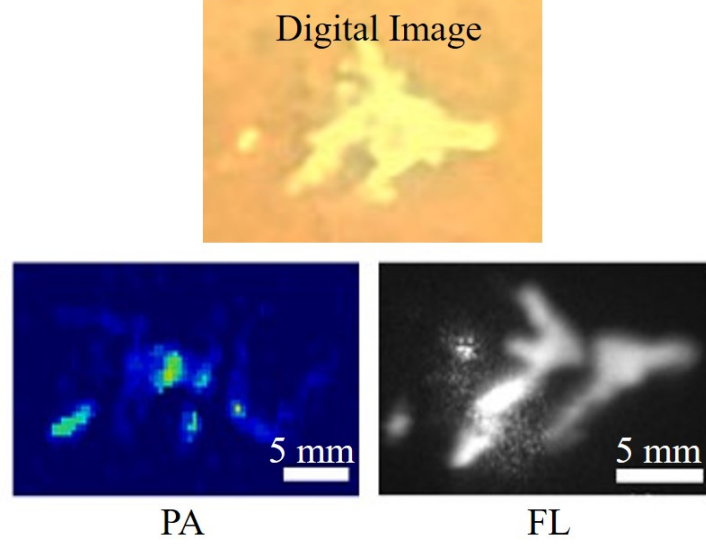


Figure B.2: System sensitivity comparison between PA and FL imaging of an ICG phantom.

B.3 Imaging Sensitivity on an ICG

Fluorescence Phantom

At 20 Hz, we recorded a maximum intensity projection (MAP) of both PA and the corresponding FL images on ex-vivo experiments using the designed phantoms. Further in-vivo experiments on bovine model will be conducted to support the clinical significance of the system specifically in the navigation for prostatectomy and ovarian cancer surgeries.

Bibliography

- [1] Olympus. Origin of endoscopes. [Online]. Available: <https://www.olympus-global.com/brand/museum/endo/>
- [2] N. Instrument. Parts of a stereo vision system. [Online]. Available: http://zone.ni.com/reference/en-XX/help/372916T-01/nivisionconcepts/stereo_parts_of_a_stereo_vision_system/
- [3] Z. Wang, H. Du, S. Park, and H. Xie, “Three-dimensional shape measurement with a fast and accurate approach,” *Applied optics*, vol. 48, no. 6, pp. 1052–1061, 2009.
- [4] Justin D. Opfermann, S. Leonard, R. S. Decker, N. A. Uebele, C. E. Bayne, A. S. Joshi, and A. Krieger, “Autonomous Electrosurgery for Tumor Resection Using a Multi-Degree of Freedom Electrosurgical Tool and Visual Servoing,” in *Proceedings of the 2017 IEEE/RSJ International Conference on Intelligent Robots and Systems*, 2017.
- [5] P. Kazanzides, G. Fichtinger, G. D. Hager, A. M. Okamura, L. L. Whit-

BIBLIOGRAPHY

- comb, and R. H. Taylor, “Surgical and interventional robotics-core concepts, technology, and design [tutorial],” *IEEE Robotics & Automation Magazine*, vol. 15, no. 2, 2008.
- [6] G. Fichtinger, P. Kazanzides, A. M. Okamura, G. D. Hager, L. L. Whitcomb, and R. H. Taylor, “Surgical and interventional robotics: Part ii,” *IEEE Robotics & Automation Magazine*, vol. 15, no. 3, 2008.
- [7] G. D. Hager, A. M. Okamura, P. Kazanzides, L. L. Whitcomb, G. Fichtinger, and R. H. Taylor, “Surgical and interventional robotics: part iii: surgical assistance systems,” *IEEE robotics & automation magazine / IEEE Robotics & Automation Society*, vol. 15, no. 4, p. 84, 2008.
- [8] D. Hu, Y. Gong, B. Hannaford, and E. J. Seibel, “Path planning for semi-automated simulated robotic neurosurgery,” in *Intelligent Robots and Systems (IROS), 2015 IEEE/RSJ International Conference on*. IEEE, 2015, pp. 2639–2645.
- [9] A. Shademan, R. S. Decker, J. D. Opfermann, S. Leonard, A. Krieger, and P. C. W. Kim, “Supervised autonomous robotic soft tissue surgery,” *Science Translational Medicine*, vol. 8, no. 337, pp. 337ra64–337ra64, May 2016.
- [10] L. Joskowicz and R. H. Taylor, “Computers in imaging and guided

BIBLIOGRAPHY

- surgery,” *Computing in Science & Engineering*, vol. 3, no. 5, pp. 65–72, 2001.
- [11] U. Wiesel, A. Lahmer, M. Tenbusch, and M. Borner, “Total knee replacement using the robodoc system,” in *Proc. 1st Annu. Meeting CAOS Int*, 2001, p. 88.
- [12] R. H. Taylor, L. Joskowicz, B. Williamson, A. Guéziec, A. Kalvin, P. Kazanzides, R. Van Vorhis, J. Yao, R. Kumar, A. Bzostek *et al.*, “Computer-integrated revision total hip replacement surgery: concept and preliminary results,” *Medical image analysis*, vol. 3, no. 3, pp. 301–319, 1999.
- [13] D. Stoianovici, L. L. Whitcomb, J. H. Anderson, R. H. Taylor, and L. R. Kavoussi, “A modular surgical robotic system for image guided percutaneous procedures,” in *International Conference on Medical Image Computing and Computer-Assisted Intervention*. Springer, 1998, pp. 404–410.
- [14] R. C. Susil, J. H. Anderson, and R. H. Taylor, “A single image registration method for ct guided interventions,” in *International Conference on Medical Image Computing and Computer-Assisted Intervention*. Springer, 1999, pp. 798–808.
- [15] K. Masamune, “Development of ct-paky frame system-ct image guided

BIBLIOGRAPHY

- needle puncturing manipulator and a single slice registration for urological surgery,” in *Proc. 8th annual meeting of JSCAS. Kyoto. 1999*, 1999.
- [16] I. S. Inc. [Online]. Available: <https://www.intuitive.com/en/products-and-services>
- [17] U. Hagn, R. Konietzschke, A. Tobergte, M. Nickl, S. Jörg, B. Kübler, G. Passig, M. Gröger, F. Fröhlich, U. Seibold *et al.*, “Dlr mirosurge: a versatile system for research in endoscopic telesurgery,” *International journal of computer assisted radiology and surgery*, vol. 5, no. 2, pp. 183–193, 2010.
- [18] M. J. Lum, D. C. Friedman, G. Sankaranarayanan, H. King, K. Fodero, R. Leuschke, B. Hannaford, J. Rosen, and M. N. Sinanan, “The raven: Design and validation of a telesurgery system,” *The International Journal of Robotics Research*, vol. 28, no. 9, pp. 1183–1197, 2009.
- [19] J. Ruurda, I. Broeders, B. Pulles, F. Kappelhof, and C. Van der Werken, “Manual robot assisted endoscopic suturing: time-action analysis in an experimental model,” *Surgical endoscopy and other interventional techniques*, vol. 18, no. 8, pp. 1249–1252, 2004.
- [20] P. Štádler, L. Dvůráček, P. Vitásek, and P. Matouš, “The application of robotic surgery in vascular medicine,” *Innovations: Technology and Tech-*

BIBLIOGRAPHY

- niques in Cardiothoracic and Vascular Surgery*, vol. 7, no. 4, pp. 247–253, 2012.
- [21] M. Salman, T. Bell, J. Martin, K. Bhuva, R. Grim, and V. Ahuja, “Use, cost, complications, and mortality of robotic versus nonrobotic general surgery procedures based on a nationwide database,” *The American surgeon*, vol. 79, no. 6, pp. 553–560, 2013.
- [22] J. Troccaz, M. Peshkin, and B. Davies, “The use of localizers, robots and synergistic devices in cas,” in *CVRMed-MRCAS’97*. Springer, 1997, pp. 725–736.
- [23] P. J. Berkelman, D. L. Rothbaum, J. Roy, S. Lang, L. L. Whitcomb, G. Hager, P. S. Jensen, E. De Juan, R. H. Taylor, and J. K. Niparko, “Performance evaluation of a cooperative manipulation microsurgical assistant robot applied to stapedotomy,” in *International Conference on Medical Image Computing and Computer-Assisted Intervention*. Springer, 2001, pp. 1426–1429.
- [24] H. Mayer, I. Nagy, A. Knoll, E. U. Schirmbeck, and R. Bauernschmitt, “The endo [pa] r system for minimally invasive robotic surgery,” in *Intelligent Robots and Systems, 2004.(IROS 2004). Proceedings. 2004 IEEE/RSJ International Conference on*, vol. 4. IEEE, 2004, pp. 3637–3642.

BIBLIOGRAPHY

- [25] H. Mayer, F. Gomez, D. Wierstra, I. Nagy, A. Knoll, and J. Schmidhuber, “A system for robotic heart surgery that learns to tie knots using recurrent neural networks,” *Advanced Robotics*, vol. 22, no. 13-14, pp. 1521–1537, 2008.
- [26] A. Murali, S. Sen, B. Kehoe, A. Garg, S. McFarland, S. Patil, W. D. Boyd, S. Lim, P. Abbeel, and K. Goldberg, “Learning by observation for surgical subtasks: Multilateral cutting of 3d viscoelastic and 2d orthotropic tissue phantoms,” in *Robotics and Automation (ICRA), 2015 IEEE International Conference on*. IEEE, 2015, pp. 1202–1209.
- [27] S. McKinley, A. Garg, S. Sen, D. V. Gealy, J. P. McKinley, Y. Jen, and K. Goldberg, “Autonomous multilateral surgical tumor resection with interchangeable instrument mounts and fluid injection device,” in *2016 IEEE International Conference on Robotics and Automation (ICRA)*, 2016.
- [28] B. Jaffray, “Minimally invasive surgery,” *Archives of disease in childhood*, vol. 90, no. 5, pp. 537–542, 2005.
- [29] C. W. B. Peng, W. M. Yue, S. Y. Poh, W. Yeo, and S. B. Tan, “Clinical and radiological outcomes of minimally invasive versus open transforaminal lumbar interbody fusion,” *Spine*, vol. 34, no. 13, pp. 1385–1389, 2009.

BIBLIOGRAPHY

- [30] C. Nezhat, *Nezhat's History of Endoscopy: A Historical Analysis of Endoscopy's Ascension Since Antiquity*. CNezhatMD, 2011.
- [31] P. Rathert, W. Lutzeyer, and W. E. Goddwin, "Philipp bozzini (1773–1809) and the lichtleiter," *Urology*, vol. 3, no. 1, pp. 113–118, 1974.
- [32] A. K. Saxena and M. E. Höllwarth, *Essentials of pediatric endoscopic surgery*. Springer Science & Business Media, 2008.
- [33] J. Bhatt, A. Jones, S. Foley, Z. Shah, P. Malone, D. Fawcett, and S. Kumar, "Harold horace hopkins: a short biography," *BJU international*, vol. 106, no. 10, pp. 1425–1428, 2010.
- [34] M. J. Zinner and S. W. Ashley, *Maingot's abdominal operations*. McGraw Hill Professional, 2012.
- [35] T. H. Tomkinson, J. L. Bentley, M. K. Crawford, C. J. Harkrider, D. T. Moore, and J. L. Rouke, "Rigid endoscopic relay systems: a comparative study," *Applied optics*, vol. 35, no. 34, pp. 6674–6683, 1996.
- [36] S. Dobson and H. Hopkins, "A new rod-lens relay system offering improved image quality," *Journal of Physics E: Scientific Instruments*, vol. 22, no. 7, p. 450, 1989.
- [37] S. S. Gambhir, "Molecular imaging of cancer with positron emission tomography," *Nature Reviews Cancer*, vol. 2, no. 9, p. 683, 2002.

BIBLIOGRAPHY

- [38] V. Hartung-Knemeyer, K. J. Beiderwellen, C. Buchbender, H. Kuehl, T. C. Lauenstein, A. Bockisch, and T. D. Poeppel, “Optimizing positron emission tomography image acquisition protocols in integrated positron emission tomography/magnetic resonance imaging,” *Investigative radiology*, vol. 48, no. 5, pp. 290–294, 2013.
- [39] G. H. Glover, “Overview of functional magnetic resonance imaging,” *Neurosurgery Clinics*, vol. 22, no. 2, pp. 133–139, 2011.
- [40] R. H. Silverman, “High-resolution ultrasound imaging of the eye—a review,” *Clinical & experimental ophthalmology*, vol. 37, no. 1, pp. 54–67, 2009.
- [41] B. W. Pogue, M. Testorf, T. McBride, U. Osterberg, and K. Paulsen, “Instrumentation and design of a frequency-domain diffuse optical tomography imager for breast cancer detection,” *Optics express*, vol. 1, no. 13, pp. 391–403, 1997.
- [42] J. C. Hebden and T. Austin, “Optical tomography of the neonatal brain,” *European radiology*, vol. 17, no. 11, p. 2926, 2007.
- [43] M. Ferrari and V. Quaresima, “A brief review on the history of human functional near-infrared spectroscopy (fnirs) development and fields of application,” *Neuroimage*, vol. 63, no. 2, pp. 921–935, 2012.

BIBLIOGRAPHY

- [44] D. A. Boas, A. M. Dale, and M. A. Franceschini, “Diffuse optical imaging of brain activation: approaches to optimizing image sensitivity, resolution, and accuracy,” *Neuroimage*, vol. 23, pp. S275–S288, 2004.
- [45] P. Patel, N. V. Patel, and S. F. Danish, “Intracranial mr-guided laser-induced thermal therapy: single-center experience with the visualase thermal therapy system,” *Journal of neurosurgery*, vol. 125, no. 4, pp. 853–860, 2016.
- [46] J. H. Siewerdsen, “Cone-beam ct with a flat-panel detector: From image science to image-guided surgery,” *Nuclear Instruments and Methods in Physics Research Section A: Accelerators, Spectrometers, Detectors and Associated Equipment*, vol. 648, pp. S241–S250, 2011.
- [47] H. B. van der Zwaan, W. A. Helbing, J. S. McGhie, M. L. Geleijnse, S. E. Luijnenburg, J. W. Roos-Hesselink, and F. J. Meijboom, “Clinical value of real-time three-dimensional echocardiography for right ventricular quantification in congenital heart disease: validation with cardiac magnetic resonance imaging,” *Journal of the American Society of Echocardiography*, vol. 23, no. 2, pp. 134–140, 2010.
- [48] R. M. Schols, N. J. Connell, and L. P. Stassen, “Near-infrared fluorescence imaging for real-time intraoperative anatomical guidance in minimally

BIBLIOGRAPHY

- invasive surgery: a systematic review of the literature,” *World journal of surgery*, vol. 39, no. 5, pp. 1069–1079, 2015.
- [49] F. Ris, R. Hompes, C. Cunningham, I. Lindsey, R. Guy, O. Jones, B. George, R. A. Cahill, and N. J. Mortensen, “Near-infrared (nir) perfusion angiography in minimally invasive colorectal surgery,” *Surgical endoscopy*, vol. 28, no. 7, pp. 2221–2226, 2014.
- [50] S. J. Monteith, S. Harnof, R. Medel, B. Popp, M. Wintermark, M. B. S. Lopes, N. F. Kassell, W. J. Elias, J. Snell, M. Eames *et al.*, “Minimally invasive treatment of intracerebral hemorrhage with magnetic resonance-guided focused ultrasound,” *Journal of neurosurgery*, vol. 118, no. 5, pp. 1035–1045, 2013.
- [51] M. Ahmed, L. Solbiati, C. L. Brace, D. J. Breen, M. R. Callstrom, J. W. Charboneau, M.-H. Chen, B. I. Choi, T. De Baère, G. D. Dodd III *et al.*, “Image-guided tumor ablation: standardization of terminology and reporting criteria—a 10-year update,” *Journal of Vascular and Interventional Radiology*, vol. 25, no. 11, pp. 1691–1705, 2014.
- [52] M. P. Fronheiser, J. Whitman, N. M. Ivancevich, and S. W. Smith, “P6d-3 3-d ultrasound guidance of surgical robotics: Autonomous guidance and catheter transducers,” in *Ultrasonics Symposium, 2007. IEEE*. IEEE, 2007, pp. 2527–2530.

BIBLIOGRAPHY

- [53] K. Liang, E. D. Light, A. J. Rogers, D. Von Allmen, and S. W. Smith, “3-d ultrasound guidance of autonomous surgical robotics: Feasibility studies,” in *Ultrasonics Symposium (IUS), 2009 IEEE International*. IEEE, 2009, pp. 582–585.
- [54] A. Krupa, “Automatic calibration of a robotized 3d ultrasound imaging system by visual servoing,” in *Robotics and Automation, 2006. ICRA 2006. Proceedings 2006 IEEE International Conference on*. IEEE, 2006, pp. 4136–4141.
- [55] A. Krupa, G. Fichtinger, and G. D. Hager, “Full motion tracking in ultrasound using image speckle information and visual servoing,” in *Robotics and Automation, 2007 IEEE International Conference on*. IEEE, 2007, pp. 2458–2464.
- [56] A. Marano, F. Priora, L. M. Lenti, F. Ravazzoni, R. Quarati, and G. Spinoglio, “Application of fluorescence in robotic general surgery: review of the literature and state of the art,” *World journal of surgery*, vol. 37, no. 12, pp. 2800–2811, 2013.
- [57] G. Spinoglio, F. Priora, P. P. Bianchi, F. S. Lucido, A. Licciardello, V. Maglione, F. Grosso, R. Quarati, F. Ravazzoni, and L. M. Lenti, “Real-time near-infrared (nir) fluorescent cholangiography in single-site

BIBLIOGRAPHY

- robotic cholecystectomy (ssrc): a single-institutional prospective study,” *Surgical endoscopy*, vol. 27, no. 6, pp. 2156–2162, 2013.
- [58] R. Speich, B. Saesseli, U. Hoffmann, K. A. Neftel, and J. Reichen, “Anaphylactoid reactions after indocyanine-green administration,” *Annals of internal medicine*, vol. 109, no. 4, pp. 345–346, 1988.
- [59] Novadaq. [Online]. Available: <http://novadaq.com/products/pinpoint-endoscopic-fluorescence-imaging-system-spy-fluorescence-imaging/>
- [60] K. Storz. [Online]. Available: <https://www.karlstorz.com/hk/en/nir-icg-near-infrared-fluorescence.htm>
- [61] I. Surgical. [Online]. Available: <https://intuitivesurgical.com/company/media/images/firefly.html>
- [62] G. Dogangil, B. Davies, and F. Rodriguez y Baena, “A review of medical robotics for minimally invasive soft tissue surgery,” *Proceedings of the Institution of Mechanical Engineers, Part H: Journal of Engineering in Medicine*, vol. 224, no. 5, pp. 653–679, 2010.
- [63] P. Modi, A. Hassan, and W. R. Chitwood Jr, “Minimally invasive mitral valve surgery: a systematic review and meta-analysis,” *European Journal of Cardio-Thoracic Surgery*, vol. 34, no. 5, pp. 943–952, 2008.

BIBLIOGRAPHY

- [64] P. Breedveld, H. Stassen, D. Meijer, and L. Stassen, "Theoretical background and conceptual solution for depth perception and eye-hand coordination problems in laparoscopic surgery," *Minimally invasive therapy & allied technologies*, vol. 8, no. 4, pp. 227–234, 1999.
- [65] B. M. Ure, J. F. Kuebler, N. Schukfeh, C. Engelmann, J. Dingemann, and C. Petersen, "Survival with the native liver after laparoscopic versus conventional kasai portoenterostomy in infants with biliary atresia: a prospective trial," *Annals of surgery*, vol. 253, no. 4, pp. 826–830, 2011.
- [66] Y. S. Tanagho, G. L. Andriole, A. G. Paradis, K. M. Madison, G. S. Sandhu, J. E. Varela, and B. M. Benway, "2d versus 3d visualization: impact on laparoscopic proficiency using the fundamentals of laparoscopic surgery skill set," *Journal of Laparoendoscopic & Advanced Surgical Techniques*, vol. 22, no. 9, pp. 865–870, 2012.
- [67] L. G. Svensson, F. A. Atik, D. M. Cosgrove, E. H. Blackstone, J. Rajeswaran, G. Krishnaswamy, U. Jin, A. M. Gillinov, B. Griffin, J. L. Navia *et al.*, "Minimally invasive versus conventional mitral valve surgery: a propensity-matched comparison," *The Journal of Thoracic and Cardiovascular Surgery*, vol. 139, no. 4, pp. 926–932, 2010.
- [68] D. Stoyanov, "Stereoscopic scene flow for robotic assisted minimally inva-

BIBLIOGRAPHY

- sive surgery,” in *International Conference on Medical Image Computing and Computer-Assisted Intervention*. Springer, 2012, pp. 479–486.
- [69] D. Stoyanov, M. V. Scarzanella, P. Pratt, and G.-Z. Yang, “Real-time stereo reconstruction in robotically assisted minimally invasive surgery,” in *International Conference on Medical Image Computing and Computer-Assisted Intervention*. Springer, 2010, pp. 275–282.
- [70] P.-L. Chang, D. Stoyanov, A. J. Davison *et al.*, “Real-time dense stereo reconstruction using convex optimisation with a cost-volume for image-guided robotic surgery,” in *International Conference on Medical Image Computing and Computer-Assisted Intervention*. Springer, 2013, pp. 42–49.
- [71] J. Penne, K. Höller, M. Stürmer, T. Schrauder, A. Schneider, R. Engelbrecht, H. Feußner, B. Schmauss, and J. Hornegger, “Time-of-flight 3-d endoscopy,” in *International Conference on Medical Image Computing and Computer-Assisted Intervention*. Springer, 2009, pp. 467–474.
- [72] A. Groch, A. Seitel, S. Hempel, S. Speidel, R. Engelbrecht, J. Penne, K. Höller, S. Röhl, K. Yung, S. Bodenstedt *et al.*, “3d surface reconstruction for laparoscopic computer-assisted interventions: comparison of state-of-the-art methods,” in *Medical Imaging 2011: Visualization*,

BIBLIOGRAPHY

- Image-Guided Procedures, and Modeling*, vol. 7964. International Society for Optics and Photonics, 2011, p. 796415.
- [73] P. Fürsattel, S. Placht, M. Balda, C. Schaller, H. Hofmann, A. Maier, and C. Riess, “A comparative error analysis of current time-of-flight sensors,” *IEEE Transactions on Computational Imaging*, vol. 2, no. 1, pp. 27–41, 2016.
- [74] T. Georgiev and A. Lumsdaine, “The multifocus plenoptic camera,” in *Digital Photography VIII*, vol. 8299. International Society for Optics and Photonics, 2012, p. 829908.
- [75] V. Boominathan, K. Mitra, and A. Veeraraghavan, “Improving resolution and depth-of-field of light field cameras using a hybrid imaging system,” in *Computational Photography (ICCP), 2014 IEEE International Conference on*. IEEE, 2014, pp. 1–10.
- [76] C. Perwass and L. Wietzke, “Single lens 3d-camera with extended depth-of-field,” in *Human Vision and Electronic Imaging XVII*, vol. 8291. International Society for Optics and Photonics, 2012, p. 829108.
- [77] R. Decker, A. Shademan, J. Opfermann, S. Leonard, P. C. Kim, and A. Krieger, “Performance evaluation and clinical applications of 3d plenoptic cameras,” in *Next-Generation Robotics II; and Machine Intel-*

BIBLIOGRAPHY

- ligence and Bio-inspired Computation: Theory and Applications IX*, vol. 9494. International Society for Optics and Photonics, 2015, p. 94940B.
- [78] T. Georgiev, Z. Yu, A. Lumsdaine, and S. Goma, “Lytro camera technology: theory, algorithms, performance analysis,” in *Multimedia Content and Mobile Devices*, vol. 8667. International Society for Optics and Photonics, 2013, p. 86671J.
- [79] H. N. Le, R. Decker, J. Opferman, P. Kim, A. Krieger, and J. U. Kang, “3-d endoscopic imaging using plenoptic camera,” in *CLEO: Applications and Technology*. Optical Society of America, 2016, pp. AW4O–2.
- [80] J. Han, L. Shao, D. Xu, and J. Shotton, “Enhanced computer vision with microsoft kinect sensor: A review,” *IEEE transactions on cybernetics*, vol. 43, no. 5, pp. 1318–1334, 2013.
- [81] K. Khoshelham and S. O. Elberink, “Accuracy and resolution of kinect depth data for indoor mapping applications,” *Sensors*, vol. 12, no. 2, pp. 1437–1454, 2012.
- [82] J. Smisek, M. Jancosek, and T. Pajdla, “3d with kinect,” in *Consumer depth cameras for computer vision*. Springer, 2013, pp. 3–25.
- [83] N. T. Clancy, D. Stoyanov, L. Maier-Hein, A. Groch, G.-Z. Yang, and D. S. Elson, “Spectrally encoded fiber-based structured lighting probe for in-

BIBLIOGRAPHY

- traoperative 3d imaging,” *Biomedical Optics Express*, vol. 2, no. 11, pp. 3119–3128, 2011.
- [84] N. T. Clancy, D. Stoyanov, G.-Z. Yang, and D. S. Elson, “An endoscopic structured lighting probe using spectral encoding,” in *European Conference on Biomedical Optics*. Optical Society of America, 2011, p. 809002.
- [85] C. Albitar, P. Graebbling, and C. Doignon, “Robust structured light coding for 3d reconstruction,” in *Computer Vision, 2007. ICCV 2007. IEEE 11th International Conference on*. IEEE, 2007, pp. 1–6.
- [86] C. Schmalz, F. Forster, A. Schick, and E. Angelopoulou, “An endoscopic 3d scanner based on structured light,” *Medical image analysis*, vol. 16, no. 5, pp. 1063–1072, 2012.
- [87] J. Laloš, M. Mrak, U. Pavlovčič, and M. Jezeršek, “Handheld optical system for skin topography measurement using fourier transform profilometry,” *Strojniški vestnik-Journal of Mechanical Engineering*, vol. 61, no. 5, pp. 285–291, 2015.
- [88] J. Yagnik, G. S. Siva, K. Ramakrishnan, and L. K. Rao, “3d shape extraction of human face in presence of facial hair: A profilometric approach,” in *TENCON 2005 2005 IEEE Region 10*. IEEE, 2005, pp. 1–5.
- [89] T. Hain, R. Eckhardt, K. Kunzi-Rapp, and B. Schmitz, “Indications for

BIBLIOGRAPHY

- optical shape measurements in orthopaedics and dermatology,” *Medical Laser Application*, vol. 17, no. 1, p. 55, 2002.
- [90] P. F. Gomes, M. Sesselmann, C. D. Faria, P. A. Araújo, and L. F. Teixeira-Salmela, “Measurement of scapular kinematics with the moiré fringe projection technique,” *Journal of biomechanics*, vol. 43, no. 6, pp. 1215–1219, 2010.
- [91] C. Liu, L. Chen, X. He, V. D. Thang, and T. Kofidis, “Coaxial projection profilometry based on speckle and fringe projection,” *Optics Communications*, vol. 341, pp. 228–236, 2015.
- [92] H. Fuchs, M. A. Livingston, R. Raskar, K. Keller, J. R. Crawford, P. Rademacher, S. H. Drake, A. A. Meyer *et al.*, “Augmented reality visualization for laparoscopic surgery,” in *International Conference on Medical Image Computing and Computer-Assisted Intervention*. Springer, 1998, pp. 934–943.
- [93] J. D. Ackerman, K. Keller, and H. Fuchs, “Surface reconstruction of abdominal organs using laparoscopic structured light for augmented reality,” in *Three-Dimensional Image Capture and Applications V*, vol. 4661. International Society for Optics and Photonics, 2002, pp. 39–47.
- [94] L. Chen, V. Bavigadda, T. Kofidis, and R. D. Howe, “Fiber optic projection-

BIBLIOGRAPHY

- imaging system for shape measurement in confined space,” *The Scientific World Journal*, vol. 2014, 2014.
- [95] C. Ohrt, M. Kästner, and E. Reithmeier, “Endoscopic geometry inspection by modular fiber optic sensors with increased depth of focus,” in *Optical Measurement Systems for Industrial Inspection VII*, vol. 8082. International Society for Optics and Photonics, 2011, p. 808215.
- [96] —, “High resolution measurements of fligree, inner geometries with endoscopic micro fringe projection,” in *Optical Measurement Systems for Industrial Inspection VIII*, vol. 8788. International Society for Optics and Photonics, 2013, p. 878817.
- [97] I. Merta, L. Jaroszewicz, and S. Swillo, “Simple method of the 3-d shape measurement by system of fibre-optic fringe projection,” in *Optical Fibers: Applications*, vol. 5952. International Society for Optics and Photonics, 2005, p. 59521S.
- [98] H. N. Le, H. Nguyen, Z. Wang, J. Opfermann, S. Leonard, A. Krieger, and J. Kang, “An endoscopic 3d structured illumination imaging system for robotic anastomosis surgery (conference presentation),” in *Advanced Biomedical and Clinical Diagnostic and Surgical Guidance Systems XVI*, vol. 10484. International Society for Optics and Photonics, 2018, p. 104840C.

BIBLIOGRAPHY

- [99] H. N. Le, H. Nguyen, Z. Wang, J. Opfermann, S. Leonard, A. Krieger, and J. U. Kang, “Demonstration of a laparoscopic structured-illumination three-dimensional imaging system for guiding reconstructive bowel anastomosis,” *Journal of Biomedical Optics*, vol. 23, no. 5, p. 056009, 2018.
- [100] H. N. Le, H. Nguyen, Z. Wang, and J. U. Kang, “A demonstration of structured-illumination-based technique using commercial surgical endoscope,” in *Lasers and Electro-Optics (CLEO), 2017 Conference on*. IEEE, 2017, pp. 1–2.
- [101] —, “3d endoscopic imaging using structured illumination technique (conference presentation),” in *Advanced Biomedical and Clinical Diagnostic and Surgical Guidance Systems XV*, vol. 10054. International Society for Optics and Photonics, 2017, p. 1005416.
- [102] H. N. Le, R. Decker, A. Krieger, and J. U. Kang, “Experimental assessment of a 3-d plenoptic endoscopic imaging system,” *Chinese Optics Letters*, vol. 15, no. 5, p. 051701, 2017.
- [103] J. U. Kang and H. N. Le, “Compact endoscope design for three-dimensional surgical guidance,” Feb. 15 2018, uS Patent App. 15/674,553.
- [104] N. Instruments. 3d imaging with ni labview. [Online]. Available: <https://www.olympus-global.com/brand/museum/endo/>

BIBLIOGRAPHY

- [105] R. Rao. Stereo and 3d vision. [Online]. Available: <https://courses.cs.washington.edu/courses/cse455/09wi/Lects/lect16.pdf>
- [106] H. Nguyen, Z. Wang, and J. Quisberth, “Accuracy comparison of fringe projection technique and 3d digital image correlation technique,” in *Advancement of Optical Methods in Experimental Mechanics, Volume 3*. Springer, 2016, pp. 195–201.
- [107] A. Shademan, R. S. Decker, J. Opfermann, S. Leonard, P. C. Kim, and A. Krieger, “Plenoptic cameras in surgical robotics: Calibration, registration, and evaluation,” in *Robotics and Automation (ICRA), 2016 IEEE International Conference on*. IEEE, 2016, pp. 708–714.
- [108] C. Heinze, S. Spyropoulos, S. Hussmann, and C. Perwass, “Automated robust metric calibration algorithm for multifocus plenoptic cameras,” *IEEE Transactions on Instrumentation and Measurement*, vol. 65, no. 5, pp. 1197–1205, 2016.
- [109] O. Johannsen, C. Heinze, B. Goldluecke, and C. Perwaß, “On the calibration of focused plenoptic cameras,” in *Time-of-Flight and Depth Imaging. Sensors, Algorithms, and Applications*. Springer, 2013, pp. 302–317.
- [110] M. Vo, Z. Wang, B. Pan, and T. Pan, “Hyper-accurate flexible calibration technique for fringe-projection-based three-dimensional imaging,” *Optics Express*, vol. 20, no. 15, pp. 16 926–16 941, 2012.

BIBLIOGRAPHY

- [111] J. Schwiegerling, *Optical specification, fabrication, and testing*. SPIE Press, 2014.
- [112] M. MYLES JOYCE, K. J. SWEENEY, J. GERARD, and M. GERAGHTY, “Techniques of bowel resection and anastomosis,” *CME*, vol. 7, pp. 284–289, 2002.
- [113] W. Eisenbeiß, J. Marotz, and J.-P. Schrade, “Reflection-optical multispectral imaging method for objective determination of burn depth,” *Burns*, vol. 25, no. 8, pp. 697–704, 1999.
- [114] H. N. Le, M. S. Kim, J. Hwang, Y. Yang, P. U. Thainual, J. U. Kang, and D.-H. Kim, “An average enumeration method of hyperspectral imaging data for quantitative evaluation of medical device surface contamination,” *Biomedical optics express*, vol. 5, no. 10, pp. 3613–3627, 2014.
- [115] P. B. Jones, H. K. Shin, D. A. Boas, B. T. Hyman, M. J. Moskowitz, C. Ayata, and A. K. Dunn, “Simultaneous multispectral reflectance imaging and laser speckle flowmetry of cerebral blood flow and oxygen metabolism in focal cerebral ischemia,” *Journal of biomedical optics*, vol. 13, no. 4, p. 044007, 2008.
- [116] M. B. Bouchard, B. R. Chen, S. A. Burgess, and E. M. Hillman, “Ultra-fast multispectral optical imaging of cortical oxygenation, blood flow,

BIBLIOGRAPHY

- and intracellular calcium dynamics,” *Optics express*, vol. 17, no. 18, pp. 15 670–15 678, 2009.
- [117] M. G. Sowa, J. R. Payette, M. D. Hewko, and H. H. Mantsch, “Visible-near infrared multispectral imaging of the rat dorsal skin flap,” *Journal of biomedical optics*, vol. 4, no. 4, pp. 474–482, 1999.
- [118] H. N. Le, J. Opferman, R. Decker, G. W. Cheon, P. C. Kim, J. U. Kang, and A. Krieger, “In vivo perfusion assessment of an anastomosis surgery on porcine intestinal model (conference presentation),” in *Imaging, Manipulation, and Analysis of Biomolecules, Cells, and Tissues IX*, vol. 9711. International Society for Optics and Photonics, 2016, p. 971112.
- [119] J. Cha, A. Shademan, H. N. Le, R. Decker, P. C. Kim, J. U. Kang, and A. Krieger, “Multispectral tissue characterization for intestinal anastomosis optimization,” *Journal of biomedical optics*, vol. 20, no. 10, p. 106001, 2015.
- [120] L. Wang, S. L. Jacques, and L. Zheng, “Mcm1—monte carlo modeling of light transport in multi-layered tissues,” *Computer methods and programs in biomedicine*, vol. 47, no. 2, pp. 131–146, 1995.
- [121] B. Park, W. Windham, K. Lawrence, and D. Smith, “Contaminant classification of poultry hyperspectral imagery using a spectral angle mapper algorithm,” *Biosystems Engineering*, vol. 96, no. 3, pp. 323–333, 2007.

BIBLIOGRAPHY

- [122] Z. I. Botev, J. F. Grotowski, D. P. Kroese *et al.*, “Kernel density estimation via diffusion,” *The annals of Statistics*, vol. 38, no. 5, pp. 2916–2957, 2010.
- [123] S. Prahl, “Optical absorption of hemoglobin,” <http://omlc.ogi.edu/spectra/hemoglobin>, 1999.
- [124] N. T. Clancy, S. Arya, D. Stoyanov, M. Singh, G. B. Hanna, and D. S. Elson, “Intraoperative measurement of bowel oxygen saturation using a multispectral imaging laparoscope,” *Biomedical optics express*, vol. 6, no. 10, pp. 4179–4190, 2015.
- [125] J. Waninger, G. W. Kauffmann, I. A. Shah, and E. H. Farthmann, “Influence of the distance between interrupted sutures and the tension of sutures on the healing of experimental colonic anastomoses,” *The American journal of surgery*, vol. 163, no. 3, pp. 319–323, 1992.
- [126] H. C. Sagi, S. Papp, and T. DiPasquale, “The effect of suture pattern and tension on cutaneous blood flow as assessed by laser doppler flowmetry in a pig model,” *Journal of orthopaedic trauma*, vol. 22, no. 3, pp. 171–175, 2008.
- [127] Y. Hirohara, Y. OKawa, T. Mihashi, T. Yamaguchi, N. Nakazawa, Y. Tsuruga, H. Aoki, N. Maeda, I. Uchida, and T. Fujikado, “Validity of retinal oxygen saturation analysis: Hyperspectral imaging in visible wavelength

BIBLIOGRAPHY

- with fundus camera and liquid crystal wavelength tunable filter,” *Optical review*, vol. 14, no. 3, p. 151, 2007.
- [128] P. A. van Beest, J. van Ingen, E. C. Boerma, N. D. Holman, H. Groen, M. Koopmans, P. E. Spronk, and M. A. Kuiper, “No agreement of mixed venous and central venous saturation in sepsis, independent of sepsis origin,” *Critical Care*, vol. 14, no. 6, p. R219, 2010.
- [129] J. K. Noel, K. Fahrbach, R. Estok, C. Cella, D. Frame, H. Linz, R. R. Cima, E. J. Dozois, and A. J. Senagore, “Minimally invasive colorectal resection outcomes: short-term comparison with open procedures,” *J. of the American College of Surgeons*, vol. 204, no. 2, pp. 291–307, 2007.
- [130] T. M. Fullum, J. A. Ladapo, B. J. Borah, and C. L. Gunnarsson, “Comparison of the clinical and economic outcomes between open and minimally invasive appendectomy and colectomy: evidence from a large commercial payer database,” *Surgical endoscopy*, vol. 24, no. 4, pp. 845–853, 2010.
- [131] J. Finkelstein, E. Eckersberger, H. Sadri, S. S. Taneja, H. Lepor, and B. Djavan, “Open versus laparoscopic versus robot-assisted laparoscopic prostatectomy: the European and US experience,” *Reviews in urology*, vol. 12, no. 1, p. 35, 2010.
- [132] H. N. Le, J. D. Opfermann, M. Kam, S. Raghunathan, H. Saeidi, S. Leonard, J. U. Kang, and A. Krieger, “Semi-autonomous laparoscopic

BIBLIOGRAPHY

- robotic electro-surgery with a novel 3d endoscope* research reported in this paper was supported by national institute of biomedical imaging and bioengineering of the national institutes of health under award numbers 1r01eb020610 and r21eb024707. the content is solely the responsibility of the authors and does not necessarily represent the official views of the national institutes of health.” in *2018 IEEE International Conference on Robotics and Automation (ICRA)*. IEEE, 2018, pp. 6637–6644.
- [133] H. Saeidi, H. N. Le, J. D. Opfermann, S. Leonard, A. Kim, H. M., J. U. Kang, and A. Krieger, “Autonomous laparoscopic robotic suturing with a novel actuated suturing tool and 3d endoscope,” in *2019 IEEE International Conference on Robotics and Automation (ICRA)*, under review. IEEE, 2019.
- [134] N. Le Hanh, S. Wei, S. Leonard, J. Opfermann, A. Krieger, and J. U. Kang, “Suture maps based on structural enhanced imaging endoscope for laparoscopic robotic surgery,” in *CLEO: QELS Fundamental Science*. Optical Society of America, 2018, pp. JTu2A–106.
- [135] C. Hennemersperger, B. Fuerst, S. Virga, O. Zettinig, B. Frisch, T. Neff, and N. Navab, “Towards MRI-Based Autonomous Robotic US Acquisitions: A First Feasibility Study,” *IEEE Transactions on Medical Imaging*, vol. 36, no. 2, pp. 538–548, Feb. 2017.

BIBLIOGRAPHY

- [136] H. Bruyninckx, P. Soetens, and B. Koninckx, “The real-time motion control core of the Orocos project,” in *2003 IEEE International Conference on Robotics and Automation (Cat. No.03CH37422)*, vol. 2, Sep. 2003, pp. 2766–2771 vol.2.
- [137] T. Kröger, “Opening the door to new sensor-based robot applications #x2014;The Reflexxes Motion Libraries,” in *2011 IEEE International Conference on Robotics and Automation*, May 2011, pp. 1–4.
- [138] K. S. Arun, T. S. Huang, and S. D. Blostein, “Least-Squares Fitting of Two 3-D Point Sets,” *IEEE Transactions on Pattern Analysis and Machine Intelligence*, vol. PAMI-9, no. 5, pp. 698–700, Sep. 1987.
- [139] R. B. Rusu, Z. C. Marton, N. Blodow, M. Dolha, and M. Beetz, “Towards 3d point cloud based object maps for household environments,” *Robotics and Autonomous Systems*, vol. 56, no. 11, pp. 927–941, 2008.
- [140] M. Alexa, J. Behr, D. Cohen-Or, S. Fleishman, D. Levin, and C. T. Silva, “Computing and rendering point set surfaces,” *IEEE Transactions on visualization and computer graphics*, vol. 9, no. 1, pp. 3–15, 2003.
- [141] D.-T. Lee and B. J. Schachter, “Two algorithms for constructing a delaunay triangulation,” *International Journal of Computer & Information Sciences*, vol. 9, no. 3, pp. 219–242, 1980.

BIBLIOGRAPHY

- [142] E. W. Dijkstra, “A note on two problems in connexion with graphs,” *Numerische mathematik*, vol. 1, no. 1, pp. 269–271, 1959.
- [143] S. Leonard, A. Shademan, Y. Kim, A. Krieger, and P. C. W. Kim, “Smart Tissue Anastomosis Robot (STAR): Accuracy evaluation for supervisory suturing using near-infrared fluorescent markers,” in *2014 IEEE International Conference on Robotics and Automation (ICRA)*, May 2014, pp. 1889–1894.
- [144] Z. Wang, <http://optacist.org>.
- [145] “Package summary,” http://wiki.ros.org/camera_calibration.
- [146] S. Leonard, A. Shademan, Y. Kim, A. Krieger, and P. C. Kim, “Smart Tissue Anastomosis Robot (STAR): Accuracy evaluation for supervisory suturing using near-infrared fluorescent markers,” in *Int. Conf. on Robotics and Automation (ICRA)*, 2014, pp. 1889–1894.
- [147] S. Leonard, K. L. Wu, Y. Kim, A. Krieger, and P. C. Kim, “Smart tissue anastomosis robot (STAR): A vision-guided robotics system for laparoscopic suturing,” *IEEE Trans. on Biomedical Engineering*, vol. 61, no. 4, pp. 1305–1317, 2014.
- [148] C. M. Kang, H. S. Chi, J. Y. Kim, G. H. Choi, K. S. Kim, J. S. Choi, W. J. Lee, and B. R. Kim, “A case of robot-assisted excision of choledochal cyst,

BIBLIOGRAPHY

- hepaticojejunostomy, and extracorporeal Roux-en-y anastomosis using the da Vinci surgical system,” *Surgical Laparoscopy, Endoscopy & Percutaneous Techniques*, vol. 17, no. 6, pp. 538–541, Dec. 2007.
- [149] M. Honda, A. Kuriyama, H. Noma, S. Nunobe, and T. A. Furukawa, “Hand-sewn versus mechanical esophagogastric anastomosis after esophagectomy: a systematic review and meta-analysis,” *Annals of surgery*, vol. 257, no. 2, pp. 238–248, 2013.
- [150] Y. Cengiz, P. Blomquist, and L. A. Israelsson, “Small tissue bites and wound strength: an experimental study,” *Archives of Surgery*, vol. 136, no. 3, pp. 272–275, 2001.
- [151] D. Millbourn, Y. Cengiz, and L. A. Israelsson, “Effect of stitch length on wound complications after closure of midline incisions: a randomized controlled trial,” *Archives of Surgery*, vol. 144, no. 11, pp. 1056–1059, 2009.
- [152] Reflexxes motion libraries for online trajectory generation. [Online]. Available: <http://www.reflexxes.ws/>
- [153] R. Smits. KDL: Kinematics and Dynamics Library. <http://www.orocos.org/kdl>.
- [154] G. Schreiber, A. Stemmer, and R. Bischoff, “The fast research inter-

BIBLIOGRAPHY

- face for the kuka lightweight robot,” in *IEEE Workshop on Innovative Robot Control Architectures for Demanding (Research) Applications How to Modify and Enhance Commercial Controllers (ICRA 2010)*. Citeseer, 2010, pp. 15–21.
- [155] P. Soetens, “RTT: Real-Time Toolkit,” <http://www.orocos.org/rtt>.
- [156] H. H. Young, “The early diagnosis and radical cure of carcinoma of the prostate.” *Transactions of the Southern Surgical and Gynecological Association*, vol. 18, p. 253, 1906.
- [157] P. C. Walsh, “The discovery of the cavernous nerves and development of nerve sparing radical retropubic prostatectomy,” *The Journal of urology*, vol. 177, no. 5, pp. 1632–1635, 2007.
- [158] —, “Perfecting nerve-sparing radical prostatectomy: sailing in uncharted waters.” *The Canadian journal of urology*, vol. 15, no. 5, pp. 4230–4232, 2008.
- [159] Y. H. Park, C. W. Jeong, and S. E. Lee, “A comprehensive review of neuroanatomy of the prostate,” *Prostate international*, vol. 1, no. 4, pp. 1–7, 2013.
- [160] N. M. Fried and A. L. Burnett, “Novel methods for mapping the cav-

BIBLIOGRAPHY

- ernous nerves during radical prostatectomy,” *Nature Reviews Urology*, vol. 12, no. 8, p. 451, 2015.
- [161] A. Magheli, J. Busch, N. Leva, M. Schrader, S. Deger, K. Miller, and M. Lein, “Comparison of surgical technique (open vs. laparoscopic) on pathological and long term functional outcomes following radical prostatectomy,” *BMC urology*, vol. 14, no. 1, p. 18, 2014.
- [162] M. E. Nielsen, E. M. Schaeffer, P. Marschke, and P. C. Walsh, “High anterior release of the levator fascia improves sexual function following open radical retropubic prostatectomy,” *The Journal of urology*, vol. 180, no. 6, pp. 2557–2564, 2008.
- [163] J. Binder and W. Kramer, “Robotically-assisted laparoscopic radical prostatectomy,” *BJU international*, vol. 87, no. 4, pp. 408–410, 2001.
- [164] T. B. Manny, M. Patel, and A. K. Hemal, “Fluorescence-enhanced robotic radical prostatectomy using real-time lymphangiography and tissue marking with percutaneous injection of unconjugated indocyanine green: the initial clinical experience in 50 patients,” *European urology*, vol. 65, no. 6, pp. 1162–1168, 2014.
- [165] S. L. Troyan, V. Kianzad, S. L. Gibbs-Strauss, S. Gioux, A. Matsui, R. Oketokoun, L. Ngo, A. Khamene, F. Azar, and J. V. Frangioni, “The flareTM intraoperative near-infrared fluorescence imaging system: a

BIBLIOGRAPHY

- first-in-human clinical trial in breast cancer sentinel lymph node mapping,” *Annals of surgical oncology*, vol. 16, no. 10, pp. 2943–2952, 2009.
- [166] M. H. Park, H. Hyun, Y. Ashitate, H. Wada, G. Park, J. H. Lee, C. Njiojob, M. Henary, J. V. Frangioni, and H. S. Choi, “Prototype nerve-specific near-infrared fluorophores,” *Theranostics*, vol. 4, no. 8, p. 823, 2014.
- [167] V. E. Coterio, S. Y. Kimm, T. M. Siclovan, R. Zhang, E. M. Kim, K. Matsumoto, T. Gondo, P. T. Scardino, S. Yazdanfar, V. P. Laudone *et al.*, “Improved intraoperative visualization of nerves through a myelin-binding fluorophore and dual-mode laparoscopic imaging,” *PloS one*, vol. 10, no. 6, p. e0130276, 2015.
- [168] C. W. Barth and S. L. Gibbs, “Direct administration of nerve-specific contrast to improve nerve sparing radical prostatectomy,” *Theranostics*, vol. 7, no. 3, p. 573, 2017.
- [169] S. L. Gibbs-Strauss, K. A. Nasr, K. M. Fish, O. Khullar, Y. Ashitate, T. M. Siclovan, B. F. Johnson, N. E. Barnhardt, C. A. T. Hehir, and J. V. Frangioni, “Nerve-highlighting fluorescent contrast agents for image-guided surgery,” *Molecular imaging*, vol. 10, no. 2, pp. 7290–2010, 2011.
- [170] K. He, J. Zhou, F. Yang, C. Chi, H. Li, Y. Mao, B. Hui, K. Wang, J. Tian, and J. Wang, “Near-infrared intraoperative imaging of thoracic sym-

BIBLIOGRAPHY

- pathetic nerves: From preclinical study to clinical trial,” *Theranostics*, vol. 8, no. 2, p. 304, 2018.
- [171] O. J. Wagner, B. E. Louie, E. Vallières, R. W. Aye, and A. S. Fari-var, “Near-infrared fluorescence imaging can help identify the contralat-eral phrenic nerve during robotic thymectomy,” *The Annals of thoracic surgery*, vol. 94, no. 2, pp. 622–625, 2012.
- [172] H. K. Zhang, P. Yan, J. Kang, D. S. Abou, H. N. Le, A. K. Jha, D. L. Thorek, J. U. Kang, A. Rahmim, D. F. Wong *et al.*, “Listening to mem-brane potential: photoacoustic voltage-sensitive dye recording,” *Journal of Biomedical Optics*, vol. 22, no. 4, p. 045006, 2017.
- [173] J. Kang, H. K. Zhang, S. D. Kadam, J. Fedorko, H. Valentine, A. P. Malla, P. Yan, J. U. Kang, A. Rahmim, A. Gjedde *et al.*, “Transcranial in vivo recording of neural activity in the rodent brain with near-infrared pho-toacoustic voltage-sensitive dye imaging,” *bioRxiv*, p. 202408, 2018.
- [174] M. Yang and W. J. Brackenbury, “Membrane potential and cancer pro-gression,” *Frontiers in physiology*, vol. 4, p. 185, 2013.
- [175] R. W. Pak, J. Kang, H. Valentine, L. M. Loew, D. L. Thorek, E. M. Boc-tor, D. F. Wong, and J. U. Kang, “Voltage-sensitive dye delivery through the blood brain barrier using adenosine receptor agonist regadenoson,” *bioRxiv*, p. 316505, 2018.

BIBLIOGRAPHY

- [176] S. F. Sezen and A. L. Burnett, “Intracavernosal pressure monitoring in mice: responses to electrical stimulation of the cavernous nerve and to intracavernosal drug administration,” *Journal of andrology*, vol. 21, no. 2, pp. 311–315, 2000.
- [177] L. V. Wang and S. Hu, “Photoacoustic tomography: in vivo imaging from organelles to organs,” *science*, vol. 335, no. 6075, pp. 1458–1462, 2012.
- [178] K. S. Valluru, K. E. Wilson, and J. K. Willmann, “Photoacoustic imaging in oncology: translational preclinical and early clinical experience,” *Radiology*, vol. 280, no. 2, pp. 332–349, 2016.
- [179] S. Y. Emelianov, P.-C. Li, and M. O’Donnell, “Photoacoustics for molecular imaging and therapy,” *Physics today*, vol. 62, no. 8, p. 34, 2009.
- [180] J. Kang, H. N. Le, H. K. Zhang, J. U. Kang, M. M. Harraz, and E. M. Bector, “Initial proof-of-concept of photoacoustic cell stimulation approach: preliminary in vitro study,” in *Optogenetics and Optical Manipulation*, vol. 10052. International Society for Optics and Photonics, 2017, p. 100520U.
- [181] J. Kang, J. H. Chang, S. M. Kim, H. J. Lee, H. Kim, B. C. Wilson, and T.-K. Song, “Real-time sentinel lymph node biopsy guidance using combined ultrasound, photoacoustic, fluorescence imaging: in vivo proof-

BIBLIOGRAPHY

- of-principle and validation with nodal obstruction,” *Scientific Reports*, vol. 7, p. 45008, 2017.
- [182] S. Tozburun, G. A. Lagoda, A. L. Burnett, and N. M. Fried, “Subsurface near-infrared laser stimulation of the periprostatic cavernous nerves,” *Journal of biophotonics*, vol. 5, no. 10, pp. 793–800, 2012.
- [183] S. Tozburun, C. M. Cilip, G. A. Lagoda, A. L. Burnett, and N. M. Fried, “Continuous-wave infrared optical nerve stimulation for potential diagnostic applications,” *Journal of biomedical optics*, vol. 15, no. 5, p. 055012, 2010.
- [184] S. Tozburun, C. D. Stahl, T. C. Hutchens, G. A. Lagoda, A. L. Burnett, and N. M. Fried, “Continuous-wave infrared subsurface optical stimulation of the rat prostate cavernous nerves using a 1490-nm diode laser,” *Urology*, vol. 82, no. 4, pp. 969–973, 2013.
- [185] J. Mueller, W. Legon, A. Opitz, T. F. Sato, and W. J. Tyler, “Transcranial focused ultrasound modulates intrinsic and evoked eeg dynamics,” *Brain stimulation*, vol. 7, no. 6, pp. 900–908, 2014.
- [186] W. Legon, T. F. Sato, A. Opitz, J. Mueller, A. Barbour, A. Williams, and W. J. Tyler, “Transcranial focused ultrasound modulates the activity of primary somatosensory cortex in humans,” *Nature neuroscience*, vol. 17, no. 2, p. 322, 2014.

BIBLIOGRAPHY

- [187] O. Canguven and A. Burnett, “Laboratory forum: Cavernous nerve injury using rodent animal models,” *The journal of sexual medicine*, vol. 5, no. 8, pp. 1776–1785, 2008.
- [188] J. Fang, H. Nakamura, and H. Maeda, “The epr effect: unique features of tumor blood vessels for drug delivery, factors involved, and limitations and augmentation of the effect,” *Advanced drug delivery reviews*, vol. 63, no. 3, pp. 136–151, 2011.
- [189] W. Arap, R. Pasqualini, and E. Ruoslahti, “Cancer treatment by targeted drug delivery to tumor vasculature in a mouse model,” *Science*, vol. 279, no. 5349, pp. 377–380, 1998.
- [190] P. Carmeliet and M. Tessier-Lavigne, “Common mechanisms of nerve and blood vessel wiring,” *Nature*, vol. 436, no. 7048, p. 193, 2005.
- [191] M. R. Metea and E. A. Newman, “Glial cells dilate and constrict blood vessels: a mechanism of neurovascular coupling,” *Journal of Neuroscience*, vol. 26, no. 11, pp. 2862–2870, 2006.
- [192] D. Attwell, A. M. Buchan, S. Charkpak, M. Lauritzen, B. A. MacVicar, and E. A. Newman, “Glial and neuronal control of brain blood flow,” *Nature*, vol. 468, no. 7321, p. 232, 2010.
- [193] K. Welsher, Z. Liu, S. P. Sherlock, J. T. Robinson, Z. Chen, D. Daranciang,

BIBLIOGRAPHY

- and H. Dai, “A route to brightly fluorescent carbon nanotubes for near-infrared imaging in mice,” *Nature nanotechnology*, vol. 4, no. 11, p. 773, 2009.
- [194] B. J. Bacskai, S. T. Kajdasz, R. H. Christie, C. Carter, D. Games, P. Seubert, D. Schenk, and B. T. Hyman, “Imaging of amyloid- β deposits in brains of living mice permits direct observation of clearance of plaques with immunotherapy,” *Nature medicine*, vol. 7, no. 3, p. 369, 2001.
- [195] L. Tian, S. A. Hires, T. Mao, D. Huber, M. E. Chiappe, S. H. Chalasani, L. Petreanu, J. Akerboom, S. A. McKinney, E. R. Schreiter *et al.*, “Imaging neural activity in worms, flies and mice with improved gcamp calcium indicators,” *Nature methods*, vol. 6, no. 12, p. 875, 2009.
- [196] Q. T. Nguyen, E. S. Olson, T. A. Aguilera, T. Jiang, M. Scadeng, L. G. Ellies, and R. Y. Tsien, “Surgery with molecular fluorescence imaging using activatable cell-penetrating peptides decreases residual cancer and improves survival,” *Proceedings of the National Academy of Sciences*, p. 200910261, 2010.
- [197] K. Welsher, S. P. Sherlock, and H. Dai, “Deep-tissue anatomical imaging of mice using carbon nanotube fluorophores in the second near-infrared window,” *Proceedings of the National Academy of Sciences*, vol. 108, no. 22, pp. 8943–8948, 2011.

BIBLIOGRAPHY

- [198] G. Hong, J. C. Lee, J. T. Robinson, U. Raaz, L. Xie, N. F. Huang, J. P. Cooke, and H. Dai, “Multifunctional in vivo vascular imaging using near-infrared ii fluorescence,” *Nature medicine*, vol. 18, no. 12, p. 1841, 2012.
- [199] G. Hong, S. Diao, J. Chang, A. L. Antaris, C. Chen, B. Zhang, S. Zhao, D. N. Atochin, P. L. Huang, K. I. Andreasson *et al.*, “Through-skull fluorescence imaging of the brain in a new near-infrared window,” *Nature Photonics*, vol. 8, no. 9, p. 723, 2014.
- [200] H. N. Le, Y.-T. A. Gau, A. Rahmim, D. F. Wong, D. E. Bergles, and J. U. Kang, “Through-skull vasculature assessment using fluorescence brain imaging on murine models at around 800 nm,” in *Neural Imaging and Sensing*, vol. 10051. International Society for Optics and Photonics, 2017, p. 100510M.
- [201] R. W. Pak, H. N. Le, H. Valentine, D. Thorek, A. Rahmim, D. Wong, and J. U. Kang, “Assessment of lexiscan for blood brain barrier disruption to facilitate fluorescence brain imaging,” in *CLEO: Applications and Technology*. Optical Society of America, 2017, pp. ATu3B–2.
- [202] H. K. Zhang, P. Yan, J. Kang, D. Abou, H. N. Le, A. K. Jha, D. Thorek, J. Kang, A. Rahmim, D. F. Wang *et al.*, “Photoacoustics as a new modality for recording membrane potential changes,” *Biophysical Journal*, vol. 112, no. 3, p. 285a, 2017.

BIBLIOGRAPHY

- [203] Y. Zhu, A. K. Jha, J. K. Dreyer, H. N. Le, J. U. Kang, P. E. Roland, D. F. Wong, and A. Rahmim, “A three-step reconstruction method for fluorescence molecular tomography based on compressive sensing,” in *Optical Tomography and Spectroscopy of Tissue XII*, vol. 10059. International Society for Optics and Photonics, 2017, p. 1005911.
- [204] H. K. Zhang, J. Kang, P. Yan, D. S. Abou, H. N. Le, D. L. Thorek, J. U. Kang, A. Gjedde, A. Rahmim, D. F. Wong *et al.*, “Recording membrane potential changes through photoacoustic voltage sensitive dye,” in *Photons Plus Ultrasound: Imaging and Sensing 2017*, vol. 10064. International Society for Optics and Photonics, 2017, p. 1006407.

Vita

Hanh N. D. Le was born and raised in Vietnam. At 20, she moved to the United States of America to continue her undergraduate degree with a university scholarship from the Catholic University of America. While enrolling in the Electrical Engineering Department, Hanh was a research assistant from the Electromagnetic Modeling and Optimization Laboratory. At the end of her undergraduate, Hanh phased her research interest to photonics and optoelectronics for medical applications, she became a research engineer at the U.S. Food and Drug Administration, with contributions in numerical laser thermal safety assessment, and hyperspectral imaging system and spectral methodological development.

Hanh later entered the PhD program in Electrical & Computer Engineering Department at Johns Hopkins University, and received the MSE while pursuing her PhD study at the department. Her PhD research interests focus on the developing of multimodal endoscopic systems for the enhancement of medical diagnostic and for the minimally invasive robotic surgery. Hanh is the

VITA

author of multiple peer-review journals and conferences and co-inventor of a patent application. Over the academic career, Hanh served as technical reviewer for Optics Express, Optics Letters and Photonics Technology Letters publications. She also served as President of the Optical Society of America, Student Chapter and Graduate Student Representative of the ECE Department. Hanh received several innovation awards from the Global Engineering Innovations (Johns Hopkins University), Joseph E. Robert Jr. Endowment Award (Children's National Health System), and won Best Design Hack and a 2nd place winner for 2018 Major League Hacking in North America.